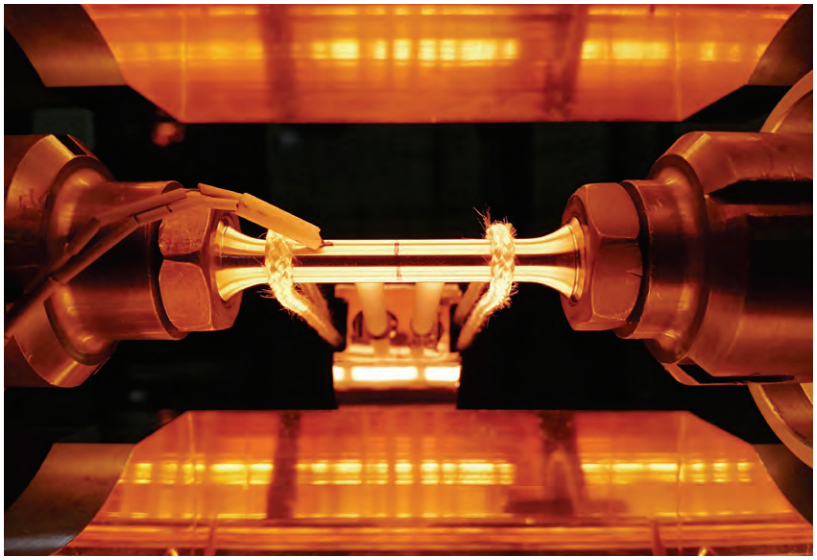

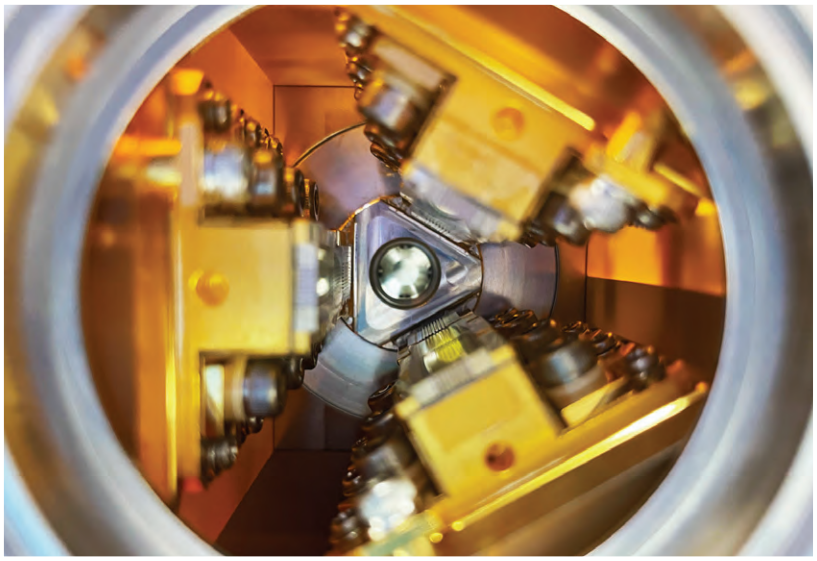

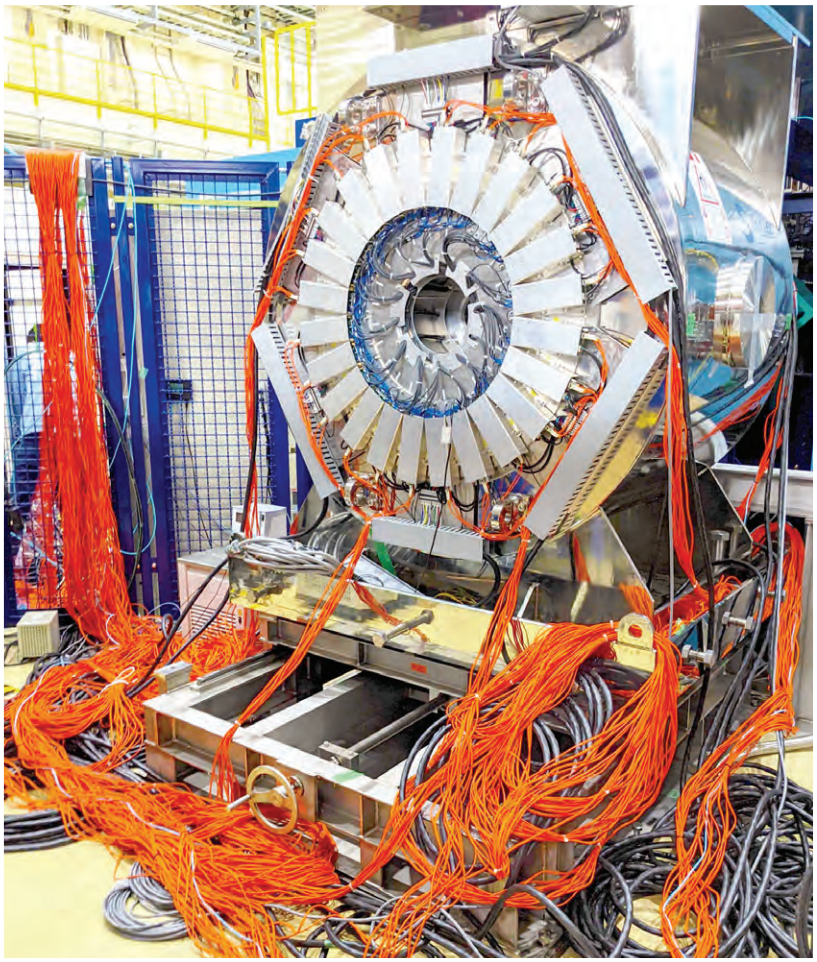

J-PARC

ANNUAL REPORT 2021

Vol.2: Materials and Life Science Experimental Facility

MLF ANNUAL REPORT

Cover photographs

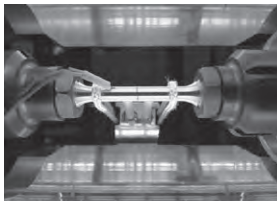

Neutron diffraction experiment under high temperature tension.
A metal sample is heated by the halogen lamps from the top and bottom in the photo, and tensile loading is applied horizontally to the metal sample.

Inside the laser amplifier excitation module, which can irradiate a total of 18 kW of excitation light from three directions to the laser crystal positioned in the center of the photo.
The high-intensity vacuum ultraviolet light produced from the laser beam amplified here is used to generate Ultra-Slow Muons.

Spectrometer for high-field muon spin relaxation/rotation/resonance up to 5 Tesla at the S-line, with 3008 scintillation fibers to detect muon decay positrons.

J-PARC MLF
Materials and Life Science Division
J-PARC Center
https://mlfinfo.jp/en

J-PARC was jointly constructed and is now operated by the High Energy Accelerator Research Organization (KEK) and the Japan Atomic Energy Agency (JAEA).

Comprehensive Research Organization for Science and Society
https://neutron.cross.or.jp/en

J-PARC 22-02

Preface

Toshiya Otomo
Division Head of Materials and Life Science Division, MLF

The proton power ramp up and instrument upgrades at the MLF were still progressing under COVID-19. Although we had to comply with the COVID-19 restrictions, the neutron and muon beams were supplied as usual. The beam power of the MLF was ramped up to 700 kW from 600 kW in April 2021 and the availability at 700 kW was more than 90%. The MLF received 740 kW during the MR operation period with slow extraction mode, which is the highest power ever attained for the long-term user operation at the MLF. With the increase of the beam power, it became more important to perform radiation prevention works and maintenance of the targets safely and on schedule. From this point of view, a long enough summer maintenance period was secured to allow the MLF and the J-PARC management to check carefully the progress, which led to the late start of the user operation in January 2022. The summer maintenance of 2021 was finished safely on schedule.

Progress was made in the development of neutron instruments, such as the low-temperature Digital image correlation technique for hybrid neutron diffraction (BL19), completion of the polarization system of the Polarized Neutron Spectrometer (BL23), noise reduction method based on deep learning which can shorten measurement time to one tenth of the conventional neutron reflectometry measurement on BL17, H_2O/D_2O vapors supply system, New 2D scintillator detectors for a single crystal diffractometer (BL18) and Fe/Ge polarizing supermirror with m = 6.2 (the highest achieved in the world).

In the muon H line, the on-beam commissioning performed since the first beam delivery in January 2022 was completed successfully, and the S-type experiment (DeeMe; an approved proposal for conducting a muon-electron conversion experiment at J-PARC MLF. http://deeme.phys.sci.osaka-u.ac.jp). The initial analysis of the samples returned by Hayabusa-2 was performed using a non-destructive elemental analysis method with negative muon capture characteristic X-rays at the D-line.

We initiated a series of internal group discussions to establish MLF's future plans, "MLF2030", based on the existing instruments and devices. This plan is expected to be connected with or to improve the plan of target station 2 of the MLF.

The users' visits from abroad were significantly limited by the COVID-19 restrictions. Many proposals were carried out and some of them were conducted by beamline scientists without user's visit. To implement these carried-out proposals, the 2020B term was shortened and the call for proposals was combined into a single term of 2020B and 2021A. On the other hand, several workshops were held online, such as the target system workshop with SNS of Oak Ridge National Laboratory, the18th Korea-Japan meeting on neutron science hosted by JSNS (The Japanese Society for Neutron Science), J-PARC MLF and KNBUA (The Korean Neutron Beam Users Association), the Annual meeting of industrial application at J-PARC MLF with 352 participants, including 150 attendees from companies, collaborative scientific and technical series of workshops with the Australian Nuclear Science and Technology Organization (ANSTO), the 5th Neutron and Muon School (NM-school) was held as KEK-IINAS (Inter-Institution Network for Accelerator Science) School for both lectures and remote hands-on (https://mlfinfo.jp/sp/school/5th-nms/index.html).

In conjunction with the reopening of the neutron user program at Japan Research Reactor - 3 (JRR-3), J-JOIN was formed by JAEA, KEK, CROSS, the University of Tokyo, and Ibaraki Prefecture in 2021. A portal site of J-JOIN has been opened, which provides one-stop consultation for neutron and muon use to support users not familiar with that field, and allow them to gain the expertise to access the neutron and muon experiments.

Although the user program at MLF was severely affected by the pandemic, we managed to continue it thanks to the efforts of the MLF staff and the understanding of the MLF users. I believe that the MLF will continue to deliver cutting-edge science and more opportunities for its users under these difficult circumstances.

Materials and Life Science Division, Japan Proton Accelerator Research Complex
https://mlfinfo.jp/en

Preface

Mitsuhiro Shibayama
Director, CROSS

The Comprehensive Research Organization for Science and Society (CROSS), a partner institution of the Materials and Life Science Experimental Facility (MLF), is honored to release the J-PARC MLF ANNUAL REPORT 2021 (MLF-AR2021), which includes sections on R&D Highlights, Neutron Sources, Neutron Science, Muon Science and more. CROSS is a registered organization of the J-PARC's Specific Neutron Beamline Facility, appointed by the Japanese government in 2011. CROSS supports the activities of the 7 public beamlines of MLF (BL01 4SEASONS, BL02 DNA, BL11 PLANET, BL15 TAIKAN, BL17 SHARAKU, BL18 SENJU, and BL22 RADEN) and provides high-quality user support to MLF users, both academic and industrial researchers, and promotes the use of the facility.

In FY2021, the neutron beam at MLF was stably operated mostly at 600 – 700 kW, which ensured highly reliable machine operation. In FY2020, due to the COVID-19 pandemic, it was necessary to merge the 2020B and 2021A terms and expand the proposal round to 2020B + 2021A. Therefore, the statistics provided in this volume, i.e., MLF-AR2021, is exclusively for 2021B. The total numbers of (short term) neutron proposals submitted and accepted in the term of 2021B were 343 and 142, respectively, and those for the Public Beamlines were 162 and 59, respectively. Regarding the outcome, 193 scientific papers (excluding proceedings) were published from the MLF in 2021, 72 of which were from the Public Beamlines. The details are included in the Research and Development Highlights collected in this volume. The numbers of press releases were 21 from the MLF and 8 from the Public Beamlines. These numbers illustrate the high activities of the Public Beamlines as well as the MLF, which have been used by a wide range of users from the academia and various industries. The special program for new users "New User Promotion (NUP)", which started in 2016, was operated also in 2021, and 9 NUP neutron users conducted experiments at the MLF.

Regarding public relations, in FY2020, a unified consultation service for the J-PARC MLF, "J-PARC JOIN" was operated by the J-PARC MLF, Ibaraki Prefecture, and CROSS. In FY2021, J-PARC JOIN was renamed "J-JOIN" and the service was strengthened because JRR-3 (JAEA and the University of Tokyo) joined in this service program (https://jrr3ring.jaea.go.jp/jjoin/index_en.php).

I hope this Annual Report would provide useful information about the current status of the MLF operations and recent scientific achievements, the technical R&D reports, and so on. On behalf of CROSS, I sincerely welcome your visit to the MLF.

Neutron Science and Technology Center, Comprehensive Research Organization for Science and Society
https://neutron.cross.or.jp/en

Contents

Research and Development Highlights

Neutron Source

Neutron Science

Muon Science

MLF Safety

MLF Operations in 2021

Organization Chart

Organization Chart of J-PARC Center

- Director, J-PARC Center
  - Deputy Director (JAEA, KEK, Safety)
    - Safety Division
  - Accelerator Division
  - Materials & Life Science Division
    - Neutron Source Section
    - Neutron Science Section
    - Neutron Instrumentation Section
    - Muon Science Section
    - Technology Development Section
  - Particle & Nuclear Physics Division
  - Nuclear Transmutation Division
  - Cryogenics Section
  - Information System Section
  - Facility Engineering Section
  - Administration Division
    - Users Office

Organization Chart of CROSS

CROSS is "Registered Institution for facility Use Promotion" for the public-access neutron beam facilities at J-PARC.

- President
  - CROSS Head Office
  - Research Center for Science and Society
  - Neutron Science and Technology Center
    - Director, Neutron Science and Technology Center
      - Science Coordinators
      - R&D Division
      - Utilization Promotion Division
      - Industrial Collaboration Promotion Division
      - Safety Division
      - Administration Division
  - New Business Creation Division

The Role of CROSS

Under the terms of the legislation that supports the Public Neutron Beam Facility, CROSS is entrusted with specific responsibilities. In practical terms, the core functions of CROSS can be summarized as follows:

- *Proposal Selection and Beamtime Allocation on the Public Beamlines*
- *User Support on the Public Beamlines*
- *Establishment of an Information Resource for Facility Users*
- *Outreach and Facility Utilization Promotion*
- *Contract Beamline Assessment and Selection*

J-PARC Map

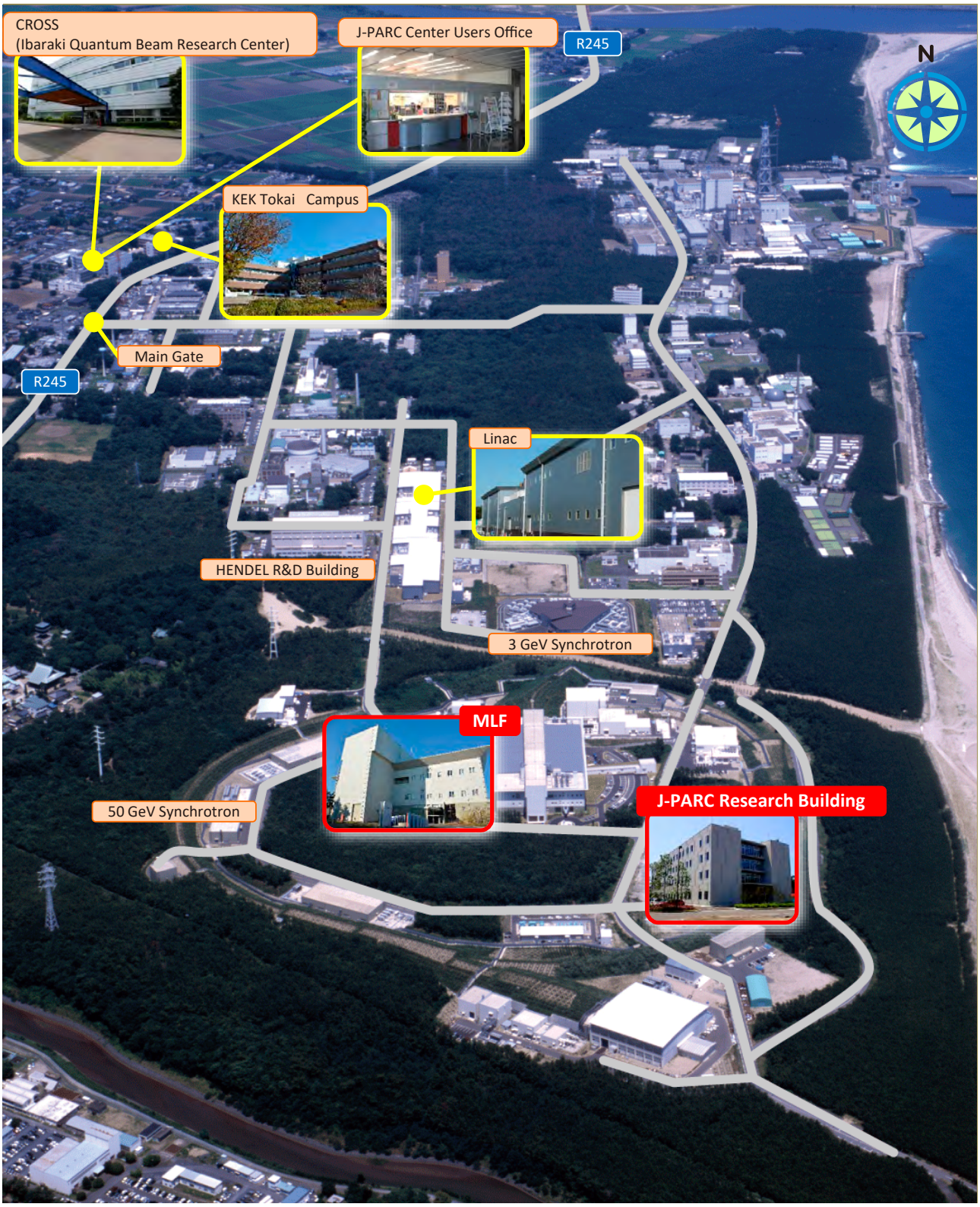
CROSS
(Ibaraki Quantum Beam Research Center)
J-PARC Center Users Office
R245
N
KEK Tokai Campus
Main Gate
R245
Linac
HENDEL R&D Building
3 GeV Synchrotron
MLF
J-PARC Research Building
50 GeV Synchrotron

Muon and Neutron Instruments

Muon Source

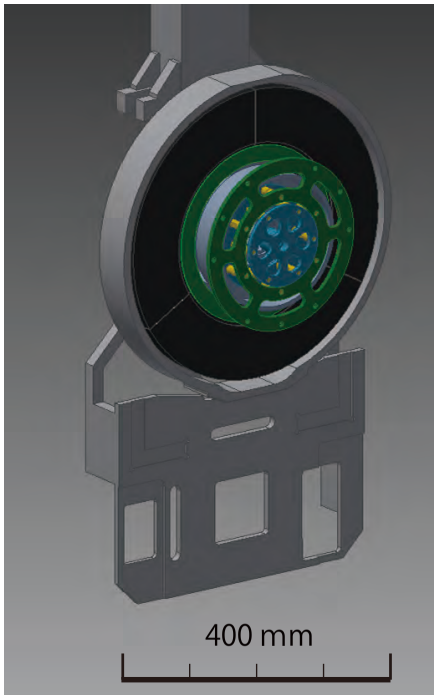

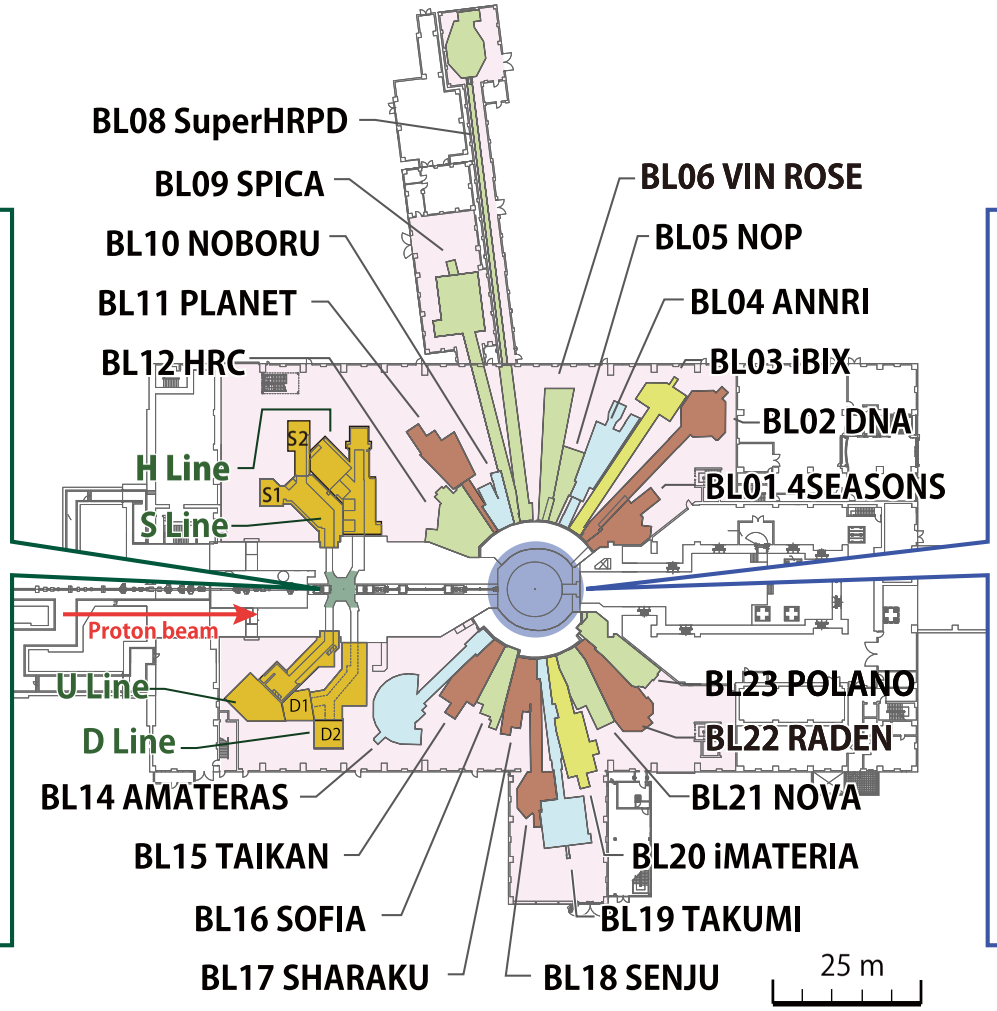

Neutron Source

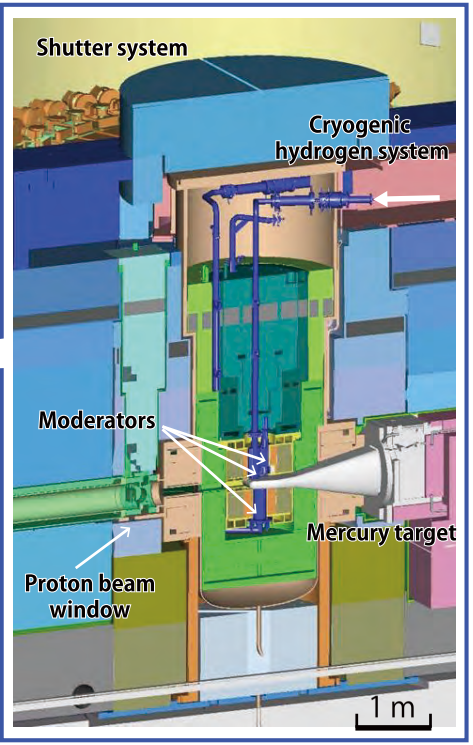

Muon Instruments

Neutron Instruments

JAEA

KEK

Public beam lines

Ibaraki Pref.

As of March 2022

Research and Development Highlights

Visualization of Local Structure around Boron in SiC Using Neutron Holography

1. Introduction

One of the basic technologies that support the infrastructure of modern society is the development of various devices using semiconductors. Silicon is still the main semiconductor material, but in order to meet the needs for higher power and high-speed communication, it is necessary to develop power devices that can efficiently control and convert power without loss. Silicon carbide (SiC) crystals are a leading candidate for this, and the competition to fabricate high-quality SiC wafers is intensifying in the world [1]. However, the crystal structure of the SiC is not as simple as silicon. SiC exhibits polymorphism, and we chose 6H-SiC among various polytypes. The 6*h*-SiC has six different crystal sites, while Si has one crystal site. In order to have functionality for these semiconductors, it is necessary to dope some impurities (dopants). Among various dopant elements for SiC, boron is used for white LEDs. It is predicted that the properties of SiC are varied depending on which crystal sites boron atoms locate. Therefore, unlike Si, it is important to control the dopant sites, and a more advanced crystal growth technology is required to realize this. However, for light element dopants such as boron and nitrogen, there had been no appropriate observation method of their local structures. Therefore, no one has known the exact locations of boron in SIC.

On the other hand, since 1998 we have developed X-ray fluorescence holography, which provides 3D atomic images around fluorescing atoms. And we have applied it to local structure analyses around dopants of many functional materials [2]. In addition, we started neutron holography in 2008, and we demonstrated successfully the multiple wavelength neutron holography using time-of-flight (TOF) technique at J-PARC in 2017 [3]. This technique uses prompt γ-rays from neutron-absorbed nuclei, like X-ray fluorescence in X-ray fluorescence holography. Therefore, neutron holography (NH) would be suitable for the investigation of the local structure around the γ-ray emitter atoms. The significant advantage of neutron holography is recording a number (50~100) of multiple-wavelength neutron holograms, which can substantially suppress ghost images. We applied neutron holography to B: $MgSi_2$ [4], and Sm: RB_6 (R = Yb, La) [5].

In the present study, we measured neutron holograms of B-doped 6H–SiC by the time-of-flight (TOF) technique and estimated the occupancies of six different sites from the reconstructed atomic images [6].

2. Experimental details

A B-doped 6H–SiC single crystal was grown by the physical vapor transport method known as the seeded sublimation process. As source materials, SiC powder was synthesized from elemental silicon and carbon with an addition of 0.065 at.% of B. The amount of doping was chosen so as to reach a chemical dopant incorporation of ca. 2×10^{19} cm^{-3}. The growth temperature was 2150°C, determined with an optical pyrometer on the top growth cell, which corresponded to ca. 2200°C at the growth interface. The total crystal height in the center of the boule was 29 mm. From this single crystal, a measurement sample with a diameter of 20.1 mm and a height of 15.2 – 21.4 mm was prepared by wire-sawing and grinding.

The NH experiment was performed at beamline 10 (BL10). The measurement was carried out in the "inverse mode," and the angular anisotropy of the sample orientation was measured from the intensity of prompt γ rays, which were mostly emitted from B. The γ-rays were detected by $Bi_4Ge_3O_{12}$ (BGO) detector with a diameter of 6 cm. The BGO detector was covered by Pb blocks to reduce the γ-ray background.

A hologram is obtained by normalizing the angular anisotropy with respect to its background. We recorded ~100 different wavelength holograms in one scan. Figure 1 shows the hologram at λ = 0.49 Å.

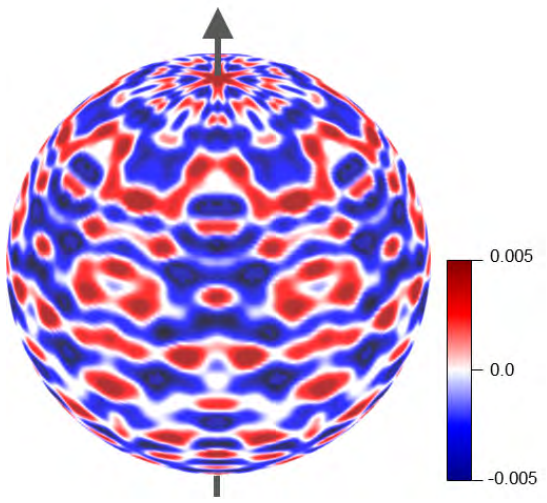

Figure 1. Neutron hologram of B-doped 6H-SiC. The wavelength is 0.49 Å.

3. Results and discussion

By applying the Barton algorithm [7], which likes to Fourier transformation, to the multiple-wavelength neutron hologram, the atomic image around the boron could be obtained as shown in Fig. 2. Boron is present at the origin. Many atomic images are observed below the boron, but none above. This result suggests that a boundary exists just above the boron.

Next, the sites occupied by boron were determined using the atomic images in the lower region of Fig. 2. As mentioned above, there are 6 different sites in boron, such as Si-*h*, Si-*c*1, Si-*c*2, C-h, C-*c*1, and C-*c*2 (see Fig. 3). The patterns of atomic images obtained from the calculated holograms with different boron sites are different. If boron was doped only at a single site, we can determine it smoothly. But the situation was not so simple.

Therefore, we assumed that the boron atoms occupied multiple sites, and calculated the site occupancy using a calculation method called the steepest descent method. As a result, it was found that 37.5% of the boron atoms were located on Si-*c*2 and 61.4% on C-*c*2, and they hardly go to other sites. We performed such a quantitative determination of boron locations in SiC for the first time.

Figure 3 shows a model diagram of the boron neighborhood created by combining the above results. The sites of Si-*c*2 and C-*c*2 are next to each other, and it is conceivable that boron is enriched there. In addition, the concentrated boron may act in forming an above boundary. The reason of the right above is related to the SiC crystal growth method. Most crystals, such as silicon, are grown by solidifying from a melt, but SiC crystals are usually grown by a physical vapor deposition, in which Si and C atoms are stacked from the bottom to the top. Therefore, the boundary would be formed when silicon or carbon are deposited directly on the boron at Si-*c*2 and C-*c*2. Such an incomplete structure may not necessarily be desirable in terms of SiC quality. However, we believe that such a discovery becomes a starting point and that the findings of this study can be applied to future SiC wafer development.

4. Perspective

Demands of power devices, which can operate with better energy efficiency, are rapidly increasing in high-speed communications, such as 5G and power control of electric vehicles.

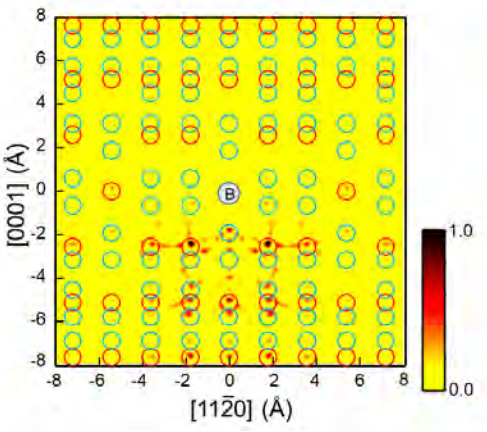

Figure 2. Images of the (11$\bar{2}$0) plane.

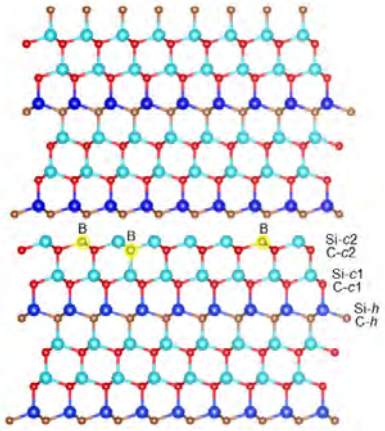

Figure 3. A possible model of the environmental structure around B.

SiC is the only material that has been put to practical use, and the control and observation of dopants that bring functionality as semiconductors is the most important issue. The material is directly related to the future social infrastructure, and the fact that we were able to accurately determine the dopant structure by neutron holography this time is considered to have a great social impact.

References

[1] P. J. Wellmann, Semicond. Sci. Technol. **33**, 103001 (2018).
[2] K. Hayashi and P. Korecki, J. Phys. Soc. Jpn. **87**, 061003 (2018).
[3] K. Hayashi et al, Sci. Adv. **3**, e1700294 (2017).
[4] W. Saito et al., ACS Appl. Energy Mater. **4**, 5123 (2021).
[5] S. Uechi, et al., N Phys. Rev. B **102**, 054104 (2020).
[6] K. Hayashi, et al., Appl. Phys. Lett. **120**, 132101 (2022).
[7] J. J. Barton, Phys. Rev. Lett. **67**, 3106 (1991).

K. Hayashi[1], K. Ohoyama[2], and P. Wellmann[3]
[1]*Nagoya Institute of Technology;* [2]*Ibaraki University;* [3]*Friedrich-Alexander Universität Erlangen-Nürnberg (FAU)*

From Translucent Liquid to Black Solid: The Irreversible Transformation of CS_2 under pressure

1. Introduction

Carbon disulfide (CS_2) is a translucent liquid made of linear S = C = S molecules. Under strong compression in the multi-GPa range, such molecules are expected to disintegrate as the C = S double-bonds break up leading to an extended solid with very different structural and electronic properties. This was indeed observed for CS_2 several decades ago [1], but despite a number of later experiments mainly carried out using diamond anvil cells [2], the nature of the transition and the properties of the final product are ill-known.

At BL11, we carried out the first in-situ high pressure neutron measurements of this famous transformation. These experiments allowed to demonstrate the possibility to recover the high-pressure product to ambient pressure and establish a recipe for mass-production of the compound in off-line compression runs. The availability of such large quantities of material at ambient pressure enables an in-depth characterization by advanced analytical methods which were not possible before [3].

2. Experimental

High pressure measurements were carried out at BL11 PLANET at 300 K using a Paris-Edinburgh high pressure cell (MG63, VX4) equipped with sintered diamond anvils. The pressure of the sample was determined from the load on the anvils and a previously established calibration curve.

3. Results and discussion

The compression of the liquid sample leads first to its crystallization into the known orthorhombic *Cmca* structure at ~1.5 GPa (Fig. 1). When the sample is then further compressed, a sudden transition occurs at ~8 GPa which leads to a complete loss of all Bragg reflections and hence to a non-crystalline material. Data collected under decompression (Fig. 1) shows that the sample can be recovered to ambient pressure without further changes of its structure and extracted from the pressure cell (Fig. 2) where the black solid material is stable over a time-scale of at least months. Laboratory analyses by Raman spectroscopy and densitometry

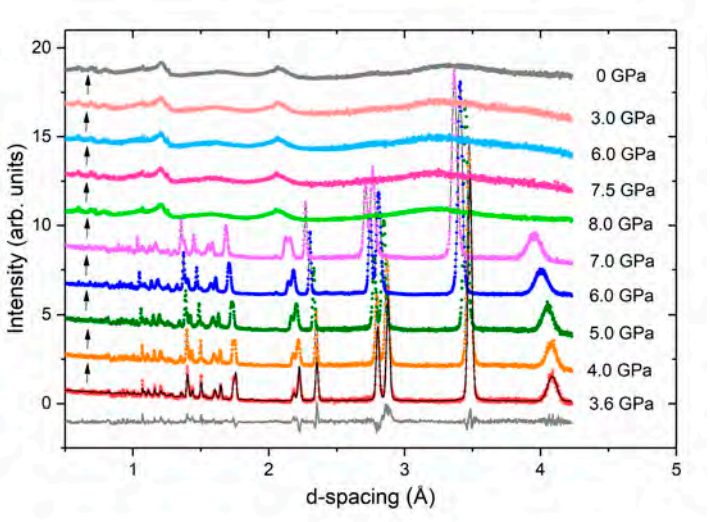

Figure 1. Neutron diffraction patterns of CS_2 under pressure, collected at BL11. At low pressures, the liquid crystallizes in an orthorhombic *Cmca* structure (a Rietveld fit and difference curve are shown for the 3.6 GPa pattern). At 8.0 GPa, the system transforms to a non-crystalline solid, which can be recovered to 0 GPa (Reprinted from Ref. [3] with permission from Elsevier).

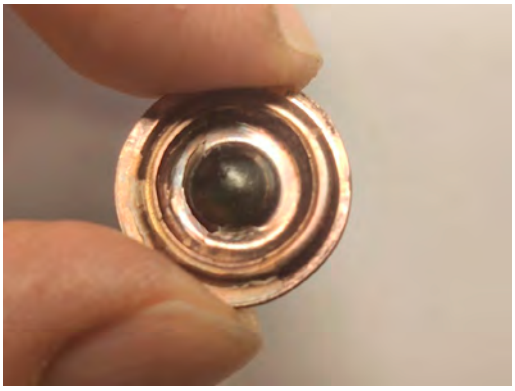

Figure 2. Picture of a sample (black sphere inside the metallic gasket) after compression of CS_2 to 8 GPa and subsequent pressure release.

carried out in the home institute of the PI showed that the recovered material is a mixture of crystalline sulfur and a compound with composition C_2S. Subsequent neutron diffraction measurements carried out also at BL11 in a vanadium can showed that C_2S has a graphitic structure with sp^2-bonded carbon flakes of nanometric size (typically 3 nm diameter). A similar analysis using X-ray diffraction (which is more sensitive to sulfur atoms) confirms the presence of sulfur and suggests bonding to the graphitic matrix through both covalent C-S and van der Waals bonds. Scanning and transmission electron microscopy also confirms the average stoichiometry as C_2S but reveals a significant scatter in the C/S ratio depending on the selected grain of the powder. The sample was also investigated by resistivity measurements in the 4–300 K range. C_2S is a semiconductor with a small gap of 45 meV, and its electrical conductivity can be described by a variable-range hopping model with the dimensional parameter $d = 1.3$ [4]. Finally, it was found by gravimetric measurements that the sulfur content can be reduced by heating the sample to beyond 200°C where the van der Waals bonded fraction of sulfur detaches from the carbon matrix. This leaves only the covalently bonded sulfur in the sample and results in an average stoichiometry of C_xS (x~10) above ~ 300°C.

The overall conclusion of these experiments is that the compound synthesized by compression of liquid CS_2 in a large-volume press (such as the Paris-Edinburgh cell) is significantly different from the apparently polymeric material obtained by compression in diamond anvils cells, commonly called "Bridgman black" [2]. The reason is most likely the following: Carbon disulfide is even at ambient conditions a metastable molecule since it has a positive formation enthalpy, i.e. the decomposition into its elements is exothermic. When CS_2 is hence compressed to a few GPa, it first transforms into polymeric Bridgman black, which still contains unsaturated C = S bonds. In a large-volume press, the reaction heat cannot be extracted rapidly and the sample heats further and is fully transformed into more stable constituents, i.e. a mixture of sulfur and C_2S. Hence, Bridgman black appears simply as an intermediate state between molecular CS_2 and the stable reaction products S and C_xS (x = 2–10).

4. Future plans

It would be interesting to confirm the structural model we have proposed, i.e. the exact location of sulfur in the graphitic matrix, by other methods. It might be possible with more advanced electron microscopy. We note that the C_xS type compounds discovered in this work could be an interesting candidate for a cathode material in Li-S batteries [5].

References

[1] P.W. Bridgman, Proc. Am. Acad. Arts Sci. **74** 399 (1942).
[2] B. Ochiai & T. Endo, Prog. Polym. Sci. **30**, 183 (2005).
[3] S. Klotz, T. Hattori, B. Baptiste, S.M. Feng, Ch. Jin, K. Béneut, J.M. Guigner, I. Estève., Carbon **185**, 491 (2021).
[4] N.F. Mott, Phil. Mag. **19**, 835 (1969).
[5] S. Zheng, Y. Wen, Y. Zhu, Z. Han, J. Wang, J.Yang, C. Wang. Adv. Energy Mat. **4**, 1400482 (2014).

S. Klotz[1], B. Baptiste[1], T. Hattori[2], S. M. Feng[3], Ch. Jin[3], K. Béneut[1], J.M. Guigner[1], and I. Estève[1]
[1]IMPMC, Sorbonne University, Paris, France; [2]Neutron Science Section, Materials and Life Science Division, J-PARC Center; [3]Institute of Physics, Chinese Academy of Science, Beijing, China

Development of Spin-Contrast-Variation Neutron Powder Diffractometry for Extracting the Structure Factor of Hydrogen Atoms

1. Introduction

The coherent polarized neutron scattering length of hydrogen, b_H, varies according to the proton spin polarization P_H with respect to the neutron spin direction,

$$b_H = b_{H0} + \Delta b_H P_H, \quad (1)$$

with $b_{H0} = -3.74$ fm and $\Delta b_H = 14.56$ fm. Thus, the scattering curves of the neutron against hydrogen-containing materials remarkably vary as a function of P_H. Spin contrast variation (SCV) is a technique to determine structure of materials by the analysis of the P_H-dependent multiple scattering curves. SCV has been used with small-angle scattering and reflectivity for nano-structure analyses of composite materials [1] and multi-layer films [2], respectively.

SCV neutron diffraction (NPD) can be used to determine positions of hydrogen atoms in crystalline samples (Fig. 1) [3]. However, SCV has been underused in diffractometry to date because the polarization technique is severely limited when applied to crystalline samples. In SCV, the sample is hyperpolarized by dynamic nuclear polarization (DNP), which transfers polarization from electron spins to proton spins using microwaves with a frequency close to electron paramagnetic resonance. Here, doping of free radicals suited for DNP such as 2,2,6,6,-tetramethyl-1-piperidinyloxy (TEMPO) is essential for DNP. However, it is impossible to dope these radicals into most of crystalline samples.

Meanwhile, Rossini et al. [4] and Miura et al. [5] succeeded DNP of crystalline samples by impregnating milled microcrystals into TEMPO-doped dispersion media. These microcrystals are polarized via spin diffusion from the dynamically polarized media. We used the new DNP technique to SCV-NPD.

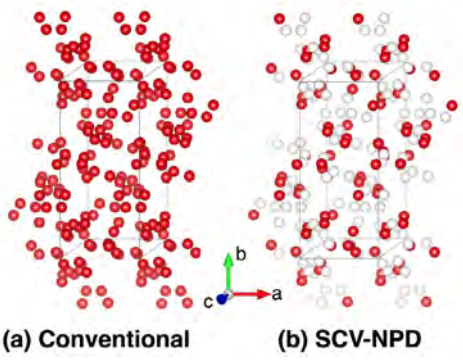

Figure 1. (a) Conventional NPD measures all elements (red spheres), but (b) SCV-NPD detects only hydrogen (red spheres) [3].

2. Experiment

The samples comprised β phase L-glutamic acid (LGA) powder dispersed in deuterated polystyrene containing 25 mM of 4-methacryloyloxy-TEMPO (TEMPO methacrylate). The four sheets of the samples with a total thickness of approximately 3 mm were stacked and set in the sample cell of the DNP apparatus, which polarized the sample by irradiating 94 GHz microwave at 3.3 T and 1.2 K [6]. The opening angle of the neutron window was so small that the DNP apparatus was rotated by 19° from the direction of the incident neutrons to cover values of the scattering angle 2θ in the ranges of 14–27° and 144–159° with the middle-angle and backward detectors, respectively. Although the overall range of 2θ was severely limited, time-of-flight measurement with neutron wavelength λ from 1.6 to 7.5 Å offered seamless cover of the magnitude of the scattering vector Q from 0.4 to 1.6 Å^{-1} and from 1.6 to 7.5 Å^{-1} with the middle-angle and backward detectors, respectively. The scattering from a positively polarized sample, a negatively polarized one, and an unpolarized one was accumulated for 5 h in each case. The incoherent scattering of the sample, the coherent scattering of the deuterated polystyrene, and the scattering of the air were subtracted from those data.

3. Result and Discussion

Figure 2 shows the SCV-NPD data in the range $1.2 \leq Q \leq 2.6$ Å^{-1}. The intensities of the peaks at $Q = 1.27$ and 1.46 Å^{-1} decrease with increasing P_H, whereas those at $Q = 1.43$ and 1.58 Å^{-1} increase, and the intensity at $Q = 1.53$ Å^{-1} is unchanged with P_H.

Intensity of each peak $I(Q, P_H)$ is given by

$$I(Q, P_H) = \{m(Q)/Q^2\} |F(Q, P_H)|^2. \quad (2)$$

Here, $m(Q)$ is the multiplicity, and $F(Q, P_H)$ the structure factor, which is rewritten using the factors of hydrogen

atoms at $P_H = 0\%$ $F_H(Q)$ and the other elements (C, N, and O in this case) $F_{others}(Q)$ as

$$F(Q, P_H) = (1 - \kappa P_H)F_H(Q) + F_{others}(Q) \quad (3)$$

with $\kappa = |\Delta b_H/b_{H0}|$. Note that the polarization dependence of the coherent scattering lengths for these other elements are negligible compared to hydrogen. From Eqs. (2) and (3), the self-correlation term of hydrogen atoms $|F_H(Q)|^2$ and the cross-correlation term $\mathrm{Re}[F_H(Q)F_{others}(Q)^*]$ are obtained from the equations,

$$\frac{I(Q,-P_H)+I(Q,+P_H)-2I(Q,0)}{2(\kappa P_H)^2} = \frac{m(Q)}{Q^2}|F_H(Q)|^2 \quad (4)$$

and

$$\frac{1}{2}\left\{\frac{I(Q,-P_H)-I(Q,+P_H)}{2\kappa P_H} - \frac{I(Q,-P_H)+I(Q,+P_H)-2I(Q,0)}{(\kappa P_H)^2}\right\} = \frac{m(Q)}{Q^2}Re[F_H(Q)F_{others}(Q)^*]. \quad (5)$$

The data shown by the blue single-line graph in Fig. 3 were obtained by substituting the intensities at $P_H = 0$ and ±16% in Fig. 3 into $I(Q,0)$ and $I(Q,\pm P_H)$ in the left sides of Eqs. (4) and (5). Meanwhile, the orange filled-line graph is of calculated $(m(Q)/Q^2)|F_H(Q)|^2$ and $(m(Q)/Q^2)\mathrm{Re}[F_H(Q)F_{others}(Q)^*]$ in the right sides of the equations, which are broadened using the Q-resolving power of TAIKAN. As shown in Fig. 3, the experimental data reproduce the calculated peaks.

4. Future plans

We are now developing a 6.7 T DNP apparatus with wider neutron windows for improved proton polarization, Q range, and neutron count rates. Measuring at higher proton polarization would give greater differences in peak intensities between different spin configurations, and improved neutron count rates would provide statistical significance in the analysis. We are also developing a dry hydrogel with a volume filling ratio of only 2% as a dispersion media to decrease the broad diffraction peaks which overlap with peaks of crystalline domains [7]. Very recently, Okudaira et al. [8] advanced further the development of a ^{3}He neutron polarizer, which polarizes neutrons with λ smaller than 1.6 Å. The SCV-NPD technique will be used much more by installing the ^{3}He polarizer in many diffraction beamlines in near future.

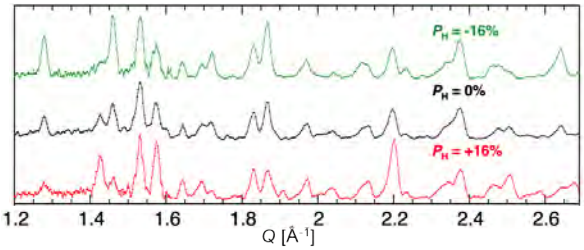

Figure 2. (a) SCV-NPD data (b) Calculated intensities of the peaks at $P_H = -16\%$ (Top), 0% (Middle), and +16% (bottom) [3].

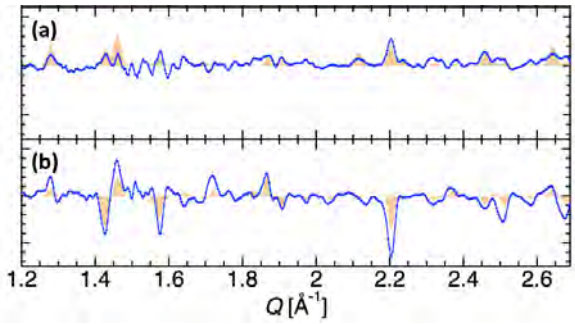

Figure 3. Blue single-line graphs of (a) $(m(Q)/Q^2)|F_H(Q)|^2$, and (b) $(m(Q)/Q^2)\mathrm{Re}[F_H(Q)F_{others}(Q)^*]$ obtained by substituting the experimental data into Eqs. (4) and (5). Orange filled-line graphs are calculated with the peaks broadened by the resolving power of TAIKAN [3].

References

[1] W. Knop et al., J. Appl. Cryst. **25**, 155 (1992).
[2] T. Kumada et al., J. Appl. Cryst. **52**, 1054 (2019).
[3] D. Miura et al., J. Appl. Cryst. **54**, 454 (2021).
[4] A. Rossini et al., J. Am. Chem. Soc. **134**, 16899 (2012).
[5] D. Miura et al., Prog. Theor. Exp. Phys. 033D01 (2019).
[6] T. Kumada et al., Physica B **404**, 2637 (2009).
[7] Y. Sekine et al., ACS Appl. Polym. Mater, **2**, 5482 (2020).
[8] T. Okudaira et al., Nucl. Instrum. Methods. Phys. Res. A, **977**, 164301 (2020).

D. Miura[1,2,3], T. Kumada[2,4], Y. Sekine[2], T. Oku[4], S. Takata[5], K. Hiroi[5], and T. Iwata[1]
[1]*Faculty of Science, Yamagata University;* [2]*Materials Sciences Research Center, JAEA;* [3]*Research Fellowship for Young Scientists of JSPS;* [4]*Technology Development Section, Materials and Life Science Division, J-PARC Center;* [5]*Neutron Science Section, Materials and Life Science Division, J-PARC Center*

Strengthening Contributions of CrFeCoNi High-Entropy Alloy at Low Temperatures: Insights into Multiple Deformation Mechanisms by *In Situ* Neutron Diffraction

1. Introduction

Unlike traditional alloys, high-entropy alloys (HEAs) may maintain or improve their ductility under cryogenic conditions [1–3]. Studying the high strength–ductility combination in HEAs is of broad interest for industrial applications at low temperatures but also for a better understanding of their fundamentals. Space exploration devices, superconducting magnets, and underground power transmission cables are among the possible applications of strong and tough alloys under cryogenic conditions.

The physics of HEAs has yet to be comprehended thoroughly. The occurrence of multiple deformation mechanisms has been associated with the abovementioned improvement of ductility at low temperatures [2–5]. However, those mechanisms have not been well described and the consequent strengthening contributions have not been estimated at low temperatures. *In situ* tensile loading studies are necessary to pinpoint the microscopic origin of the extreme hardening and superior ductility in HEAs. Neutron diffraction allows probing bulk samples with millions of grains and simultaneous analysis of dislocations, planar faults and phase transformation during deformation. In recent years, the development of sample environment capabilities at some neutron facilities enabled studying materials under extreme conditions. The TAKUMI beamline at the Materials and Life Science Experimental Facility (MLF) of J-PARC Center can perform *in situ* loading experiments at ultralow temperatures.

This work aimed at estimating the contribution of different strengthening mechanisms in a CrFeCoNi HEA tested at four temperatures (25, 40, 140 K, and room temperature) by *in situ* tensile measurements with neutron diffraction.

2. Experimental procedure

The equiatomic CrFeCoNi HEA alloys were prepared by arc-melting and suction-casting, followed by thermo-mechanical processing. The *in situ* neutron diffraction deformation measurements were carried out under tensile loading at the TAKUMI Engineering Materials Diffractometer. The cryogenic loading machine equipped with a GM cooler was used for low-temperature experiments. The neutron diffraction data were analyzed using Z-Rietveld and CMWP packages. More details about the experimental procedure and data analysis can be found in the original paper [6].

3. Results and discussion

The *in situ* neutron diffraction measurements were carried out for CrFeCoNi HEA alloy under tensile loading at 295 (RT), 140, 40 and 25 K. The stress-strain curves at the four temperatures are shown in Fig. 1. Both strength and ductility increased with decreasing the deformation temperature. The diffraction data demonstrated asymmetrical peak broadening with decreasing the testing temperature. Besides, the peak broadening becomes massive and undergoes a significant shift in peak positions at low temperatures (Fig. 2). Those phenomena indicated the occurrence of multiple deformation mechanisms, i.e., orientation-dependent profile broadening due to dislocations, peak shift caused by stacking faults (SFs), and profile asymmetry because of deformation twinning.

An orientation-dependent evolution of lattice strain and texture was observed for the loading and the transverse directions from the *in situ* diffraction data. The activation of different deformation mechanisms at low temperatures, in addition to the dislocation slip, resulted in the distinctive evolution of peak intensity, particularly

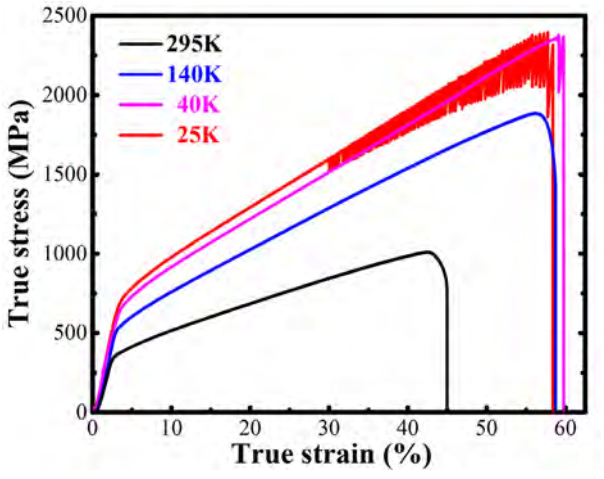

Figure 1. Stress-strain curves of CrFeCoNi HEA at 295, 140, 40 and 25 K during *in situ* tensile experiments [6].

for (111)//LD, (200)//LD, (422)//LD, and (220)//TD. At low temperatures, the texture for these orientations evolved slowly due to the increasing role of twinning and/or limited role of dislocation slip, while at RT, there was a continuous increase when deformation was facilitated by dislocation slip alone. SFs caused the difference in the lattice strains of equivalent orientations (111) and (222) as well as (200) and (400). The stacking fault probability (SFP) was determined from this difference in the lattice strain of equivalent orientations.

Regarding mechanical performance, the yield and tensile strengths increased by more than a factor of 2 with a significant increase in ductility (from 45 to 58.4%) while decreasing temperature from RT to 25 K (Fig. 1). The fractured sample at 25 K showed negligible necking and thus sustained a more significant uniform elongation. The sample at 25 K also showed massive serrations. The strain-hardening rate significantly increased at cryogenic conditions compared to the RT sample. The critical stress for SF activation was temperature-independent, and the SFs started at almost the same applied stress of 860 ± 20 MPa for all temperatures. Due to the higher yield strength at low temperatures, the activation strains for the SFs became lower with decreasing the temperature and SFP of 0.5%, 3.2%, and 4.7%, were achieved at RT, 140 K, and 40 K/25 K, respectively, as is evident from Fig. 3. Due to early activation and higher SFP, the SFs played a prominent role in deformation at low temperatures.

The dislocation density at 25 and 40 K was high and reached a similar value of ~9.2 ×10^{15} m^{-2} at both temperatures (Fig. 3). The extremely high dislocation density is the main reason for the outstanding strain hardening of HEA at low temperatures. At low temperatures, the twin fault probability (TFP) increased significantly, from 0.7% at RT to 6% at 25 K (Fig. 3). As Fig. 3 shows, TFP at 40 K was 5%, i.e., less than at 25 K. Given the similar SFP and dislocation density at both 40 and 25 K, the difference in TFP can be a possible cause of serrated deformation at 25 K.

From the above results, the contributions of the main strengthening mechanisms were estimated, as shown in Fig. 4. The grain boundaries and the initial dislocation density contributed ~183 MPa towards the

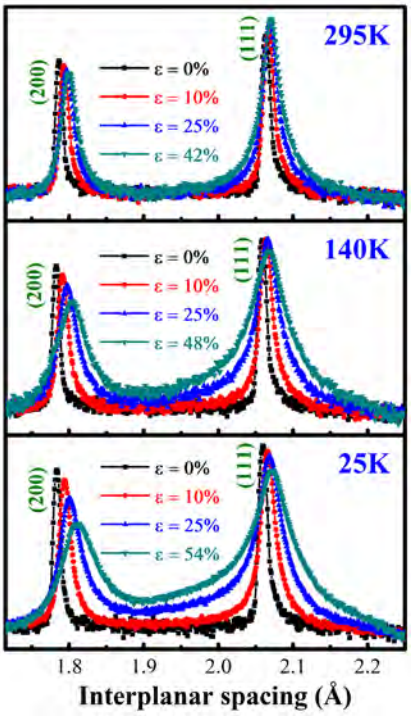

Figure 2. Evolution of peak profiles for (111) and (200) reflection with deformation at 295, 140 and 25 K [6]. The peak shift, broadening and asymmetry are evident as a function of progressive deformation strain at different temperatures, which are signatures of stacking faults, dislocations and twin faults, respectively.

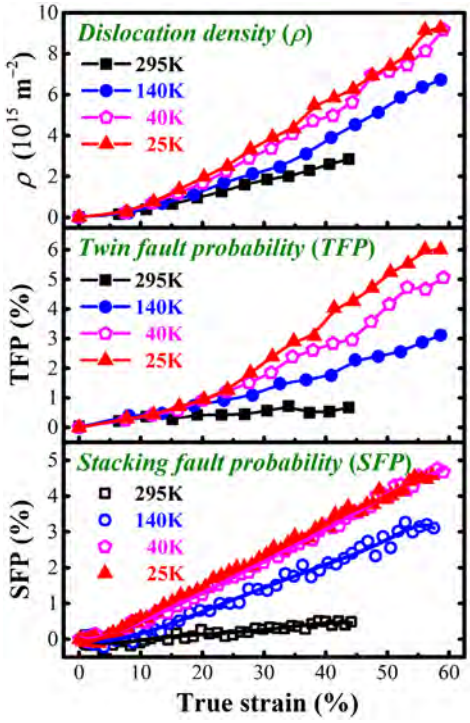

Figure 3. Evolution of dislocation density, twin fault probability and stacking fault probability with deformation at 295, 140, 40 and 25 K. Adapted from [6].

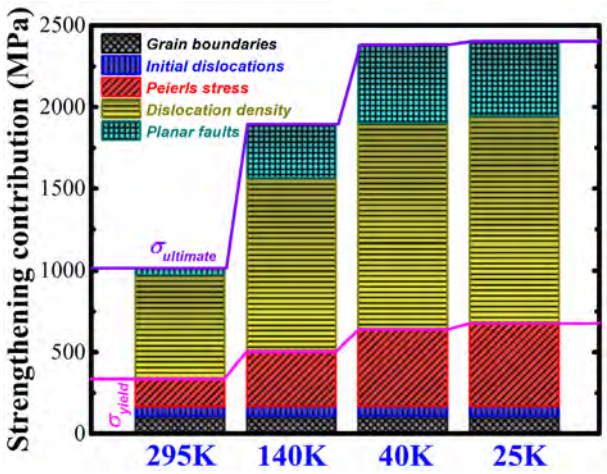

Figure 4. Temperature-dependent strengthening contributions towards the yield stress and strain hardening. Adapted from [6].

yield strength at all temperatures, while the Peierls stress increased significantly at low temperatures and contributed 148, 319, 454, and 493 MPa, at RT, 140, 40, and 25 K, respectively. The dislocation strengthening remained the major source of strain hardening at all temperatures. However, the planar faults (stacking faults and deformation twinning) contribution increased significantly from 40 MPa to 480 MPa, when the test temperature was lowered from RT to 25 K.

Acknowledgement

The *in situ* neutron diffraction experiments were conducted at the TAKUMI beamline, under proposal numbers 2016B0254, 2017B0142, and 2019A0180.

References

[1] Gludovatz et al., Science, **345** 1153 (2014).
[2] Laplanche, Acta Mater., **118** 152 (2016).
[3] Naeem et al., Sci. Adv., **6** eaax4002 (2020).
[5] He et al., Nano Lett., **21** 1419 (2021).
[6] Naeem et al., Acta Mater., **221** 117371 (2021).

M. Naeem[1], H. He[1], S. Harjo[2], T. Kawasaki[2], W. Lin[3], J.J. Kai[3], Z. Wu[4], S. Lan[1,5], and X.L. Wang[1,6]

[1]*Department of Physics, City University of Hong Kong;* [2]*Neutron Science Section, Materials and Life Science Division, J-PARC Center;* [3]*Department of Mechanical Engineering, City University of Hong Kong;* [4]*Center for Neutron Scattering and Applied Physics, City University of Hong Kong Dongguan Research Institute;* [5]*Herbert Gleiter Institute of Nanoscience, Nanjing University of Science and Technology;* [6]*City University of Hong Kong Shenzhen Research Institute*

Residual Stress in Steel Bars Processed by Cold Drawing and Straightening

1. Introduction

Special steel bars with high machinability called free-cutting steel are used for shafts and other parts that are cut for use in precision instruments, electronic equipment, etc. Using wire rod as a raw material, it is formed into bars having a high degree of straightness through complex plastic forming processes, such as cold drawing, spinner straightening, and roll straightening. On the other hand, subjecting a bar manufactured with good accuracy to a cutting process generates bending and deformation in the bar material that can lead to problems, such as drops in the degree of roundness and straightness. The cause of such bending and deformation is the release during machining of residual stress accumulated within the raw material at the time of plastic forming. Therefore, in the actual manufacturing process, a straightening process is used to reduce the residual stresses generated in the cold-drawing process. Determining the distribution of internal residual stress in products manufactured by plastic forming plays an important role in achieving product accuracy and reliability [1, 2]. The ability of neutron diffraction to penetrate deep into the material makes it possible to measure residual stress in the interior portion of the steel material. The purpose of this study is to measure the internal residual stress distribution in cold-drawn and straightened free-cutting steel bars using the neutron diffraction technique, and to clarify the mechanism of residual stress generation and residual stress reduction by straightening using the finite element method.

2. Material

A low-carbon free-cutting steel bar (SUM24L type) with a diameter of 10 mm and a length of 2500 mm was used. In the experiment, the bar material underwent a cold-drawing process consisting of drawing, spinner straightening, and roll straightening. A schematic diagram of this overall cold-drawing process is shown in Fig. 1 [3]. The rods were drawn in one pass from a 12 mm diameter to a final diameter of 10 mm (31% reduction in section). After that, the lots were subjected to spinner and roll straightening, which are rotary bending straightening processes. Details of the experiment can be found in reference [3].

3. Experiment and results

To conduct the measurements, we used the J-PARC/MLF BL19 "TAKUMI" diffractometer and measured the residual strain at 11 locations in the direction from the material surface to the central axis at 0.5 mm intervals. Additionally, each processing, we cut out 1.5 mm cubes from the steel bar by electrical discharge processing and assembled them with no directivity. We used these cubes as strain-free standard samples for use in measuring d_0. To measure strain in the hoop and radial directions, the incident beam slit was set to 1 mm × 30 mm and the radial collimator width to 1 mm to form a

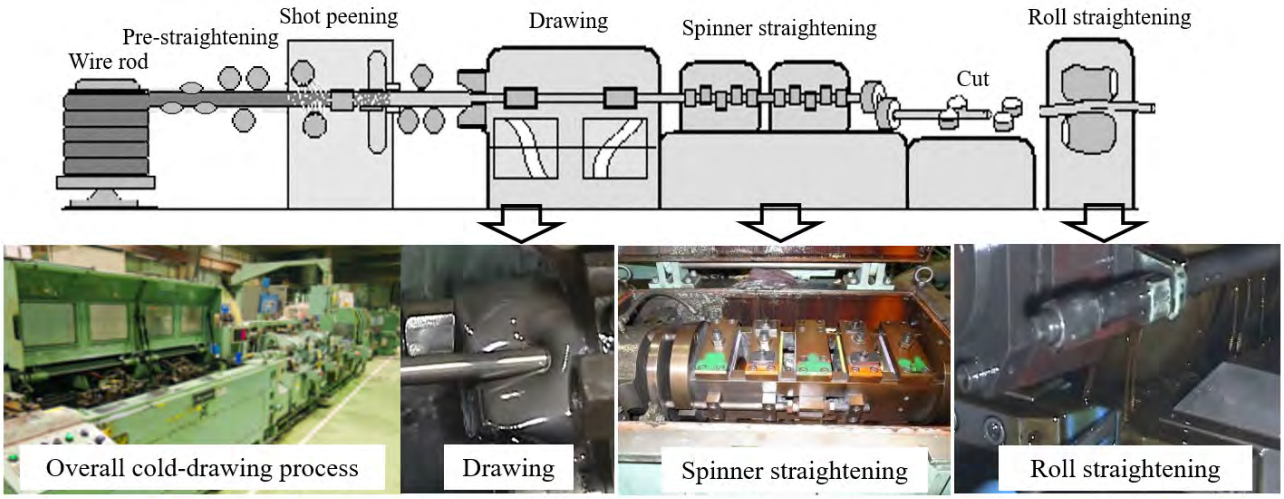

Figure 1. Schematic of cold-drawing process.

measurement region of 1 mm × 1 mm × 30 mm. To measure in the axial direction, the incident beam slit was set to 1 mm × 1 mm to form a measurement region of 1 mm × 1 mm × 1 mm. To shorten the measurement time of the neutrons, the measurement area was increased to 30 mm for axial measurements as the change along the axis is considered to be small.

The results based on the d_0 coupons for each process are shown in Fig. 2 and Fig.3 [3]. The distribution of residual stress after drawing shows tensile stress at the surface and compressive stress at the center similar to those found by neutron-based studies [3–6]. In addition, it was found that the internal residual stress generated by the drawing process tended to decrease by the subsequent straightening processes in all three directions (in the bar's hoop, radial, and axial directions). It is, therefore, clear that devising appropriate plastic forming processes can decrease the internal residual stress in a product.

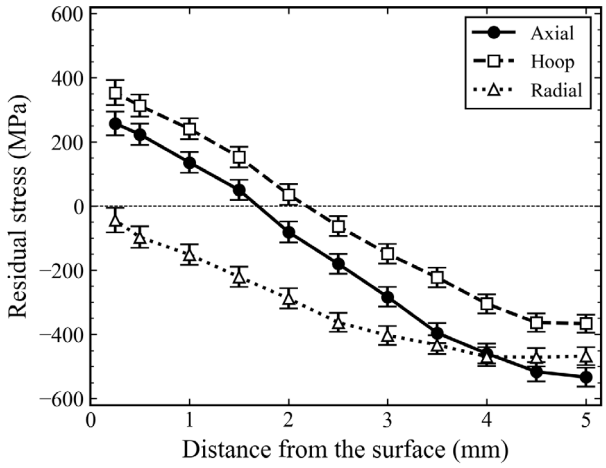

Figure 2. Distribution of residual stresses after drawing.

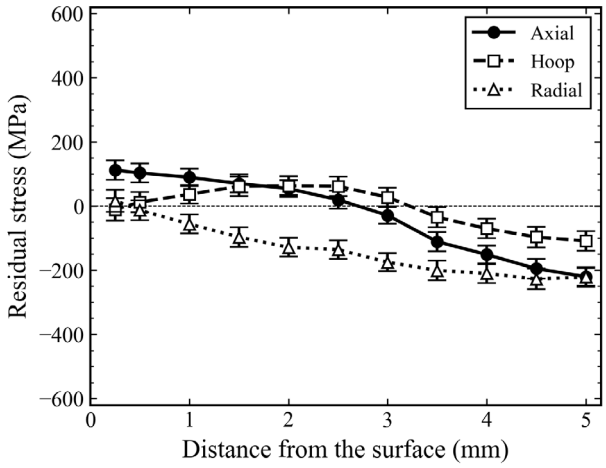

Figure 3. Distribution of residual stresses after spinner and roll straightening.

4. Numerical study

The simulation was done using open source software (integrated structural analysis system DEXCS-WinXistr). The rod and die setup were developed in SALOME and imported to EasyISTR. FrontISTR was used for the calculations and ParaView was used to analyze the results. The drawing process was simulated using the die geometry. The die was fixed and a 12 mm rod with both ends tapered to a 10 mm diameter was pulled out to enable it to be pulled out smoothly. The lot was forced to displace and pass through the die.

The distributions of stresses during drawing is shown in Fig. 4. After exiting the die, tensile stress remained in the surface layer and compressive stress in the center as in the neutron experiment. Although the mechanism of residual stress generation is complex, it can be shown as a figure by FEM.

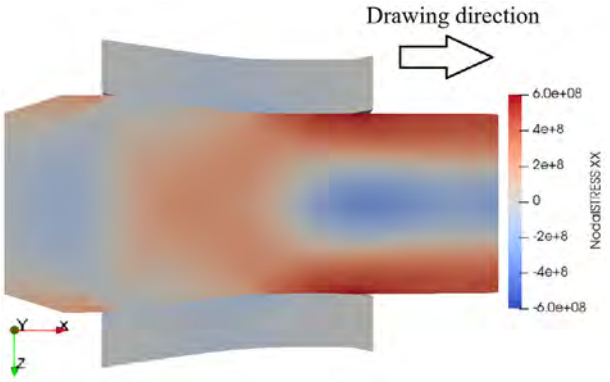

Figure 4. Distribution of residual stresses during drawing in the axial direction by FEM.

5. Summary

The residual stresses generated by the cold-drawing process were reduced by subsequent straightening, and the distribution of residual stresses by FEM simulation was consistent with the measured values by neutron diffraction. The combination of neutron diffraction and FEM can provide a detailed understanding of the residual stresses and mechanisms of the manufacturing process of the drawing process.

Acknowledgements

We would like to extend our deep appreciation to Kiyotaka Kashiwa and Takahiro Maeshima of the Industrial Technology Innovation Center of Ibaraki Prefecture for their kind cooperation during the residual stress simulations. A part of this research was supported by Hitachinaka Techno Center, Inc.

References

[1] M. Asakawa, W. Sasaki, and S. Shishido: Wire J. Int **10** (2002) 68–72.

[2] C.R. Liu and Y.B. Guo: Int. J. Mechan. Sci. **42** (2000) 1069–1086.

[3] S. Nishida, S. Nishino, M. Sekine, Y. Oka, S. Harjo, T. Kawasaki, H. Suzuki, Y. Morii and Y. Ishii: Mater. Trans. 2021, **62**, 667–674.

[4] J. M. Atienza, M. L. Martinez-Perez, J. Ruiz-Hervias, F. Mompean, M. Garcia-Hernandez, and M. Elices: Scr. Mater. **52** (2005) 305–309.

[5] T.F.de Souza, C.A.T. Soares, J. Zottis, R.M. Nunes, A.S. Rocha, T. Hirsch: Mater Res. **16**(2013) 508–14.

[6] J. Zottis, C.A.T. Soares Diehl, and A. da Silva Rocha: J Mater Res. Technol. **7** (2018) 469–478.

S. Nishino[1], S. Nishida[2], M. Sekine[2], Y. Oka[1], S. Harjo[3], T. Kawasaki[3], H, Suzuki[4], Y. Morii[5], and Y. Ishii[5]

[1]Graduate School of Science and Engineering, Ibaraki University; [2]Akiyama Seiko Co., Ltd.; [3]Neutron Science Section, Materials and Life Science Division, J-PARC Center; [4]Materials Science Research Center, Japan Atomic Energy Agency; [5]Radiation Application Development Association

Hydrogen Storage by Earth-Abundant Metals

1. Introduction

Hydrogen can take on various chemical states in materials. Hydrides, which are compounds of hydrogen, exhibit diverse functionalities due to such various chemical states of hydrogen [1]. Recently, hydrides with functionalities such as high-temperature superconductivity, H^- conduction, and fast ionic conduction have been extensively studied, while research on hydrogen storage alloys, which have a history of more than half a century of research and development, continues to be pursued intensively to realize the hydrogen energy-based society.

Hydrogen is expected to be a clean energy carrier that does not emit greenhouse gases when used. Hydrogen can be converted from various primary energy sources and stored for a long time. Hydrogen has, however, a problem of low energy density because it is a gas at the ambient conditions at which we live. Hydrogen storage alloys can store hydrogen in atomic solid form, making it possible to increase the volumetric hydrogen density above than that of liquid hydrogen. However, their gravimetric hydrogen densities are low. In addition, when mass-produced and used as an energy storage material, the cost of the material is also an issue.

In the search for hydrogen storage alloys, the guideline of "alloying metals with high- and low-hydrogen affinities" is well known [2]. Not only hydrogen storage alloys, but also other hydrides that have been synthesized follow this guideline without exception. Here, the definition "metal with high-hydrogen affinities" refers to metals that easily form hydrides with hydrogen composition close to their stoichiometric one at near ambient pressure, and include elements from the alkali metals to group V in the periodic table and Pd. In contrast, the definition "metals with low-hydrogen affinities" refers to metals that require high hydrogen pressure above 1 GPa to form hydrides with a hydrogen composition close to their stoichiometric one, and include elements in the Cr to Cu groups of the periodic table, excluding Pd. In the case of hydrogen storage alloys, hydrides consisting of metals with high-hydrogen affinities require high temperatures for hydrogen release because they are too stable. By mixing a metal with low-hydrogen affinity, thermodynamic stability of such hydrides is tuned so that hydrogen can be released at an appropriate temperature. The basis of this idea is that when two metals are alloyed and hydrogen is absorbed, the stability of the alloy hydride is intermediate to the stability of the hydrides of the constituent elements. Based on this idea, stable hydrides should not be obtained by combining only metals with low-hydrogen affinities.

While this guideline for the search of hydrogen storage alloys is very useful, it also limits the scope of material exploration. Hydrogen storage alloys such as $LaNi_5$ and TiFe with excellent hydrogen absorption and desorption properties have been developed and are already in practical use. These alloys contain relatively expensive metals and there is a need to improve the gravimetric hydrogen density. There are, however, not many effective metal combinations within the scope of the above-mentioned search guidelines, and it seems to be difficult to solve these problems by material search.

We thought that if it were possible to obtain hydrides composed solely of metals with low-hydrogen affinities, without being restricted by the conventional search guidelines for hydrogen storage alloys, the scope of material exploration would be dramatically expanded. We are exploring the hydrogenation reactions of aluminum-based alloys, where aluminum is one of the most lightweight and inexpensive metals among metals with low-hydrogen affinities. Recently, we have obtained results showing that aluminum iron alloys form hydrides, contrary to conventional search guidelines [3]. Now we need more than 7 GPa to hydrogenate the aluminum iron alloy. However, the resulting hydrides can be thermodynamically stable even near ambient pressure. In other words, the obtained material can store hydrogen around ambient pressure.

2. Experimental

The high-pressure hydrogenation experiments were carried out using a cubic-type multi-anvil press [4]. The starting material was $Al_{13}Fe_4$ alloy prepared using an arc-melting furnace. The obtained button-shaped ingot was crushed and compressed into a disk shape. The disk was set in a sample capsule made of boron nitride. The sample was placed in a hydrogen-sealed capsule made of NaCl with an internal hydrogen source of AlH_3 or AlD_3, set in a cubic pressure medium with a graphite heater for heating, and pressurized in a cubic-type multi-anvil press. The sample was pressurized to 9 GPa at room temperature and then heated to 750°C with a constant load applied to the anvil, which can be regarded as an approximately isobaric condition. After reaching 750°C, the sample was held in hydrogen for approximately 2 hours, then the temperature was lowered to room

temperature and the pressure was reduced to ambient condition. The above process was observed in-situ by powder X-ray diffraction measurement at the beamline BL14B1 at SPring-8 [5]. Samples recovered at ambient conditions were characterized by powder X-ray diffraction, powder neutron diffraction at NOVA at the Material and Life Science Experimental Facility (MLF) of the Japan Proton Accelerator Research Complex (J-PARC), and differential thermal balance-mass spectrometry (TG-MS).

3. Results and discussion

Figure 1 shows the X-ray powder diffraction profile of $Al_{13}Fe_4$ alloy under high hydrogen pressure and high temperature. Hydrogen was released from the hydrogen source at about 600°C. At the same time, a decrease in the intensity of the Bragg peaks from $Al_{13}Fe_4$ and the appearance of new Bragg peaks were observed. This profile change was completed in approximately 5 minutes after reaching 750°C. It is difficult to determine whether hydrides are formed from this in situ synchrotron radiation profile alone, however, when combined with the results of the analysis of the recovered sample described below, it was found that hydrogen treatment at 750°C and 9 GPa leads to hydrogenation of the $Al_{13}Fe_4$ alloy to form a new hydride, Al_3FeH_4. Here, the aluminum concentration of the starting material alloy is slightly (about 8 at%) higher than that of the hydride. It is possible to obtain Al_3FeH_4 by preparing an alloy with an Al_3Fe composition and hydrogenating it under the same temperature and pressure conditions. However, this would require a holding time of more than 12 h for the hydrogenation reaction. The excess aluminum may work as self-flux and enhance the hydrogenation reaction rate.

The new hydride Al_3FeH_4 could be recovered at ambient conditions. To confirm that the recovered sample was hydride, hydrogen desorption from the recovered sample upon heating was measured using TG-MS. Hydrogen desorption around 150°C was observed. Since no release of gaseous species other than hydrogen was detected, the hydrogen content of the sample was calculated from the weight loss during hydrogen release, and it was calculated to be approximately 2.9 wt%. Although this study is still in the basic research stage and comparisons with practical hydrogen storage alloys may not be meaningful, it is noteworthy that $Al_{13}Fe_4$, which are thought not to absorb hydrogen, have the hydrogen composition of 2.9 wt% that is comparable to those of hydrogen storage alloys $LaNi_5$ and TiFe.

In the high pressure and high temperature synthesis of novel hydrides, in-situ observation by synchrotron radiation X-ray diffraction is a very powerful tool for exploring synthetic conditions and evaluating stability of the obtained hydrides. However, since it is in principle difficult to obtain information on hydrogen using X-rays, it is necessary to take other measures. We performed neutron diffraction measurements and structural refinement by Rietveld analysis on Al_3FeD_4 recovered at ambient conditions.

A schematic of the crystal structure obtained by the Rietveld analysis is shown in Fig. 2(a). As confirmed by the profile change obtained by in situ synchrotron radiation observation (Fig. 1), the crystal structure is completely different from that of $Al_{13}Fe_4$. It was suggested that a different type of hydride was formed from an interstitial hydride, in which hydrogen atoms were located at interstitial sites of original alloys while maintaining

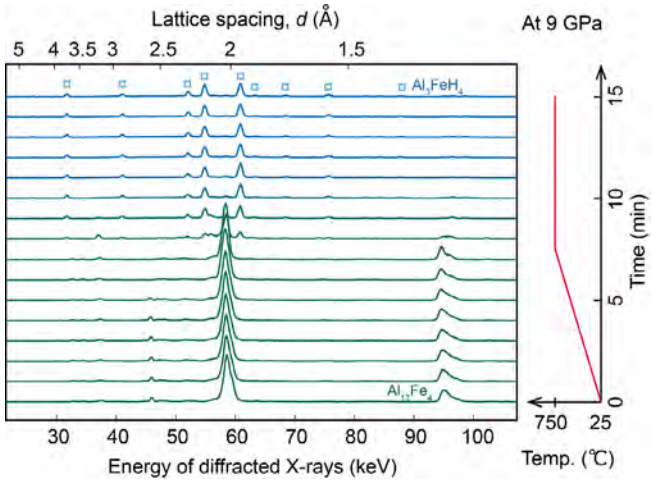

Figure 1. Series of in-situ synchrotron radiation X-ray diffraction profiles of $Al_{13}Fe_4$ during hydrogenation reaction at 9 GPa. Open squares indicate Bragg peaks from Al_3FeH_4. The right graph indicates temperature change during the measurement.

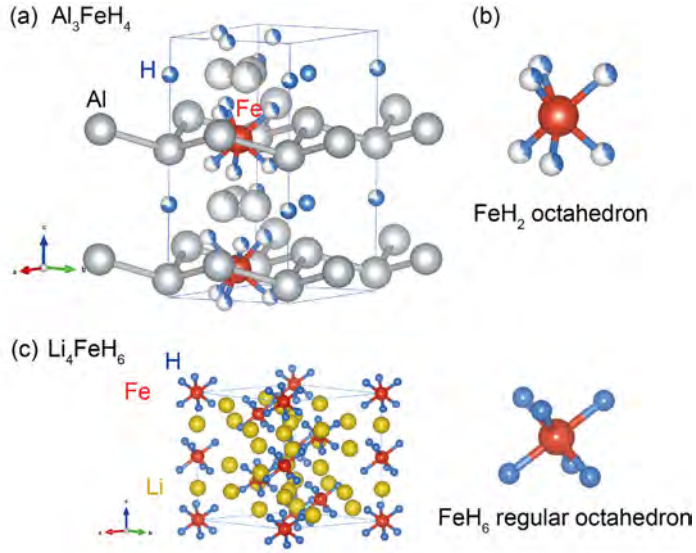

Figure 2. (a) schematic of the crystal structure of Al_3FeH_4. (b) schematic of the structure unit around the iron atom. (c) schematic of the crystal structure of Li_4FeH_6 and $[FeH_6]^{4-}$ complex ion in the hydride.

their crystal structures. The space group of the obtained crystal structure is P3c1 (No. 158) and it appears to be a simple structure with relatively high symmetry with a unit cell volume of V = 153.7 Å^3. Closer inspection of the crystal structure shows that both hydrogen sites and metal sites contain many partially occupied sites. Let us examine the crystal structure in more detail, focusing on the metal-hydrogen bonding.

Figure 2(b) shows a schematic of hydrogen sites around an iron atom. There are six hydrogen sites around the iron atom, forming an octahedron centered on the iron atom. This shape and the distance between the iron and hydrogen sites are close to those of the $[FeH_6]^{4-}$ complex ion (Fig. 2(c)) in typical complex hydrides, Mg_2FeH_6 and Li_4FeH_6. However, the $[FeH_6]^{4-}$ complex ion in the complex hydride is regular octahedral and the hydrogen sites are fully occupied, while the structural unit in Al_3FeH_4 is partially occupied with 1/3 hydrogen sites and the octahedron is distorted from the regular octahedron. We believe that the structural unit observed in Al_3FeH_4 is similar to the precursors of $[NiH_4]^{4-}$ complex ion [6] reported in the hydrogenation process of $LaMg_2Ni$. The thermodynamic stability of the hydride is thought to be enhanced by the formation of precursor-like units of a complex ion in Al_3FeH_4. These results suggest that controlling the chemical state of hydrogen can enable us to produce novel hydrides that have not been obtained so far.

Acknowledgements

This work was supported by JSPS KAKENHI Grant-in-Aid for Scientific Research on Innovative Areas "Hydrogenomics" (Nos. JP18H05513 and JP18H05518) as well as JSPS KAKENHI (No. JP22H01821) and grants from the Inter-University Cooperative Research Program of the Institute for Materials Research, Tohoku University (Proposal Nos. 20K0022, 202012-RDKGE-0066, and 202112-RDKGE-0025). The crystal structures shown in Fig. 2 were drawn using VESTA program [7].

References

[1] S. Takagi and S. Orimo, Scr. Mater. **109**, 1 (2015).
[2] A. Züttel, Mater. Today **6**, 23 (2003).
[3] H. Saitoh, T. Sato, M. Tanikami, K. Ikeda, A. Machida, T. Watanuki, T. Taguchi, S. Yamamoto, T. Yamaki, S. Takagi, T. Otomo, and S. Orimo, Mater. Des. **208**, 109953 (2021).
[4] Y. Fukai and N. Okuma, Jpn. J. Appl. Phys. **32**, L1256 (1993).
[5] H. Saitoh, A. Machida, K. Aoki, Chin. Sci. Bull. **59**, 5290 (2014).
[6] T. Sato, K. Ikeda, M. Matsuo, K. Miwa, T. Otomo, S. Deledda, B.C. Hauback, G. Li, S. Takagi, and S. Orimo, Int. J. Hydrogen Energy **42**, 22449 (2017).
[7] K. Momma and F. Izumi, J. Appl. Crystallogr. **41**, 653 (2008).

H. Saitoh
Quantum Beam Science Directorate, National Institutes for Quantum Science and Technology

Liquid Structure in Superconcentrated Electrolytes for Next Generation Aqueous Li ion Batteries

1. Introduction

Aqueous lithium ion batteries (ALIBs) have received much attention as the next generation lithium ion batteries (LIB) because of their favorable safety features and environmental friendliness. Water is not used in the current LIB due to its narrower electrochemical window, however, Suo et al. have resolved this problem with a simple increase of the Li salt concentration, which is called Water-in-Salt electrolyte consisting of 21 mol kg^{-1} lithium bis-(trifluoromethanesulfonyl)amide (LiTFSA), with molar ratio $[H_2O]/[LiTFSA] = 2.6$ [1]. It is assumed that the intermolecular interaction with the Li^+ causes the change of the HOMO energy level of the water molecule, which makes the anodic potential limit expand through a thermodynamic mechanism [1, 2]. Furthermore, the stability of the solid electrolyte interphase (SEI) is important to expand the life and increase the energy of the battery because the passivation thin layer restrains further electrolyte decomposition and allows reversible Li^+ transport between electrodes. Suo et al. revealed the differences between the structure of the Salt-in-Water and that of the Water-in-Salt solutions by MD simulations and that these conditions inside solutions, such as liquid structure and Li^+ local structure, influence the SEI formation [1]. Therefore, it is essential to understand the liquid structure of the electrolyte solution, especially, the local structure of Li^+ in the solutions at molecular level.

The structure of concentrated and super-concentrated LiTFSA aqueous solutions has been reported both theoretically and experimentally [2, 3]. More knowledge of the liquid structure and the Li^+ local structure in super-concentrated aqueous LiTFSA solutions is still needed because the local structure is crucial for the ARLIBs performance. Here, the Li^+ local structure in the super-concentrated LiTFSA aqueous solution is determined using neutron total scattering experiments with $^{6/7}$Li and H/D isotopic substitution technique. We found a formation of oligomer and a significantly weak hydrogen-bonded interaction.

2. Experimental

We prepared the typical super-concentrated aqueous LiTFSA solutions (^{6}Li samples, $(^6LiTFSA)_{0.25}(D_2O)_{0.75}$ and $(^6LiTFSA)_{0.25}(^0H_2O)_{0.75}$, and ^{nat}Li samples, $(^{nat}LiTFSA)_{0.25}(D_2O)_{0.75}$, $(^{nat}LiTFSA)_{0.25}(^0H_2O)_{0.75}$ and $(^{nat}LiTFSA)_{0.25}(^{0\text{-}2}H_2O)_{0.75}$). The solutions were sealed into Ni-V null alloy cells (8 mm in diameter and 0.1 mm in thickness). Neutron diffraction measurements were carried out at 25°C using the NOVA total scattering spectrometer installed at BL21 of the MLF high intensity pulsed neutron source in J-PARC, Tokai, Japan. The incident beam power of the proton accelerator was 200 kW. The observed total interference term of solutions, $i(Q)$, consists of the sum of intra- and intermolecular interference terms.

$$i(Q) = i^{\text{intra}}(Q) + i^{\text{inter}}(Q) \quad (1)$$

$i^{\text{intra}}(Q)$ includes intramolecular interference terms of H_2O and TFSA, and the respective $i^{\text{intra}}(Q)$ is evaluated by

$$i^{\text{intra}}_{\text{molecular}}(Q) = \sum\sum_{i\neq j} b_i b_j \exp(-l_{ij}^2 Q^2/2) \sin(Qr_{ij})/(Qr_{ij}) \quad (2)$$

where, l_{ij} and r_{ij} stand for the root-mean-square amplitude and internuclear distance, respectively.

The Fourier transform of $i(Q)$ leads to the real space correlation function, the total distribution function $g(r)$,

$$g(r) = 1 + (2\pi^2\rho r)^{-1}(\sum c_i b_i)^{-2} \int_0^{Q_{\max}} Qi(Q)dQ \quad (3)$$

where, ρ is the number density of the stoichiometric unit. c_i and b_i are the number and the coherent scattering length of atom i involved in the stoichiometric unit. The upper limit of the integral was set to 40 $Å^{-1}$ in the present analysis.

If the two solutions have identical compositions, except for the isotopic ratio of Li, the difference in the observed scattering intensities of these solutions gives the first-order difference function, $\Delta_{Li}(Q)$. The $\Delta_{Li}(Q)$ normalized for the stoichiometric unit can be represented as a linear combination of partial structures, $a_{Lij}(Q)$, involving correlations form the Li-j pair

$$\Delta_{Li}(Q) = \sum A_{Li\,j}[a_{Li\,j}(Q) - 1] + B[a_{LiLi}(Q) - 1] \quad (4)$$

where $A_{Li\,j} = 2xc_j(b_{^6Li} - b_{^{nat}Li})b_j$ and $B = x^2(b^2_{^6Li} - b^2_{^{nat}Li})$. The real-space first order difference function, $G_{Li}(r)$, distribution function around Li^+, is obtained by Fourier transform of $\Delta_{Li}(Q)$.

The partial distribution function, $g_{LiH}(r)$, is obtained by the Fourier transform of the Li-H partial structure factor, $a_{LiH}(Q)$. Structural parameters concerning the interactions between Li^+ and H_2O or $TFSA^-$ were determined through the simultaneous least-squares

fitting of the first-order difference function observed for $^{0}H_2O$ solution, $^{0H}\Delta_{Li}(Q)$, and $2c_{Li}c_{H}\left(b_{^{6}Li}-b_{^{nat}Li}\right)b_{D}[a_{LiH}(Q)-1]$ employing the following model function

$$^{0H}\Delta_{Li}^{model}(Q)=\sum 2c_{Li}n_{Li\,j}b_j(b_{^{6}Li}-b_{^{nat}Li})\exp(-l_{Li\,j}^2Q^2/2)\times\sin(Qr_{Li\,j})/(Qr_{Li\,j})+4\pi\rho(\sum A_{Li\,j}+B)\times\exp(-l_0^2Q^2/2)[Qr_0\cos(Qr_0)-\sin(Qr_0)]Q^{-3} \quad (5)$$

$$a_{LiH}^{model}(Q)-1=\sum n_{LiH}\exp(-l_{LiH}^2Q^2/2)\sin(Qr_{LiH})/(Qr_{LiH})+4\pi\rho\exp(-l_0'^2Q^2/2)[Qr'_0\cos(Qr'_0)-\sin(Qr'_0)]Q^{-3} \quad (6)$$

where n_{Lij} denotes the coordination number of j atom around Li^+, respectively. Parameters l_{Lij} and r_{Lij} are the root-mean-square amplitude and internuclear distance of the $Li^+\ldots j$ pair, respectively. The long-range parameters r_0 and r_0' are distances beyond which continuous distribution of atoms around Li^+. To determine the structural parameters, n_{Lij}, l_{Lij}, r_{Lij}, l_0, l_0', r_0 and r_0', simultaneous least squares fitting procedures to the observed $^{0H}\Delta_{Li}(Q)$ and $a_{LiH}(Q)$ were performed in the range of $0.1 \le Q \le 20$ Å^{-1}.

The intermolecular H-H, X-H and X-X (X: Li, O, S, C, F, N) partial structure factors, $a_{HH}^{inter}(Q)$, $a_{XH}^{inter}(Q)$ and $a_{XX}^{inter}(Q)$ were derived from the linear combination of intermolecular interference terms observed for ^{nat}Li samples, $(^{nat}LiTFSA)_x(D_2O)_{1-x}$, $(^{nat}LiTFSA)_x(^{0}H_2O)_{1-x}$, and $(^{nat}LiTFSA)_x(^{0\text{-}2}H_2O)_{1-x}$.

3. Results and discussion

Neutron diffraction with the isotopic substitution method is one of the most powerful techniques to obtain direct insight into hydrogen bonding and the environmental structure around Li^+. Figure 1 represents the inter-molecular H-H, X-H and X-X partial distribution functions observed for aqueous 25 mol% LiTFSA-*H_2O solutions (X excludes H atom). These partial distribution functions were obtained by the Fourier transformation intermolecular H-H, X-H, and X-X (X : Li, C, N, O, F, S) partial structure factors, respectively. The position of the first inter-molecular peak appearing at $r \sim 2.8$ Å of the present $g_{HH}^{inter}(r)$ is much longer than that observed for liquid pure water (~2.44 Å) implying that the interaction between the nearest neighbor water molecules in the solution should be significantly weaker. The inter-molecular hydrogen-bonded interaction between the neighboring water molecules is well known to be characterized by the inter-molecular O…H peak located at $r = 1.81$~1.84 Å, in the inter-molecular $g_{OH}(r)$ function. In the present inter-molecular $g_{XH}^{inter}(r)$, no indication can be observed for the nearest neighbor hydrogen-bonded interaction. This suggests significantly weaker hydrogen-bonded interaction in the aqueous 25 mol% LiTFSA solution.

Figure 2 shows the $Li^+\ldots H$ partial distribution function $g_{LiH}(r)$ and the distribution function around Li^+, $^{0H}G_{Li}(r)$. $^{0H}G_{Li}(r)$ and $g_{LiH}(r)$ were obtained by the

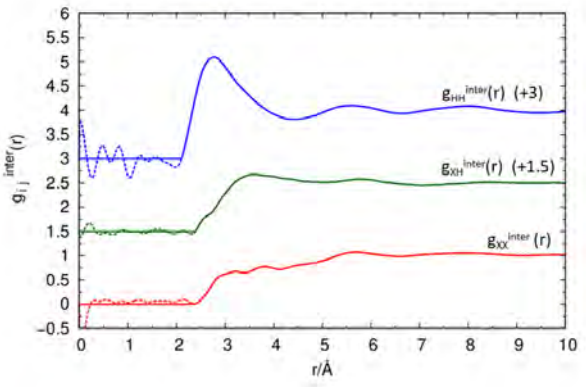

Figure 1. Intermolecular H-H, X-H, and X-X partial distribution functions, $g_{HH}^{inter}(r)$, $g_{XH}^{inter}(r)$ and $g_{XX}^{inter}(r)$, observed for aqueous 25 mol% LiTFSA solutions. Reprinted with permission from [6]. Copyright 2021 American Chemical Society.

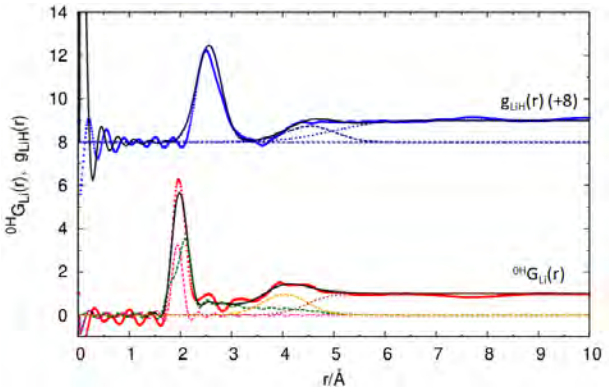

Figure 2. The Li-H partial distribution function, $g_{LiH}(r)$, and distribution function around Li^+, $^{0H}G_{Li}(r)$, observed for the aqueous 25 mol% LiTFSA solutions (dots). Fourier transform of the calculated $a_{LiH}(Q)$ -1, and $^{0H}{}_{\Delta Li}(Q)$ are indicated by solid lines. The short- and long-range interactions are denoted by broken- and dotted lines, respectively. Reprinted with permission from [6]. Copyright 2021 American Chemical Society.

Fourier transformation of ${}^{0H}\Delta_{Li}(Q)$ and $a_{LiH}(Q)$-1, respectively. The calculated model structure agrees well with the experimental ${}^{0H}G_{Li}(r)$ and $g_{LiH}(r)$. The present value of r_{LiO} (H_2O) for the first hydration shell of Li^+, r_{LiO} = 1.970 ± 0.003 Å, agrees well with values reported for the other aqueous solutions (1.96 ± 0.02 Å for 14.0 m LiCl [4]). The present r_{LiO} value for the nearest neighbor Li^+…$TFSA^-$ interaction, 1.966 ± 0.005 Å, agrees with that observed in organic solution (r_{LiO} = 1.98 ± 0.01 Å for 25 mol% LiTFSA-EC solution [5]). The coordination numbers of the oxygen atoms of H_2O and $TFSA^-$ molecules in the first hydration shell of Li^+ are determined to be 1.930 ± 0.006 and 2.28 ± 0.01, respectively.

To obtain a detailed picture of the Li ion local structure, we demonstrated MD simulations. The simulated neutron total interference terms are in good agreement with the experimental data. The coordination numbers of Li-O in the H_2O and TFSA are between 2.3 and 3.7 and between 1.7 and 2.8, respectively. The experimental coordination number of H_2O is significantly smaller than that predicted from the MD simulations. On the other hand, the experimental coordination number of TFSA is much larger than the estimated from the MD simulation. This suggests that a variety of $TFSA^-$ and H_2O coordination manners would exist in the solution, in particular, an oligomer is formed in which the monodentate TFSA cross-links Li^+, as shown in the liquid structure of the 25 mol% LiTFSA-H_2O solution obtained by the MD simulation.

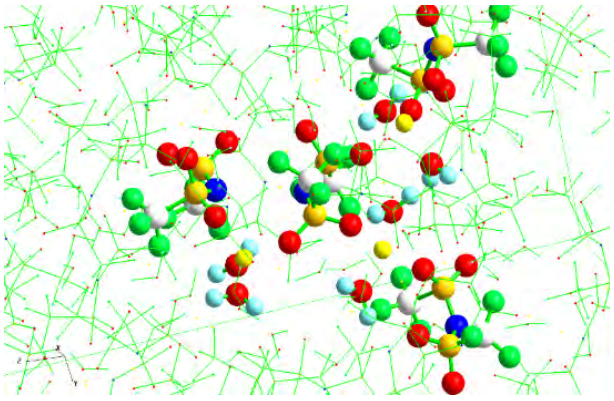

Figure 3. Liquid structure of the aqueous 25 mol% LiTFSA solution estimated by MD simulation. Reprinted with permission from [6]. Copyright 2021 American Chemical Society.

4. Future plans

Here, we demonstrated the neutron scattering with the ${}^{6/7}Li$ and H/D isotopic substitution technique, which evidently reveals the Li^+ local structure in the super concentrated LiTFSA aqueous solution for the ALIB. More recently, several super concentrated electrolyte solutions have been proposed to build electrochemical devices such as Li ion batteries with high energy density and high safety. The liquid structure plays a crucial role in realizing the next generation batteries. Neutron scattering techniques strongly support further development of science and technology in this field.

References

[1] L. Suo et al., Science, **350** 938 (2015).
[2] Y. Yamada et al., Nat. energy, **1** 16129 (2016).
[3] T. Tsurumura et al., Anal. Sci., **35** 289 (2019).
[4] I. Howell and G. W. Neilson, J. Phys.: Condens. Matter, **8** 4455 (1996).
[5] S. Maeda et al., J. Phys. Chem. B, **121** 10979 (2017).
[6] H. Watanabe et al., J. Phys. Chem. B, **125**, 7477 (2021).

H. Watanabe[1], Y. Umebayashi[2], and Y. Kameda[3]
[1]Department of Pure and Applied Chemistry, Faculty of Science and Technology, Tokyo University of Science; [2]Graduate School of Science and Technology, Niigata University; [3]Department of Material and Biological Chemistry, Faculty of Science, Yamagata University

Distinguishing Adsorbed and Deposited Ionomers in the Catalyst Layer of Polymer Electrolyte Fuel Cells Using Contrast-Variation Small-Angle Neutron Scattering

1. Introduction

Polymer electrolyte fuel cells (PEFCs) are indispensable devices for hydrogen economy. Meanwhile, innovation in component materials and manufacturing processes as well as improvement in their development efficiency are required to achieve higher-power and lower-cost PEFCs. Thus, we are creating a digital twin of a PEFC system to design and optimize the enormous parameters in silico.

In the PEFC system simulation, power generation in a catalyst layer of PEFC has been tackled while complicated by structure modeling difficulties due to lack of experimental data, especially in operando conditions. Since neutrons are a promising probe, we report an application of small-angle neutron scattering (SANS) measurements on a catalyst layer to investigate the effect of their multi-component hierarchical structure on the PEFC performance.

2. Ionomer distribution in the catalyst layer of PEFC

The power of a PEFC increases as the electrochemical reaction between oxygen and protons in the catalyst layer becomes smoother. A schematic diagram of the catalyst layer is shown in Fig. 1. The reaction takes place on the catalyst nanoparticles, such as platinum, which are supported on carbon particles forming a porous network structure. Oxygen diffuses through the voids to the catalyst and electrons are provided via the carbon. Protons conduct through a fluorinated polyelectrolyte thin film called ionomer, which continuously covers the surface of the catalyst-supported carbon (Pt/C).

In the catalyst layer, ionomers do not coat homogeneously the Pt/C. In Fig. 2, a scanning electron microscope image of a catalyst layer is shown. The gray particles are the ionomer-coated Pt/C aggregating hierarchically with sizes of tens to hundreds nanometers. The white spots on the aggregates are the platinum catalysts. Although the coating ionomer is not clearly distinguished from the Pt/C, the ionomer appears to be deposited between the Pt/C particles on which the ionomer is adsorbed. These two types of ionomers are expected from the formation process of the catalyst layer by applying and drying of a catalyst ink (dispersion of Pt/C and ionomer in a solvent) as well. Therefore, we focus on the thickness of the adsorbed ionomer and the volume fraction of the deposited ionomer as descriptors representing the heterogeneity of the ionomer distribution, which can be used to explain proton conduction and oxygen diffusion in a catalyst layer.

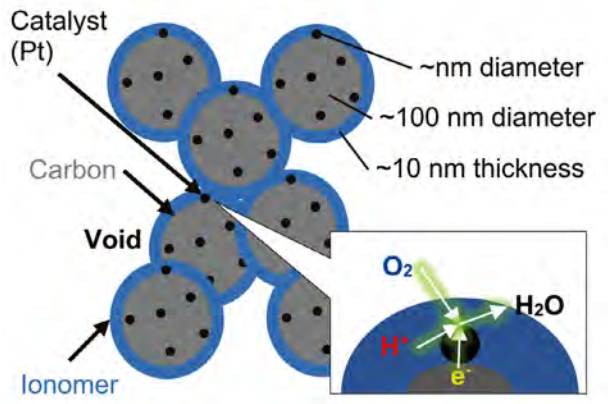

Figure 1. Typical components of a catalyst layer for polymer electrolyte fuel cells. Catalyst nanoparticles are supported on carbon particles which form a porous network structure with voids. The surface of the network is coated with ionomer thin films. Proton conductivity in the ionomer should be high enough for a smooth reaction with oxygen.

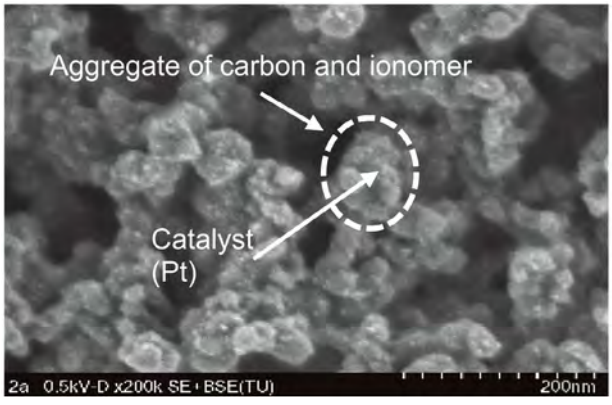

Figure 2. Image of a catalyst layer observed by scanning electron microscopy. Distribution of an ionomer coating on carbon particles looks heterogeneous; adsorbed parts and deposited parts could be observed for the ionomer.

3. Contrast-variation small-angle neutron scattering from the catalyst layer

We applied contrast-variation small-angle neutron scattering (SANS) to quantitatively evaluate the ionomer distribution in the catalyst layer [1]. Since the catalyst layer is regarded as a three-component system consisting of Pt/C, ionomer, and voids, the scattering curves reflect the self-correlation for the Pt/C and the ionomer, respectively, as well as the cross-correlation between the Pt/C and the ionomer. Although the scattering from a three-component system is hard to model-fit in general, the three correlation functions can be analyzed separately by varying the contrast of one component with an isotope. The SANS curves of a catalyst layer measured with six contrasts of the void-filling liquids are demonstrated in Fig. 3 by decreasing the H/D ratio from the top to bottom. Here, after calculating three kinds of correlation curves, a core-shell structure with the Pt/C core and the ionomer shell under consideration of the density fluctuation in the ionomer were applied with referring to the catalyst ink used to fabricate the catalyst layer [2].

The fitting parameter for the shell thickness was 5.1 nm, indicating that the adsorbed ionomer coats on the Pt/C uniformly. In contrast, density fluctuation with 7.8 nm was observed for the ionomer, due to the deposited part because the thin adsorbed part could not affect it. From the peak intensity of the fluctuation, the volume fraction of the deposited ionomer was evaluated to be 8.5 vol% of the total catalyst layer volume, which was consistent with the volume fraction of adsorbed ionomer calculated from the specific surface area of the Pt/C. Furthermore, the scattering curve for the cross-correlation function between the Pt/C and the ionomer was fitted by a model with adsorbed part only and no deposited part, supporting the hypothesis that the deposited part has no positional correlation to the Pt/C and arranges randomly.

4. Structure model of the catalyst layer

The structure of the catalyst layer has been quantitatively evaluated by contrast-variation SANS as represented in Fig. 4. The Pt/C structure is modeled as fractal aggregates of spheres with a size distribution, where two types of ionomers are distinguished: uniformly adsorbed thin one and randomly deposited thick one.

The two distinct types of coating ionomers are considered to have a critical effect on the proton conduction in a catalyst layer, because the proton conductivity depends on the thickness of the ionomer, which is about one order of magnitude lower at a thickness of 10 nm than in the bulk as reported in [3]. Comparing the proton conduction path to a road, the adsorbed part is a country road and the deposited part is a highway. Therefore, it is proposed that the contribution of adsorbed ionomer is relatively small and the amount of deposited ionomer is dominant for the proton conduction in the catalyst layer.

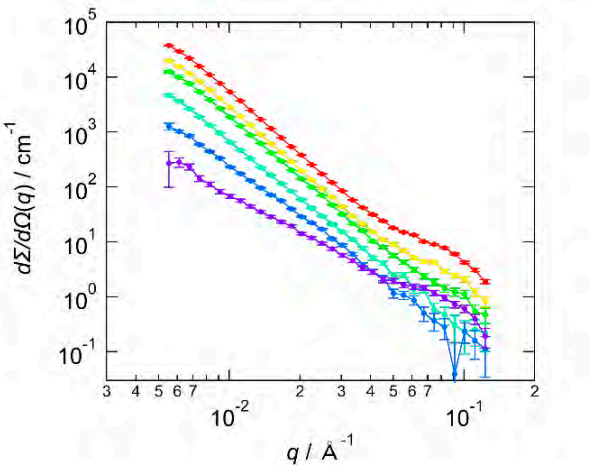

Figure 3. Contrast-variation small-angle neutron scattering of a catalyst layer, in which the voids are filled by liquids with a varying H/D fraction. Decrease of the scattering intensity is induced by a contrast change in the voids.

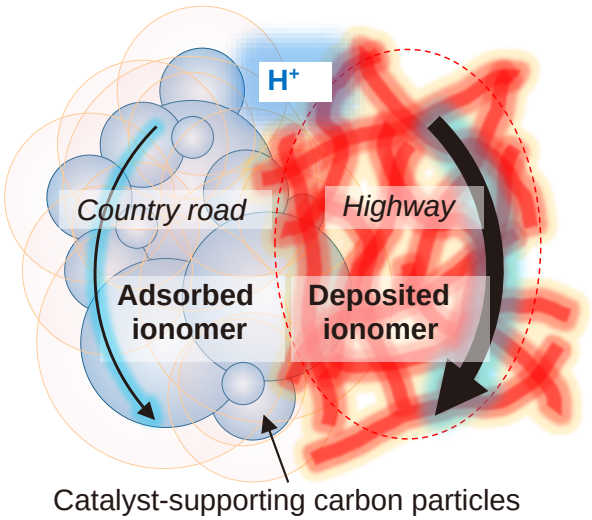

Figure 4. Proton conduction mechanism in the ionomer of a catalyst layer. The adsorbed part with a thin path has higher resistance than the deposited part.

5. Conclusion

The distribution of the ionomer in the catalyst layer was modeled by using contrast-variation small-angle neutron scattering and the coating structure was distinguished between uniformly adsorbed and randomly deposited ionomer on the catalyst-supported carbon. The impact of the ionomer structure on the proton conduction in the catalyst layer was discussed by focusing on the thickness dependence of the conductivity in the ionomer. The amount of the deposited ionomer was responsible for the proton conductivity in a catalyst layer.

Acknowledgement

This research is a part of a collaboration between J-PARC and Toyota Central R&D Labs, Inc. We thank Japan Atomic Energy Agency (JAEA), Comprehensive Research Organization for Science and Society (CROSS), and High Energy Accelerator Research Organization for supporting the project. The small-angle neutron scattering experiments were performed under the approval of MLF Long-term Proposals (2019L0400).

References

[1] M. Harada et al., ACS Omega, **6** 15257 (2021).
[2] M. Shibayama et al., J. Appl. Polym. Sci., **131** 39842 (2014).
[3] G. Gao et al., Solid State Ionics, **357** 115456 (2020).

M. Harada[1], S. Takata[2], H. Iwase[3], S. Kajiya[1], H. Kadoura[1], and T. Kanaya[2,4]
[1]Toyota Central R&D Labs., Inc.; [2]Neutron Science Section, Materials and Life Science Division, J-PARC Center; [3]Neutron Science and Technology Center, CROSS; [4]Institute of Materials Structure Science, KEK

Evaluation of Interfacial Water between Polypropylene and Si Substrate

1. Introduction

In transportation equipment, including automobiles, an improvement in fuel efficiency via weight reduction is urgently required to abate environmental pollution. Accordingly, various parts, including structural materials made from metals, have been replaced with polymer/inorganic filler nanocomposites or metal/resin bonding materials. Isotactic polypropylene (PP) is a promising polymer-matrix material for such materials. PP is not only inexpensive but has superior mechanical properties and high stability in various chemical environments. However, nonpolar PP does not strongly interact with the metal surfaces, resulting in weak bonding at the interface, which degrades the mechanical properties and thermal conductivity of PP-based nanocomposites and metal/resin bonding materials. This weak bonding at the interfaces along with the hydrophilicity of the metal surfaces also lead to interfacial water accumulation for substrates under high-temperature and high-humidity conditions, which are the typical usage conditions of PP-based materials. Water accumulation further degrades the aforementioned properties of these materials as a result of weakening the interfacial interaction [1, 2]. Therefore, it is necessary to quantitatively evaluate the interfacial water accumulation between PP and metal surfaces under humid conditions. We attempted to quantitatively evaluate the amount of interfacial water by the neutron reflectivity (NR) measurement. Neutron reflectometry is a powerful tool because when used in combination with deuterated water (D_2O) with an extremely high scattering length density (SLD) compared with those of polymers and metals, it enables a quantitative evaluation of the amount of water at interfaces [3, 4].

2. Experiment

PP powder with a molecular weight of approximately 250000 g/mol produced by Sigma Aldrich Co. was used to prepare polymer thin films for this study. PP thin films were prepared on Si wafers with diameters of 50 mm and thicknesses of 2 mm using the spin-coating technique. First, PP powder was dissolved in p-xylene at 130°C. Polymer solution with concentrations of 1.2 wt% was spun cast at 5000 rpm on a clean silicon wafer heated at 200°C.

NR measurements were performed at BL16 SOFIA, which is a horizontal type time-of-flight neutron reflectometer installed in J-PARC MLF (Japan Proton Accelerator Research Complex, Material and Life Science Experimental Facility). Neutron pulses of 25 Hz were generated with a wavelength band of 0.2 nm < λ < 0.88 nm. Reflectivity profiles were recorded at reflection angles of 0.3, 0.7, 1.6, and 3.5° to yield a q range of 0.07–3.5 nm^{-1}. Here, q is the magnitude of the scattering vector defined by $q = 4\pi/\lambda \cdot sin\theta$, where λ and θ are the wavelength of the incident neutrons and the incident angle, respectively.

The NR measurements of the PP films were performed in vacuum and at the saturated vapor pressure of D_2O at 25°C using a simple sealed sample chamber with a cup of D_2O.

3. Results and discussion

Figure 1 shows the NR profiles obtained in vacuum and at the saturated vapor pressure of D_2O at 25°C for the PP thin film. The NR data in vacuum could be represented well by a simple single-layer model consisting of a PP thin film on a Si wafer with a native oxide layer. The best fitting result is denoted by the solid line shown in Fig. 1. Meanwhile, the NR data obtained at the saturated vapor pressure of D_2O could not be entirely reproduced by the single-layer model. In the NR profile obtained at the saturated vapor pressure of D_2O, a fringe with a relatively long period centered at approximately 1 nm^{-1} is superimposed on the short periodic fringe structure originating from the PP layer, indicating that a thin single layer is located at the interface of the sample;

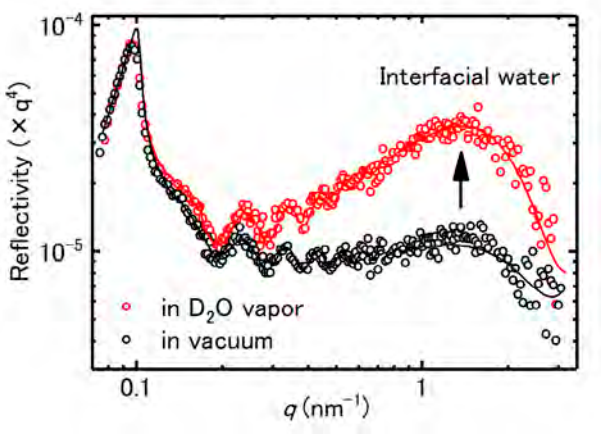

Figure 1. NR profiles of the PP thin film deposited on a Si substrate in vacuum and at the saturated vapor pressure of D_2O. Single-layer model and two-layer model were used to fit the NR data in vacuum and at the saturated vapor pressure of D_2O, respectively.

hence, the NR profile was represented by a two-layer model with an additional interfacial layer. The fitting result of the two-layer model is denoted by a solid line in Fig. 1, indicating that the two-layer model can accurately represent the experimental data. The SLD profiles in the vicinity of the interfacial region as the best fitting results for the NR profiles obtained in vacuum and at the saturated vapor pressure of D_2O are shown in Fig. 2. The interfacial layer with a high SLD should be attributed to the interfacial water accumulation because the interfacial layer has a much higher SLD than the surface oxide layer located on the Si substrate.

We attempted to quantitatively evaluate the concentration profile of D_2O at the interface between the PP thin film and the Si substrate with a native oxide layer [3]. Considering the SLD profile in the film thickness direction as the fitting result of the NR profile of the Si wafer used in this study, the concentration profiles of Si, SiO_2, and air in the film thickness direction have been determined to be $\varphi'_{Si}(x)$, $\varphi'_{SiO_2}(x)$, and $\varphi'_{air}(x)$, respectively, for the Si/SiO_2/air system. When the PP layer was spun-cast on the Si substrate, the concentration profile of the PP overlayer, $\varphi'_{PP}(x)$ in the Si/SiO_2/PP system could be assumed to be identical to $\varphi'_{air}(x)$ in the Si/SiO_2/air system. The concentration profiles of Si, SiO_2, D_2O, and PP in the PP thin film deposited on the Si substrate at the saturated vapor pressure of D_2O are denoted by $\varphi''_{Si}(x)$, $\varphi''_{SiO_2}(x)$, $\varphi''_{D_2O}(x)$, and $\varphi''_{PP}(x)$, respectively. $\varphi''_{D_2O}(x)$ is determined as follows:

$$\varphi''_{D_2O}(x) = \frac{SLD''(x) - SLD_{Si}\cdot\varphi'_{Si}(x) - SLD_{SiO_2}\cdot\varphi'_{SiO_2}(x) - SLD_{PP}\cdot\varphi'_{air}(x)}{SLD_{D_2O} - SLD_{Si}\cdot\varphi'_{Si}(x) - SLD_{SiO_2}\cdot\varphi'_{SiO_2}(x) - SLD_{PP}\cdot\varphi'_{air}(x)} \quad \cdots(1)$$

$\varphi''_{Si}(x)$, $\varphi''_{SiO_2}(x)$ and $\varphi''_{PP}(x)$ are obtained by the following equations with the substitution of values obtained from Eq. (1)

$$\varphi''_{Si}(x) = \varphi'_{Si}(x)\cdot\left(1-\varphi''_{D_2O}(x)\right) \quad \cdots(2)$$

$$\varphi''_{SiO_2}(x) = \varphi'_{SiO_2}(x)\cdot\left(1-\varphi''_{D_2O}(x)\right) \quad \cdots(3)$$

$$\varphi''_{PP}(x) = \varphi'_{air}(x)\cdot\left(1-\varphi''_{D_2O}(x)\right) \quad \cdots(4)$$

The $SLD''(x)$ is the SLD profile as a function of the distance from the substrate surface (Fig. 2) and is obtained as the best fitting result for the NR profile at the saturated vapor pressure of D_2O (Fig. 1). The SLD_{Si}, SLD_{SiO_2}, SLD_{D_2O}, and SLD_{PP} are the SLDs of Si, SiO_2, D_2O, and PP, respectively, and are 2.07×10^{-4}, 3.30×10^{-4}, 6.35×10^{-4}, and -0.33×10^{-4} nm^{-2}, respectively. The concentration (volume faction) profiles obtained using Eqs. (1), (2), (3), and (4) are shown in Fig. 3 [3]. The peak concentration of interfacial water was approximately 0.5, and the full width of the peak in the concentration profile of the water-rich layer was approximately 3 nm. These values are comparable to those obtained in previous studies [4, 5]. The driving forces of water accumulation at the interface are considered to be electrostatic and dispersion forces working within a relatively short distance from the hydroxylated metal oxide surface [2]. Therefore, in almost all cases, the water-rich layer thicknesses were within 3 nm. The results in Fig. 3 seem reasonable.

In general, surface modifications of metal oxides with silane coupling agents are performed routinely to enhance the interactions between nonpolar polymers and metal surfaces and reduce water accumulation at the interfaces owing to hydrophobization of the substrate surfaces. Therefore, we attempted to suppress

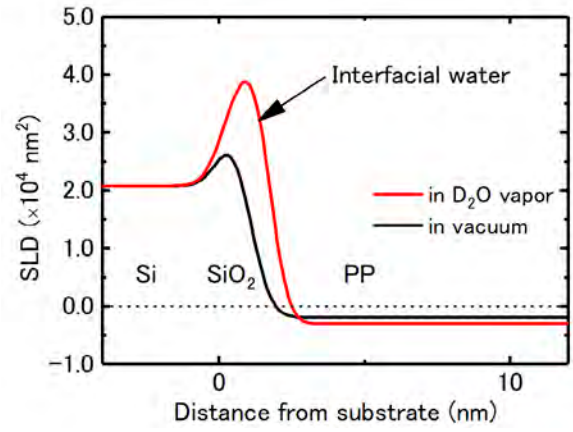

Figure 2. SLD profiles of the PP thin film deposited on a Si substrate in vacuum and at the saturated vapor pressure of D_2O, as the fitting results of NR data in Fig. 1.

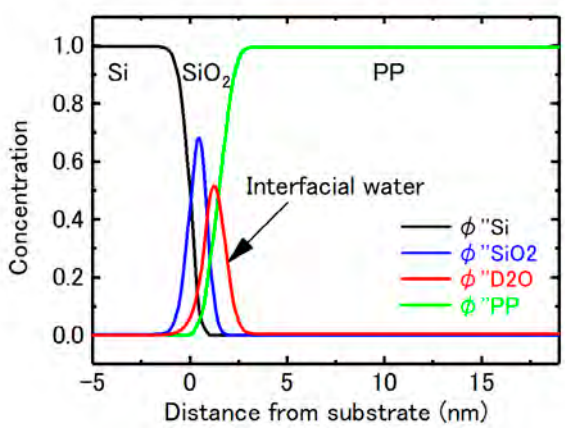

Figure 3. Concentration profiles of Si, SiO_2, D_2O, and PP in the PP thin film deposited on a Si substrate at the saturated vapor pressure of D_2O as a function of the distance from the substrate surface.

water accumulation at the interface between a PP thin film and Si substrate by surface modification of the substrate by a silane coupling agent. A silane coupling agent significantly prevents water molecules from accumulating at the PP/Si interface [6].

4. Conclusion

We quantitatively evaluated the water accumulation at the interface between the PP thin film and the Si substrate using the NR technique. Based on the NR profile of the Si substrate with a native oxide layer and that of the PP thin film deposited on it at the saturated vapor pressure of D_2O, the concentration profiles of Si, SiO_2, D_2O, and PP can be obtained as a function of the distance from the substrate. The results clearly indicate that a water-rich layer with a layer width of approximately 3 nm and a maximum concentration of 0.5 is formed at the interface between the PP thin film and the Si substrate at the saturated vapor pressure of D_2O.

References

[1] K. T. Tan et al., Langmuir, **24** 9189 (2008).
[2] K. Yoshizawa et al., Langmuir, **34** 14428 (2018).
[3] K. Shimokita, K. Yamamoto, N. Miyata, Y. Nakanishi, H. Ogawa, M. Takenaka, N. L. Yamada, and T. Miyazaki, Langmuir, **37** 14550 (2021).
[4] B. D. Vogt et al., Langmuir, **21** 2460 (2005).
[5] E. P. O'Brien et al., Adv. Eng. Mater., **8** 114 (2006).
[6] K. Shimokita, T. Miyazaki et al., Langmuir, **38** 12457 (2022).

T. Miyazaki[1,2], K. Shimokita[3,4], K. Yamamoto[4], N. Miyata[2], Y. Nakanishi[5], H. Ogawa[5], M. Takenaka[5], and N. L. Yamada[6]
[1]Office of Society-Academia Collaboration for Innovation, Kyoto University; [2]Neutron Science and Technology Center, CROSS; [3]Functional Base Products Sector, Nitto Denko Corporation; [4]Gradual School of Engineering, Nagoya Institute of Technology; [5]Institute for Chemical Research, Kyoto University; [6]Neutron Science Section, Materials and Life Science Division, J-PARC Center, Institute of Materials Structure Science, KEK

Conformational Dynamics of a Multi-Domain Protein by Neutron Scattering and Computational Analysis

1. Introduction

Proteins are composed of nanometer-sized 3D structures called domains. Relatively large proteins are composed of multiple domains and are referred to as multidomain proteins. While each domain has a stable structure, the domains change their relative positions and orientations through flexible hinge regions that connect the domains. In the case of the MurD protein, structure changes of the adenosine triphosphate (ATP)-binding site are coupled with the domains (Fig. 1) [1]. Elucidation of such domain-scale structural dynamics over the scales corresponding to the domain size is necessary to understand the mechanisms of protein functional expressions [1, 2].

In current structural biology, various experimental techniques have been developed to analyze structural changes and dynamics of proteins. Each method only partially reveals their realistic structure and dynamics. Correlative structural analysis uses a combination of several techniques and is applied to clarify a more realistic protein structure and its dynamics, which is also called integrated structural biology. Quasi-elastic neutron scattering (QENS), such as neutron backscattering (NBS) and neutron spin echo (NSE), is one of the powerful methods to unveil the equilibrium thermal fluctuations of a protein structure and a global diffusion in the nanometer length and picosecond to nanosecond timescales [3,4].

We studied the dynamics of MurD, a typical multidomain protein, which is an enzyme involved in cell wall synthesis and the conformational change upon ATP binding is essential for its function. We combined QENS and molecular dynamics (MD) simulation to elucidate the correlation between the domain structure and the structure of the ATP binding site.

2. Experimental procedures

MurD protein was expressed in E. coli strain BL21 (DE3), and purified. The protein solutions were prepared in D_2O buffer with 20 mM Tris-HCl (pD 7.2), 200 mM NaCl, 10 mM Dithio Threitol, and 0.05% NaN_3 at a protein concentration of 57 mg/mL, where M indicate molarity (mol/L). An ATP analog adenylyl imidodiphosphate (AMP-PNP) and Mg^{2+} were added to the above protein solutions for the ATP-bound state with 3 mM AMP-PNP and 6 mM $MgCl_2$.

NSE experiments were conducted using the NGA-NSE spectrometer at NIST in USA [5]. The data were collected over a scattering vector, Q, range from 0.03 $Å^{-1}$ to 0.21 $Å^{-1}$ at 25 °C. The data were corrected for the scattering from the D_2O buffer solvent and instrumental resolution effects to obtain $I(Q, t)/I(Q, 0)$, at several Q-values.

NBS experiments were conducted using BL02 at J-PARC MLF in Japan [6]. The energy resolution was 12 μeV with an Si(111) crystal analyzer. The data were collected over a Q range from 0.21 $Å^{-1}$ to 1.79 $Å^{-1}$ at 25°C. The spectra of D_2O buffer were subtracted from the protein solution spectra by taking the protein volume fraction into account. NBS spectra were fitted with a two-component model function, which describes internal motion and global diffusion.

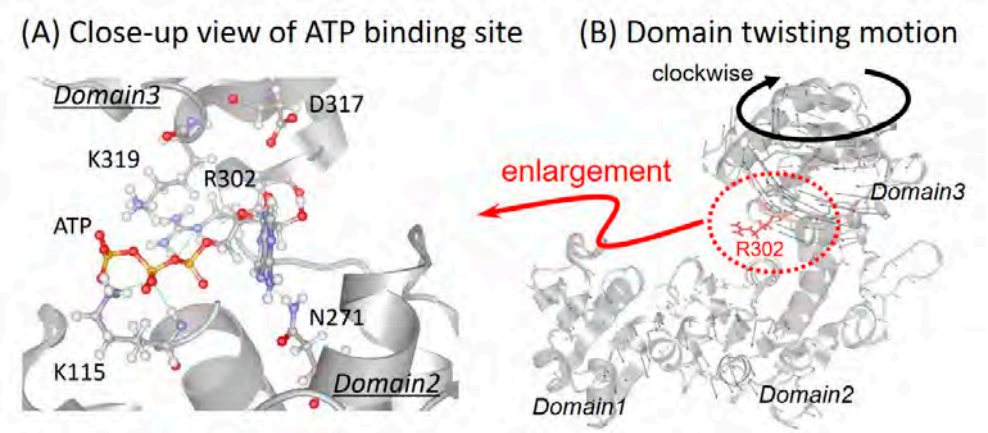

Figure 1. (A) Close-up view of the ATP-binding site, in which the amino acid residues (R302, K115 and D317) are indicated as a ball-and-stick model. (B) Domain twisting motion.

Dynamic light scattering (DLS) measurements were performed using an ALV-5000 digital correlator (ALV, Germany) at a laser wavelength of 632.8 nm. The resulting time-correlation function of the scattered intensity $g^2(Q, t)$, which was directly derived from the measurement, was converted to the field time-correlation function $g^1(Q, t)$ using the Siegert relation. The intensity was well fitted with a single exponential, and the translational diffusion coefficient D_0 was obtained. To eliminate the effects of aggregates, CONTIN analysis was used.

3. Results and discussion

Figure 2A shows the effective diffusion coefficient, D_{eff}, obtained by the NSE experiments. The coefficient includes contributions from translational and rotational diffusion as well as internal domain motions [3]. The low Q limit of D_{eff} reasonably corresponds to D_0 obtained by the DLS [7]. The self-diffusion coefficients were obtained by NBS, and the rotational diffusion coefficients were calculated using HYDROPRO [3]. The apparent diffusion coefficients derived from domain motion, ΔD_{eff}, were calculated by subtracting the self-diffusion and rotational diffusion contributions from D_{eff}. Shown in Fig. 2B are ΔD_{eff} in the Apo and ATP bound states. The peak around $Q = 0.15$ Å^{-1} is reduced by ATP binding. The origin of the reduction of ΔD_{eff} was identified as a suppression of a twisting domain motion (see Fig. 1B) by the principal component analysis of the trajectories of our molecular dynamics simulations [8, 9]. Furthermore, the computational analysis showed that this domain motion is linked to the fluctuation of the side chain of the ATP-binding site (Fig. 3), indicating that the fluctuation of the local structure controlled by the domain motion is important for ATP binding. The present study identified the details of the changes in domain motions upon ATP binding for the first time and advanced our understanding of the molecular mechanism of MurD enzyme activity.

This analysis reveals that the amino acid residues of the active site are not randomly fluctuating thermally, but are controlled by the cooperative thermal fluctuations of the domain structure. As such, understanding of the relationship of structural dynamics in different hierarchies is important for elucidating protein function.

4. Outlook

In this work, we studied the domain motions and conformational variations of the MurD enzyme both computationally and experimentally. We found that the binding of ATP suppresses the nanosecond domain dynamics. The ligand bindings change the interdomain dynamics as well as the local structures at the active site, and more interestingly, the structural dynamics in the different spatial scales are coupled with each other. The large-scale Brownian motions of interdomain con-

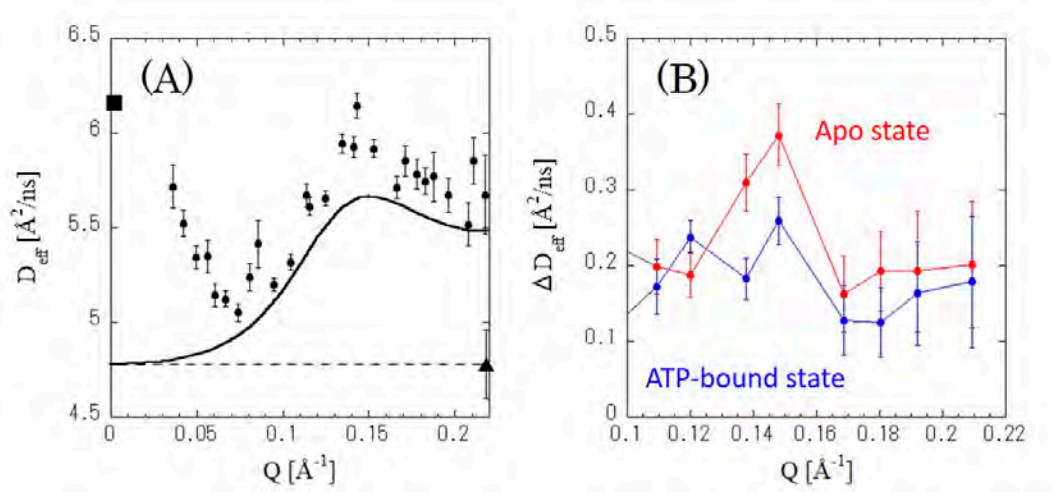

Figure 2. (A) Effective diffusion coefficients of MurD in the apo state. The solid lines indicate the calculated diffusion coefficients using HYDROPRO, including the translational and rotational diffusions. The square and triangle indicate the diffusion coefficients by DLS and NBS experiments, respectively. (B) The difference in the experimental effective diffusion coefficients and the calculated rotational diffusion coefficient, ΔD_{eff}.

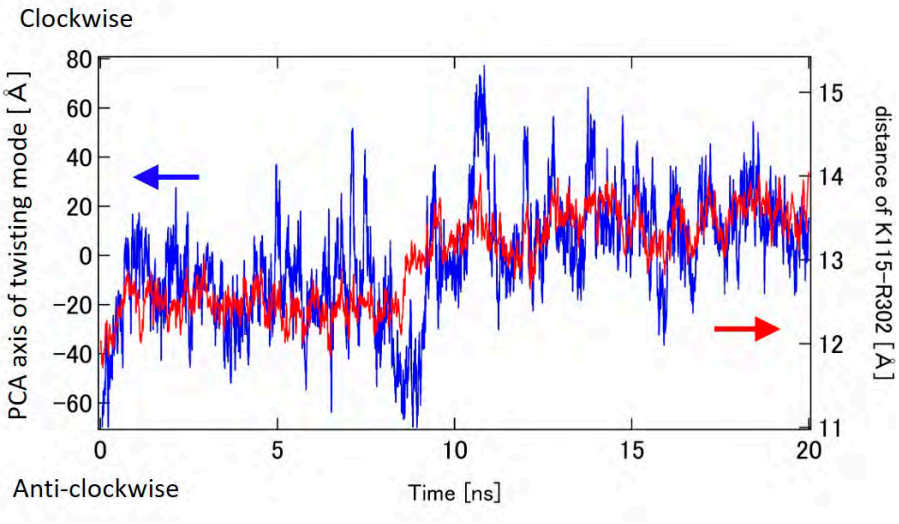

Figure 3. Time course of PCA axis of twisting mode and distance between C_α carbons of K115 and R302 in the apo state.

formation on the nanosecond timescale regulate the enzymatic reaction through the dynamical coupling. To uncover complex mechanisms of enzymatic reactions, computational analyses and integration of different experimental techniques that cover different space and timescales are effective.

The identification of any commercial product or trade name does not imply endorsement or recommendation by the National Institute of Standards and Technology.

References

[1] T. Saio et al., Sci. Rep., **5** 16685 (2015).
[2] H. Nakagawa et al., Biophys. J., **120** 3341 (2021).
[3] R. Inoue et al., Biophys. J., **99** 2309 (2010).
[4] F. Roosen-Runge et al., Proc. Natl. Acad. Sci. USA. **108** 11815 (2011).
[5] N. Rosov et al., ACS Symp. Ser. **739** 103 (1999).
[6] K. Shibata et al., JPS Conf. Proc. **8** 036022 (2015).
[7] W. Doster et al., Biophys. J., **93** 1360 (2007).
[8] A. Kitao et al., Curr. Opin. Struct. Biol., **9** 164 (1999).
[9] N. Smolin et al., Biophys. J., **102** 1108 (2012).

H. Nakagawa[1,2], T. Saio[3], M. Nagao[4,5,6], R. Inoue[7], M. Sugiyama[7], T. Tominaga[8], and Y. Kawakita[2]
[1]Materials Sciences Research Center, JAEA; [2]Neutron Science Section, Materials and Life Science Division, J-PARC Center; [3]Division of Molecular Life Science, Institute of Advanced Medical Sciences, Tokushima University; [4]NIST Centre for Neutron Research, National Institute of Standards and Technology; [5]Department of Materials Science and Engineering, University of Maryland; [6]Department of Physics and Astronomy, University of Delaware; [7]Institute for Integrative Radiation and Nuclear Science, Kyoto University; [8]Neutron Science and Technology Center, CROSS

Spin Texture Induced by Non-Magnetic Impurity in the Triangular Lattice Antiferromagnet *h*-Y(Mn,Al)O_3

1. Introduction

Impurities are an unavoidable problem in condensed matter physics and material science studies. As magnetic materials are no exception to this, understanding how impurities affect magnetic properties is one of the important research topics. This issue becomes more crucial in frustrated magnets; impurities in frustrated magnets are expected to cause very unusual phenomena compared to magnets without frustration. A representative example is continuum-like dynamical susceptibility induced by impurities, similar to that of quantum spin liquid (QSL) and thus usually concealing the true nature of several QSL candidates [1, 2].

When it comes to frustrated magnets with long-range order, it was proposed that impurities can significantly modify the original spin configuration [3, 4]. This is because an impurity can relieve the frustration, leading to a change in the local spin arrangement (Fig. 1). Interestingly, this change can be transmitted to a very long distance from the impurity, forming a giant spin texture like a Skyrmion [5]. However, the presence of such a texture has yet to be confirmed by any experiment.

In this report, we present the experimental results combined with theoretical analysis supporting the presence of the spin texture. We have studied this problem experimentally by replacing some Mn ions with non-magnetic aluminum (Al) in *h*-$YMnO_3$, a geometrically frustrated triangular lattice antiferromagnet having 120° magnetic order. We successfully grew large single-crystal *h*-$YMn_{1-x}Al_xO_3$ with $x = 0$, 0.1, and 0.15. Using inelastic neutron scattering, we measured the spin dynamics of as-grown *h*-$YMn_{1-x}Al_xO_3$ and found clear traces of the spin texture [6].

2. Spin-wave spectra of $YMn_{1-x}Al_xO_3$ ($x = 0$, 0.1, 0.15)

The spin-wave spectra of *h*-$YMn_{0.9}Al_{0.1}O_3$ and *h*-$YMn_{0.85}Al_{0.15}O_3$ were measured using the 4SEASONS time-of-flight spectrometer (BL1). Figure 1 shows the measured spectra along the high-symmetry momentum contour, including a comparison with those of pristine *h*-$YMnO_3$. The linewidth broadening appears due to Al doping over a wide momentum space, typical behavior of magnetic materials with impurities. However, we found that the amount of linewidth broadening was highly momentum-dependent. As demonstrated by a stack of const-**Q** cuts along the C-B line (Fig. 2), magnon linewidth broadening was much larger in the Brillouin zone boundary than in the zone center. This is unusual since magnon decay due to a typical impurity effect should be momentum-independent; impurities act as a point-like scattering potential to magnons, whose scattering cross-section should be uniform regardless of the scattered direction [5]. Only a spatially-extended object can induce such momentum-dependent damping [5], which would be related to the spin texture in our case.

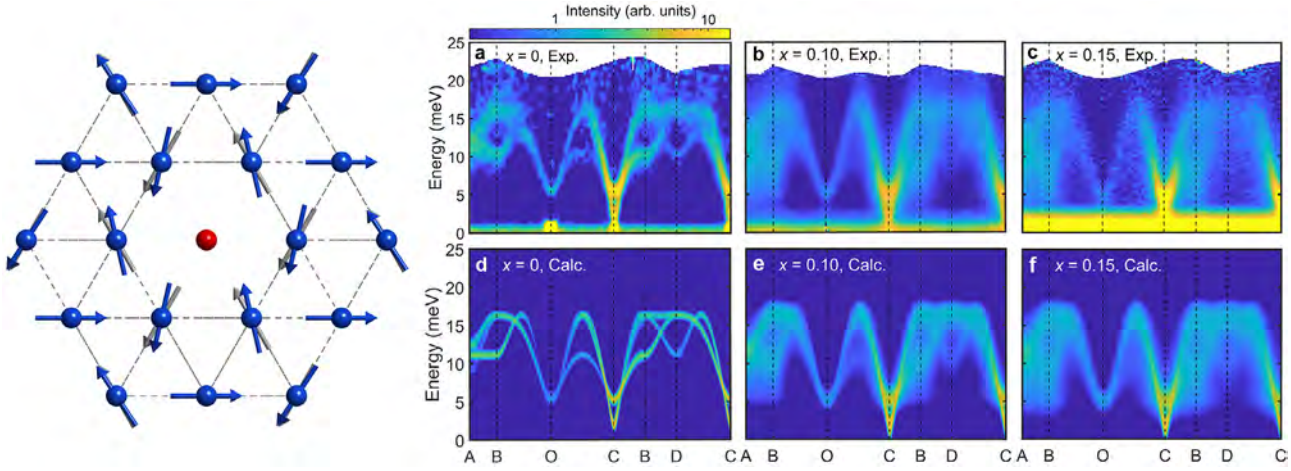

Figure 1. (Left) Non-collinear 120° magnetic order of *h*-$YMnO_3$ (grey arrows) and the formation of spin texture (blue arrows) by a non-magnetic impurity. (Right) a–c, Spin dynamics of *h*-$YMn_{1-x}Al_xO_3$ measured by inelastic neutron scattering. d–f, Calculated spin-wave spectra of *h*-$YMn_{1-x}Al_xO_3$ with spin texture originating from Al impurities.

3. Theoretical calculations

To further confirm the presence of the spin texture, we calculated the theoretical spin-wave spectra with non-magnetic impurities. First, the correct magnetic ground state of *h*-$YMn_{1-x}Al_xO_3$ was derived by the conjugate gradient method with simulated annealing on a 30×30 triangular lattice. We used the spin Hamiltonian obtained from the spin-wave spectra of *h*-$YMnO_3$ [7]. As expected, the calculations yield spin configurations containing the spin texture mentioned earlier. Next, we calculated the dynamical structure factor with these spin configurations; the results are shown in Fig. 1d–f and Fig. 2a–c. The simulations were in good agreement with our data. In particular, they reproduced precisely the observed momentum-dependent linewidth broadening, which further supported the presence of theoretically suggested spin texture in *h*-$YMn_{1-x}Al_xO_3$.

4. Discussion

Our INS data clearly show the unusual spin dynamics driven by the spin texture, but a more direct measurement of the spin texture will also be interesting. For instance, small-angle neutron scattering may reveal the detailed spatial profile of the texture.

References

[1] Han, T.-H. *et al., Nature* **492**, 406-410 (2012).
[2] Han, T.-H. *et al., Physical Review B* **94**, 060409 (2016).
[3] Wollny, A., Fritz, L. & Vojta, M. *Physical Review Letters* **107**, 137204 (2011)
[4] Maryasin, V. S. & Zhitomirsky, M. E. *Physical Review Letters* **111**, 247201 (2013).
[5] Brenig, W. & Chernyshev, A. L. *Physical Review Letters* **110**, 157203 (2013).
[6] Park, P. *et al*., *Nature Communications* **12**, 2306 (2021).
[7] Oh, J. *et al., Nature Communications* **7**, 13146 (2016).

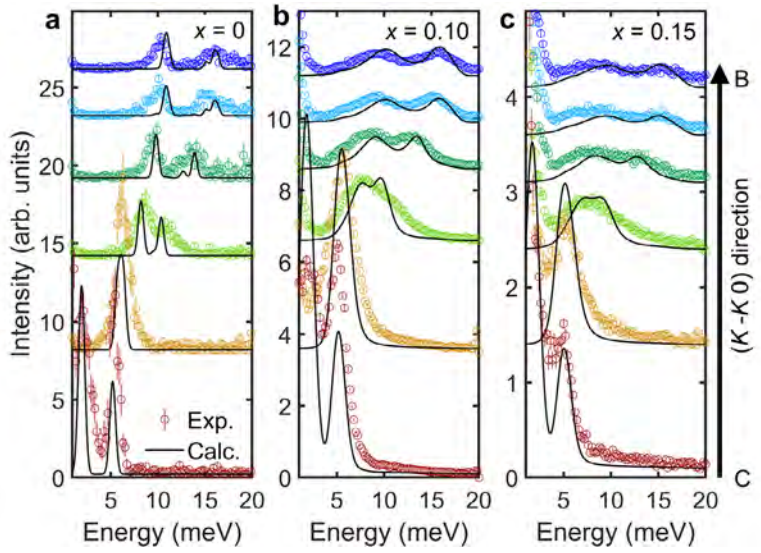

Figure 2. Constant-q cuts of the INS data in Fig. 1a–c along the C–B line. Black solid lines are the calculated spin-wave spectra shown in Fig. 1d–f.

Pyeongjae Park[1,2,3], Kisoo Park[2,3], Joosung Oh[2,3], Ki Hoon Lee[2,3,4,5], Jonathan C. Leiner[2,3,6], Hasung Sim[2,3], Taehun Kim[1,2,3], Jaehong Jeong[1,2,3], Kirrily C. Rule[7], Kazuya Kamazawa[8], Kazuki Iida[8], T. G. Perring[9], Hyungje Woo[9,10], S.-W. Cheong[11], M. E. Zhitomirsky[12], A. L. Chernyshev[13], and Je-Geun Park[1,2,3]

[1]*Center for Quantum Materials, Seoul National University;* [2]*Center for Correlated Electron Systems, Institute for Basic Science, Seoul National University;* [3]*Department of Physics and Astronomy & Institute of Applied Physics, Seoul National University;* [4]*Center for Theoretical Physics of Complex Systems, Institute for Basic Science;* [5]*Department of Physics, Incheon National University;* [6]*Physik-Department, Technische Universität München;* [7]*Australian Nuclear Science and Technology Organisation;* [8]*Neutron Science and Technology Center, CROSS;* [9]*ISIS Pulsed Neutron and Muon Source, STFC Rutherford Appleton Laboratory;* [10]*Department of Phys-ics, Brookhaven National Laboratory;* [11]*Department of Physics and Astronomy, and Rutgers Center for Emergent Materials, Rutgers University;* [12]*Université Grenoble Alpes, CEA,* [13]*Department of Physics and Astronomy, University of California, Irvine*

Duality of Magnetic Excitations and Kondo Effect in Metallic Ferromagnet $Fe_{3-x}GeTe_2$

1. Introduction

For a long time, magnetism has been a mysterious issue in condensed matter physics. Its understanding can usually be divided into two opposite camps: the local-moment or itinerant picture. But in the intermediate range, where both local moments and itinerant electrons are present, the nature of magnetism remains elusive.

This is also the case in the van der Waals (vdW) metallic ferromagnet $Fe_{3-x}GeTe_2$, which can sustain tunable room-temperature ferromagnetism down to the monolayer limit [1]. With the involvement of electronic itinerancy, the microscopic origin of its magnetism becomes controversial. There has been contradictory evidence from previous works, with some supporting the itinerant picture [1, 2], while others support the local-moment picture [3, 4]. To shed light on this question, we performed inelastic neutron scattering (INS) on high-quality single crystals of $Fe_{3-x}GeTe_2$ on 4SEASONS of J-PARC.

2. Duality of magnetic excitations

Figures 1(a) and (b) show the overall profiles of the spin excitation spectra along two high-symmetry directions in the (*h*, *k*) plane. There are two distinct patterns of spin excitations. First, it has been found that spin-wave-like excitations disperse up from the zone center and propagate toward the zone boundary in the lower panels. This fact indicates the ferromagnetic correlations in $Fe_{3-x}GeTe_2$. Second, we have found that the dispersive mode merges into a broad continuum above ~20 meV. The fluctuation continuum has a columnlike shape and extends to high energies around the zone boundary, as shown in the upper panels of Figs. 1(a) and (b). The latter mode is beyond general spin waves.

Then, we consider spin-flip particle-hole (p-h) excitations within the itinerant Stoner model to account for such columnlike excitations. By using the density-functional theory (DFT) to calculate the electronic bands [Figs. 1(c) and (d)] and considering p-h scattering [Fig. 1(e)], the calculated magnetic excitation spectra by random phase approximation (RPA) well reproduce the observed columnlike excitations in Figs. 1(f) and (g). Therefore, we think that this high-energy (*E*) mode originates from itinerant electrons, while the low-*E* mode is generated from local moments that we will discuss in the following section.

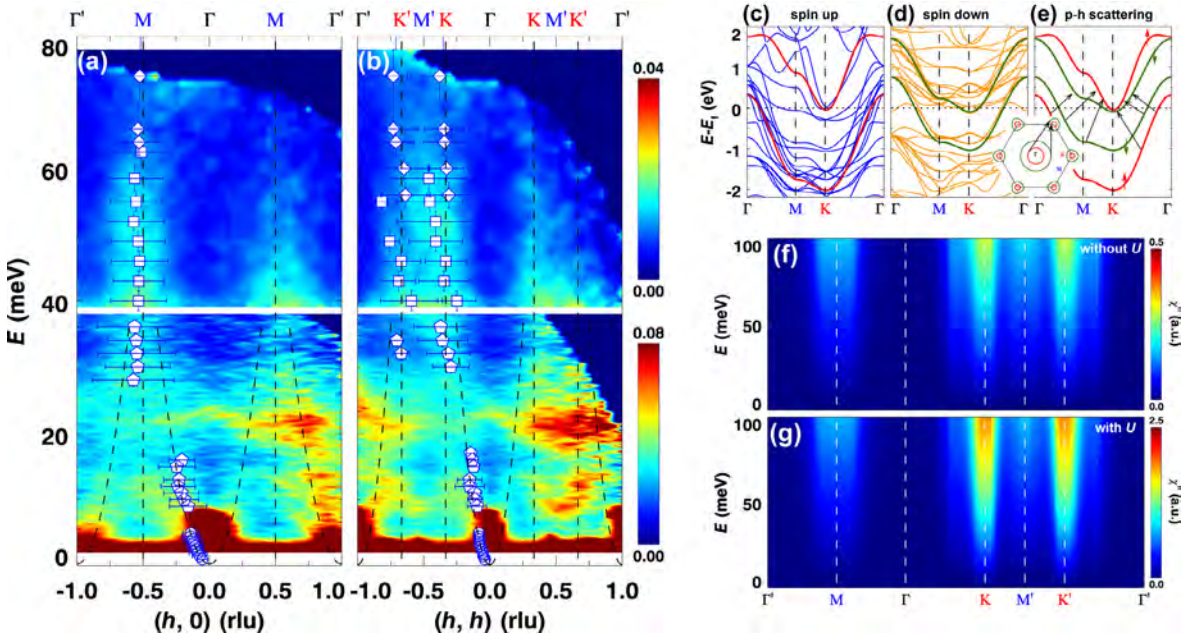

Figure 1. (a, b) INS results for the spin excitation spectra at 4 K, along two high-symmetry directions [1, 0] and [1, 1], respectively. (c, d) DFT calculations of spin-up and spin-down bands in the ferromagnetic state, respectively. (e) Schematic diagram for the p-h scattering processes via tight-binding model. Calculated bare (f) and RPA renormalized (g) spin excitation spectra below 100 meV.

3. Low-*E* spin waves and Kondo effect

Figures 2(a) and (c) show the low-*E* spin-wave-like excitations at 4 K for in-plane and out-of-plane directions, respectively. No spin gap is observed. Also, through quantitative analyses, we find that the spin-wave stiffness for the two directions has a comparable value. It suggests the three-dimensional nature of the magnetism in $Fe_{3-x}GeTe_2$, despite its quasi-two-dimensional vdW lattice structure.

Figures 2(b) and (d) show the low-*E* spin waves at 100 K. By naked-eye observations, it can be found that the excitations at 100 K are sharper both along the energy and momentum axes than those at 4 K, especially for the in-plane directions. To further quantify this temperature effect, we plot constant-***Q*** scans through the in-plane [Figs. 2(e) and (f)] and out-of-plane dispersions [Figs. 2(h) and (i)] at 4 and 100 K. At ***Q*** =(−0.09, 0, 2), a peak of the spin excitations can only be found at 100 K, while at 4 K, no such peak is observed, but instead there is a broad hump just above zero energy [Figs. 2(e) and (f)]. At ***Q*** =(0, 0, 1.7), inelastic peaks can be found at both 4 and 100 K. The peak centers do not change obviously, but the peak becomes sharper at 100 K than at 4 K. We have used a damped harmonic oscillator (DHO) formula to fit these data, which is often used to describe damped spin waves [5]. By fitting, we can extract the magnon energy and damping constant (inversely proportional to the lifetime of the damped magnons) of the energy scans for a series of ***Q*** values. We have plotted the damping constant as a function of magnon energy at 4 and 100 K in Figs. 2(g) and (j) for in-plane and out-of-plane directions, respectively. It has been found that the damping constant at 4 K is larger than that at 100 K along both directions, especially for the in-plane cuts.

These results reveal that the low-*E* spin waves at 100 K are more coherent than those at 4 K in $Fe_{3-x}GeTe_2$. It is quite different from the effect of thermal fluctuations, which always make magnons lose correlation and coherence upon warming. This unusual temperature evolution can be understood when considering the Kondo screening effect of the itinerant electrons on the local moments [6, 7]. In a Kondo lattice, each local moment is coupled with and screened by the surrounding itinerant electrons. The interplay between them directly contributes to the damping character of the spin waves by local moments. Moreover, the Kondo screening effect by surrounding itinerant electrons is expected to be more significant at low temperatures, and will weaken upon warming. Then, a more coherent spin waves at higher temperatures can be expected as what we can observe in Fig. 2.

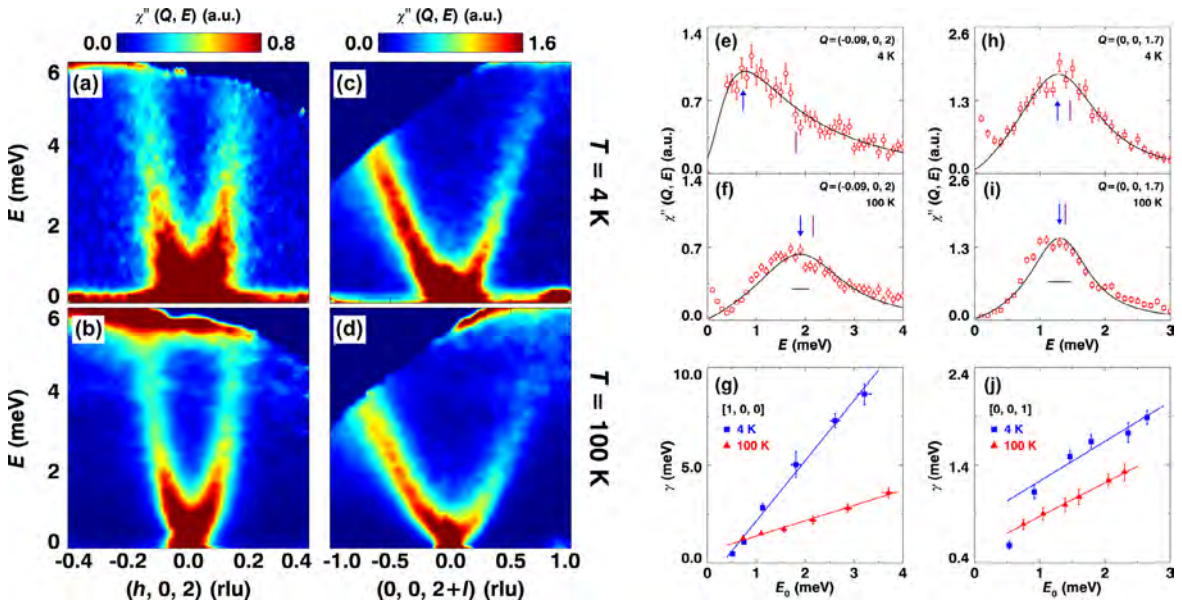

Figure 2. Low-*E* spin excitation spectra for the in-plane (a, b) and out-of-plane (c, d) directions at 4 K and 100 K, respectively. Constant-***Q*** cuts and extracted damping constant at 4 and 100 K for in-plane (e-g) and out-of-plane (h-j) directions.

4. Summary

In summary, our INS study on single crystals of Fe-deficient $Fe_{3-x}GeTe_2$ has revealed that the spin excitation spectra are composed of a low-*E* collective mode dispersing from the zone center and a columnlike continuum at the zone boundary that extends to above 100 meV. We attribute the origin of these two modes to the ferromagnetic spin waves of the local moments and particle-hole continuum from the scattering between the spin-up and spin-down bands, respectively. The local spins and itinerant electrons couple with each other through the Kondo effect, as evident from the unusual temperature effect of the low-*E* spin-wave excitations. Our work provides a rare example that spin-wave excitations, particle-hole continuum, and Kondo-lattice behavior coexist in a *d*-electron system, and sheds light on the understanding of magnetism in correlated electronic materials. This work was published in ref. [8].

References

[1] Y. Deng et al., Nature 563, 94 (2018).
[2] B. Chen et al., J. Phys. Soc. Jpn. 82, 124711 (2013).
[3] X. Xu et al., Phys. Rev. B 101, 201104(R) (2020).
[4] S. Calder et al., Phys. Rev. B 99, 094423 (2019).
[5] J. Zhao et al., Nat. Phys. 5, 555 (2009).
[6] Y. Zhang et al., Sci. Adv. 4, eaao6791 (2018).
[7] M. Zhao et al., Nano Lett. 21, 6117 (2021).
[8] S. Bao et al., Phys. Rev. X 12, 011022 (2022).

Song Bao[1], Wei Wang[2], Yanyan Shangguan[1], Zhengwei Cai[1], Zhao-Yang Dong[3], Zhentao Huang[1], Wenda Si[1], Zhen Ma[4], Ryoichi Kajimoto[5], Kazuhiko Ikeuchi[6], Shin-ichiro Yano[7], Shun-Li Yu[1], Xiangang Wan[1], Jian-Xin Li[1], and Jinsheng Wen[1]

[1]*National Laboratory of Solid State Microstructures and Department of Physics, Nanjing University;* [2]*School of Science, Nanjing University of Posts and Telecommunications;* [3]*Department of Applied Physics, Nanjing University of Science and Technology;* [4]*Institute for Advanced Materials, Hubei Normal University;* [5]*Neutron Science Section, Materials and Life Science Division, J-PARC Center;* [6]*Neutron Science and Technology Center, CROSS;* [7]*National Synchrotron Radiation Research Center*

Nontrivial Temperature Dependence of Magnetic Anisotropy in Multiferroics $Ba_2MnGe_2O_7$

1. Introduction

Spin-driven multiferroics [1] have been extensively studied since the discovery of an enhanced magnetoelectric (ME) effect in $TbMnO_3$ [2]. Through spin-orbit coupling (SOC), a spin order induces a change of charge distribution, leading to emergence of electric polarization. In the spin-dependent *d-p* hybridization mechanism [3], hybridized *d* and *p* orbitals of magnetic ion and ligand are modulated by spin states via SOC, and this induces an electric polarization. The relation between the electric polarization *P* and the spin moment *S* is described locally. The mechanism has been identified in number of materials [3–5]. Since the direction of the local spin moment determines the direction of the electric polarization, magnetic anisotropy plays a key role in forming a multiferroic structure [5–7]. The magnitude of the anisotropy gives the energy scale for the control of the magnetism by the electric field as well as magnetic field, which was tested in an åkermanite $Ba_2CoGe_2O_7$ [8]. Although the temperature (*T*) dependence of the anisotropy gap in magnon spectrum in conventional magnet scales by a power of the sublattice magnetic moment [9,10], it may not be the case for the multiferroics. The change of the polarization with *T* affects the spin-interaction parameters through the *d-p* hybridization, which leads to a nontrivial behavior in *T* dependence of the anisotropy and low-energy spin dynamics near the magnetic Γ point. In this study, we measured inelastic neutron scattering spectra to observe the nontrivial temperature dependence of spin dynamics in a multiferroics $Ba_2MnGe_2O_7$ using a state-of-the-art spectrometer with ultra-high resolution [11].

2. Experimental details

The INS experiment was carried out using the near backscattering spectrometer DNA in J-PARC MLF [12]. The horizontal scattering plane was the crystallographic *ac* plane, and the final energy of neutrons E_f was set to 2.084 meV by using Si (111) analyzer. The energy resolution was estimated to be 5.5 μeV in FWHM at an elastic condition of incoherent scattering near $\boldsymbol{Q}$ = (1, 0, 1/2). A dilution refrigerator was used to cool the sample to 0.05 K.

3. Results and discussion

Figure 1(a) shows the INS spectrum measured at

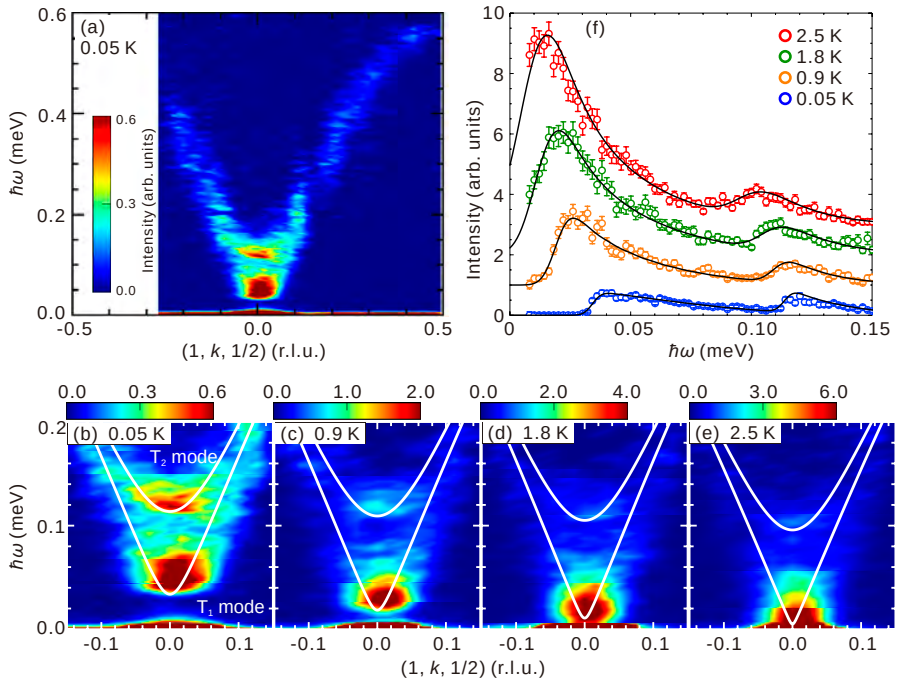

Figure 1. Inelastic neutron scattering (INS) spectra. (a) False color plot of the INS spectrum measured at 0.05 K projected onto the *ħω*-(1, *k*, 1/2) plane. (b)–(e) The INS spectra focused on the low-energy range measured at (b) 0.05 K, (c) 0.9 K, (d) 1.8 K and (e) 2.5 K. White solid curves are calculated dispersions. (f) Temperature evolution of constant-q cuts at $\boldsymbol{Q}$ = (1, 0, 1/2); data at different temperature are vertically offset. Black solid curves are the calculated magnon cross section.

0.05 K. Two dispersive modes with the boundary energy of 0.55 meV and with gaps 0.05 meV and 0.1 meV are clearly observed. The overall energy scale is consistent with the previous study [13]. It is remarkable that the two dispersive modes with finite gaps are clearly resolved because of very good resolution of DNA spectrometer. Anisotropy gaps (E_g) of the low- and high-energy modes, T_1 and T_2, respectively, at the magnetic Γ point, $\boldsymbol{Q}$ = (1, 0, 1/2), are identified at 36 μeV and 113 μeV. E_g of the T_1 mode (E_{g1}) is drastically suppressed with the increase of T as shown in Figs. 1(b)–1(e), while E_g of the T_2 mode (E_{g2}) is moderately suppressed. The intensities of the modes at the Γ point increase with the increasing *T* according to the thermal balance factor, as shown in Fig. 1(f).

The *T* dependences of E_{g2} and the sublattice moment $g\mu_B\langle S\rangle$ are shown in Fig. 2(a). The change of E_{g2} in the measurement range is small, and it scales as $g\mu_B\langle S\rangle$. The behavior is consistent with conventional antiferromagnets, where single-ion anisotropy is dominated by quadratic forms of spin operators [9, 10]. In contrast, E_{g1} in Fig. 2(b) increases continuously with the decrease of T, and it cannot be scaled either by the sublattice moment or any power of it. This indicates that the T_1 mode is not purely magnetic dynamics of electronic spin, but is hybridized with some other degrees of freedom.

Based on the spin-wave calculation, the gap energies of the magnetic anisotropy at the magnetic Γ-point are $\Delta_1^{\mathrm{SWT}} \sim 16\langle S(T)\rangle^2\sqrt{J_N(T)(2J_1+J_2+D/2)}$ for the T_1 mode and $\Delta_2^{\mathrm{SWT}} \sim 4\langle S(T)\rangle\sqrt{D(2J_1+J_2)}$ for the T_2 mode. Here $J_N(T)$ is spin nematic interaction, and it is included in the magnetic anisotropy term $\sum_{i,j} J_N O_i^{XY} O_j^{XY}$. The obtained *T* dependence of Δ_1^{SWT} in Fig. 2(b), however, is not consistent with E_{g1}, particularly in the low *T* region. Here we note that a Mn atom has a nuclear spin *I* = 5/2 and that the hyperfine coupling between nuclear and electron spins induces a low energy gap [14] in addition to the magnetic anisotropy gap. The energy gap induced by the hyperfine coupling has no *q* dependence. Then the magnon dispersion relation is modified; $\left(\hbar\omega_i(\boldsymbol{q})\right)^2 = \left(\hbar\omega_i^{\mathrm{SWT}}(\boldsymbol{q})\right)^2 + (\Delta^{\mathrm{HF}})^2$ where $\hbar\omega_i^{\mathrm{SWT}}(\boldsymbol{q})$ is the pure magnon dispersion for T_i mode (i = 1, 2) and Δ^{HF} is the hyperfine gap [15]. The two gaps E_{g1} and E_{g2} at $\boldsymbol{Q}$ = (1, 0, 1/2) are described as $E_{g1}^2 = (\Delta_1^{\mathrm{SWT}})^2 + (\Delta^{\mathrm{HF}})^2$ and $E_{g2}^2 = (\Delta_1^{\mathrm{SWT}})^2 + (\Delta^{\mathrm{HF}})^2$, where $\Delta^{HF} = \sqrt{(\chi_n(T)/\chi_c}Ag\mu_B\langle S(T)\rangle$. Here $\chi_n(T)$ is the paramagnetic nuclear spin susceptibility following Curie law, χ_c is the electron spin susceptibility along the crystallographic c direction, and *A* is the hyperfine coupling. In order to estimate Δ^{HF} and *D*, we fit the

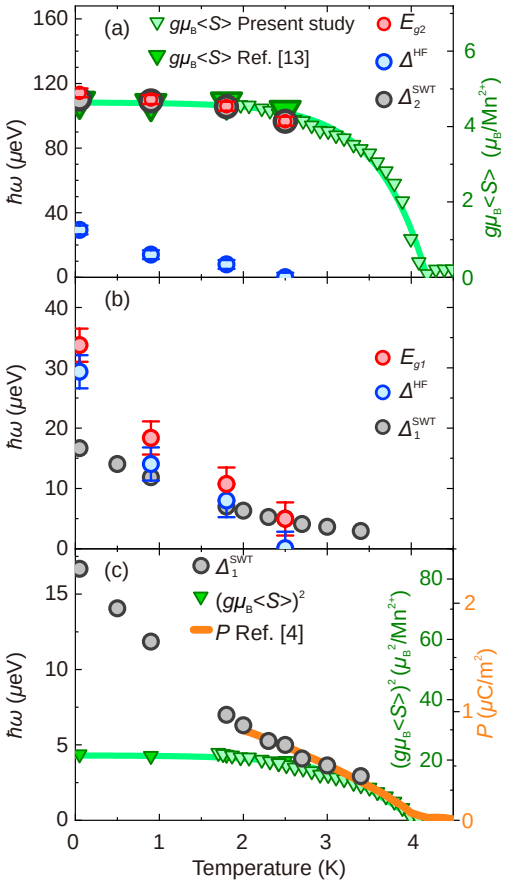

Figure 2. The temperature dependences of gap energies observed in INS spectra, anisotropy energies, sublattice moment and electric polarization. (a) *T* dependences of E_{g2} (red circles), Δ_2^{SWT} (black circles), Δ^{HF} (blue circles) and sublattice moment. (b) T dependences of E_{g1} (red circles), Δ_1^{SWT} (black circles) and Δ^{HF} (blue circles). (c) T dependences of Δ_1^{SWT} (black circles), electric polarization P (orange curve from Ref. [4]) and the second power of the sublattice moment (light green triangles).

constant-q cut in Fig. 1(f) to the calculated magnon cross-section. The fit to the data is good as shown by black solid curves. The T_1 and T_2 modes in Figs. 1(b)–1(e) are reasonably reproduced by the calculated magnon- dispersions shown by the white curves. The obtained hyperfine coupling constant is *A* = 240 kOe, and it is consistent with Ref. [14] and the value reported in $^{55}Mn^{2+}$ ions in Mn-diluted ZnF_2 [16]. The T_1 mode is, thus, hybridized with the nuclear spin. The T dependence of Δ^{HF} is shown in Figs. 2(a) and 2(b), and that of Δ_2^{SWT} is shown in Fig. 2(a). *T* dependences of Δ_1^{SWT}, a scaled electric polarization P [4] and the second power of the scaled sublattice moment $(g\mu_B\langle S\rangle)^2$ are shown in Fig. 2(c). We find that Δ_1^{SWT} does not scale as $(g\mu_B\langle S\rangle)^2$, but is rather consistent with the temperature dependence of electric polarization, *P*. From the local relation

between ***S*** and ***P***, one has, $P_i^Z = \Lambda_Z O_i^{XY}$ [5, 6]. This relation leads to $\mathcal{H}_N = \sum_{i,j} J_N O_i^{XY} O_j^{XY} = \sum_{i,j} J_P P_i^Z P_j^Z$, where J_P is an effective interaction between the electric polarizations; $J_P = J_N/\Lambda_Z^2$. By considering the structures of the spin and electric polarization at $T < T_N$, we obtain $\Delta_1^{\mathrm{SWT}} = 16\langle P(T)\rangle\sqrt{J_P(2J_1 + J_2 + D/2)}\sin(2\kappa)$, where κ is a parameter in the crystal structure. The fact that the magnetic anisotropy gap, Δ_1^{SWT}, is scaled by the electric polarization, $P(T)$, means that *P* induces an emergent magnetic field. In addition, we notice that J_P is *T* independent. Drastic *T* dependence of J_N thus results from the change of Λ_Z with *T*; the modification of the hybridized orbitals of Mn^{2+} and O^{2-} ions with *T* leads to a small change of the energy, which is negligible in highly anisotropic system but is enhanced in the nearly isotropic system such as the symmetric half-filled shell of Mn^{2+} ion, and it is probed as the change of J_N thorough SOC. Since the change of the hybridized *d-p* orbital with *T* explicitly affects the anisotropy gap of the acoustic magnon, we call it hybridized magnon with the *d-p* orbital. This is a characteristic quasiparticle of the multiferroics originating from the hybridization of spin and orbital momenta.

4. Conclusion

In conclusion, we found that the temperature dependence of the biaxial magnetic anisotropy energy in the multiferroic $Ba_2MnGe_2O_7$ is scaled by the electric polarization. The change of the hybridized orbitals of the metal and the ligands with the temperature determines the spin-nematic interaction, leading to nontrivial temperature dependence of the anisotropy energy in the neutron spectrum as well as that of the spin-flop field. In contrast, conventional single-ion anisotropy energy of easy-plane type is independent of temperature. The effect of hyperfine coupling between nuclear and electron spins is also observed in the low temperature region. Thorough account of this effect is important for accurate understanding of the temperature evolution of the electronic spin gap.

References

[1] Y. Tokura, S. Seki, and N. Nagaosa, Rep. Prog. Phys. **77**, 076501 (2014).
[2] T. Kimura et al., Nature **426**, 55 (2003).
[3] T.-h. Arima, J. Phys. Soc. Jpn. **76**, 073702 (2007).
[4] H. Murakawa et al., Phys. Rev. B **85**, 174106 (2012).
[5] M. Soda et al., Phys. Rev. Lett. **112**, 127205 (2014).
[6] J. Romhanyi et al., Phys. Rev. B **84**, 224419 (2011).
[7] S. Hayashida et al., Phys. Rev. B **92**, 054402 (2015).
[8] M. Soda et al., Phys. Rev. B **94**, 094418 (2016).
[9] F. M. Johnson and A. H. Nethercot, Phys. Rev. **114**, 705 (1959).
[10] R. J. Birgeneau, J. Skalyo, and G. Shirane, Phys. Rev. B **3**, 1736 (1971).
[11] S. Hasegawa et al.,,Phys. Rev. Research **3**, L032023 (2021).
[12] K. Shibata et al., JPS Conference Proceedings **8**, 036022 (2015).
[13] T. Masuda et al., Phys. Rev. B **81**, 100402(R) (2010).
[14] A. S. Borovik-Romanov and V. Tulin, JETP Lett. **1**, 134 (1965).
[15] I. A. Zaliznyak, N. N. Zolin, and S. V. Petrov, JETP Lett. **64,** 473 (1996).
[16] A. M. Clogston et al., Phys. Rev. **117**, 1222 (1960).

S. Hasegawa[1], S. Hayashida[1], S. Asai[1], M. Matsuura[2], I. Zaliznyak[3], and T. Masuda[1]
[1]*Institute for Solis State Physics, the University of Tokyo;* [2]*Neutron Science and Technology Center, CROSS;* [3]*Brookhaven National Laboratory*

Study of a Low Temperature Crystal Structure of a New Magnetoelectric Material

1. Introduction

The coupling between magnetic and electric dipole degrees of freedom (magnetoelectric coupling) in insulating quantum materials enables us to manipulate magnetism by an electric field and dielectricity by a magnetic field, which may contribute to the design of novel functional devices. Continued efforts have been made to explore new types of magnetoelectric couplings and materials.

$Mn_3Ta_2O_8$ has an anion-deficient fluorite-related crystal structure with centrosymmetric tetragonal space group $I4_1/a$ at room temperature (T) (see Fig. 1) [1]. It undergoes an antiferromagnetic phase transition at T_N = 24 K (Fig. 2a), below which collinear spin arrangement emerges [2]. Recently, we predicted by symmetry consideration that this AFM order breaks both space inversion and time reversal symmetries, thereby inducing the linear magnetoelectric effect [3], and confirmed this prediction by electric polarization measurements. Furthermore, we also found a previously unknown phase transition at T_S = 55 K as evidenced by a specific heat anomaly (Fig. 2c). Consequently, $Mn_3Ta_2O_8$ involves three phases at low temperatures: phase I ($T > T_S$), phase II ($T_S > T > T_N$), and phase III ($T < T_N$). Upon the 55 K transition, the magnetic susceptibility does not exhibit any anomaly (Fig. 2a), whereas the dielectric constant shows a clear kink (Fig. 2b). The electric polarization is absent in phase II. These observations suggest that the 55 K transition is of antiferroelectric-like origin. However, our powder x-ray diffraction measurement could not detect any change in the crystal structure, presumably due to a tiny structural change. Thus, the origin of this new phase transition remains unsolved.

Here we carry out high-resolution powder neutron diffraction experiments to elucidate the crystal structure in phase II and hence the origin of the 55 K transition in $Mn_3Ta_2O_8$.

2. Methods

To obtain a high-quality powder sample, we first prepared single crystals of $Mn_3Ta_2O_8$ by a floating-zone method [4]. An impurity phase was observed in the

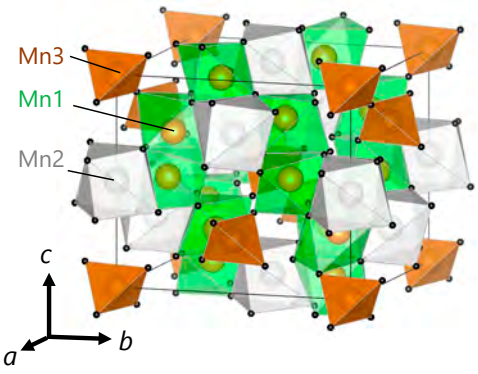

Figure 1. The crystal structure of $Mn_3Ta_2O_8$, consisting of $Mn1O_7$, $Mn2O_8$, and $Mn3O_4$ polyhedra. The Ta ions are omitted for clarity.

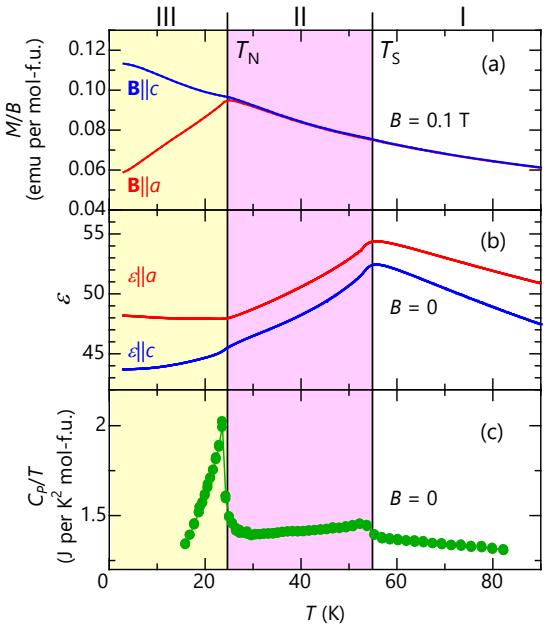

Figure 2. Temperature (T) dependences of (a) magnetization (M) divided by an applied magnetic field (B = 0.1 T) along the a and c axes, (b) a and c axes' dielectric constant ε at 0 T, and (c) heat capacity (C_p) divided by T at 0 T (Ref. 3).

outer skins of the obtained crystalline rods. The dirty skins were mechanically removed, and the left portions were confirmed to be phase-pure single crystals of $Mn_3Ta_2O_8$. The powder sample was obtained by crushing the single crystals.

Time-of-flight neutron diffraction measurements were carried out on a powder sample of $Mn_3Ta_2O_8$ using a powder diffractometer SuperHRPD on BL08 [5]. The crystal structure was refined using Z-Rietveld software [6]. VESTA software was used to draw the crystal structures in this report [7].

3. Results and discussions

Figure 3 shows diffraction patterns at 30 (phase II) and 60 K (phase I) in a specific *d* region. It is seen that tiny but detectable peaks newly appear at 30 K. The new peaks can be indexed in the tetragonal notation as *hkl* ($h+k+l = 2n+1$). The body-centered symmetry of the $I4_1/a$ space group is thus broken in phase II.

As mentioned above, the electric polarization is absent in phase II. This indicates that the crystal structure of phase II belongs to a nonpolar space group. There are four nonpolar space groups (*P*-4, $P2/a$, $P2_1$/a, and *P*-1) that are the subgroups of $I4_1/a$ (The *c* axis is taken as the unique axis of $P2/a$ and $P2_1$/a). Among them, we consider that $P2_1/a$ is most reasonable for the following reasons. In the parent $I4_1/a$ structure, the site symmetry of all ions is 1, except for -4 of Mn2 and Mn3 ions. It is thus likely that a lowering of the site symmetry of Mn2 and Mn3 due to off-center displacements is responsible for the antiferroelectric-like ordering in phase II. The possibility of *P*-4 and $P2/a$ can be excluded because off-center displacements in this case are allowed only along the tetragonal *c* axis, which is inconsistent with the fact that the dielectric anomalies at 55 K appear in both the *a* and *c* axes (Fig. 2b). For $P2_1$/a and *P*-1, by contrast, the site symmetry of Mn2 and Mn3 is 1, allowing the displacement along any direction, consistent with the observations. Moreover, no peaks were observed that violate extinction rules for $P2_1$/a. Thus, although the possibility of *P*-1 cannot be excluded, the higher-symmetry $P2_1/a$ seems to be the most appropriate choice.

Based on $P2_1/a$, we refined the 30 K crystal structure using the Rietveld method. We achieved good agreement between the observed and calculated patterns ($\chi^2 = 2.17$, $R_{wp} = 2.27\%$, $R_p = 1.87\%$, and $R_e = 1.54\%$). It has been found from the refinement that Mn2 exhibits a small but finite off-center displacement, whose direction is illustrated in Fig. 4. The resulting changes in the Mn2-O bond lengths are smaller than 0.2 Å. The component of the displacement is finite along both the *a* and *c* axes, in agreement with the emergence of the dielectric anomalies both along the *a* and *c* axes. Such a displacement is not observed for Mn3. These results show that the Mn2 off-center displacement plays a key role for the antiferroelectric-like ordering at 55 K.

It is worthy to note that the Mn^{2+} ion has nonempty d orbitals (d^5). In the common ABO_3 perovskite oxide ferroelectrics such as $BaTiO_3$, the ferroelectricity is usually driven by the off-center displacement of the *B* site cation having a d^0 configuration. This so-called "d^0-ness" excludes the magnetism that needs nonempty *d* orbitals [8]. However, a recent statistical structural analysis [9] of various Fe^{3+} oxides demonstrated that the second order Jahn-Teller (SOJT) effect, which leads to the off-center displacement of d^0 cations, is also allowed for high-spin

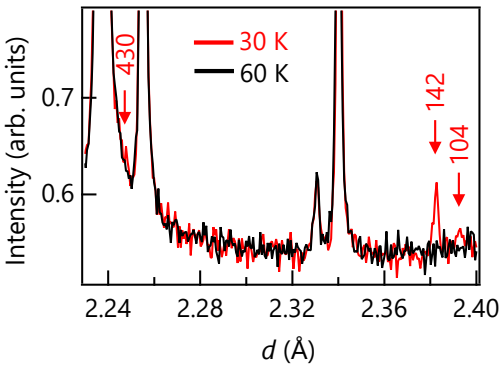

Figure 3. Time-of-flight powder neutron diffraction patterns at 30 K (red) and 60 K (black) (Ref. 3). The arrows indicate new peaks appearing at 30 K.

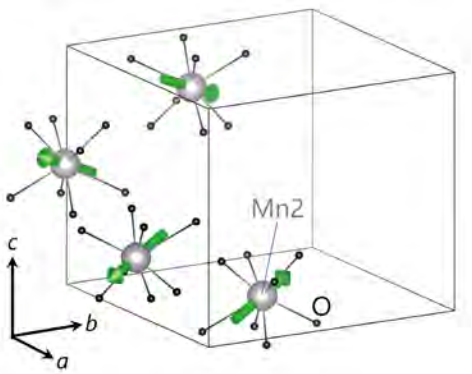

Figure 4. The Mn2 off-center displacements at 30 K (phase II), whose direction is denoted by the green arrows (Ref. 3).

d^5 cations because they have the same electronic symmetry. Thus, the Mn^{2+} (d^5) off-center displacements in $Mn_3Ta_2O_8$ can be explained by the SOJT effect.

4. Conclusion

By means of high-resolution powder neutron diffraction measurements, we have studied the origin of the new antiferroelectric-like ordering in the magnetoelectric compound $Mn_3Ta_2O_8$. We have found that the off-center displacement of magnetic Mn^{2+} ions is responsible for the antiferroelectric-like ordering. The present study reveals that $Mn_3Ta_2O_8$ is a new system where Mn^{2+} ions carry both magnetic and electric dipole degrees of freedom.

References

[1] S. Esmaeilzadeh et al., J. Mater. Chem., **8** 2493 (1998).
[2] J. Grins et al., J. Mater. Chem., **9** 1575 (1999).
[3] K. Kimura et al., Inorg. Chem., **60** 15078 (2021).
[4] K. Rickert et al., Inorg. Chem., **54** 6513 (2015).
[5] S. Torii et al., J. Phys.: Conf. Ser. **503** 012052 (2014).
[6] R. Oishi et al., Nucl. Instrum. Methods Phys. Res., Sect. A, **600** 94 (2009).
[7] K. Momma and F. Izumi, J. Appl. Crystallogr., **44** 1272 (2011).
[8] N. Hill, J. Phys. Chem., **104** 6694 (2000).
[9] J. Cumby and J. P. Attfield, Nat. Commun. **8** 14235 (2017).

K. Kimura[1], N. Yagi[1], M. Hagihala[2,3], and T. Kimura[1]
[1]Department of Advanced Materials Science, University of Tokyo; [2]Institute of Materials Structure Science, KEK; [3]Materials Science Research Center, Japan Atomic Energy Agency

Crystalline Electric Field in Non-Centrosymmetric $CeTX_3$

1. Introduction

In recent years, the influence of inversion symmetry breaking on physical properties has become one of the most attractive fields of research. In the $CeTSi_3$ (T = transition metal) system, anomalously high upper critical field H_{c2} behavior has been reported due to Cooper pair mixing in the superconducting state [1–4]. More recently, it has been theoretically predicted that the reentrant superconducting behavior of UTe_2 is realized by local inversion symmetry breaking around uranium [5, 6]. In addition, topology due to inversion symmetry breaking plays an important role in the physical properties not only in the bulk but also at surfaces and interfaces, such as the anomalous Hall effect observed in magnetic skyrmions.

In the broken inversion symmetry system, antisymmetric spin-orbit interaction (ASOI) is expected to play an important role in the physical properties. The ASOI lifts the degeneracy of electronic states in momentum space without magnetic fields. The splitting width of the electronic band is about ~1000 K [7], and the significant change in the electronic state due to the effect of ASOI is expected to affect the magnetic properties.

$CeTSi_3$ is a tetragonal structure with space group *I4mm* and it breaks the inversion symmetry along the interplane direction. In these compounds, there are differences in physical properties such as $CeRhSi_3$ [1] and $CeIrSi_3$ [2], which exhibit superconductivity under pressure, and $CePdSi_3$ [8] and $CePtSi_3$ [9], which exhibit multiple metamagnetic transitions. In addition, superconductivity has also been reported in isostructural $CeTGe_3$. Therefore, we investigated the difference in physical properties by determining their crystalline electric field (CEF) level schemes by inelastic neutron scattering (INS) experiments and discussed the anomalous superconducting properties.

2. Experimental procedure

Polycrystalline samples of $CeTSi_3$ were grown by arc melting. The polycrystalline samples were cut into thin strips and glued to aluminum plates to reduce neutron absorption. INS experiments were carried out with non-magnetic and isostructural lanthanum compounds using High Resolution Chopper spectrometer (HRC) installed at BL12 in J-PARC MLF. The sample was cooled to 3.0 and 4.2 K, and the INS spectra were acquired with an incident energy of E_i = 72 meV ($CeRhSi_3$) and 153 meV ($CeIrSi_3$).

3. Results and discussion

The magnetic scattering of $CeTSi_3$ was extracted by subtracting the measurement data of non-magnetic $LaTSi_3$ from the results of the INS data for $CeTSi_3$. Figures 1(a) and 1(b) show the magnetic scattering of

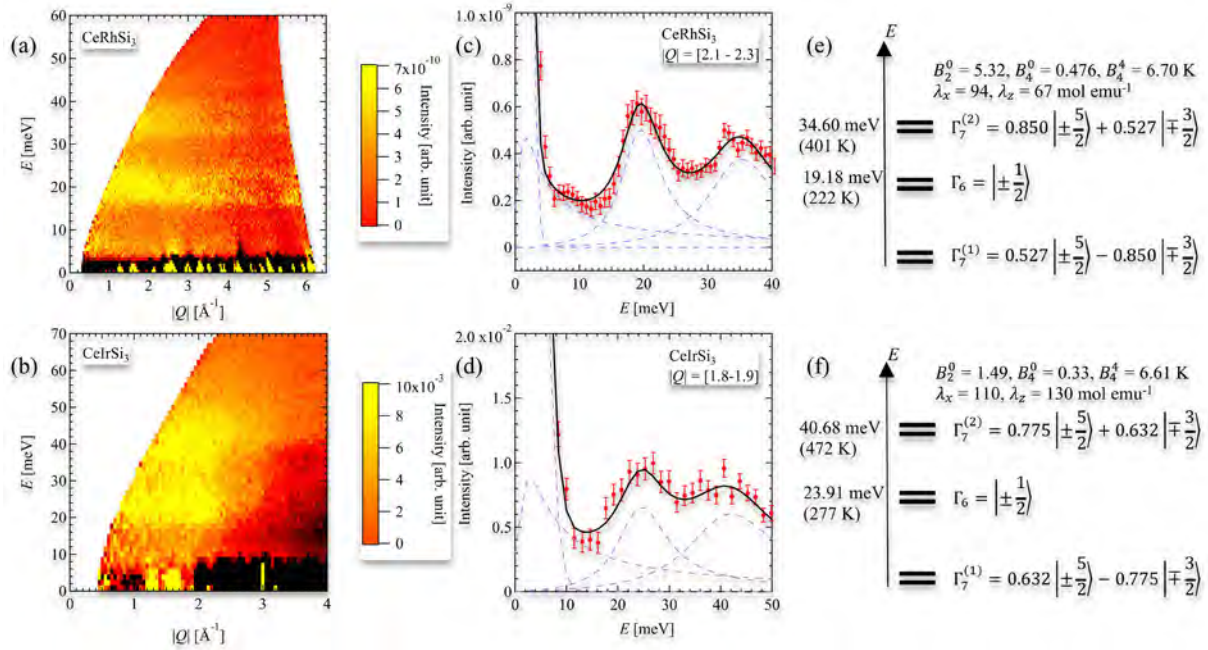

Figure 1. Color-coded plots of the magnetic INS intensity for (a) $CeRhSi_3$ and (b) $CeIrSi_3$. One-dimensional cut-out of (c) $CeRhSi_3$ and (d) $CeIrSi_3$. Dashed lines show the elastic scattering, the quasi-elastic scattering, and CEF excitations. The vertical bars represent statistical errors. Schematic illustration of the CEF eigenenergies and eigenstates of (e) $CeRhSi_3$ and (f) $CeIrSi_3$ [10].

$CeRhSi_3$ with incident neutron energy of $E_i = 72$ meV and $CeIrSi_3$ with $E_i = 153$ meV, respectively. Here, the vertical axis represents the energy transfer and the horizontal axis represents the scattering vector, respectively. We can easily find the CEF excitations marked in yellow in these figures. Figures 1(c) and 1(d) show the one-dimensional cut-out after subtracting the effects of the background and phonons of $CeRhSi_3$ and $CeIrSi_3$, respectively, and black solid lines show the fitting results with the CEF model. The tetragonal CEF Hamiltonian with point group C_{4v} is given by the three CEF parameters B_2^0, B_4^0, and B_4^4. In $CeRhSi_3$, the fitting results show the presence of CEF excitations centered at 19.2 and 34.6 meV with CEF parameters of $B_2^0 = 5.32$ K, $B_4^0 = 0.476$ K, and $B_4^4 = 6.70$ K. On the other hand, the CEF excitations of $CeIrSi_3$ exist around 23.9 and 40.7 meV with CEF parameters of $B_2^0 = 1.49$ K, $B_4^0 = 0.33$ K, and $B_4^4 = 6.61$ K. Furthermore, the calculated magnetic susceptibility using the CEF parameters obtained from these INS experiments explains well the experimentally observed behavior above the Kondo temperature. Therefore, from these results we determined revised and accurate CEF level schemes of $CeRhSi_3$ and $CeIrSi_3$ as shown in Figs. 1(e) and 1(f).

Table 1 summarizes the properties of $CeTX_3$. This table shows that $CeTX_3$ can be categorized into three groups, and that the ground state of $\Gamma_7^{(1)}$ is a necessary condition for superconductivity to appear. The two ground states differ in the spread of the wave function, as can be seen in Ref. 10. The wave function of Γ_6 shows an extended shape along the [001] direction, making it difficult for it to hybridize with the orbits of other elements. In contrast, the wave function of $\Gamma_7^{(1)}$ shows a three-dimensional spread, and possibly hybridizes with other orbits. Thus, a hybridization of the three-dimensional extended wave function of Ce^{3+} ions is suggested to be responsible for the appearance of superconductivity due to the *f*-electron band.

Table 1. Physical properties of $CeTX_3$. The 2nd column is the orientation of magnetic moment in the magnetically ordered state. The 3rd column indicates the presence of superconductivity. The 4th column indicates the wave function of the ground state [10].

Sample	orientation of magnetic moment	S.C.	g.s. wave function
$CeRhSi_3$	μ // a	◎	$\Gamma_7^{(1)}$
$CeIrSi_3$	μ // a	◎	$\Gamma_7^{(1)}$
$CePdSi_3$	μ // a (ac)	×	Γ_6
$CePtSi_3$	μ // a (ac)	×	Γ_6
$CeCoGe_3$	μ // c	○	$\Gamma_7^{(1)}$
$CeRhGe_3$	μ // c	○	$\Gamma_7^{(1)}$
$CeIrGe_3$	μ // c	○	$\Gamma_7^{(1)}$

The double circles of superconductivity in Table 1 indicate that the upper critical field exceeds both Pauli- and orbital-limiting fields. The behavior exceeding the two limits is explained by the hybridization of Cooper pairs. However, a lack of inversion symmetry generally disfavors the formation of spin triplet Cooper pairs. For hybridization to be realized under these conditions, the *d*-vector of Cooper pair and the orientation of ASOI must be parallel. Here, Table 1 shows that the orientation of the magnetic moment in the ordered state is different for $CeTSi_3$, which exceeds two limits, and $CeTGe_3$, which exceeds only the Pauli-limit. In this crystal structure, the orientation of ASOI is in the in-plane direction. Therefore, it is suggested that the magnetic fluctuations in $CeTSi_3$ with the magnetic moment in the *a*-axis are predominantly responsible for the formation of spin-triplet Cooper pairs, resulting in anomalous superconductivity.

References

[1] N. Kimura et al., Phys. Rev. Lett., **95** 197001 (2007).
[2] R. Settai et al., J. Phys. Soc. Jpn., **77** 073705 (2008).
[3] M. Sigrist et al., J. Magn. Magn. Mater., **310** 536 (2007).
[4] S. Fujimoto, J. Phys. Soc. Jpn., **76** 051008 (2007).
[5] S. Ran et al., Nat. Phys., **15** 1250 (2019).
[6] M. H. Fischer et al., arXiv, 2204.02449.
[7] T. Kawai et al., **77** 064717 (2008).
[8] D. Ueta et al., J. Phys. Soc. Jpn., **85** 104703 (2016).
[9] D. Ueta et al., J. Phys. Soc. Jpn., **90** 064712 (2021).
[10] D. Ueta et al., J. Phys. Soc. Jpn., **90** 104706 (2021).

D. Ueta[1,2,3], T. Kobuke[3], H. Shibata[3], M. Yoshida[3], Y. Ikeda[4], S. Itoh[1,2], T. Yokoo[1,2], T. Masuda[3,2], and H. Yoshizawa[3]

[1]Neutron Science Section, Materials and Life Science Division, J-PARC Center; [2]Institute of Materials Structure Science, KEK; [3]Neutron Science Laboratory, Institute for Solid State Physics, The University of Tokyo; [4]Institute for Materials Research, Tohoku University

Spin Dynamics of the Dual Isolated Antiferromagnetic System Ba_2CoTeO_6

1. Introduction

Ba_2CoTeO_6, abbreviated as BCTO, is a trigonal complex perovskite compound [1]. The magnetic ions Co^{2+} occupy two different sites in the unit cell. Uniquely, it has been reported that the two magnetic subsystems (A and B) composed of Co^{2+} ions, which behave independently as a spin-1/2 triangular-lattice Heisenberg antiferromagnet (TLHAF) and honeycomb-lattice Ising-like antiferromagnet (HLIAF), respectively [2, 3]. The phase transitions at $T_{N1} = 12$ and $T_{N2} = 3$ K observed by specific heat measurements correspond to long-range orders in subsystems B and A, respectively [2]. In magnetization measurements, the magnetization curve of BCTO is given by the sum of those for the two subsystems. This study shows that magnetic excitation can also be the superposition of those two subsystems [4].

In spin-1/2 TLHAF studies, the results of $Ba_3CoSb_2O_9$ abbreviated as BCSO, one of the best experimental realizations of a spin-1/2 TLHAF, have provided many insights. In recent years, much attention has been paid to magnetic excitations in BCSO [5–7]. The magnetic excitation spectrum of the ordered state of BCSO shows a roton-like minimum in the dispersion curve at the M point (the center of the edge in the Brillouin zone), which is much different from the linear spin wave theory (LSWT), in contrast with a dispersion maximum predicted by the LSWT. It has been interpreted that the roton-like minimum is caused by the coupling between a single magnon excitation and a continuum of fermionic spinons [8–10] or two magnons [11].

The structured excitation continuum in BCSO appears in the high-energy spectrum. These excitations have a strong intensity that cannot be explained as a two-magnon continuum [12]. This phenomenon has been reproduced computationally by tensor-network calculation [13], bond operator theory [14], and bosonic spinon-based analysis [15]

We must pay attention to the material-specific interactions in BCSO, even if they are small. For example, there is a discussion of the effect on magnetic spectra concerning easy-plane anisotropy and interactions between triangular layers [11]. It is essential to measure the magnetic spectra of other systems and extract universal features in spin-1/2 TLHAFs.

2. Experimental details

Inelastic neutron scattering experiments were performed on BCTO using the cold-neutron disk chopper spectrometer AMATERAS (BL14) [16]. The BCTO crystals were grown by the $BaCl_2$ flux method, according to Ref. [2]. The hexagonal plate-shaped single crystal with dimensions of $2 \times 2 \times 0.3$ mm^3 was selected. We coaligned approximately 400 crystals on two aluminum plates using CYTOP as glue. The data were collected at $T = 0.3$, 6.0, and 20 K with incident energies $E_i = 3.6$, 5.6, 9.7, and 20.9 meV using a ^{3}He refrigerator. We used the software suite UTSUSEMI [17] for statistical computing.

3. Results and discussion

Figures 1 (a)-(c) show the excitation spectra of BCTO at $T = 0.3$, 6.0, and 20 K. Across two magnetic transitions, the change in the magnetic spectra was partial. The change in the low-energy excitation part of the magnetic spectra (< 5 meV) occurs between T = 0.3 and 6.0 K, while the high-energy excitation part (5–7 meV) changes between $T = 6.0$ and 20 K. We emphasize that the spectrum of subsystem B, including its intensity, does not change across the magnetic ordering of subsystem A. This result indicates that the two subsystems are well decoupled.

Figure 2 shows the excitation spectrum of BCTO measured with $E_i = 3.6$ meV, where the low-energy part is found to be in very good agreement with the excitation spectrum of BCSO, including intensity and structure. The single magnon dispersion has roton-like minima with energies of 1.25 and 1.55 meV at the M point. A structured excitation continuum has been observed in an energy range of 3–5 meV, as shown in Fig. 1(a). These results demonstrate that the magnetic excitations of BCTO and BCSO are less affected by material-specific properties (especially by interlayer interactions). These results also indicate that subsystem A of BCTO is a good realization of a spin-1/2 TLHAF.

The dispersion relation for subsystem B is well reproduced by the LSWT for an Ising-like honeycomb lattice antiferromagnet (HLAF). In the Ising model, the excitations are localized, and the dispersion relation is flat. The dispersive magnetic spectrum observed suggests a finite XY component. The dispersion relations for subsystem B can be described by a J_1-J_2-J_3 XXZ model on the honeycomb lattice, including a ferromagnetic

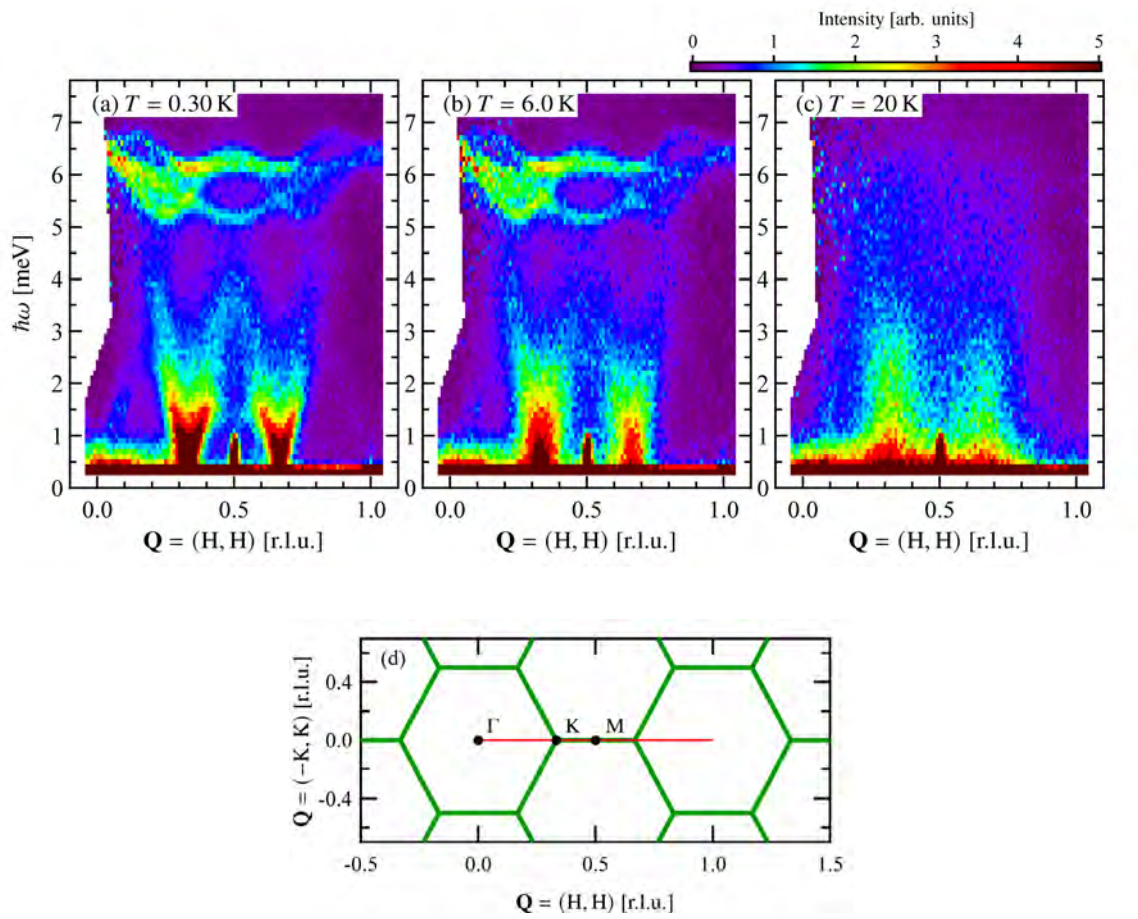

Figure 1. Excitation spectra of Ba_2CoTeO_6 at $T = 0.3$ (a), 6.0 (b), and 20 K (c) measured with the incident energy $E_i = 9.7$ meV along the high-symmetry directions $Q = (H, H)$ of the Brillouin zone, which are shown by red line in (d). Figure (a)–(c) are reproduced from Ref. [4].

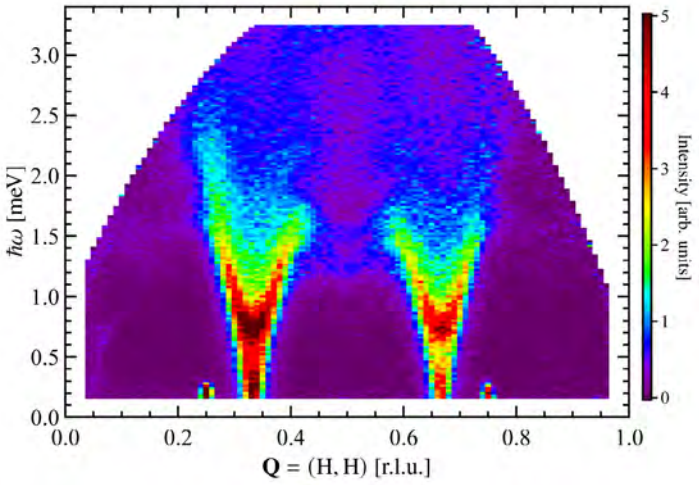

Figure 2. Excitation spectrum of Ba_2CoTeO_6 at $T = 0.3$ K measured with the incident energy $E_i = 3.6$ meV along the directions $Q = (H, H)$ of the Brillouin zone. This figure is reproduced from Ref. [4].

third-nearest neighbor interaction [4]. The obtained exchange parameters are useful for determining the spin structure of subsystem B, which has been unclear in the magnetization measurements.

4. Conclusion

We have measured magnetic excitations in BCTO. We observed a two-step change in the excitation spectrum across the two ordering transitions at T_{N1} and T_{N2} for subsystems B and A, respectively. The excitation spectrum of subsystem B is not affected by the magnetic ordering of subsystem A, described as a spin-1/2 TLHAF. This result demonstrates that the excitation spectrum of BCTO is produced by the superposition of the two independent magnetic excitation spectra originating from two subsystems. This indicates that the magnetic model of BCTO is described by decoupled spin-1/2 Heisenberg-like TLAF and Ising-like HLAF.

The low-energy excitation spectrum for subsystem A is very similar to that for BCSO. Observed roton-like minima and structured excitation continuum are common to BCTO and BCSO. This shows that the excitation spectra of subsystem A and BCSO are universal in spin-1/2 TLHAFs.

References

[1] S. A. Ivanov, P. Nordblad, R. Mathieu, R. Tellgren, and C. Ritter, Dalton Trans. **39**, 5490 (2010).

[2] P. Chanlert, N. Kurita, H. Tanaka, D. Goto, A. Matsuo, and K. Kindo, Phys. Rev. B **93**, 094420 (2016).

[3] P. Chanlert, N. Kurita, H. Tanaka, M. Kimata, and H. Nojiri, Phys. Rev. B **96**, 064419 (2017).

[4] Y. Kojima, N. Kurita, K. Nakajima, and H. Tanaka, Phys. Rev. B **105**, L020408 (2022).

[5] J. Ma, Y. Kamiya, T. Hong, H. B. Cao, G. Ehlers, W. Tian, C. D. Batista, Z. L. Dun, H. D. Zhou, and M. Matsuda, Phys. Rev. Lett. **116**, 087201 (2016).

[6] S. Ito, N. Kurita, H. Tanaka, S. Ohira-Kawamura, K. Nakajima, S. Itoh, K. Kuwahara, and K. Kakurai, Nat. Commun. **8**, 235 (2017).

[7] D. Macdougal, S. Williams, D. Prabhakaran, R. I. Bewley, D. J. Voneshen, and R. Coldea, Phys. Rev. B **102**, 064421 (2020).

[8] F. Ferrari and F. Becca, Phys. Rev. X **9**, 031026 (2019).

[9] C. Zhang and T. Li, Phys. Rev. B **102**, 075108 (2020).

[10] R. Verresen, R. Moessner, and F. Pollmann, Nat. Phys. **15**, 750 (2019).

[11] A. L. Chernyshev and M. E. Zhitomirsky, Phys. Rev. B **79**, 144416 (2009).

[12] Y. Kamiya, L. Ge, T. Hong, Y. Qiu, D. L. Quintero-Castro, Z. Lu, H.B.Cao, M.Matsuda, E.S.Choi, C.D.Batista, M. Mourigal, H. D. Zhou, and J. Ma, Nat. Commun. **9**, 2666 (2018).

[13] R.-Z. Chi, Y. Liu, Y. Wan, H.-J. Liao, and T. Xiang, Phys. Rev. Lett. **129**, 227201 (2022).

[14] A. V Syromyatnikov, Phys. Rev. B **105**, 144414 (2022).

[15] E. A. Ghioldi, S.-S. Zhang, Y. Kamiya, L. O. Manuel, A. E. Trumper, and C. D. Batista, Phys. Rev. B **106**, 064418 (2022).

[16] K. Nakajima *et al*., J. Phys. Soc. Jpn. **80**, SB028 (2011).

[17] Y. Inamura, T. Nakatani, J. Suzuki, and T. Otomo, J. Phys. Soc. Jpn. **82**, SA031 (2013).

Y. Kojima[1], N. Kurita[2], H. Tanaka[2], and K. Nakajima[1,3]

[1]*Materials Sciences Research Center, JAEA;* [2]*Department of Physics, Tokyo Institute of Technology;* [3]*Neutron Science Section, Materials and Life Science Division, J-PARC Center*

Magnetic Excitations in Chiral-Structure Phase of $Ce_3Ir_4Sn_{13}$

1. Introduction

In the condensed matter physics field, topological electrons have been extensively researched [1, 2]. A linear dispersion relation of electronic band with respect to momentum (Dirac/Weyl fermion) is symmetrically protected by noncentrosymmetric or chiral space groups of materials [3]. In particular, the Weyl–Kondo semimetal is a new topological state because an electronic correlation effect is added to form the linear electronic band [4, 5]. It is an attractive issue to establish the mechanism of topological electron formation which appear spontaneously in the process of crystal-structure transformation.

$Ce_3Ir_4Sn_{13}$ has been studied for the Kondo effect owing to the interaction between Ce^{3+} $4f^1$ and conduction electrons [6, 7]. A previous X-ray diffraction study reported the structural modulation characterized by the wave vector $\boldsymbol{q}_{S1}$ = (1/2, 1/2, 0) with respect to the unit cell with a lattice constant of 9.72 Å [8]. The same superlattice reflections were explained by the chiral structures of $Ce_3T_4Sn_{13}$ (T: Co and Rh) [9–11]. The specific heat of $Ce_3Ir_4Sn_{13}$ shows phase transitions at T_1 = 0.6 K and T_2 = 2.1 K [6, 12]. Recent neutron diffraction study revealed the propagation vector $\boldsymbol{q}_{S2}$ = (1/4, 1/4, 1/4) below T_2, which was also attributed to the structure transition [13]. An antiferromagnetically ordered phase characterized by $\boldsymbol{q}_M$ = (1/2, 1/2, 2/5) was identified below T_1. The magnitude of ordered magnetic moment is considerably suppressed to the order of 0.1μ_B/Ce in contrast to the Ce^{3+} $4f^1$ state. Therefore, the magnetic fluctuation is expected to be significant in $Ce_3Ir_4Sn_{13}$ at low temperatures. In the present study, the crystal structure and magnetic state of $Ce_3Ir_4Sn_{13}$ were investigated using quantum beam scattering techniques [14].

2. Experimental procedure

Samples were synthesized using the molten Sn-flux method [15]. Synchrotron X-ray diffraction experiments for single crystal samples were performed using the diffractometer BL-8A of Photon Factory, High Energy Accelerator Research Organization. Inelastic neutron scattering (INS) measurements for polycrystalline samples were performed using the cold-neutron disk-chopper time-of-flight spectrometer AMATERAS (BL14) of the Materials and Life Science Facility (MLF), J-PARC [16].

3. Results and analysis

The synchrotron X-ray diffraction spots indexed by the wave vector $\boldsymbol{q}_{S1}$ were observed in addition to the fundamental reflections, as reported previously [9–11]. Based on the structural refinement using the WinGX software suite (Sir2014 and SHELX) [17], we established the chiral cubic structure with the space group $I2_13$ with a lattice constant of 19.44 Å, as depicted in Fig. 1. The Ce-ion sites split into two inequivalent Wyckoff sites shown by blue and green circles.

We conducted INS measurements to reveal the crystalline-electric-field (CEF) splitting levels of the Ce 4*f* electron and the magnetic dynamics. As shown by symbols in Fig. 2, the scattering function $S(E)$ evaluated by integrated intensities in the selected scattering-vector magnitude Q region shows peaks at 4.5, 7.5, and 47 meV, depicted by the yellow region. Because these peak energy positions are independent of Q, the

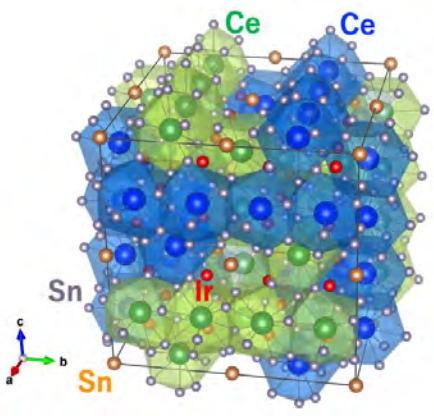

Figure 1. Chiral crystal structure of $Ce_3Ir_4Sn_{13}$, which was drawn using VESTA [18].

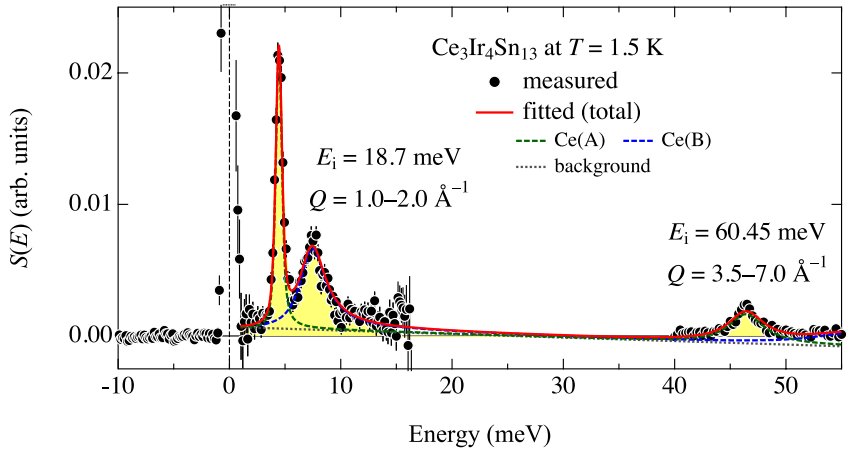

Figure 2. High-energy INS spectra of $Ce_3Ir_4Sn_{13}$ at 1.5 K measured using BL14.

peaks are attributed to CEF excitations. The point group symmetry at the Ce-ion site determined by the X-ray structural analysis allows CEF split levels composed of three Kramers doublets. The two independent Ce ions shown by the blue and green circles in Fig. 1 should carry inequivalent CEF level schemes. Lines in Fig. 2 are least-squares fitting results based on the eigenstate solutions of the CEF Hamiltonians and the spectral calculation [19], which reproduce the measurement data well. The obtained CEF level schemes are $\Gamma_6^{(2)}$ 0 meV – Γ_7 4.4 meV – $\Gamma_6^{(1)}$ 46.4 meV for the Ce(A) site and $\Gamma_6^{(2)}$ 0 meV – Γ_7 7.3 meV – $\Gamma_6^{(1)}$ 55.6 meV for the Ce(B) site. The Ce(A) site has a magnetic moment of 0.54μ_B along the direction of the Ce-ion column in Fig. 1, whereas that at the Ce(B) site is 0.91μ_B within the plane perpendicular to the Ce-ion column. It is noteworthy that the spectral widths of the excitations to the first excited states are 0.18 and 1.3 meV for the Ce(A) and Ce(B) sites, respectively.

Figure 3 shows low-energy $S(E)$ at 0.6 K obtained by integrating the intensity in the range of Q = 1.0–1.5 Å^{-1} measured using the E_i = 3.44 meV setup. The data below 0.5 meV of $Ce_3Ir_4Sn_{13}$ (filled red squares) are enhanced more than the $La_3Ir_4Sn_{13}$ data (open black squares), and the difference is plotted by blue circles. The result indicates magnetic fluctuation with characteristic energy of the order of 0.1 meV associated with the CEF doublet ground states.

4. Discussion

The broader CEF spectra at the Ce(B) site indicate hybridization between the conduction and 4*f* electrons, while the sharp spectrum at the Ce(A) site means the relatively localized 4*f* state. The same phenomenon was observed in the isomorphic compound $Ce_3Co_4Sn_{13}$; thus, $Ce_3T_4Sn_{13}$ take the electronic superlattices associated with the hybridized and localized Ce 4*f* sites under the chiral symmetry. The Kondo effect partially influences the low-temperature electronic behavior in $Ce_3T_4Sn_{13}$.

Magnetic ordering in $Ce_3T_4Sn_{13}$ is significantly depressed despite the well-localized Ce(A)-site 4*f* electrons. The ordered magnetic moment amplitude of $Ce_3Ir_4Sn_{13}$ is in the order of 0.1μ_B [13], which is less than the eigenvalues of magnetic moments estimated from the CEF analysis. Furthermore, the Weiss temperature of $Ce_3Ir_4Sn_{13}$ evaluated from the Curie–Weiss fitting to the magnetic susceptibility data is –33.1 K, whereas the antiferromagnetic ordering temperature is 0.6 K. $Ce_3Co_4Sn_{13}$ and $Ce_3Rh_4Sn_{13}$ do not undergo a magnetic ordering phase transition [9, 10]. These facts indicate that magnetic frustration may also play a role in the magnetization depression. The crystal structure shown in Fig. 1 comprises the columns with the nearest-neighbor Ce ions and the triangular lattice connections via the second neighbors. Such a triangular structure is expected to mediate geometrical frustration. Furthermore, the Dzyaloshinskii–Moriya (DM) interaction caused by the lack of inversion symmetry in the chiral structure may compete with RKKY interactions, which gives rise to frustration of interactions.

5. Summary and future plans

In $Ce_3Ir_4Sn_{13}$, the Ce ions characterized by the *c*–*f* hybridized state and the localized 4*f* electron state appear alternately in the $I2_13$ chiral structure phase. In addition, the robust magnetic fluctuation is retained even at lower temperatures, which suggest the *f* electrons

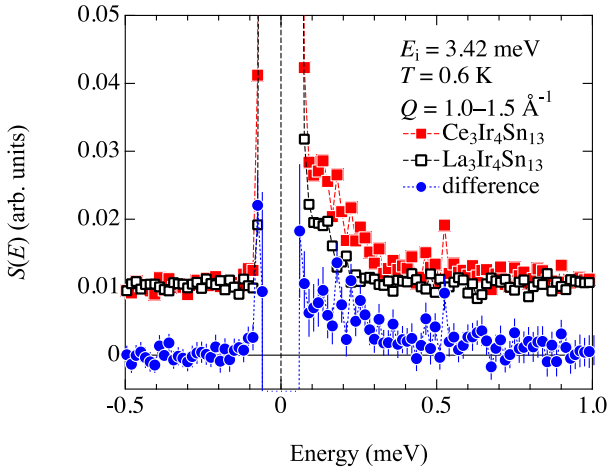

Figure 3. Low-energy INS spectra of $Ce_3Ir_4Sn_{13}$ at 0.6 K measured using BL14.

contribute to the transport property. These facts indicate that $Ce_3T_4Sn_{13}$ provides a new lattice geometry for magnetic and electronic states, which are expected to relate to the topological Weyl–Kondo state. It is a further issue to reveal such a quantum-spin-liquid behavior and the characteristic magnetic interactions by resolving the detailed ***Q*** dependence of magnetic response using the neutron scattering techniques.

References

[1] S. M. Young et al., Phys. Rev. Lett. **108**, 140405 (2012).
[2] N. P. Armitage et al., Rev. Mod. Phys. **90**, 015001 (2018).
[3] J. L. Mañes, Phys. Rev. B **85**, 155118 (2012).
[4] H.-H. Lai et al., Proc. Natl. Acad. Sci. U.S.A. **115**, 93 (2018).
[5] S. E. Grefe, et al., Phys. Rev. B **101**, 075138 (2020).
[6] H. Sato et al., Physica B **186–188**, 630 (1993).
[7] J. R. Collave et al., Solid State Commun. **177**, 132 (2014).
[8] C. Nagoshi et al., Physica B **359–361**, 248 (2005).
[9] Y. Otomo et al., Phys. Rev. B **94**, 075109 (2016).
[10] K. Suyama et al., Phys. Rev. B **97**, 235138 (2018).
[11] J. Welsch et al., Phys. Rev. Mater. **3**, 125003 (2019).
[12] S. Takayanagi et al., Physica B **199–200**, 49 (1994).
[13] S. Nakazato et al., JPS Conf. Proc. **30**, 011128 (2020).
[14] K. Iwasa et al., J. Phys. Soc. Jpn. **90**, 124701 (2021).
[15] G. P. Espinosa, Mater. Res. Bull. **15**, 791 (1980).
[16] K. Nakajima et al., J. Phys. Soc. Jpn. **80**, SB028 (2011).
[17] L. J. Farrugia, J. Appl. Crystallogr. **32**, 837 (1999).
[18] K. Momma and F. Izumi, J. Appl. Crystallogr. **41**, 653 (2008).
[19] W. Marshall and R. D. Lowde, Rep. Prog. Phys. **31**, 705 (1968).

K. Iwasa[1,2], S. Nakazato[2], D. Hashimoto[2], M. Shiozawa[2], K. Kuwahara[2], H. Sagayama[3], S. Ohira-Kawamura[4], N. Murai[4], D. T. Adroja[5,6], and A. M. Strydom[6]

[1]Frontier Research Center for Applied Atomic Sciences & Institute of Quantum Beam Science, Ibaraki University; [2]Graduate School of Science and Engineering, Ibaraki University; [3]Institute of Materials Structure Science, High Energy Accelerator Research Organiza-tion; [4]Neutron Science Section, Materials and Life Science Division, J-PARC Center; [5]ISIS Facility, Rutherford Appleton Laboratory; [6]Physics Department, University of Johannesburg

Two-Dimensional Ferromagnetism at Topological Surface of FeSi Observed by Polarized Neutron Reflectometry

1. Introduction

Two-dimensional (2D) quantum materials [*e.g.*, surfaces of topological insulators (TI) and atomic layer devices exfoliated from van der Waals (vdW) crystals] have attracted significannt attention. Their unique properties, such as energy dissipation-free conduction of charges and spins in magnetic TI [1] and emergence of versatile quantum states in vdW heterostructures [2], are expected to open a new era of electronics on the atomic scale.

Turning to spintronics applications in those 2D quantum materials, strong spin-orbit coupling (SOC) inherent in the heavy elements plays a central role. For example, strong SOC induces the band inversion necessary for topological electronic states, leading to spin-momentum locked metallic states at the surface. These spin-orbit coupled surfaces are the source of high-performance spintronic functionality, forming the basis for applications in next-generation power-saving electronic devices.

On the other hand, those heavy elements are generally scarce and toxic, and it is desirable to reduce their consumption from the viewpoint of resources and the environment. The ferromagnetic and spintronic properties of the topological surface of FeSi revealed in this study may be an important key to facilitate realistic device applications of 2D quantum materials [3].

The chiral compound FeSi has long been known as a nonmagnetic insulator with strong electron correlations [4]. Many of its unusual electronic and spin properties have been identified, such as large magnetic susceptibility at high temperature [5] and insulator-metal crossover at low temperature ($T \sim 200$ K) [6].

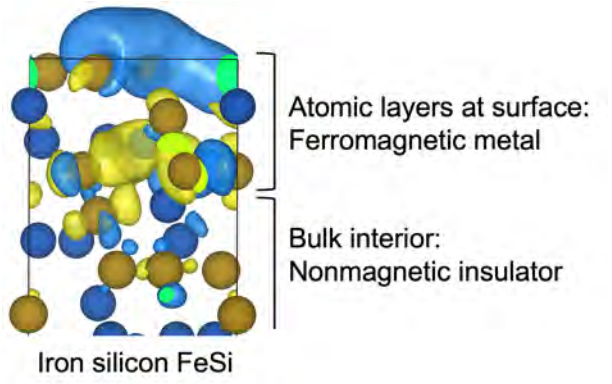

Figure 1. Visualized eigenfunction of the ferromagnetic metal state at FeSi(111) surface.

Recently, those peculiar properties of FeSi have been re-examined from a topological aspect. In this study, we successfully identified the emergence of a ferromagnetic-metal surface state in FeSi [3]. We also found that FeSi surface exhibits strong SOC properties as in the case of topological insulators, despite the fact that FeSi is composed of light elements with relatively small atomic numbers. The FeSi surface exhibits a large Rashba-type spin splitting (~ 40 meV), which enables the current-induced magnetization switching through spin-orbit torque.

Although our first-principles calculations predicted that this unique surface state exists in only a few atomic layers (Fig. 1), it had been difficult to experimentally identify and quantitatively evaluate the 2D ferromagnetism using magnetization and conductivity measurements. Here we could directly observe the ferromagnetic surface state of FeSi by polarized neutron reflectometry.

2. Experiments

Polarized neutron reflectometry (PNR) measurements were carried out at BL17 (SHARAKU) in the Materials and Life-science Experimental Facility of J-PARC in Japan [7]. The PNR measurements were performed on MgO(4 nm)/FeSi(11 nm) heterostructure at $T = 7$ K and under an in-plane magnetic field $\mu_0 H = 1$ T. The areal size of the sample was approximately 15 mm × 15 mm. The FeSi layer was grown epitaxially along [111] direction on a Si(111) substrate, while the MgO capping layer was deposited in an amorphous form. The incident neutron beams with a wavelength band of 2.2–8.8 Å were polarized either spin-up (+) or spin-down (–) with respect to H-direction. The polarized neutrons were reflected by the film in a specular geometry as shown in Fig. 2(a). The reflectivity for polarized neutrons (R^+ or R^-) was measured without polarization analysis, because the spin-flip scatterings were not expected for the fully-magnetized state. The depth profiles of nuclear and magnetic scattering length densities (SLD), which respectively correspond to the density distributions of the constituent elements and the magnetic moments, were deduced through model fitting to the PNR spectra by using GenX software [8]. Here we set layer thicknesses, densities, surface/interfacial roughness and magnetic moments as the fitting parameters.

3. Results and discussions

The reflectivity curves of R^+ and R^- as functions of the momentum transfer normal to the surface Q_z is shown in Fig. 2(b). A clear difference between R^+ and R^- represents the existence of finite net magnetization in the film. By comparing the fidelity of candidate models assuming surface-, interface- or bulk-magnetization distributions, we identified that the magnetization was confined only at the top surface of FeSi in contact with the MgO capping layer. The depth profiles of nuclear and magnetic SLD were deduced by optimizing the fitting parameters [Fig. 2(c)]. The fitting analysis concluded that the surface ferromagnetic layer had a thickness of 0.35 nm (with an error of +0.11 nm or –0.13 nm) and an average of 2.1 μ_B/Fe (with an error of +0.4 μ_B/Fe or –0.6 μ_B/Fe), whose distribution is blurred by the crystalline roughness of 0.28 ± 0.02 nm, as schematically illustrated in the inset of Fig. 2(a). This result is consistent with the calculated surface ferromagnetic state consisting mostly of the magnetic moments of the top three Fe layers.

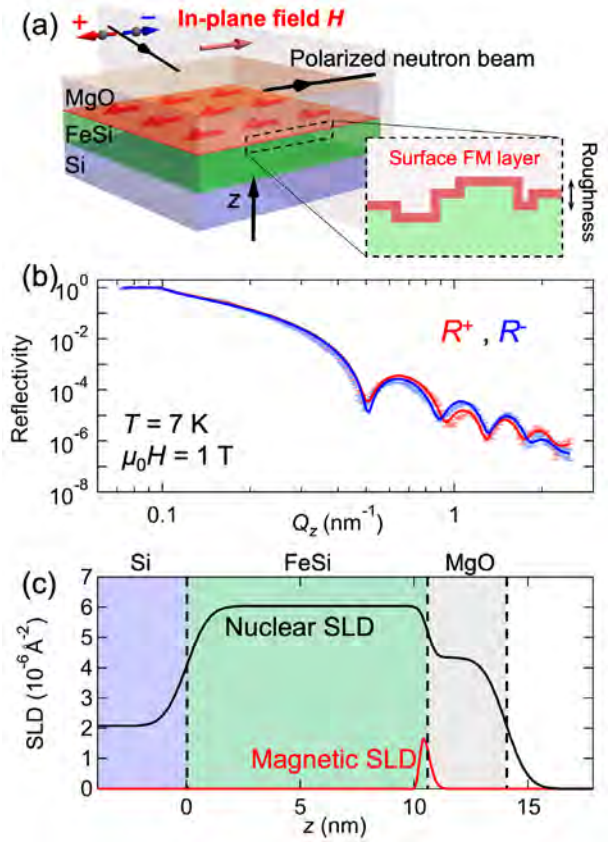

Figure 2. Direct observation of the ferromagnetic (FM) surface state of FeSi by polarized neutron reflectometry (PNR). (a) Schematic illustration of the experimental setup. The surface spins (red arrows) are aligned along the external in-plane magnetic field. (b) Measured (dots with error bars) and fitted (solid lines) reflectivities of polarized neutrons with spin-up and spin-down (R^+ and R^-) at T = 7 K and at $\mu_0 H$ = 1 T. (c) Estimated depth profiles of the nuclear (black line) and the magnetic (red line) scattering length densities (SLD).

4. Summary

We have succeeded in directly observing the 2D ferromagnetic state confined in the surface atomic layers of FeSi by PNR. The thickness of the ferromagnetic state was estimated to be approximately 0.35 nm, which is in good agreement with the prediction from first-principles calculations. Our demonstration may facilitate the design of environmentally-friendly topological materials consisting of common elements. High-resolution PNR will attract renewed attention as an important measurement technique since a variety of quantum states are being realized in complex heterostructures of topological materials and 2D quamtum materials.

References

[1] Y. Tokura, K. Yasuda and A. Tsukazaki, Nat. Rev. Phys., **1** 126 (2019).
[2] A. K. Geim and I. V. Grigorieva, Nature, **499** 419 (2013).
[3] Y. Ohtsuka, N. Kanazawa, M. Hirayama et al., Sci. Adv., **7** eabj0498 (2021).
[4] M. Imada, A. Fujimori and Y. Tokura, Rev. Mod. Phys., **70** 1039 (1998).
[5] V. Jaccarino et al., Phys. Rev., **160** 476 (1967).
[6] Z. Schlesinger et al., Phys. Rev. Lett., **71** 1748 (1993).
[7] M. Takeda et al., Chinese J. Phys., **50** 161 (2012).
[8] M. Björck and G. Andersson, J. Appl. Cryst., **40** 1174 (2007).

N. Kanazawa[1], Y. Ohtsuka[1], T. Nakajima[2,3], T. Hanashima[4], V. Ukleev[5,6], H. Aoki[7,8], and Y. Tokura[9]
[1]Department of Applied Physics, University of Tokyo; [2]Institute for Solid State Physics, University of Tokyo; [3]RIKEN Center for Emergent Matter Science (CEMS); [4]Neutron Science and Technology Center, CROSS; [5]Laboratory for Neutron Scattering and Imaging (LNS), Paul Scherrer Institute (PSI); [6]Helmholtz-Zentrum Berlin für Materialien und Energie; [7]Materials and Life Science Division, J-PARC Center; [8]Institute of Materials Structure Science, High Energy Accelerator Research Organization; [9]Tokyo College, University of Tokyo

Ferromagnetic Hysteresis Induced by Vortices in a Magnetic Superconductor $EuRbFe_4As_4$

1. Introduction

Superconductivity and magnetism, which in general compete with each other, sometimes coexist in a material. Such a material is called magnetic superconductor. It has been demonstrated that the interplay between superconductivity and magnetism induces numerous exotic phenomena, such as the reentrant superconducting transition associated with the suppression of superconductivity around the magnetic transition temperature (T_m), highlighting the impact of magnetism on superconductivity. The discovery of new magnetic superconductors has played an important role in the study of the interaction between superconductivity and magnetism. Recently, iron-based superconductors which contain Eu as a constituent element (Eu-IBSs) have attracted much attention as a new class of magnetic superconductors [1]. $EuRbFe_4As_4$ [2, 3] has the highest superconducting critical temperature (T_c ~ 37 K) among the Eu-IBSs and shows a helimagnetic order (T_m ~ 15 K) at the ground state (Fig. 1(a)) [4]. The known superconducting properties of IBSs should ensure a strong vortex pinning capability in $EuRbFe_4As_4$ that results in strong magnetic fields which possibly influence the magnetism of Eu^{2+} moments. Thus, in order to investigate the influence of superconductivity on magnetism in $EuRbFe_4As_4$, we performed neutron diffraction measurements under magnetic fields [5].

2. Experiments

Single crystals of $EuRbFe_4As_4$ were grown by the RbAs-flux method [5, 6]. The surfaces of as-grown crystals were carefully cleaved to remove the $RbFe_2As_2$ phase. X-ray diffraction (XRD) patterns were measured at room temperature using a diffractometer with Cu Kα radiation (Rigaku, Ultima IV) to verify the presence of 00*l* peaks of $EuRbFe_4As_4$. Single-crystal neutron diffraction measurements on $EuRbFe_4As_4$ were carried out using the time-of-flight (TOF) single-crystal neutron diffractometer SENJU [7] installed at the Materials and Life Science Experimental Facility (MLF), Japan Proton Accelerator Research Complex (J-PARC). The sample size was 1.8 × 0.9 × 0.08 mm^3. A neutron wavelength of 0.4–4.4 Å was used. The magnetic field was applied along the [110] direction of $EuRbFe_4As_4$ up to 2 T. The data were visualized by the software STARGazer [8].

3. Results and discussion

Figure 1(b) shows the neutron diffraction patterns along the (00*L*) direction of $EuRbFe_4As_4$ measured at 2.5 K, well below T_m. First, in the zero-field cooled (ZFC) condition (blue), diffraction peaks are observed at (00*L* ± 0.25) positions in addition to (00*L*) positions. The (0, 0, 0.25) magnetic propagation vector indicates that the direction of the Eu^{2+} moments rotates by 90° between neighboring layers, i.e. the helical structure (Fig. 1(a)). With an increasing magnetic field, at 0.4 T

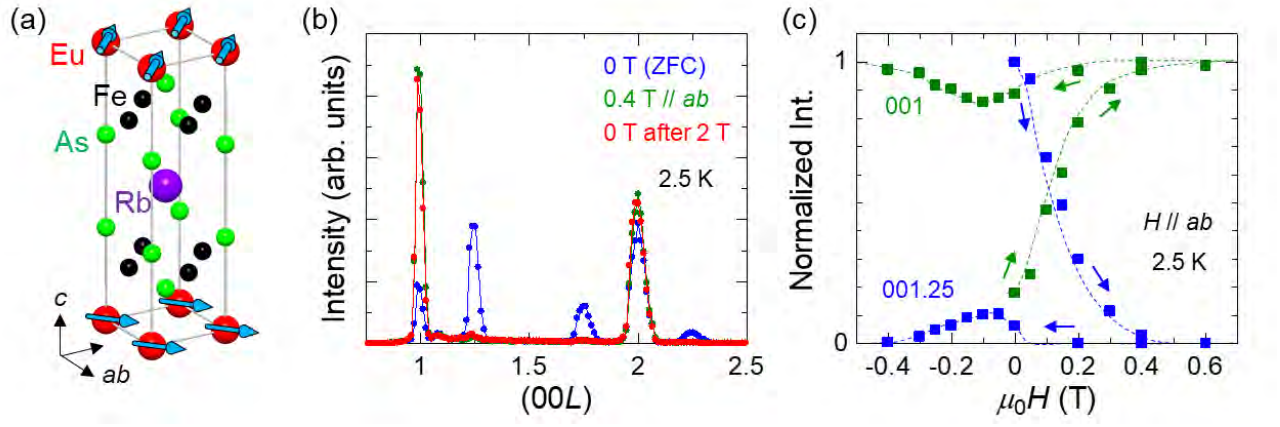

Figure 1. (a) Crystal structure of $EuRbFe_4As_4$. The light blue arrows indicate the direction of the Eu^{2+} moments in the helically ordered state. (b) Neutron diffraction patterns of $EuRbFe_4As_4$ along (00*L*) at 2.5 K and 0 T (ZFC), 0.4 T, as well as 0 T after applying a field of 2 T. (c) Magnetic field dependence of peak intensity for (001.25) peak (blue) and (001) peak (green). The peak intensity is normalized at 0 T (ZFC) and 2 T for the (001.25) and (001) peaks, where the Eu^{2+} moments are completely helical and ferromagnetic, respectively. Arrows indicate the field sweep direction.

(green), the (00L ± 0.25) peaks almost disappear, while the intensity of the (00L) peaks is enhanced. The results demonstrate the transition of the Eu^{2+} magnetic order from a helical to a ferromagnetic arrangement.

Then, the field was decreased from value 2 T, which is large enough to completely align the Eu^{2+} moments ferromagnetically. The diffraction pattern at zero field after applying 2 T (red) is found to be almost identical to that at 0.4 T. Although the peak at (001.25) can still be identified, its intensity is smaller by about one order of magnitude than that at increasing field. The results show that the Eu^{2+} moments do not return to the initial helical structure but remain mostly in the ferromagnetic arrangement even at zero field.

The magnetic field dependence ($-0.4\,T \leq \mu_0 H \leq 0.6\,T$) of the intensity of the (001.25) peak (blue) and the (001) peak (green) is summarized in Fig. 1(c). Each intensity represents the fraction of helical and ferromagnetic structure, respectively. One can see that the intensities of the (001) and (001.25) peaks are inversely correlated, suggesting that the fraction of intermediate structure is small. Notably, the (001.25) peak is slightly enhanced just after field reversal. Thus, the neutron diffraction measurements revealed a characteristic ferromagnetic hysteresis of the Eu^{2+} moments in $EuRbFe_4As_4$.

Because the hysteresis of the Eu^{2+} moments in $EuFe_2As_2$ (a related non-superconducting compound) is negligibly small [9], the ferromagnetic hysteresis is likely induced by superconductivity. Thus, we propose a model that the direction of the Eu^{2+} moments is determined by the distribution of pinned vortices in the sample [5] as illustrated in Fig. 2. Indeed, the experimental results can be reasonably reproduced by the model where the local magnetic field distribution created by vortices is calculated based on the Bean's critical state model [10].

4. Conclusion

We performed single-crystal neutron diffraction measurements on the magnetic superconductor $EuRbFe_4As_4$ which shows a high-T_c superconductivity and a helical magnetic order. We revealed a ferromagnetic hysteresis of the Eu^{2+} moments induced by the superconducting vortices. The unique interaction between local moments and vortices could be used to manipulate the spin texture, showing the potential for novel device applications of $EuRbFe_4As_4$.

References

[1] S. Zapf and M. Dressel, Rep. Prog. Phys. **80** 016501 (2017).
[2] K. Kawashima et al., J. Phys. Soc. Japan **85** 064710 (2016).
[3] Y. Liu et al., Phys. Rev. B **93** 214503 (2016).
[4] K. Iida et al., Phys. Rev. B **100** 014506 (2019).
[5] S. Ishida et al., Proc. Natl. Acad. Sci. USA **118** e210110118 (2021).
[6] J. K. Bao et al., Cryst. Growth Des. **18** 3517 (2018).
[7] T. Ohhara et al., J. Appl. Cryst. **49** 120–127 (2016).
[8] T. Ohhara et al., Nucl. Instrum. Methods Phys. Res. A **600** 195 (2009).
[9] S. Jiang et al., New J. Phys. **11** 025007 (2009).
[10] C. P. Bean, Rev. Mod. Phys. **36** 31 (1964).

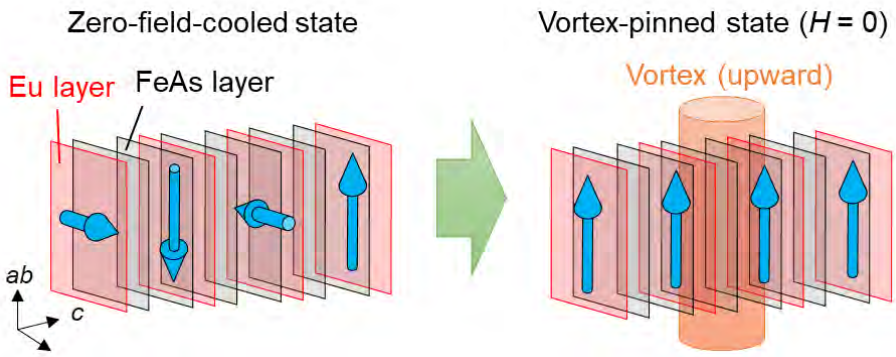

Figure 2. Schematic illustration of ferromagnetic hysteresis of the Eu^{2+} moments induced by superconducting vortices pinned in the $EuRbFe_4As_4$ sample.

S. Ishida[1], D. Kagerbauer[2], S. Holleis[2], K. Iida[3], K. Munakata[3], A. Nakao[3], A. Iyo[1], H. Ogino[1], K. Kawashi-ma[4], M. Eisterer[2], and H. Eisaki[1]
[1]*Research Institute for Advanced Electronics and Photonics, AIST;* [2]*Atominstitut, TU Wien;* [3]*Neutron Science and Technology Center, CROSS;* [4]*Research & Development Department, IMRA JAPAN CO., LTD.*

Muon-Induced Soft Errors in 20-nm SRAMs: Similarities and Differences with Neutrons and Alpha Particles

1. Introduction

Soft errors are radiation-induced transient errors in semiconductor devices, which degrade the dependability of electronic systems. The continuous scaling of CMOS technologies has made the devices more susceptible to soft errors. In the terrestrial environment, neutrons and alpha particles have been known as the major sources of the soft errors. The neutrons are part of the secondary cosmic rays. The alpha particles are emitted from radioactive impurities naturally present in the device materials.

In recent years, muons have attracted increasing attention as a potential source of the terrestrial soft errors. One reason for this is that scaled semiconductor devices are vulnerable to low-linear energy transfer (LET) particles. Another reason is that the muons are the most abundant particles in secondary cosmic rays, where negative and positive muons are produced. Despite this increased risk, there have been only a few experimental studies on the muon-induced soft error [1, 2]. Therefore, further investigation is needed for understanding their characteristics.

This work investigates muon-induced soft errors in static random-access memories (SRAMs) fabricated in a scaled 20-nm bulk planar CMOS technology [3]. Irradiation experiments are performed using negative and positive muon beams. The unique characteristics of the muon-induced soft errors are analyzed through comparison with neutron- and alpha-induced ones.

2. Irradiation experiments

Particle irradiation tests were conducted for negative muons, positive muons, high-energy neutrons, thermal neutrons, and alpha particles, as summarized in Table 1. The negative and positive muon irradiations were performed using monoenergetic beams at the muon science facility (MUSE), J-PARC [4]. The high-energy neutron irradiation was performed using a spallation neutron beam at the Research Center for Nuclear Physics (RCNP), Osaka University [5]. The thermal neutron irradiation was performed using a neutron irradiation field at the Heavy Water Neutron Irradiation Facility (HWNIF) of the Kyoto University Research Reactor (KUR) [6]. The alpha particle irradiation was performed using an ^{241}Am source in our laboratory. The energy spectra of the neutron beams were similar to the terrestrial ones, as shown in Fig. 1.

The 20-nm SRAM chips were irradiated with these particles. In the irradiation tests, we measured the occurrence rate of single-event upsets (SEUs), which are the most common soft errors causing the flipping of the stored data by a single particle strike. The SEU events were categorized into two types: single-bit upsets (SBUs) and multiple-cell upsets (MCUs). The SBU and MCU events correspond to single-bit errors and multiple-bit errors, respectively. We note that, from a reliability viewpoint, the MCU events are important to be evaluated because they can degrade error correction efficiency. For each irradiation test, the event cross sections (CSs) were calculated as $N_{\mathrm{event}} / (\Phi \times N_{\mathrm{bit}})$, where N_{event}, Φ, and N_{bit} are the number of observed events, the incident particle fluence, and the number of SRAM bits irradiated, respectively.

Table 1. Irradiation particles and facilities.

Irradiation particle	Energy	Facility
Negative/Positive muon	Monoenergetic	MUSE [4]
High-energy neutron	Terrestrial-like	RCNP [5]
Thermal neutron	Terrestrial-like	KUR [6]
Alpha particle	5.4 MeV (^{241}Am)	Lab.

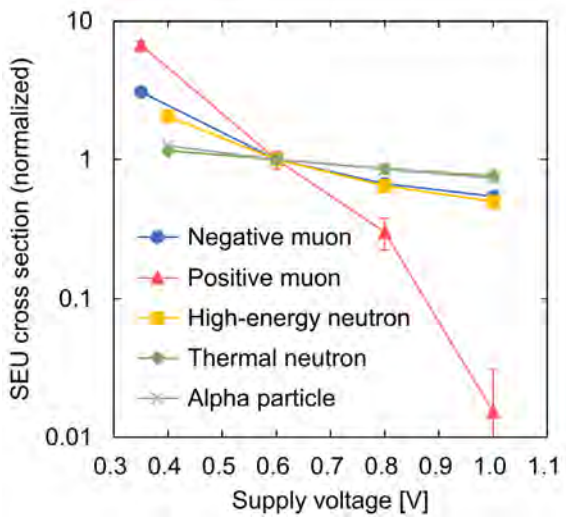

Figure 1. SEU CSs for negative and positive muons, high-energy and thermal neutrons, and alpha particles as a function of supply voltage. The CSs are normalized in each particle by the respective CS value at 0.6 V. The muon energy is 1.02 MeV. Error bars represent one standard error.

3. Results and discussion

The comparison of the SEU CS between the muons and the other particles reveals similarities and differences in the supply voltage dependence, as shown in Fig. 1. In this comparison, the muon energy was set to 1.02 MeV, where the CS peak was observed, to fully capture the muon-specific characteristics [3]. For the negative muon, the voltage dependence was very similar to that for the high-energy neutron. For the positive muon, the CS drastically decreased with the voltage, which was very different from the other particles. These contrasting behaviors are due to the difference in the amount of charge deposited by the incident particles [3]. Our results indicate that the charge deposition by the negative muons, including the secondary ions produced through the capture reactions, is comparable to that by the high-energy neutrons.

The comparison of the MCU ratios, which are calculated by dividing the MCU CS with the SEU CS, provided insight into the mechanism of the negative muon-induced MCUs. As presented in Fig. 2, the slopes in the voltage dependence for the negative muon and the high-energy neutron were similar and slightly positive. This indicates the significant contribution of the parasitic bipolar effect, which can be triggered by high-LET secondary ions and tends to cause MCUs [3]. Another point was that the MCU ratio for the negative muon was larger than that for the high-energy neutron. This is probably due to the difference in the secondary ion emission. In the muon capture reactions, the secondary ions are emitted isotropically and are thus more likely to travel multiple SRAM cells compared to the secondary ions produced by the high-energy neutrons. From our results, it is probable that the characteristics of the negative muon-induced MCUs are dominated by the nature of the muon capture reactions.

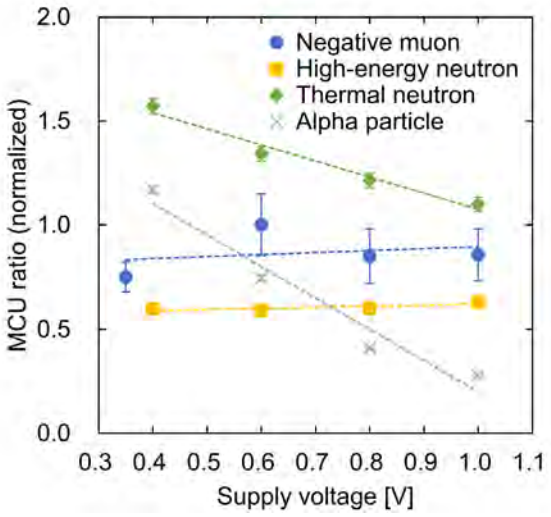

Figure 2. MCU ratios for negative muons, high-energy and thermal neutrons, and alpha particles as a function of supply voltage. The values are normalized by the value at 0.6 V of negative muon. Error bars represent one standard error. Note that the result for the positive muon is omitted because its MCU CS was significantly lower.

4. Future plans

To address the growing concern about the terrestrial soft errors, we continue to investigate the muon-induced soft errors in more advanced semiconductor devices. Specifically, the impact of the change of transistor structure needs to be explored because fin-shaped transistors, called FinFETs, are becoming widely employed instead of planar transistors used in this work. In the case of neutrons for example, it has been demonstrated that the SEU characteristics are significantly different between planar and FinFET SRAMs [7]. Further understanding of the muon-induced soft errors would be helpful in assessing and improving the dependability of advanced electronic systems.

References

[1] W. Liao et al., IEEE Trans. Nucl. Sci., **65** 1734 (2018).
[2] S. Manabe et al., IEEE Trans. Nucl. Sci., **65** 1742 (2018).
[3] T. Kato et al., IEEE Trans. Nucl. Sci., **68** 1436 (2021).
[4] Y. Miyake et al., Phys. Procedia, **30** 46 (2012).
[5] Y. Iwamoto et al., Nucl. Technol., **173** 210 (2011).
[6] Y. Sakurai et al., Nucl. Instr. Meth. A, **173** 569 (2000).
[7] T. Kato et al., IEEE Trans. Nucl. Sci., **67** 1485 (2020).

T. Kato[1], M. Tampo[2,3], S. Takeshita[2,3], H. Tanaka[4], M. Hashimoto[5], and Y. Miyake[2,3]
[1]*Reliability Engineering Department, Socionext Inc.;* [2]*Institute of Materials Structure Science, KEK;* [3]*Muon Science Section, Materials and Life Science Division, J-PARC Center;* [4]*Institute for Integrated Radiation and Nuclear Science, Kyoto University;* [5]*Department of Communications and Computer Engineering, Kyoto University*

Li Diffusion Studied by QENS with Single Crystal

1. Introduction

All-solid-state batteries using solid electrolytes have significant advantages in terms of the energy density and safety [1]. Sulfide-based Li conductors, such as LPGS, exhibit very high ionic conductivities 10^{-2} S/cm at room temperature [2]. Although the oxide-based one shows more than one order of magnitude lower conductivity, a better oxide-based Li conductor is highly demanded because of its stability in the air. $La_{2/3-x}Li_{3x}TiO_3$ (LLTO) has been widely studied because it has the highest Li ion conductivity (about 1 [mScm-1] at room temperature) among oxide solid electrolytes [3]. In addition, LLTO has simple double-perovskite structure (Fig. 1b), which makes LLTO an ideal system for investigating the mechanism of Li ion conduction.

Quasielastic neutron scattering (QENS) provides detailed information on the dynamical conduction path of Li^+ on a microscopic scale. So far, the number of QENS studies on solid-state Li conductors was limited because detecting Li diffusion by QENS was a challenge due to their weak signal. Furthermore, if a single crystal is available, precise directional information of Li^+ jump can be obtained. Here, we show the first example of QENS study using a single crystal of Li conductors [4]. Combined with first principle MD simulation, we could obtain microscopic information on Li^+ diffusion in LLTO.

2. Experimental details

To avoid strong neutron absorption of ^{6}Li, ^{7}Li-enriched LLTO powder was synthesized from ^{7}Li-enriched Li_2CO_3, La_2O_3, and TiO_2. The single crystals of LLTO ($x = 0.13$) were grown at Shinshu University using a directional solidification method [5]. Although there were some grains in the as-grown single crystal, we sliced the sample into 1.5-mm-thick slices and took X-ray Laue diffraction with 5 mm intervals to select single grain portions. Finally, a single-grain single-crystal with total volume of ~1 cm^3 was obtained by pasting back using special glue CYTOP which is transparent to neutrons. QENS data were measured using backscattering spectrometer DNA at J-PARC [6]. DNA can offer various resolution and energy range by using pulse-shaping chopper. In this study, we used high-resolution mode ($\Delta E = 2.5$ μeV, $-20 < E < 80$ meV) with 3 cm slit and chopper frequency of 300 Hz. Scan trajectory of DNA in the horizontal scattering plane forms arc around origin. By aligning the arc with the three main crystal axes, [110], [001], and [111], we can measure QENS approximately along these directions up to 1 $Å^{-1}$ (Fig. 1a). In the Chudley-Elliot model, Lorentzian linewidth Γ is zero when Q is perpendicular to jump vector l. Thus, we can obtain directional information of Li dynamics from these measurements.

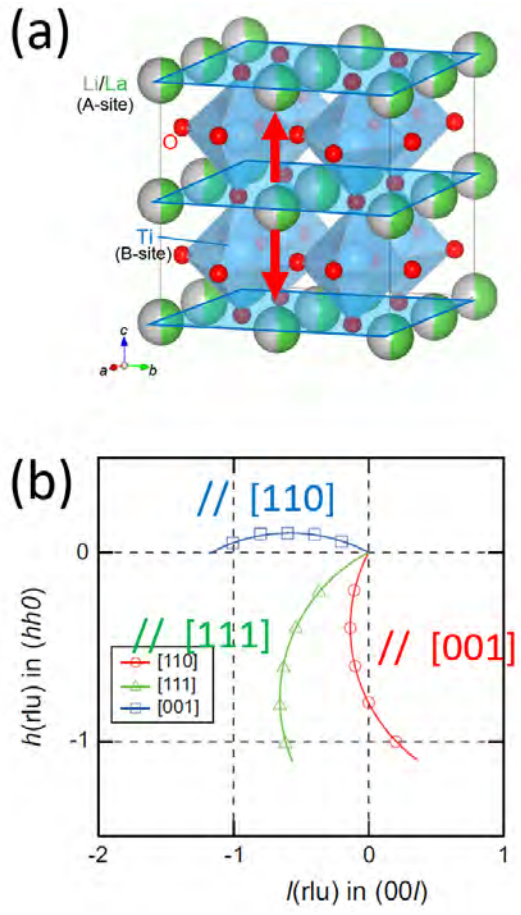

Figure 1. (a) Scan trajectories of [110], [001], and [111] measurements. (b) Crystal structures of LLTO [4].

3. Results

Figure 2a shows Q-dependence of Lorenzian linewidth Γ obtained from fits of $T = 600$ K data with the sum of a Lorentzian and a delta function convoluted with the resolution function estimated from the $T = 150$ K data. To analyze $\Gamma(Q)$, we performed first principle MD simulations (Fig. 2b). Figure 2b shows trajectory of Li ions by yellow lines. Here we assume no La in La-poor layer. Li ions are moving around the A site, and some Li ions jump to the neighboring site. This is consistent with Reverse Monte Carlo results [7, 8]. Therefore, we assumed a jump in the direction of [100], [010], and the Q-dependence are well reproduced with jump vector between a-sites (dotted lines in Fig. 2a).

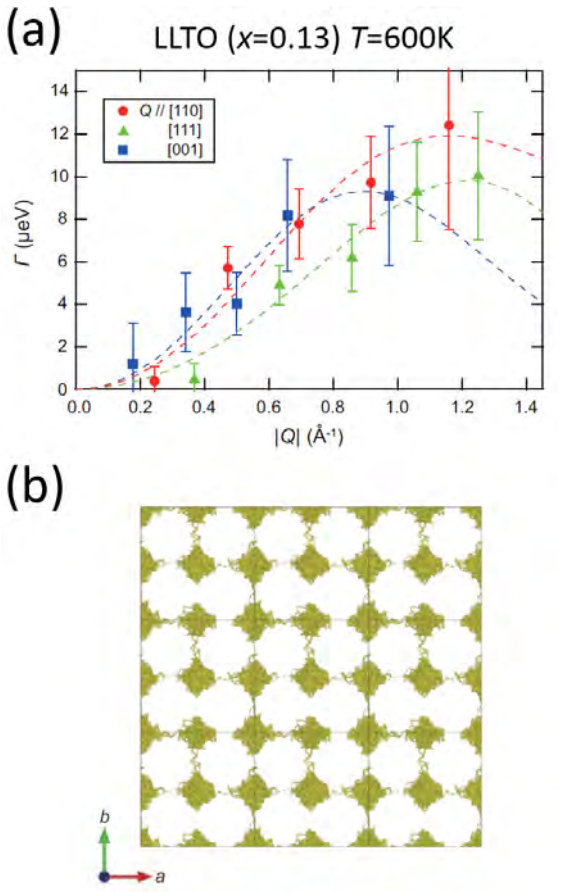

Figure 2. (a) Q-dependences of Lorentzian linewidth G along three principal axes [110], [111], and [001] measured at T = 600 K. (b) Trajectories of Li^+ ions in the ab-plane of La-poor layer simulated by MD using first-principles modeling for LLTO [4].

From the obtained jump distance and residence time, we estimated the diffusion coefficient D as $6.8 \pm 0.5 \times 10^{-6}$ cm^2/s at $T = 600$ K and $1.9 \pm 0.1 \times 10^{-6}$ cm^2/s at $T = 410$ K. The ratio of the diffusion constant between 600 K and 410 K is 3.6, which agrees with the activation energy of 0.15 eV obtained from the bulk ionic conductivity of LLTO above 400 K [3]. Thus, QENS captures the same Li dynamics as the macroscopic ionic conductivity measurements.

It is interesting to compare the results with that of the sulfide-based Li ionic conductor $Li_7P_3S_{11}$ measured with the same instrument [9]. Although the measured temperatures are different, QENS with almost the same line width were observed at $T = 473$ K for $Li_7P_3S_{11}$. For LLTO, D at $T = 473$ K is estimated from D at 600 K and $E_a = 0.15$ eV as $3.1 \pm 0.3 \times 10^{-6}$ cm^2/s, which is close to $D = 5.7 \times 10^{-6}$ cm^2/s at $T = 473$ K for $Li_7P_3S_{11}$. This indicates that same level of fast diffusion is realized in sulfide and oxide-based Li conductor in microscopic scale.

4. Summary

We precisely determined the dynamical conduction path of Li^+ ions in solid state electrolyte LLTO from anisotropic QENS using ^{7}Li enriched single crystal and first principles MD simulations. The self-diffusion coefficients of Li^+ ions in LLTO were found to be comparable with those in sulfide-based Li^+ ions conductor $Li_7P_3S_{11}$ even though they had 10 times smaller ionic conductivity than $Li_7P_3S_{11}$. This microscopic information on Li^+ diffusion can provide a way to increase Li^+ ionic conductivity in oxide-based solid electrolytes.

References

[1] M. Armand and J.-M. Tarascon, Nature (London) 451, 652 (2008).
[2] N. Kamaya, et al., Nat. Mater. 10, 682 (2011).
[3] Y. Inaguma et al., Solid State Commun. 86 (1993) 689.
[4] M. Matsuura et al., Phys. Rev. B 104 (2021) 094305.
[5] Y. Fujiwara et al., J. Cryst. Growth 433, 48 (2016).
[6] K. Shibata et al., JPS Conf. Proc. 8, 036022 (2015).
[7] K. Ohara et al., J. Phys. Condens. Matter 22, 404203 (2010).
[8] K. Mori et al., Solid State Ion. 268, 76 (2014).
[9] K. Mori et al., Phys. Rev. Appl. 4, 054008 (2015).

M. Matsuura[1], Y. Fujiwara[2], H. Moriwake[3], K. Ohara[4], and Y. Kawakita[5]
[1]Neutron Science and Technology Center, CROSS; [2]Faculty of Engineering, Shinshu University; [3]Nanostructures Research Laboratory, Japan Fine Ceramics Center; [4]Research and Utilization Division, SPring-8/JASRI; [5]Neutron Science Section, Materials and Life Science Division, J-PARC Center

Visualization of Generated Water in Newly-designed Polymer Electrolyte Fuel Cell during Power Generation

1. Introduction

For increasing power density and durability, while reducing the costs of polymer electrolyte fuel cells (PEFCs), the importance of water management in PEFC is well known. Not only new materials and operational protocols but also the cell structures directly affect the water management.

The structure of the gas diffusion layers (GDLs) has been extensively studied for better water and gas management [1–3]. When the water produced at the cathode during power generation remains in the GDL or in the gas flow channels (GFC), the liquid water inhibits the diffusion of oxygen from the air to the catalyst layer (CL). On the other hand, the liquid water enhances the power generation when properly distributed.

Yamanashi University and ENOMOTO have developed an innovative GDL, "GDLFC$^+$", with gas flow channels fabricated on a flat separator that has enabled both cost reduction and high performance [4]. The water distribution in a PEFC with GDLFC$^+$ during the power generation was visualized by neutron radiography to further improve the cell performance [5].

2. Experimental

Figure 1 shows the illustration of a PEFC used in the experiment and Fig. 2 shows the structure of the GFC. The separator was made of gold-plated aluminum. On the cathode side, we adopted a newly designed GDLFC$^+$ with 0.4 mm thick with a 0.04 mm thick microporous layer as a GDL. On the anode side, a single serpentine GFC was formed on the separator in a direction perpendicular to the cathode GFC (Fig. 2, middle panel), and a commercial GDL (22BB, SGL Co.) was used. The active

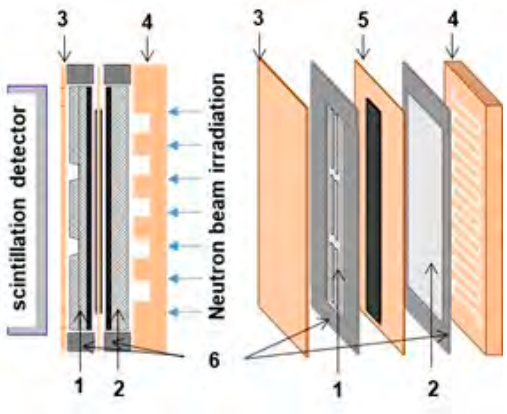

Figure 1. Schematic illustration of the cell assembly for visualization of water distribution by neutron radiography during operation. 1: Cathode side GDLFC$^+$. 2: Anode side GDL (SGL Co., 22BB). 3: Cathode side Al flat separator. 4: Anode side Al separator with GFC. 5: Catalyst Coated Membrane (CCM). 6: Gasket.

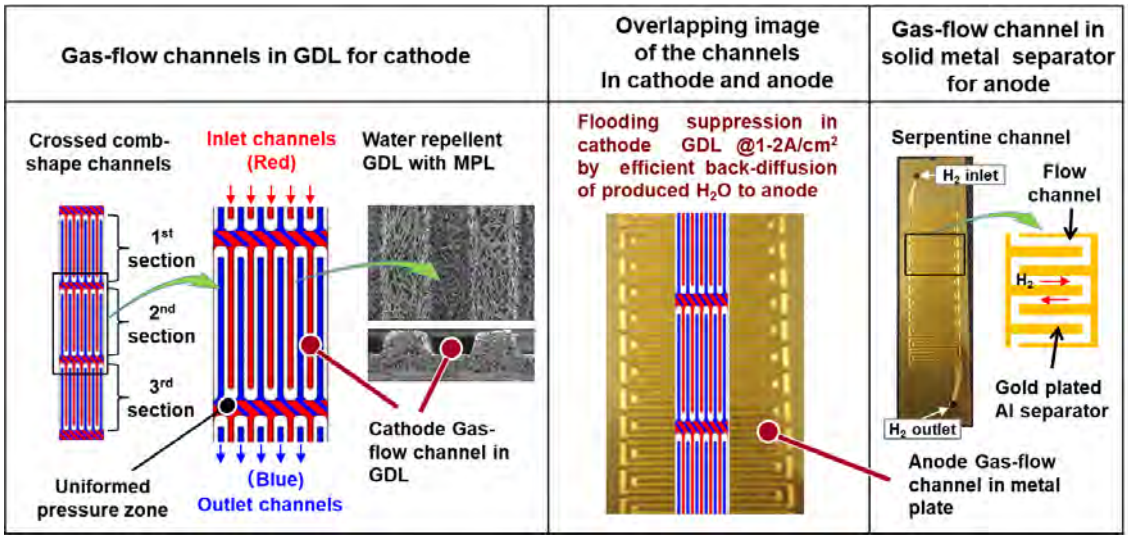

Figure 2. Structures of GFCs applied to a single cell for visualization of liquid water during power generation, and the locations of the GFCs both at the cathode and anode.

area of the cell was 1.0 cm × 9.7 cm [5].

In beamline BL22 of J-PARC MLF, the generated water in the cell was continuously monitored for 30 minutes with a pulsed neutron beam of 25 Hz repetition rate during the power generation (Fig. 3) [6]. During the power generation, humidified hydrogen and humidified air/oxygen were supplied to the cell. The current density was set between 1.0 and 3.0 A cm^{-2}.

3. Results

Figure 4(A) is an image of water distribution in the PEFC perpendicular to the MEA during power generation using oxygen humidified at 73%RH at the current density of 3.0 A cm^{-2}. Under this condition, the amounts of water observed in the outflow gas channel (OF) region, the inflow gas channel (IF) region and the porous rib between the OF and IF changed from the upstream to downstream. Figure 4(B) shows the water distribution in the gas upstream area (B-B cross section), where the thickness of water in the OF region was apparently larger than that in the IF region. Notably, in Fig. 4(C) showing the water distribution in the gas downstream area (C-C cross section), the water thickness inside the ribs increased more than that observed both in the OF and IF regions. The accumulation of water was not the only obstacle to gas diffusion via the ribs but should be carefully controlled.

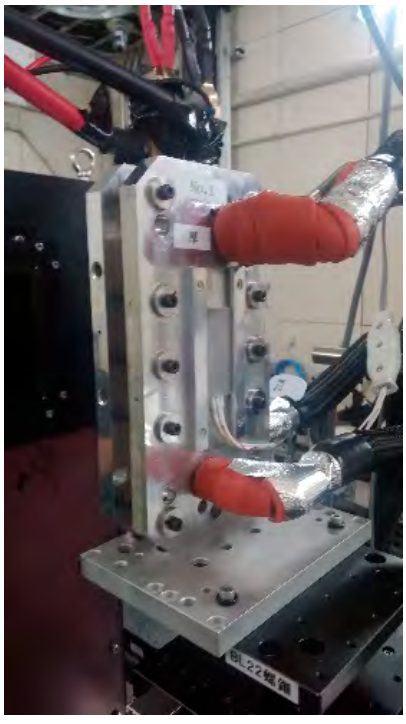

Figure 3. Photograph of the PEFC for water visualization.

We, then, changed the gas flow velocity in the GFC from 1.35 to 2.34 m/s to find out that the gas flow velocity was a key factor for removing liquid water from the GDL. With a water-repellent GDL, the water generated at the cathode back-diffused efficiently through the electrolyte to the anode side. In addition, the heat generated by the cathode overvoltage also contributed to the suppression of dew condensation on both the cathode and anode.

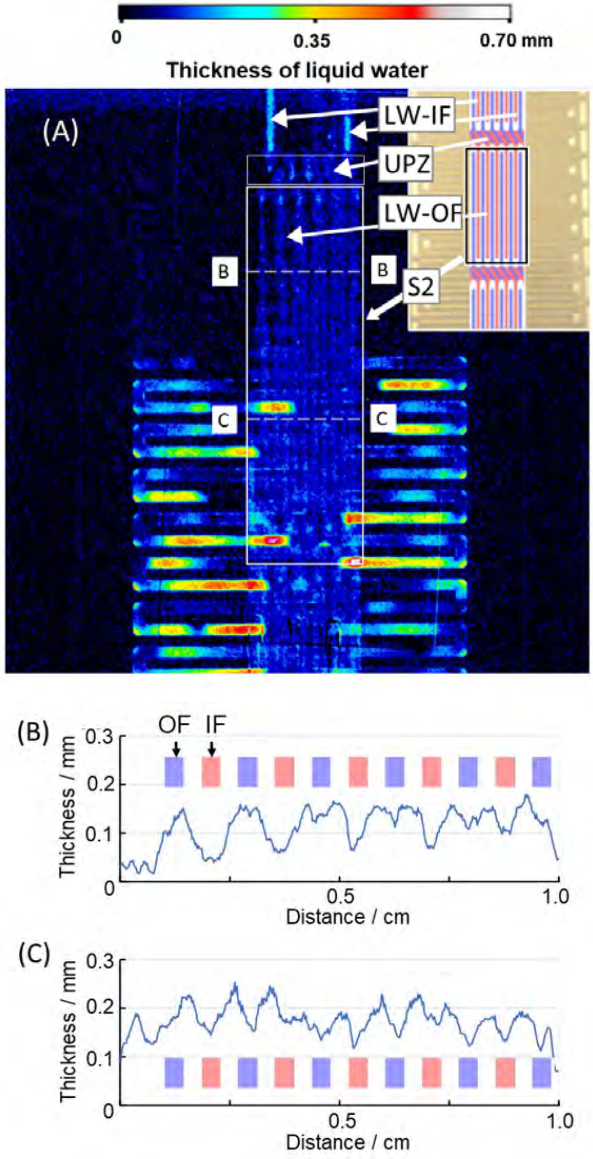

Figure 4. (A): Water distribution. Cell temperature = 75°C, RH = 73%, current density = 3.0 A cm^{-2}, oxidant = oxygen. LW-IF: Water observed in the incoming gas channel (IF). LW-OF: Water observed in the outflow gas channel (OF). UPZ: Uniformed pressure zone. (B): (B-B) Line profile of water thickness across the GFC upstream of the gas. (C): (C-C) Line profile of water thickness downstream of the gas.

4. Summary

We have succeeded in visualizing liquid water in an operating PEFC using a newly-developed GDL, GDLFC$^+$. The relationship between the distribution of water and the cell performance was clearly understood. With the results obtained, we are designing new cells with higher power output.

Acknowledgments

This research was partially promoted by the Ministry of Education, Culture, Sports, Science and Technology (MEXT) and the New Energy and Industrial Technology Development Organization (NEDO).

References

[1] S. Litster, C.R. Buie, T. Fabian, J.K. Eaton, J.G. Santiago, J. Electrochem. Soc. 154, B1049 (2007).
[2] Z. Wang, L. Qu, Y. Zeng, X. Guo, Z. Shao, B. Yia, RSC Adv. 8, 1503 (2018).
[3] Z. Bao, Z. Niu, K. Jiao, J. Power Sources, 438, 226995 (2019).
[4] M. Watanabe, H. Yanai, M. Nasu, J. Electrochem. Soc., 166, F3210 (2019).
[5] M. Nasu, H. Yanai, N. Hirayama, H. Adachi, Y. Kakizawa, Y. Shirase, H. Nishiyama, T. Kawamoto, J. Inukai, T. Shinohara, H. Hayashida, M. Watanabe, J. Power Sources, 530, 231251 (2022).
[6] T. Shinohara, T. Kai, K. Oikawa, T. Nakatani, M. Segawa, K. Hiroi, Y. Su, M. Ooi, M. Harada, H. Iikura, H. Hayashida, J.D. Parker, Y. Matsumoto, H. Sato, Y. Kiyanagi, Rev. Sci. Instrum., 91, 043302 (2020).

Mitsunori Nasu[1], Hiroshi Yanai[1], Naoki Hirayama[1], Hironori Adachi[1], Yu Kakizawa[2], Yuto Shirase[2], Hiromichi Nishiyama[2], Teppei Kawamoto[2], Junji Inukai[2], Takenao Shinohara[3], Hirotoshi Hayashida[4], and Masahiro Watanabe[2]
[1]ENOMOTO Co., Ltd.; [2]University of Yamanashi; [3]Materials and Life Science Division, J-PARC Center; [4]Neutron Science and Technology Center, CROSS

Molecular Motion Improves Solar Cell Performance: a Muon Spin Relaxation Study

1. Introduction

One of the most promising materials for next-generation solar cells that combine high efficiency and lower cost is hybrid organic-inorganic perovskites (HOIPs). Over 25% efficiency has been achieved using HOIP-based solar cells, which is on level with silicon-based solar cells. The cost of manufacturing HOIP solar cells is dramatically lower than that of producing solar cells using the existing commercial technique.

The microscopic principles underlying the high solar cell efficiency of HOIP are still not fully understood, despite the advances that have been made. The long carrier lifetime (≥1 μs) of HOIP is thought to be the key factor in its outstanding photovoltaic conversion performance. Despite this material having a relatively low charge mobility, it has a long carrier lifetime, which extends the carrier diffusion length [1]. Additionally, it has been noted that solar cells can still function when the hybrid structure of the solar cell is replaced with pure inorganic perovskite. This indicates that inorganic metal halide atoms are excited by photons to produce electrons and holes, which is in line with density functional calculations that show that neither organic nor inorganic cations included inside the metal halide frames directly contribute to the band-edge states. However, the current efficiency of pure inorganic perovskites is only 11%, which is significantly lower than the 25% seen in HOIP-based solar cells. This implies that the presence of organic cations may be the key to reaching high solar cell efficiency, however at this point, it is unknown exactly how organic cations increase efficiency on a microscopic level.

Muon provides information on a time scale of 10^{-9}-10^{-5} s, which may be significant for carrier dynamics, whereas quasi-elastic neutron scattering [2] and nuclear magnetic/quadrupole resonance (NMR/NQR) using ^{1}H and ^{14}N [3] probe molecular motion on a time scale of 10^{-12} s. In this regard, the failure of NMR experiments using ^{207}Pb and ^{127}I due to fast spin-spin relaxation rate further supports the use of μSR to examine molecular motion. Therefore, we conducted μSR studies on the prototype methylamidinium (MA) lead iodide, in which the implanted muons investigate the fluctuation of local magnetic fields at interstitial points.

2. Results and discussion

As seen in Fig. 1a, the 3D network of corner-shared PbI_6-octahedra and MA molecule ions at the perovskite A site form up the crystal structure of HOIP. It is known that when temperature rises, $MAPbI_3$ passes through

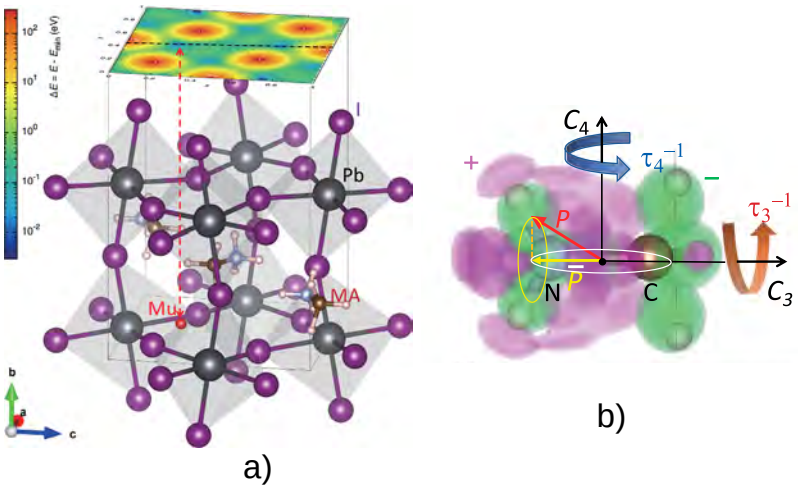

Figure 1. a) Schematic diagram of the perovskite unit cell for $CH_3NH_3PbI_3$. The organic cation is located in the center of a PbI_6 octahedral cage. The color contour plot shows the differential total formation energy for an interstitial hydrogen on the *ac*-plane obtained by the DFT calculation. b) Geometry of the MA molecule with schematic drawing for the two modes of jumping rotation, where C_3/C_4 denotes the threefold/fourfold rotation symmetry with τ_i^{-1} being the respective jumping frequencies. The calculated local charge asymmetry is also shown superimposed as green and purple regions that produce an electric dipole moment P, which results in the effective electric dipole moment $\bar{P}$ due to the C_3/C_4 motion.

two structural transitions: first, from an orthorhombic to a tetragonal structure at T_{OT} = 165 K, then from a tetragonal to a cubic structure at T_{TC} = 327 K. The resultant μSR time spectra are well represented by the quasi-static Kubo-Toyabe relaxation function, which is characterized by the nuclear dipolar width Δ and the fluctuation rate ν, as shown in Fig. 2. Simultaneous curve-fits of the spectra at different longitudinal fields successfully determined the parameters. Figure 3 displays the temperature dependence of Δ and ν. In response to the change in the anisotropic motion of a cation molecule brought on by such structural phase transitions, it turns out that the magnitude of Δ exhibits a strong temperature dependence. The molecular motion of MA is restricted around its three-fold rotational symmetry (C_3) in the orthorhombic phase, according to earlier studies using neutron scattering and NMR/NQR [2, 3], whereas four-fold rotational symmetry (C_4) is observed in addition to C_3 in the tetragonal and cubic phases at higher temperatures. Considering that the time scale for these rotational jumps is 10^{-11}-10^{-12} s for the relevant temperature range (>10 K) [2, 3], it is reasonable to assume that the averaging out of the nuclear dipolar fields, or the so-called motional narrowing effect, is what causes the reduction of Δ above 120 K.

On the other hand, the fluctuation rate νdisplays a diverging increase synchronous with the reduction of Δ above ~120 K, which is then dramatically reduced approaching 165 K. When reaching 200 K, it shows a sharp increase before plateauing at a constant value (~0.2 μs^{-1}). Even while there appears to be some link between the feature of Δ at 120–165 K and that of ν, we should point out that the slower variation of Δ, as represented by the parameter ν, cannot be directly attributed to the MA molecular motion, which is orders of magnitude faster than that estimated from ν.

More intriguingly, at about T = 165 K, a small hump of Δ is observed. In Fig. 3c, it is noticeable that the entire temperature dependence of Δ is strikingly analogous to that observed in the temperature dependence of photoluminescence (PL) lifetime τ_{PL} [4, 5]. This strongly implies a connection between the MA molecular motion and the long lifetime of the photoexcited carriers. It is assumed that the dielectric response, which prevents carrier recombination, is significant for the lifetime of the photoexcited carriers. The MA molecule moves to

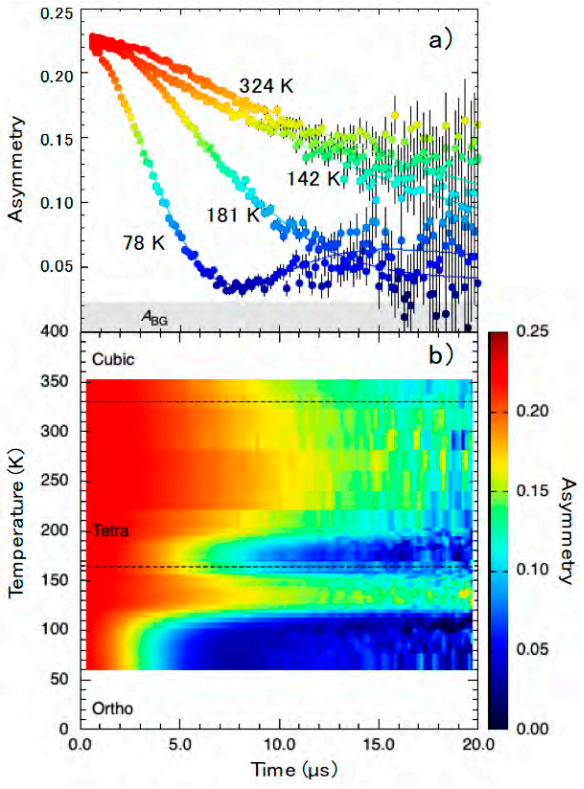

Figure 2. a) Typical examples of ZF-μSR time spectra (asymmetry) observed in $MAPbI_3$ at various temperatures, and b) the corresponding contour plot for asymmetry versus temperature.

inductively protect the photoexcited carriers when its rotating motion is moderate, enhancing the carrier lifetime. In other words, our findings imply that one of the prerequisites for the MA molecule to demonstrate an effective dielectric response is local freedom of motion on a time scale comparable to the carrier lifetime.

3. Summary

In conclusion, the local field fluctuation brought on by nuclear magnetic moments allows muons to detect changes in the MA molecular motion. The variation in the carrier lifetime determined by the PL measurement is commensurate with the variation in nuclear dipole width. It is suggested that the effective electric dipole moment of the MA molecules, which is related to the local dielectric susceptibility, strongly influences the carrier lifetime.

References

[1] T. M. Brenner et al., Nat. Rev. Mater. **1** (2016) 15007.
[2] T. Chen et al., Phys. Chem. Chem. Phys. **17** (2015) 31278-31286.
[3] G. M. Bernard et al., J. Phys. Chem. A **122** (2018) 1560.
[4] T. Chen et al., PNAS **114** (2017) 7519-7524.
[5] S.H. Lee, private communication.

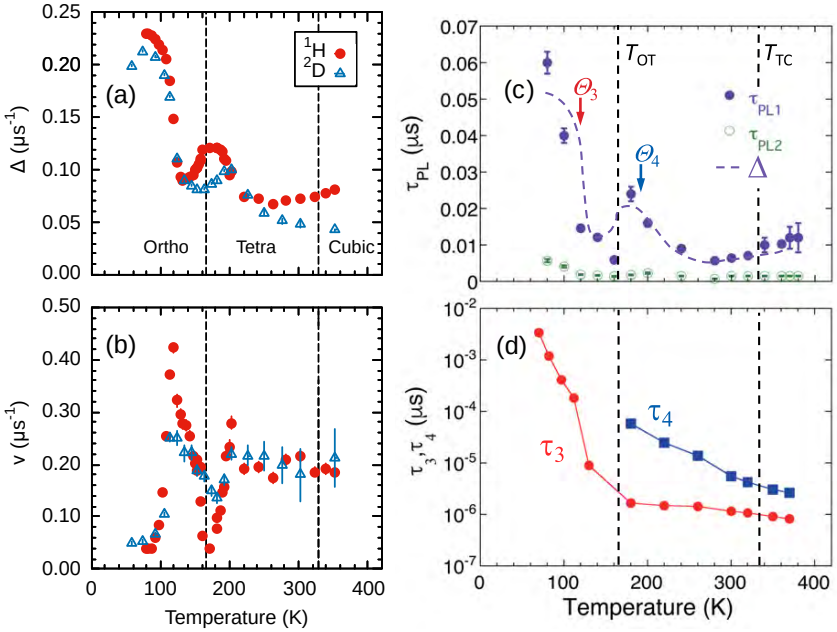

Figure 3. Temperature dependence of a) the dipolar width, b) the fluctuation rate, c) the photoluminescence (PL) lifetime quoted from Ref. [4] and d) the relaxation time $\tau_3(\tau_4)$ of the rotational motion around the $C_3(C_4)$ axis determined by quasi-elastic neutron scattering (after Ref. [2]). Circle (triangle) symbols in panels a) and b) represent data on sample consisting of $CH_3NH_3^+$ ($CD_3NH_3^+$), respectively. The dashed curve in panel c) indicates the *T*-dependence of $\Delta(^1H)$.

A. Koda[1,2], H. Okabe[1,2], M. Hiraishi[1,2], R. Kadono[1,2], K. A. Dagnall[3], J. J. Choi[3], and S. H. Lee[3]

[1]Muon Science Section, Materials and Life Science Division, J-PARC Center; [2]Institute of Materials Structure Science, KEK; [3]Department of Physics, University of Virginia

High Resolution Spectroscopy of Electronic K X Rays from Muonic Atoms

1. Introduction

When a negative muon is captured by an atom, normally in a highly excited level ($n_\mu > 20$, where n_μ represents a muon principal quantum number), the muon starts to cascade towards the nucleus first by muon-induced Auger decay and then via radiative decay emitting muonic x rays. The former process dominates at the beginning of the cascade, accompanying electron ejection from M shell, followed by L and K shell. The latter radiative decay is important when the muon approaches the lower levels. When an electronic hole is formed during this cascade process, it is filled by the upper-level electrons via emission of electronic characteristic x rays or electronic Auger decay. In addition, inside a solid-state target, electron side feeding also takes place, where an electron transfers from the surrounding atoms to the muonic atom [1]. Finally, the muon reaches the atomic 1s ground state. The timescale of the cascade process is typically ~10 fs for an Fe atom.

Dynamical aspect of the muon cascade has been studied by examining the intensity distribution of the muonic x-ray line series. The energies of the muonic x rays also encode information on the bound electrons, because the screening of the nuclear charge by these electrons modifies their energies [2]. An alternative approach is provided by observation of the electronic characteristic x ray from muonic atoms [3]. The electronic K x ray is a sensitive probe for the electron dynamics because the electron-electron interaction contributes more significantly to the energy of the K x rays than the muonic x rays. However, the insufficient resolution of conventional x-ray detectors has prevented further detailed study.

In this study, we report high-resolution measurements of electronic K x rays emitted from a muonic Fe (μFe) using state-of-the-art superconducting transition-edge sensor (TES) microcalorimeters [4]. The TES detector utilizes the steep temperature dependence of resistance at the superconducting phase transition [5] and realizes both a high energy resolution and a high detection efficiency.

2. Experiment

The measurement was carried out at the D2 beam line of the Materials and Life Science Experimental Facility (MLF) at J-PARC. Details of the experimental setup can be found elsewhere [4]. Briefly, the pulsed negative muon beam with low momentum (20.5 MeV/c) was irradiated to a 100 μm-thick Fe foil target tilted by 45° with respect to the muon-beam direction. X rays emitted from the target were measured by the TES x-ray detector placed normally to the muon-beam direction. The x-ray energy and detection time with respect to the pulsed muon beam injection were simultaneously accumulated.

The x-ray detector is based on a 240-pixel TES array developed by the National Institute of Standards and Technology (NIST) [5]. Each pixel contains a TES consisting of a bilayer of thin Mo/Cu films whose superconducting critical temperature is about 107 mK, and a 4 μm-thick Bi absorber for converting x-ray energy into heat. The effective area of each pixel is 305 × 290 μm^2 and the total active area of the array is about 23 mm^2. The TES array was cooled with a pulse-tube-backed adiabatic demagnetization refrigerator (ADR). The TES bath temperature was regulated to 70 mK ± 5 μK rms. Energy calibration of the TES detector was performed by using an x-ray generator installed at the front of the detector. The characteristic x rays from Cr, Co, and Cu were used as calibration x-ray lines. The accuracy of the energy calibration was better than 0.6 eV.

3. Results and discussion

The x-ray spectrum shown in Fig. 1(a)was obtained after applying a time window to extract the beam-correlated signals. The energy resolution was evaluated to be 5.2 eV (FWHM). We observed an asymmetric and broad structure starting from the Mn $K_\alpha 1$ and $K_\alpha 2$ energies (5899 and 5888 eV) and extending across 200 eV. This peak was assigned to electronic K_α x rays from μFe. A similar structure for electronic K_β x rays from μFe was identified, which starts from the energy of Mn K_β x-ray line at 6490 eV. We also found a broad tail-like structure beneath the peak of muonic x rays from μBe at 6179 eV, which was determined to be the hypersatellite Kh_α x rays from μFe, the characteristic x rays from double K-shell hole states [6].

The energies of the electronic K x rays emitted from μFe during the cascade process were affected both by the muon state and by the electron configuration at the moment of the x-ray emission. To evaluate these energy shifts, we calculated the energies of the electronic K x

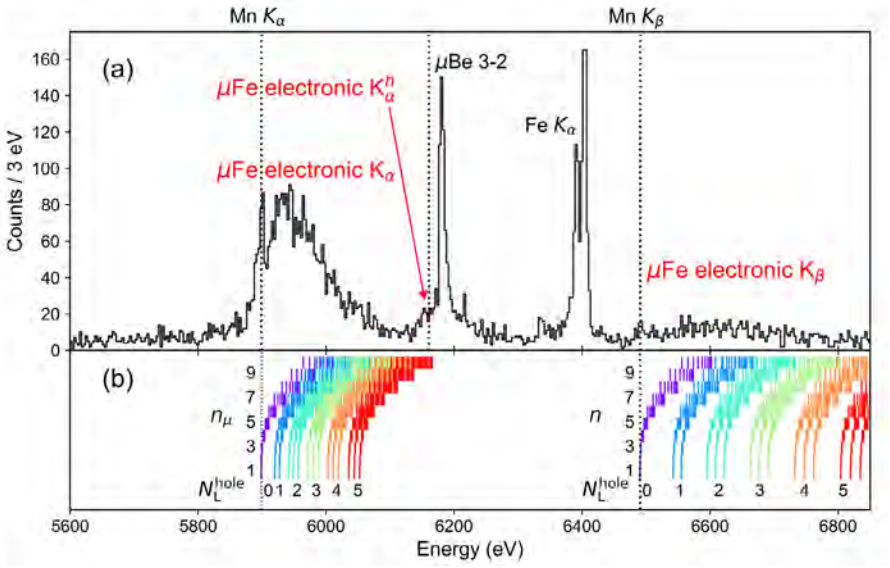

Figure 1. (a) The x-ray spectrum in the energy range from 5600 to 6850 eV measured by the TES detector [4]. The Fe K_α peak is emitted due to direct ionization of the target by the incident beam. We also observed a sharp peak of muonic x-rays from μBe around 6200 eV, which is emitted from a Be x-ray window at the front of the TES detector. (b) Calculated K_α and K_β x-ray energies from μFe under different muon states n_μ and electron configurations with L holes N_L^{hole}.

rays from μFe by employing a non-relativistic density functional theory [7]. The calculated μFe K_α and K_β x-ray energies are shown in Figs. 1(b) for various muon states and electron configurations, which are represented by the muon principal quantum number n_μ and the number of the L-shell electron holes N_L^{hole}, respectively. The K x-ray energies decrease at the lower muon levels n_μ because the muon screens the nuclear charge and this screening effect gets stronger at the lower n_μ. When n_μ =1, the K x-ray energy almost corresponds to that from the Z - 1 atom, i.e., Mn K x rays. On the other hand, the shift due to different electron configurations strongly depends on N_L^{hole} and we found a systematic shift to higher energy for large N_L^{hole}. The observed broadening can be explained by the convolution of these two effects.

The net peak shapes of the μFe K x rays reflect the temporal evolution of the muon state and electron configuration during the muon cascade. We performed a simulation of the cascade, which involved not only muon-induced but also electron-induced processes. Particularly, we took into account the M-shell side-feeding process, the electron transfer from the surrounding Fe to the M shell of the μFe.

Figure 2(a) shows the results of the simulation for Kα x rays. The experimental K_α spectrum was fitted with the simulation curve, where the M-shell per-hole side-feeding rate Γ_M was treated as a fitting parameter. It is clearly seen that the M-shell side-feeding rate changes the whole spectrum drastically, and a simulation neglecting side feeding ($\Gamma_M = 0.0$ fs^{-1}) does not explain the observed feature at all. The best result was obtained at the side-feeding rate of $\Gamma_M = 0.35$ (2) fs^{-1}. Using the same values of Γ_M, we also reproduced the hypersatellite Kh_α x-ray and K_β x-ray spectra as shown in Figs. 2(b) and 2(c), respectively. The excellent agreement of the present simulation with the spectrum obtained experimentally strongly supports our interpretation of the involved dynamics.

4. Summary

We showed that the high-resolution spectroscopy of electronic K x rays from muonic atoms could be used as a good probe for studying the temporal evolution of electron dynamics during the muon cascade process, which has remained unresolved for decades. In addition, we found that the K X-ray spectrum is very sensitive to the side-feeding effect from the surroundings. This method suggests a new way to revisit the dynamics of muonic atoms not only in metals but also in semiconductors, insulators, and molecules.

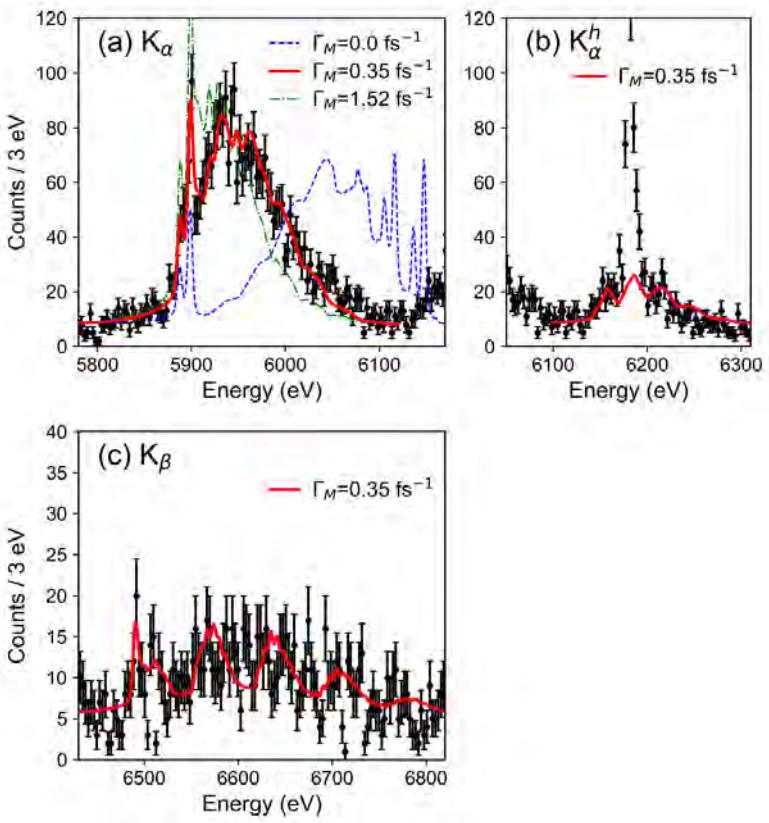

Figure 2. Comparison of the simulated and corresponding measured K x-ray spectra [4]. The simulated spectra are after convolution by the energy response function of the TES detector. (a) Simulated K_α x-ray spectrum with three side-feeding rates. (b), (c) Simulated hyper satellite Kh_α and K_β x-ray spectra under the same parameters as (a) with $\Gamma_M = 0.35$ fs^{-1}.

References

[1] F. J. Hartmann, in *Muonic Atoms and Molecules*, edited by L. A. Schaller and C. Petitjean (Birkhäuser Verlag Basel, Basel, 1993), pp. 157–165.

[2] L. Simons et al., Nucl. Instr. and Meth. B, **87** 293 (1994).

[3] H. Schneuwly and P. Vogel, Phys. Rev. A, **22** 2081 (1980).

[4] T. Okumura et al., Phys. Rev. Lett., **127** 053001 (2021).

[5] J. N. Ullom and D. A. Bennett, Supercond. Sci. Technol. **28** 084003 (2015).

[6] R. Diamant et al., Phys. Rev. A **79** 062511 (2009).

[7] X. M. Tong and S. I. Chu, Phys. Rev. A **55** 3406 (1997).

T. Okumura[1,2], T. Azuma[2], D.A. Bennett[3], P. Caradonna[4], I. Chiu[5], W.B. Doriese[3], M.S. Durkin[3], J.W. Fowler[3], J.D. Gard[3], T. Hashimoto[6], R. Hayakawa[7], G.C. Hilton[3], Y. Ichinohe[7], P. Indelicato[8], T. Isobe[9], S. Kanda[10,11], D. Kato[12], M. Katsuragawa[4], N. Kawamura[10,11], Y. Kino[13], M.K. Kubo[14], K. Mine[4], Y. Miyake[10,11], K.M. Morgan[3], K. Ninomiya[5], H. Noda[15], G.C. O'Neil[3], S. Okada[16,2], K. Okutsu[13], T. Osawa[17], N. Paul[8], C.D. Reinstema[3], D.R. Schmidt[3], K. Shimomura[10,11], P. Strasser[10,11], H. Suda[18], D.S. Swetz[3], T. Takahashi[4], S. Takeda[4], S. Takeshita[10,11], M. Tampo[10,11], H. Tatsuno[18], X.M. Tong[19], Y. Ueno[2], J.N. Ullom[3], S. Watanabe[20], and S. Yamada[7]

[1]Department of Chemistry, Tokyo Metropolitan University; [2]Atomic, Molecular, and Optical Physics Laboratory, RIKEN; [3]National Institute of Standard Technology; [4]Kavli IPMU, The University of Tokyo; [5]Department of Chemistry, Osaka University; [6]Advanced Science Research Center, JAEA; [7]Department of Physics, Rikkyo University; [8]Laboratoire Kastler Brossel, Sorbonne Université, CNRS, ENS-PSL Research University; [9]RIKEN Nishina Center, RIKEN; [10]Technology Development Section, Materials and Life Sci-ence Division, J-PARC Center; [11]Institute of Materials Structure Science, KEK; [12]National Institute of Fusion Science; [13]Department of Chemistry, Tohoku University; [14]Department of Natural Science, College of Liberal Arts, International Christian University; [15]Department of Earth and Space Science, Osaka University; [16]Engineering Science Laboratory, Chubu University; [17]Materials Sci-ences Research Center, JAEA; [18]Department of Physics, Tokyo Metropolitan University; [19]Center for Computational Sciences, Uni-versity of Tsukuba; [20]Department of Space Astronomy and Astrophysics, JAXA

Rabi-Oscillation Spectroscopy for Precise Measurement of Hyperfine Structure of Muonium Atom

The muonium (Mu), in which a positive muon and an electron are bound together, is known as one of the exotic atoms. The spectroscopy of Mu atoms is a potential tool for discovering novel physics in particle physics research. The positive muon and the electron are point-like lepton particles in the Standard Model (SM) of particle physics, hence their contribution to the strong interaction is minor and well known when compared to hydrogen. The Mu hyperfine structure (HFS) can be used to calculate the muon-to-electron mass ratio. Since the electron mass has been carefully determined, muonium HFS spectroscopy offers the most precise estimate of the muon mass, which is an important input parameter for determining SM parameters like the Fermi coupling constant [1, 2]. Also, the precise measurement of the muonium HFS is important in order to determine the muon anomalous magnetic moment, $g-2$ [3–5].

We developed a novel method of atomic spectroscopy, which we named Rabi-oscillation spectroscopy. In this method, the resonance frequency is obtained from the time response to only one frequency. Time-integrated data were utilized in standard spectroscopy to analyze the behavior of atoms when the frequency was changed. We came up with a new notion – or, to put it another way, an inverse way of thinking – and developed a new approach for measuring the resonance frequency by solving an inverse problem. The answer is found by comparing the resonance signal to a theoretical simulation of Rabi oscillations without transforming the signal from the time domain resonance signals to frequency domain resonance signals.

In the atomic world, allowed states appear as discrete energy quantum levels, with the frequency of the electromagnetic wave produced or absorbed during a transition between levels severely determined by the energy difference between those levels. We will be able to precisely test the rules of physics in microscopic events if we can properly determine this resonance frequency. An atom or molecule is stimulated by electromagnetic radiation, such as lasers or microwaves in conventional spectroscopy, and the resonance center is the position where the signal is the highest.

In practice, the resonance frequency is determined by changing the frequency of the electromagnetic wave. The symmetrical resonance curve obtained by drawing each signal strength on a graph is used to determine the resonance frequency at which the curve reaches its maximum peak. Controlling the experimental conditions, such as the consistent power of the electromagnetic wave, is necessary for exact measurements. Furthermore, data at frequencies with low signal intensity, which correspond to the foothills on the curve, are required in order to obtain correct resonance curves. As a result, this approach is not always effective for exact measurements.

We paid attention to the Rabi oscillations, which are induced by atoms interacting with electromagnetic waves and cause the signal intensity of the transition to oscillate over time. The signal oscillations are large and slow if the electromagnetic wave frequency matches or is close to the resonance frequency, but small and quick if the difference between the two frequencies, or the detuning, is considerable. The power of electromagnetic waves is another determining factor. When the power is high, the signal grows large and quick, and when the power is low, the signal becomes small and slow. These combinations are distinct from the case in which the detuning is changed as shown in Fig. 1.

Using this feature, the detuning and power can be determined simultaneously from the combination of signal strength and oscillation speed. In other words, since the detuning is known, the resonance frequency can be obtained by subtracting it from the known frequency of the electromagnetic wave, regardless of the power.

After confirming the validity of the principle through theoretical simulations, we conducted experiments to measure Mu HFS with actual Mu atoms at J-PARC MLF, and analyzed the experimental data using the Rabi-oscillation method. The obtained result is shown in Fig. 2 and is nearly twice as precise as the previous experiment [6]. In the future, further experiments will be conducted aiming at 100 times higher precision.

In spectroscopy of atoms, containing short lived subatomic particles and nuclei produced using accelerator facilities, it is necessary to make brief observations with as much power as possible to obtain the maximum signal from a limited observation time and a small number of atoms. Since it can measure resonance frequencies with high precision and efficiency, Rabi-oscillation spectroscopy is a novel and powerful technique applicable to the measurement of atomic resonances.

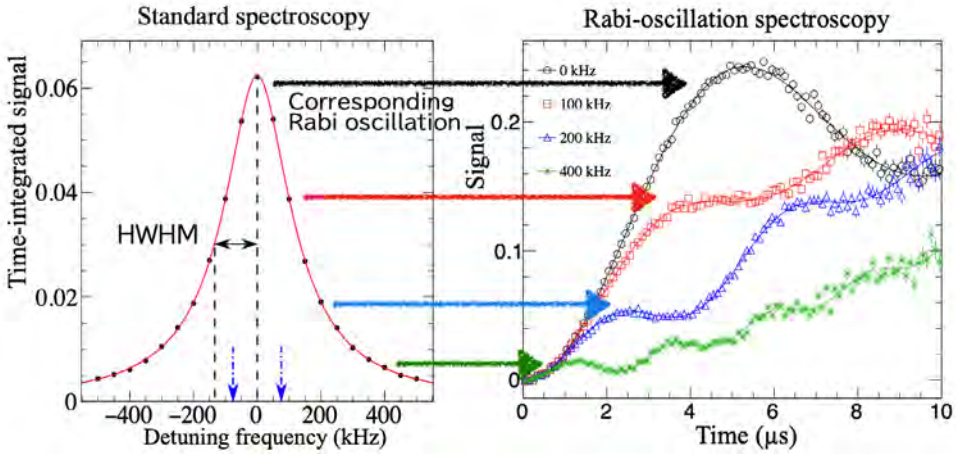

Figure 1. Standard spectroscopy on the left-hand side and Rabi-oscillation spectroscopy on the right-hand side.

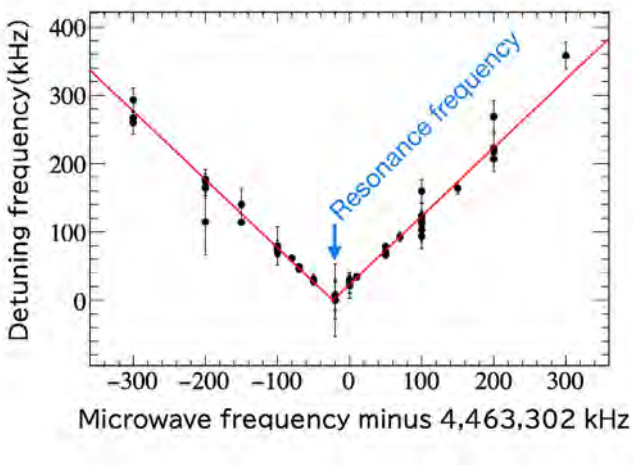

Figure 2. Results obtained by Rabi-oscillation spectroscopy.

References

[1] K. S. Tanaka et al., Prog. Theor. Exp. Phys. **2021**, 053C01 (2021).
[2] S. Kanda et al., Phys. Lett. B **815**, 136154 (2021).
[3] M. Abe et al., Prog. Theor. Exp. Phys. **2019**, 053C02 (2019).
[4] A. Keshavarzi, D. Nomura, T. Teubner. Phys. Rev. D **101** 014029, (2020).
[5] B. Abi et al. Phys. Rev. Lett. **126**, 141801 (2021).
[6] S. Nishimura et al. Phys. Rev. A **104**, L020801 (2021).

S. Nishimura[1,2] (MuSEUM Collaboration)
[1]*Muon Science Section, Materials and Life Science Division, J-PARC Center;* [2]*Institute of Materials Structure Science, KEK*

Measurements of the Neutron Capture Cross Section of ^{243}Am around 23.5 keV

1. Introduction

Accurate nuclear data for minor actinides (MAs) in high level nuclear waste (HLW) have been important since they are necessary for developing the design and performance of transmutation systems to reduce the inventory of HLW [1]. A promising option among the proposed nuclear transmutation systems is the accelerator-driven system (ADS), a subcritical reactor that compromise an accelerator-driven neutron source together with a fuel containing MAs. The contribution of uncertainties of the evaluated nuclear data JENDL-4.0 to reactor physics parameters was quantified in a recent work [2]. It has been shown that the ^{243}Am neutron capture cross section is one of the main contributors among all MAs. In the neutron energy of interest, from 0.5 to 500 keV, the uncertainties for the capture cross section of ^{243}Am in JENDL-4.0 have been evaluated to be 10% or higher, that stem from the poor quality of the experimental data.

There are only two data sets for the neutron capture cross section of ^{243}Am in the fast neutron energy region using the time-of-flight (TOF) method [3, 4]. Both results have discrepancies, although they agree with the large uncertainties.

In the present work, the neutron capture cross section of ^{243}Am was measured using the neutron filtering system in BL04 named the Accurate Neutron-Nucleus Reaction measurement Instrument (ANNRI) at the Materials and Life Science Experimental Facility (MLF) in the Japan Proton Accelerator Research Complex (J-PARC).

2. Experiments

The present measurements were performed at BL04 with a highly intense pulsed neutron beam provided by the spallation reaction of a mercury target. The incident neutron energy was determined by the neutron TOF method. However, the reconstruction of the neutron TOF to neutron energy is complicated due to the double-bunch mode, where two proton bunches with a time difference of 0.6 μs are shot to the spallation target to generate the neutron beam. In the keV energy region, the time difference is not negligible for the neutron TOF measurements. Both proton pulses cause two neutron production times, leading the energy ambiguities of neutrons at the same TOF. To solve this serious issue, the recently implemented neutron beam filtering system was employed in the present measurements [5]. A 20 cm Fe filter was used to make a quasi-monoenergetic neutron beam with the averaged energy of 23.5 keV. In addition, a Cd filter was used to cut off frame-overlap neutrons, which are low-energy neutrons coming from preceding neutron bursts. Capture gamma-rays emitted from a sample were detected with a NaI(Tl) detector located at a distance of 27.9 m from the moderator of the neutron source. Anode signals from the NaI(Tl) detector are fed into a digital data acquisition system (CAEN V1720) [6], recording the neutron TOF and pulse height (PH) of the signals.

A pellet of 38.14 mg of ^{243}Am dioxide enclosed in an Al container with Y_2O_3 binder was used in the present measurements. A disk-shaped sample with a mass of 38.14 mg enclosed in an Al container was used for the present work. A dummy sample containing only Y_2O_3 in Al case was measured to derive the background induced by the Al case and a ^{nat}C sample was used to estimate the scattering neutron background by a sample. In the present analysis, the neutron capture cross section of ^{243}Am was derived relative to the capture cross section of ^{197}Au. Thus, a gold sample was used as standard in this measurement. Additionally, a boron sample was used to measure the incident neutron energy spectrum by detecting 478 keV γ-rays from the ^{10}B(n, $\alpha\gamma$)^{7}Li reaction. Finally, a "blank" measurement with no sample was performed to estimate the sample-independent background.

3. Analysis

The experimental data were analyzed in offline analysis, which was stored in two-dimensional list data with the neutron TOF and the PH. The TOF spectra for ^{243}Am, boron and the dummy sample measurements are shown in Fig. 1. A clear peak appears in the TOF region from 12.6 μs to 15.0 μs, corresponding to 23.5 keV, at the total cross section of Fe becomes minimum and the transmission rate of neutrons is high. A TOF gate shown as the colored region in Fig. 1 was set for data analysis. PH spectra in the TOF gate were extracted for ^{243}Am, dummy, carbon, blank and gold runs. In the PH analysis, the backgrounds related to sample-independent components, dummy case and the scattered neutrons were subtracted from the ^{243}Am spectrum. After background subtractions, the neutron capture yield of ^{243}Am

was derived by applying the pulse-height weighting technique [6]. The data of the gold measurement were analyzed in the same manner and the capture yield of ^{197}Au was obtained. The neutron capture cross section of ^{243}Am was determined at the neutron energy of 23.5 keV relative to the ^{197}Au neutron capture yield with the evaluated cross section data of ^{197}Au.

4. Result

The neutron capture cross section of ^{243}Am around 23.5 keV was found to be 2.52 ± 0.14 b. The major components of the uncertainties were the statistical uncertainties (3.1% for ^{243}Am and 2.5% for ^{197}Au) and the uncertainty of the evaluated cross section of ^{197}Au (3%). The present result was compared to the past TOF experimental results of Wisshak *et al*. [3] and Weston *et al*. [4] together with the evaluated data from the JENDL-4.0 [7] and ENDF/B-VIII.0 [8] in Fig. 2. The cross section was determined with a smaller uncertainty than the past measurements. The data of Wisshak et al. are 20% lower than the present result and the data of Weston et al. is slightly lower than the present result. For the evaluated data, the JENDL-4.0 data are 7% smaller than the present value and ENDF/B-VIII.0 data are 5% larger but agree within the experimental uncertainty.

Both past measurements used old evaluation data for normalization: the capture cross section of ^{197}Au in ENDF/B-V 5% smaller than that of JENDL-4.0 by Weston et al. and the thermal capture cross section of ^{243}Am 15% lower than the latest value reported by Kimura et al. [9]. In accordance with the update of the nuclear data, both data were renormalized by the JENDL-4.0 capture cross section of ^{197}Am for the data from Ref. [3] and the thermal cross section of ^{243}Am in Ref. [9] for the data from Ref. [4]. The renormalized past experimental data are compared with the present value in Fig. 2(b). Agreement with the data of Weston et al. with the present value has been improved, but the data of Wisshak et al. are still lower than the present value.

5. Conclusion

The neutron capture cross section of ^{243}Am around 23.5 keV was measured with the quasi-monoenergetic neutron beam by the neutron filtering system in ANNRI (BL04). The cross section was determined with a smaller uncertainty than the past measurements. It has been shown that the disagreement between the present result and the data of Ref. [3, 4] has been improved after renormalization of the past data to the latest value of the thermal capture cross section of ^{243}Am. Further information about the present measurements can be found in Ref. [10].

6. Acknowledgments

The present work is funded by the MEXT Innovative Nuclear Research and Development Program of the Ministry of Education, Culture, Sport, Science and Technology. Grant Number: JPMXD0217942969.

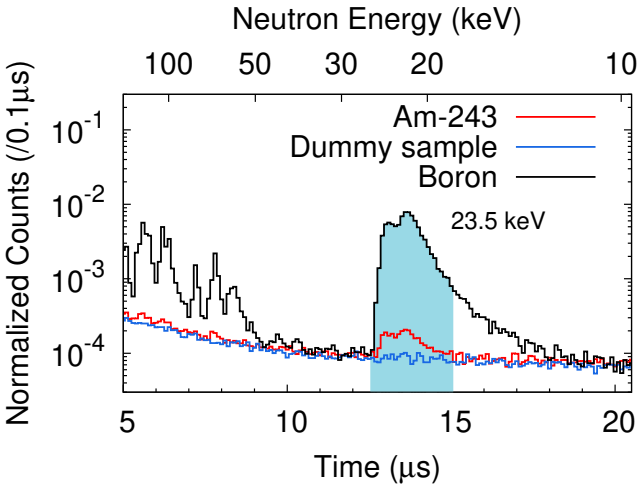

Figure 1. TOF spectra of the ^{243}Am sample (red), the boron sample (black) and the dummy sample (blue) measured with the NaI (Tl) detector.

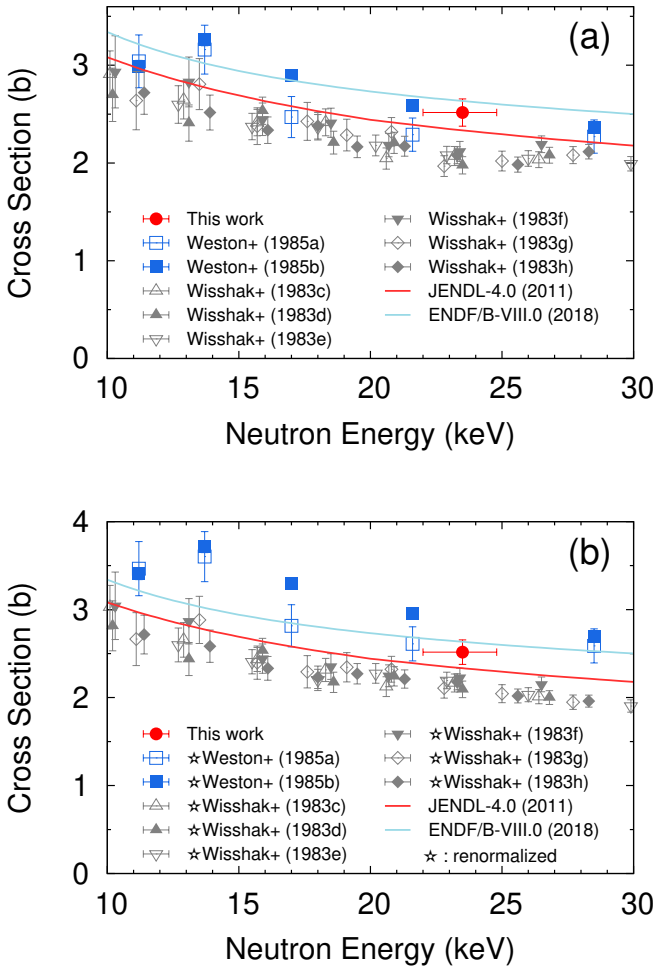

Figure 2. (a) Capture cross section of ^{243}Am. Comparison of the present result with past measurements and the evaluated data. (b) Comparison with the past data renormalized with the latest standard cross section.

References

[1] M. Salvatore et al., "uncertainty And Target Accuracy Assessment for Innovative Systems using Recent Covariance Data Evaluations." WPEC-26, OECD NEA, (2008).

[2] H. Iwamoto et al., J Nucl. Sci. Technol., **50** 8 (2013).

[3] K. Wisshak et al., Nucl. Sci. Eng. **85** 3 (1983).

[4] L.W. Weston et al., Nucl. Sci. Eng. **91** 4 (1985).

[5] G. Rovira et al., Nucl. Instrum. Methods. Phys Res. 1003 (2021).

[6] R. L. Macklin et al., Phys. Rev. **159** (1967).

[7] K. Shibata et al., J. Nucl. Sci. Technol., **48** 1 (2011).

[8] D.A. Brown et al., Nucl Data Sheets. **149** (2018).

[9] A. Kimura et al., Nucl. Sci. Technol., **56** 6 (2019).

[10] Y. Kodama et al., Nucl. Sci. Technol., **58** 11 (2021).

Y. Kodama[1], T. Katabuchi[1], G. Rovira[2], A. Kimura[2], S. Nakamura[2], S. Endo[2], N. Iwamoto[2], O. Iwamoto[2], J. Hori[3], Y. Shibahara[3], K. Terada[3], H. Nakano[1], and Y. Sato[1]

[1]Laboratory for Zero Carbon Energy, Tokyo Institute of Technology; [2]Nuclear Science and Engineering Directorate, Japan Atomic Energy Agency; [3]Institute for Integrated Radiation and Nuclear Science, Kyoto University

Wide Bandwidth Neutron-Spin Polarizer Due to Ferromagnetic Interlayer Exchange Coupling

1. Introduction

A neutron polarizing supermirror is one of the most important optical devices to polarize a neutron beam [1, 2]. It is a stack of alternating layers of ferromagnetic (FM) and non-magnetic materials with a variation in bilayer thickness to extend the bandwidth of the neutron polarization. We have developed an Fe/Ge polarizing supermirror by using the ion-beam sputtering technique [3]. A wide bandwidth is important especially for time-of-flight instruments installed at spallation neutron sources, such as the J-PARC MLF, since it determines the available wavelength-range of polarized neutrons. It is important to increase the ratio m of the critical momentum transfer of the supermirror to that of nickel to extend the bandwidth. The spontaneous magnetization of the ion-beam sputtered Fe/Ge multilayer, however, disappears when the Fe layer thickness is reduced to 2-3 nm because the Curie temperature drops below the room temperature. This limits the m-value of the polarizing supermirror because the multilayer fails to form a high and low contrast in the scattering length density profile for spin-up and -down neutrons [4].

To overcome this problem, we propose a modification of the layer sequence, where the minimum Fe thickness has been set to 3.5 nm, with the Ge thickness reduced to keep the bilayer thickness at the reference value of a standard supermirror. This invoked the FM interlayer exchange coupling in the Fe/Ge multilayer in a Ge thickness range from 1.2 to 2.2 nm. The performance test of the Fe/Ge neutron polarizing supermirror showed a marked increase in the m-value, meaning that the modified layer sequence offered a solution to the problem of the decrease of saturation magnetization when the Fe thickness decreases in the original layer sequence.

2. Polarized neutron off-specular scattering measurement

The polarized neutron off-specular scattering measurement was performed on the polarized neutron reflectometer SHARAKU with a horizontal scattering geometry at the J-PARC MLF [5]. Figure 1 shows the polarized neutron off-specular scattering images of Fe/Ge periodic multilayers with 50 bilayers (sample (A) Fe: 3.5 nm, Ge: 2.2 nm, sample (B) Fe: 3.5 nm, Ge: 1.2 nm). The scattering was spread over a wide q_z range for (A). This means that moments were not correlated in the out-of-plane direction. Contrary, the scattering was concentrated on the first Bragg condition ($q_z \approx 1.34$ nm^{-1}) for (B). The simulation based on the distorted wave Born approximation demanded a model where areas with a uniform orientation of moments between neighboring

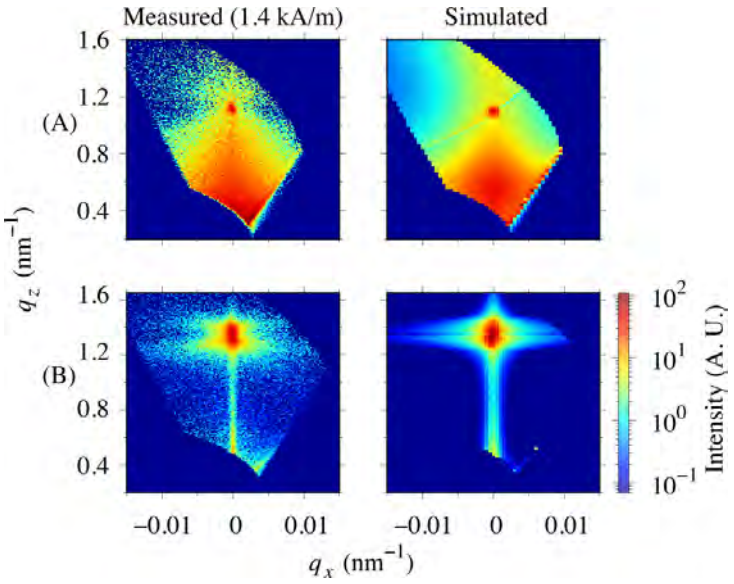

Figure 1. Measured and simulated polarized neutron off-specular scattering images of ion-beam sputtered Fe/Ge periodic multilayers with 50 bilayers. Sample (A) Fe: 3.5 nm, Ge: 2.2 nm, Sample (B) Fe: 3.5 nm, Ge: 1.2 nm. The FM interlayer exchange coupling when the Ge thickness is less than 2 nm resulted in a scattering localized at the first Bragg condition ($q_z \approx 1.34$ nm^{-1}).

Fe layers were ferromagnetically coupled. The measured and simulated result indicates that the FM interlayer exchange coupling in our Fe/Ge system grows with decreasing Ge thickness when the Ge thickness is reduced to less than 2 nm. The FM interlayer exchange coupling observed here contributed to the presence of saturation magnetization comparable to the bulk and to smaller coercivity and larger initial permeability than the multilayer without the FM interlayer exchange coupling. This offers a possibility to keep the spontaneous magnetization for the multilayer with a thin bilayer thickness and hence to increase the m-value of the polarizing supermirror.

3. Performance test of Fe/Ge neutron polarizing supermirror

An Fe/Ge neutron polarizing supermirror with $m = 6.2$ was fabricated by an ion-beam sputtering system with dual bucket Ar^+ ion sources. The layer sequence was designed by the algorithm proposed by Hayter and Mook [6]. To avoid a reduction in the saturation magnetization in thin Fe layers corresponding to $q_z > 1.085$ nm^{-1} ($m > 5$), we proposed a modified layer sequence, where the minimum Fe thickness was set to 3.5 nm, whereas the Ge thickness was reduced. This resulted in a total number of layers of 10436 and total thickness of 32 μm. The polarized neutron reflectivity (PNR) measurement at room temperature was performed for the Fe/Ge polarizing supermirror under an external field of 40 kA/m. The measured PNR profiles and polarization are plotted in Fig. 2. The spin-up reflectivity was higher than 0.70 for $q_z < 1.302$ nm^{-1} ($m < 6$) and the polarization was higher than 0.93 for $0.217 \leq q_z \leq 1.194$ nm^{-1} ($1 \leq m \leq 5.5$). The performance test of the neutron polarizing supermirror showed that the FM interlayer exchange coupling contributed to the presence of the magnetization comparable to the bulk and resulted in a marked enhancement in the m-value larger than 6 [7].

4. Summary

The polarized neutron off-specular scattering measurement revealed that the FM interlayer exchange coupling occurred in the ion-beam sputtered Fe/Ge multilayer when the Ge thickness was reduced to less than 2.2 nm. The FM interlayer exchange coupling contributed to the presence of the saturation magnetization comparable to the bulk. The Fe/Ge polarizing supermirror fabricated with the modified layer sequence proposed here showed a marked extension in the m-value larger than 6. The bandwidth extended in this study is not enough to cover a full spectrum available at the MLF. The origin of the magnetic interlayer exchange coupling across a semiconductor spacer has not been fully understood. Further study including this point is needed to improve the performance of the polarizing supermirror and to promote the science using polarized neutrons.

References

[1] V.F. Turchin, Sov. J. At. En., **22** 124 (1967).
[2] F. Mezei, Commun. Phys., **1** 81 (1976).
[3] R. Maruyama et al., Nucl. Instrum. Methods Phys. Res. A, **888** 70 (2018).
[4] M. Hino et al., Physica B, **385-386** 1187 (2006).
[5] M. Takeda et al., Chinese J. Phys., **50** 161 (2012).
[6] J.B. Hayter and H.A. Mook, J. Appl. Crystallogr., **22** 35 (1989).
[7] R. Maruyama et al., J. Appl. Phys., **130** 083904 (2021).

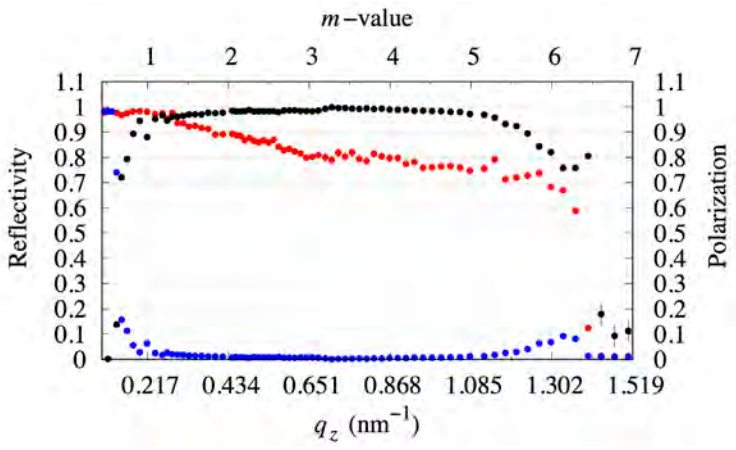

Figure 2. Polarized neutron reflectivity profiles of the Fe/Ge neutron polarizing supermirror fabricated in this study. Spin-up and -down reflectivities are plotted in red and blue, respectively. The polarization is shown in black.

R. Maruyama
Neutron Instrumentation Section, Materials and Life Science Division, J-PARC Center

Neutron Source

Neutron Source Section

1. Overview

At the beginning of fiscal year 2021, on April 5, the beam power was raised to over 700 kW from 600 kW, which was the highest level of beam power on record for the long-term user program at the MLF. The stable operation continued, but due to the humid and hot weather in the summer, the beam power had to be decreased to 600 kW again from June 24 in order to increase the cooling capacity margin of the accelerator devices. The beam operation ended on July 17, before the start of the long outage.

As the beam power increases gradually to the final goal of 1 MW, promotion of the radiation work safety, especially in the maintenance period, becomes more and more important. In order to check and review the criteria for radiation work safety and procedures of maintenance works, sufficient maintenance period was secured and parallel works that could increase the risk of radiation release or contamination were avoided to concentrate on each maintenance task one by one. The results of check and review were used to improve the planning of maintenance works from the next year on. These procedures led to the late start of the beam operation for the user program from January 15 in 2022.

After the beam operation resumed, the neutron source continued its stable operation at 730 kW and the average operational efficiency in fiscal year 2021 reached 95.9%.

2. Pitting damage mitigation of the mercury target vessel

On October 18, specimens were cut out from the forefront wall, the beam window, of the used target vessel, which was operated with 740 kW at maximum, to investigate the efficiency of technologies for pitting damage mitigation, which involve the double walled structure with a narrow channel and the microbubble injection into the mercury flow as shown in Fig. 1. The maximum damage depth on the bulk side of the inner wall specimen was less than 1 mm and the surface of the narrow channel side was almost intact, which was a promising result for the stable beam operation with greater beam power.

On November 1, the used mercury target vessel was replaced with a new one with an improved structure of the mercury flow channel. That is, the bubble generator was installed at a position 92 mm closer to the beam window than the former one to increase the bubble number density near the beam window for promoting the pressure wave mitigation effect. Improvement of the mercury target design was further continued to install the bubbler as closer to the beam window as possible to realize the long and stable target operation with a final goal of 1 MW, which is shown in the following chapter.

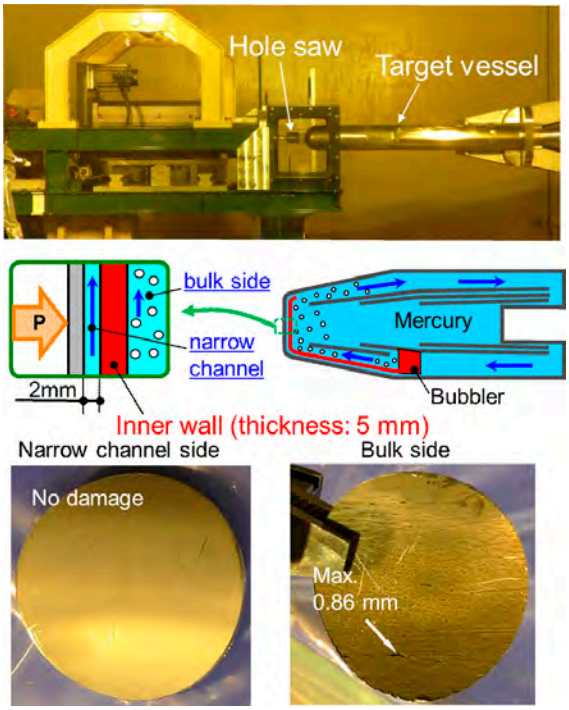

Figure 1. Cutting machine (top) and structure of the target vessel (middle) and the surfaces of an inner wall specimen (bottom).

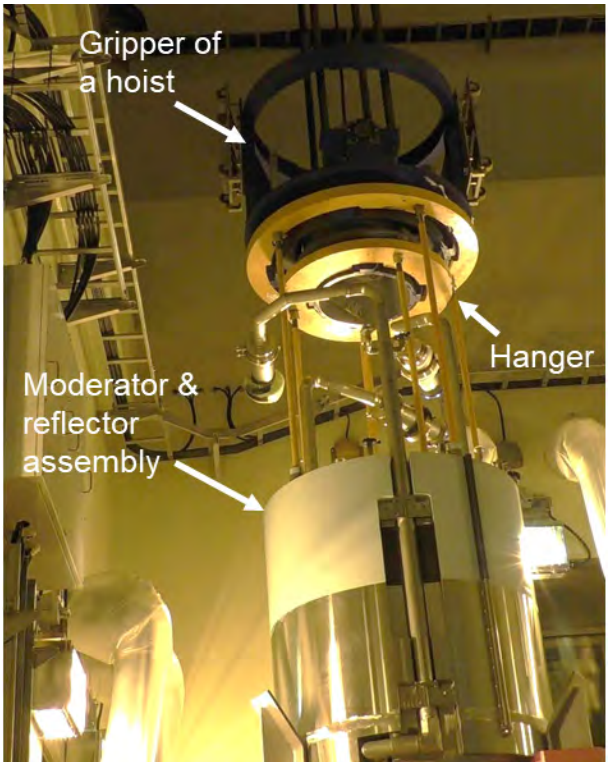

Figure 2. Engaging the gripper of a hoist with the hanger of the moderator & reflector assembly.

Figure 3. Chilled towers of the 3NBT water cooling system.

3. Remote handling test of the moderator & reflector assembly

The remote handling test of the moderator & reflector assembly was carried out for the first time since the beam operation of the MLF started in 2008. The spare assembly, which would be replaced with the present one in a few years, was used for the handling tests. First, the handling tests were carried out by hands-on in the HENDEL building where was a non-controlled area. Then the spare assembly was transported to the MLF, and remote handling tests were conducted in the hot-cell using the remote handling tools including the transportation cask equipped with a hoist and gripper in it, as shown in Fig. 2. In 2021, the assembling and disassembling procedures of the decoupled moderator were checked and successfully completed. The other components of the assembly, such as the coupled and poisoned moderators, and the reflector, would be tested during the maintenance period in the next year.

4. Noticeable maintenance works

The maintenance work to replace a vacuum pump of the gas process system, which is a crucial device for the target replacement, was a significant task. It needed special care to suppress the release of radioactive materials and the requirement was fulfilled through a well-prepared procedure plan, which is also shown in the following chapter.

The cooling tower of the coolant water loop for the devices of the 3 GeV proton beam transport line was replaced to the chilled towers, shown in Fig. 3, as a countermeasure against aging deterioration. The increased cooling capacity will contribute to a stable beam operation in the summer.

K. Haga
Neutron Source Section, Materials and Life Science Division, J-PARC Center

Optimization of Mercury Target Vessel Design to Extend the Lifetime by Using Machine Learning

1. Introduction

In a mercury target for neutron sources, pulsed proton beams repeatedly bombard the flowing mercury which is confined in a stainless-steel vessel (target vessel (Fig. 1)). The bombardments of the proton beams cause instantaneous thermal expansion of the mercury which generates pressure waves in the mercury. Cavitation damage, which is induced by the pressure waves, is one of crucial issues to determine the lifetime of the target vessel. To reduce the damages, we developed a narrow channel structure [1, 2] and a technique to inject the gas microbubbles into the flowing mercury by the swirl bubbler [3], which can reduce the pressure waves inducing the cavitation damage [4]. The neutron source continued its stable operation at 730 kW and the average operational efficiency in fiscal year 2021 reached 95.9%. The beam power increases gradually to the final goal of 1 MW.

On the other hand, the spent target vessels occupy a storage area. Therefore, further reduction of the damage is required to extend the lifetime of the target vessel and to reduce the generation frequency of spent target vessels. The sufficiently small gas bubbles are required to reduce the pressure waves because the natural frequency of the smaller bubbles is higher, and they can respond to and absorb the instantaneous thermal expansion of the mercury. And to increase the gas volume fraction of gas microbubbles is also effective to absorb the thermal expansion and to reduce the pressure waves [5]. The severe damaged area is the beam window where the proton beam is injected as show in Fig.1 because heat deposition and generated pressure waves are high. It is considered that the volume fraction of gas microbubble near the beam window can be increased by moving the bubbler closer to the beam window since the injected gas bubbles rise due to buoyancy. However, the space near the beam window is restricted as shown in Fig. 1(a). Therefore, the bubbler design and setting position as well as the flow guide vanes for the mercury flowing pattern were optimized by means of a machine learning technique to increase the volume fraction of microbubbles near the beam window [6].

2. Design for optimization

Figure 1(a) shows the schematic of the original mercury target structure. Flow guide vanes are installed inside the target vessel so that distribution of mercury flow rate can be achieved to correspond with distribution of heat deposition in mercury. The bubbler was installed on the inlet side. In the original design, 5 elements were installed in one unit. However, the unit is bombarded directly by the proton beam when the unit moves to the beam window as shown in Fig. 1(a). Therefore, in the design for optimization, the unit was divided into 2 units as shown in Fig. 1(b). Each unit includes 3 elements. Figure 2 shows the bubbler element. In the optimization, the parameters shown in Fig. 1, 2 were used for the design variables for the machine learning. Here, P1 is the distance of the bubbler unit B1 from the original position, Θ the angle of flow guide vane, D the Inlet diameter of the bubbler element, θ the angle of the swirl blade, and D_e the diameter of the throat in the bubbler element.

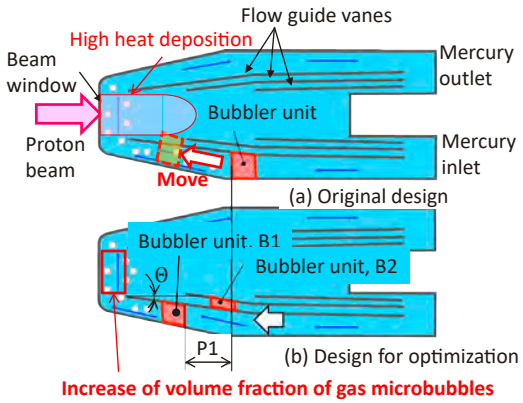

Figure 1. Schematic of the mercury target vessel: (a) original design, (b)design for optimization.

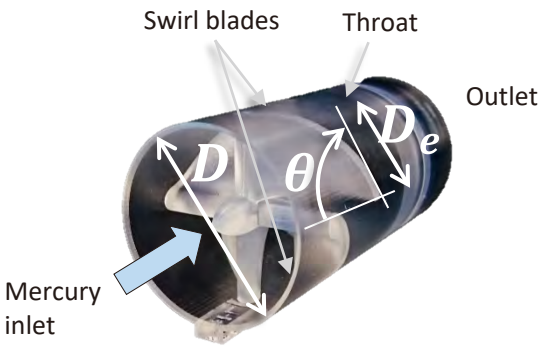

Figure 2. Swirl bubbler element.

3. Machine learning and optimization

To generate data for machine learning, 1000 cases of CFD (Computational Fluid Dynamics) simulations with bubble flow were performed by changing the design parameters shown in Fig. 1, 2. Fluent ver. 19.2 [7] was used for the simulation, and Realizable k-ε was used for the turbulence model. As for the boundary condition, the pressure difference between the mercury inlet and outlet was set to 0.23 MPa which was decided according to the capability of the mercury pump. The motion of bubbles in mercury was modeled using a discrete phase model. Since the interaction between bubbles is not taken into consideration, the bubbles do not break up and coalesce. Since the generated bubble size distribution depends on the bubbler design and mercury flow speed in the bubbler, the injected bubble size distribution was changed based on the empirical formula [3].

Based on the simulation results, surrogate models to predict the volume fraction of the gas bubble near the beam window (objective function), the mercury flow rate and the generated bubble size (constraint conditions) were derived by Gaussian process. By using the obtained surrogate models, optimization to maximize the objective function by means of the sequential quadratic programming was performed to fit the constraint conditions. As of the constraint conditions, the mercury flow rate was set to be over 36 m^3/h to keep the temperature rise of the mercury and the target vessel similar to or less than the original one. And bubble diameter was set to less than 100 μm so that the gas bubbles can respond to the instantaneous thermal expansion. After the optimization, the CFD simulation was carried out by using the optimized design variables for verification.

Figure 3 shows the volume fraction of gas microbubbles near the beam window and mercury flow rate as a function of bubbler position, which is calculated by using the obtained surrogate models. It is noted that the design parameters except for the bubbler position are optimized values. As mentioned above, the volume fraction is increased as the bubbler unit B1 moves near the beam window. However, the mercury flow rate is decreased. Therefore, the optimized results for the bubbler position did not show the nearest position to the beam window.

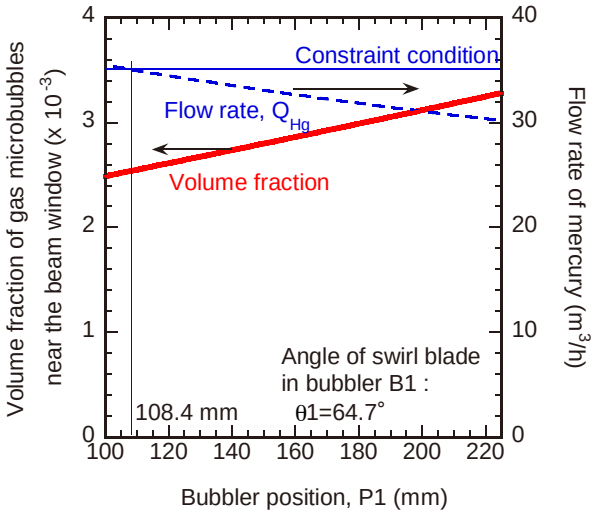

Figure 3. The volume fraction of gas microbubbles near the beam window and mercury flow rate as a function of the bubbler position.

4. Optimization result

As an optimization result, we developed the design of a mercury target vessel that can increase the volume fraction of gas microbubbles near the beam winodow by ca. 2.5 times higher than the original design. As for the damage, an empirical formula to estimate the damage depth was derived based on the result of off-beam test [8] and the relationship between the observed damage and operational condition of the target was acquired. And the effect of the gas injection rate on the reduction of the pressure waves was measured [4]. Based on these empirical formulae and relationships, the optimized target vessel will endure for 2-year operation at 1 MW. The fabrication of the target vessel based on the optimized results will be completed in fiscal year 2023.

References

[1] K. Haga et al., JPS Conf. Proc., **8** 051008 (2015).
[2] T. Naoe et al., Mat. Sci. Forum, **1024** 111 (2021).
[3] H. Kogawa et al., J. Nucl. Sci. Tech., **52** 1461 (2015).
[4] H. Kogawa et al., J. Nucl. Sci. Tech., **54** 733 (2017).
[5] K. Okita et al., J. Fluid Sci. Technol., **3** 116 (2008).
[6] H. Kogawa et al., JAEA-Technology 2022-023, (2022).
[7] ANSYS Inc., ANSYS Fluent Theory Guide, Release 19.2 (2018).
[8] M. Futakawa et al., J.Nucl. Sci. Technol., **40** 895 (2003).

H. Kogawa[1], T. Wakui[1], M. Futakawa[2], T. Naoe[1], and K. Haga[1]
[1]Neutron Source Section, Materials and Life Science Division, J-PARC Center; [2]Invited Researcher, J-PARC Center

Radiation Safety Countermeasures for Pump Replacement of the Off-gas Processing System

1. Introduction

An off-gas processing system is adopted in the MLF to remove radioactive material, produced by mercury spallation reactions, from the cover gas and purge gas used in the mercury circulation loop. Figure 1 shows a photo of the off-gas processing system. The radioactive gas is transferred to this system with a vacuum pump in advance of the maintenance works of the mercury circulation loop. The pump is also used to form an inflow of air to suppress the release of gaseous radioactivity during the replacements of a target vessel, pressure gauges, etc. Those gases are stored, processed, and finally released to atmosphere from the stack.

We replaced one of the vacuum pumps, which had been used for 14 years as a backup of the main pump, in a viewpoint of preventive maintenance. Here, we report how we secured the radiation safety of the vacuum pump replacement work in which the control of radioactive gas release was thought to be a challenge.

2. Method

Radioactive gas passes through the vacuum pump, thus it is concerning that the radioactivity remaining in the pump could be released from the opening of the piping during the pump replacement. To minimize the release, we enclosed couplings of piping connection parts with ready-made plastic bags with gloves named "glove bags". To ensure airtightness, we sealed the glove bags by welding the opening parts and taping pipe-penetrating parts with vinyl tape. We filled the glove bags with dry air through a small nozzle with a valve and confirmed that no air leaked from the bags.

We also set a "barrier box" made by welding polyvinyl acetate (PVAC) sheets to cover the pump and the glove bags. The inner area of the barrier box was exhausted by local ventilation to prevent internal radiation exposure of workers. We checked the air flowing into the box from the opening on the workers' side. Figure 2 shows a photo of the vacuum pump in the barrier box before the replacement.

The radioactive gas is released to the barrier box when the glove bags are removed and is exhausted with the local ventilation. Based on experiences of previous replacements of vacuum pumps and other instruments, we decided to transfer the gas in the glove bags to the off-gas processing system before dismantling the bags. For such purpose, we connected a tube to each nozzle of the glove bag. It contributed to suppressing not only the internal exposure of workers but also the release of radioactivity to the local ventilation as much as possible.

We assigned two workers and one supervisor to approach the working area. These three persons were equipped with demand-type airline respirators and vinyl anorak suits to minimize inner exposure not only by breathing but also through skin absorption. Two teams of

Figure 1. Photo of the off-gas processing system.

Figure 2. Photo of the vacuum pump in the barrier box before the replacement.

workers relayed the work to lighten their loads because the expected total working time with such equipment was too long. During the work, the radioactivity concentrations both in the barrier box and around the workers' respiration area were monitored.

3. Procedure

The working procedure is mentioned below and illustrated in Fig. 3.

(1) Covering the couplings with the glove bags (by the day before).
(2) Demounting the couplings.
(3) Moving the pump back to make a space.
(4) Closing the 4 openings with blank flanges.
(5) Evacuating gas in the glove bags to the off-gas processing system.
(6) Cutting the glove bags.
(7) Removing the old pump.
(8) Covering both openings of newly installed metallic valves and the pipes with glove bags.
(9) Connecting the metallic valves and the pipes with couplings.
(10) Leak checks.
(11) Removing the glove bags.
(12) Connection of a new pump (on the next day).

4. Result

The pump replacement was carried out on September 27. Increases in the monitored radioactivity concentrations in the barrier box and the respiration area were much lower than the predicted by prior estimation. The workers' inner exposures were less than the lower detection limit. Contamination around the working area after the replacement was not detected.

We performed a test run of the new pump and found no problems.

On a later day, we put the used pump into a stainless-steel double-walled container and encapsulated it by welding an outer container.

5. Summary

We prepared the glove bags, the evacuation of gas in them, the barrier box, the demand-type airline respirators, and vinyl anorak suits for radiation safety. No workers' inner exposure was detected, and the vacuum pump was successfully replaced.

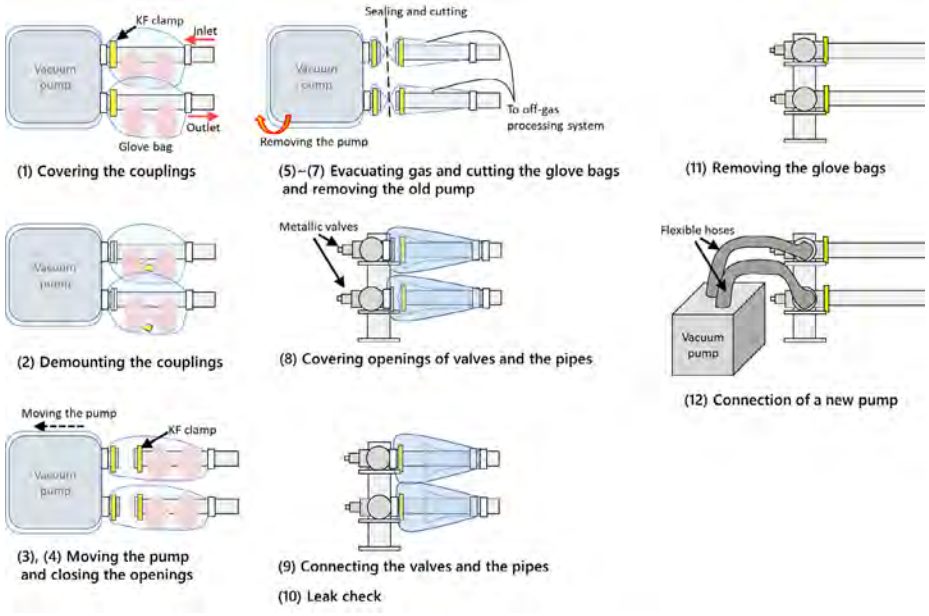

Figure 3. The procedure of the vacuum pump replacement.

S. Takamiya and T. Kai
Neutron Source Section, Materials and Life Science Division, J-PARC Center

Neutron Science

Neutron Science Section

1. Introduction

The mission of the Neutron Science Section (NSS) is to lead scientific research as a world neutron center, build and maintain state-of-the-art instruments, organize collaborative research, support user programs, and carry out our own scientific research. COVID-19, still being the rage across the globe, disturbs those activities in the facility, we have to keep making significant efforts to maintain or even to improve the activities and the scientific work. For most users from abroad, it is still difficult to visit Japan because of the COVID-19 restrictions, so many proposals have been canceled and the rest have been conducted as deputized experiments by the beamline scientists.

2. User program

The proposal round of 2021A,merged with that of 2020B, has been called but no new long-term proposals had been called for 2021 due to delay in conducting the approved ones for 2018L to 2020L. In the period of 2021B, we received 338 neutron proposals, including short-term, one-year, NUP (new user promotion) and post deadline proposals. Among them 137 have been approved. Although the number of submitted proposals showed an abrupt drop in the 2020A, it is now recovering or even exceeding the submissions for 2020. The breakdown of the distribution of applicant affiliations are summarized in Fig. 1.

3. Instruments up to date

Initially, 23 beamlines (BL) for neutron experiment were designed for future instruments in the MLF and 21 are under operation at moment. The MLF beam operation started officially in May 2008, 14 years have already passed particularly for BL in the early stage of the MLF (day-one instruments). All the BL, infrastructures, and equipment must be kept maintained, specifically the BL were required to be upgraded for the most advanced experiments. Here we report on one of those unremitting endeavors of beamline works.

BL17 is the neutron reflectometer (NR), which enables us to study mechanisms and functions of thin film material by revealing surface structures and buried interfaces. To prove dynamical phenomena varying in time, it was necessary to shorten the measurement time which is longer in conventional NR from several tens of minutes to few hours for one measurement. The BL17 team developed a new data processing method based on deep learning, which can successfully eliminate statistical noise from the raw data obtained in a rather short time like one tenth of the conventional NR [1]. It means that we can effectively extract the signals out of short measurement data and explore dynamic behavior of surface and interface (Fig. 2).

The new data treatment method, such as machine learning or deep learning, can be classified into the artificial intelligence (AI) technology. The huge volume of data created on a daily basis in the MLF operation would bury a human researcher. But the AI technologies can take that data and quickly turn it into meaningful information. This can be the "must" technique for the future data analysis in the MLF.

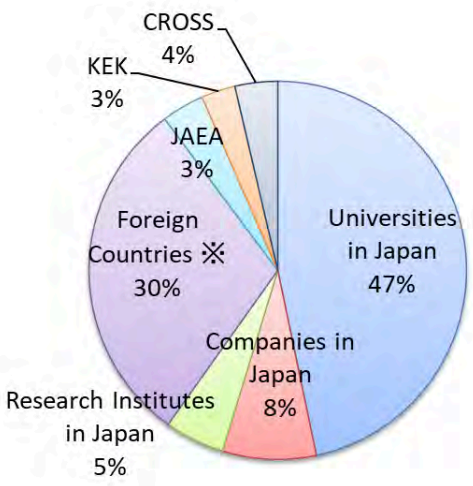

Figure 1. Distribution of applicants' affiliation for proposal round 2021B.

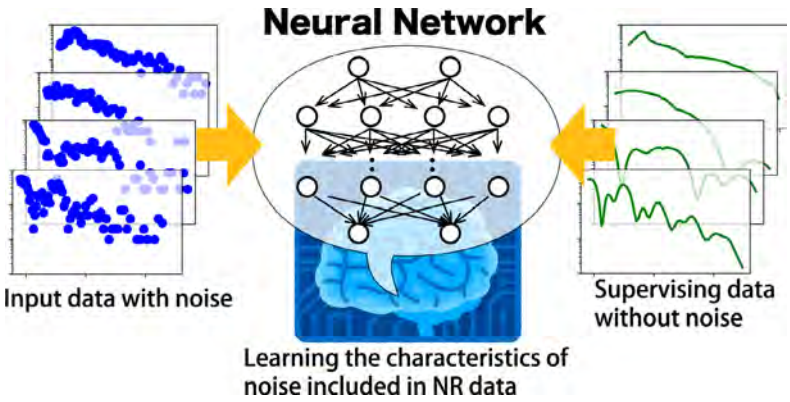

Figure 2. Schematic illustration of deep learning to remove the noise from the neutron reflectometry (NR) data. The characteristics of the noise in NR measurements is disclosed by the deep learning by a convolutional neural network using a data set of the NR data with a statistical noise and the supervising NR data without noise.

4. Other activities

As mentioned above, it had been over 14 years since the MLF operation was started. We always need to look at the future vision of the MLF to continuously step forward the facility and neutron science. In order to establish a clear vision of the MLF, we initiated "MLF2030", the series of group discussions about MLF's future plans, branched into three scientific (or instrumental) groups of fundamental instruments, elastic instruments and inelastic instruments. In addition to the scientific groups, some specific device groups of neutron polarization, detector, vacuum chamber, and choppers had independently summarized their future direction.

Australian Nuclear Science and Technology Organization (ANSTO) is one of the most significant national infrastructures for research in Australia, operating the research reactor OPAL. The MLF has arranged cooperation on research and development in neutron science with ANSTO since 2016. In 2021, the arrangement has been extended for the next five years and was expanded to include the registered institute CROSS. At the beginning of the renewal, collaborative scientific and technical series of workshops were held online, and the following topics were discussed, 1) dynamics, 2) sample environment, 3) reflectometry, 4) small angle diffraction, 5) structural analysis, 6) neutron polarization, 7) deuteration, 8) imagining technique, 9) computation, 10) industrial. All the workshops were summarized on January 13.

Also, the Workshop on "Neutron and Muon Methods for J-PARC MLF Users in Korea" was hosted by J-PARC in April. After reporting on the present status of the MLF, including neutron and muon instruments, several new ideas and aspects of science and method were presented.

A few of our yearly activities, which we had to skip in FT2020 due to the pandemic, have been re-organized as online events in FT2021. Quantum Beam Science Festa, which is a domestic conference gathering users of several facilities providing different type of quantum beams including neutron, was successfully opened online in March 2022. The 5th-Neutron and Muon School, which is an international school providing lectures by outstanding experts over the world and experimental practices, was also held as a virtual event sponsored by IINAS (Inter-Institution Network for Accelerator Science) program of KEK in December.

5. Award

Prof. Hideki Seto received the Science Prize of the Japanese Society for Neutron Science (JSNS) for the application and development of neutron scattering to soft matter research. Dr. Takashi Ohhara won the Research Award from Crystallographic Society of Japan for the structural chemical study with hydrogen atoms as a key by high precision single-crystal neutron diffraction method.

Reference

[1] H. Aoki et al., Sci. Rep., 11, 22711 (2021).

Y. Kawakita[1], T. Yokoo[1,2], and M. Nakamura[1]
[1]Neutron Science Section, Materials and Life Science Division, J-PARC Center; [2]Institute of Materials Structure Science, KEK

BL01: 4D-Space Access Neutron Spectrometer 4SEASONS

1. Use trends

4SEASONS is a direct-geometry time-of-flight neutron spectrometer for thermal neutrons, and one of the Public Beamlines in the MLF [1]. In 2021, 8 General Use (short-term) proposals, 1 CROSS Development Use proposal, and 1 Instrument Group Use proposal were approved for 4SEASONS. Due to the COVID-19 pandemic, the expiration dates of proposals in previous proposal rounds were extended and the call for proposals in the 2021A proposal round was canceled, which resulted in the decrease in the number of the approved proposals. 88% of the General Use proposals were submitted by international users. Conversely, 5 2020B reserved proposals and 3 2021B reserved proposals were given beamtime to compensate for the vacancy. Some of the users' experiments, for which the research group had difficulties visiting the MLF due to the pandemic restrictions, were carried out by the instrument group instead of the research group. 67% of the submitted proposals were in the field of magnetism, while the rest of them targeted phonons and other atomic vibrations. 9 peer-reviewed papers were published in 2021.

2. Instrument upgrade

Remote control using IROHA2: 4SEASONS uses the software IROHA2 [2] to control devices remotely via a web-based interface. In FY2021, we newly made the following devices controllable via IROHA2: the oscillating radial collimator (ORC), the top-loading GM refrigerator, and the LakeShore 336 temperature controller. In addition, we updated the IROHA2 driver for the Fermi chopper whose controller had been updated, because it was incompatible with the new controller. We also upgraded the IROHA2 from the old Python 2 based version to the new Python 3 based one.

Oscillating Radial Collimator: 4SEASONS uses the ORC to suppress scattering from sample environment devices [3]. The collimator blades are made of Cd-plated aluminum plates. Recently, however, deformation of the metallic blades and neutron scattering at the blades in the direct beam became serious problems. Then, we developed $^{10}B_4C$-painted Kapton blades. We tested 6 new blades which were installed around the direct beam path. The plastic-based $^{10}B_4C$ blades showed less deformation compared with the metallic ones. On-beam tests with the top-loading cryostat showed that the $^{10}B_4C$ blades suppressed the background more effectively at 500 meV, and Bragg peaks of Cd observed with the Cd blades at low energies (~10 meV) were disappeared. However, the $^{10}B_4C$ blades produced more intense incoherent scattering background, which was probably caused by hydrogens in the resin (Fig. 1). We are considering the use of the $^{10}B_4C$ blades at positions apart from the direct beam path.

Beam optics: Last year, we replaced a rectangular beam collimator just before the sample with a rotary optics exchanger. In FY2021, we prepared a Soller collimator whose blades are made from sintered B_4C as an exchangeable optics. We evaluated the transmission and the background of the Soller collimator with a neutron beam (Fig. 2) and found that the transmission was consistent with an analytical calculation. However, the collimator caused substantial background at high energies, though the background at low energies was reduced. Interestingly, the background at high energies appeared when the beam narrower located upstream of the Soller collimator was widely open. This result suggests that the background was caused by scattering at the incoming part of the collimator.

Detectors: 4SEASONS utilizes 2.5-m-long position

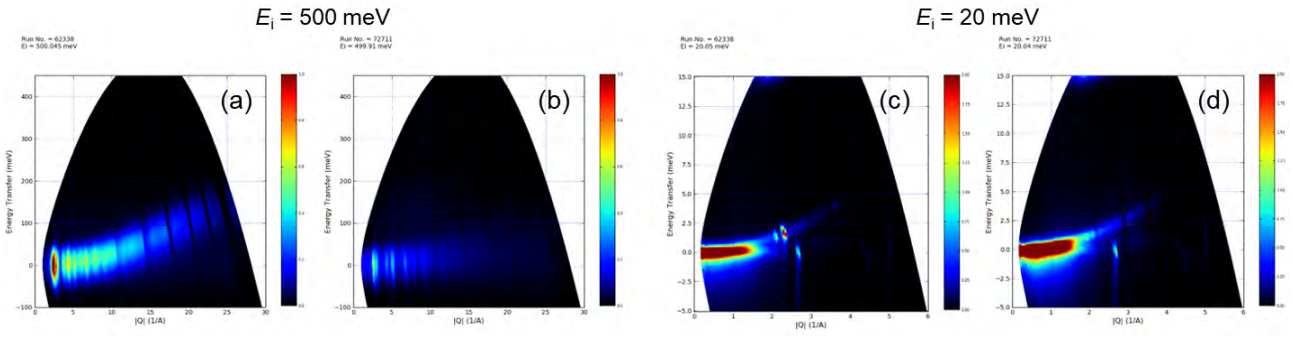

Figure 1. Color maps of powder-averaged background intensity as a function of the momentum transfer Q and the energy transfer E at E_i = 500 meV [(a) and (b)] and E_i = 20 meV [(c) and (d)] with the Cd blades [(a) and (c)] and the $^{10}B_4C$ blades [(b) and (d)].

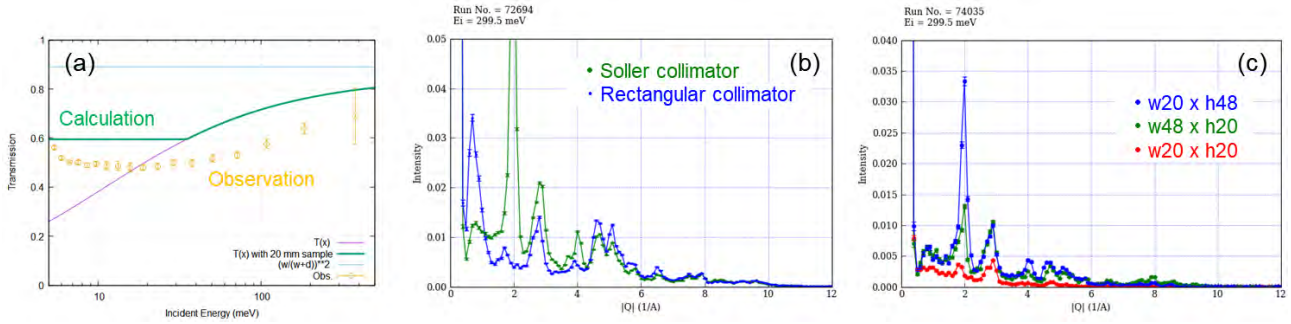

Figure 2. (a) Comparison of the calculated and observed transmission of the Soller collimator. The observed values were estimated by the scattering intensity of a Bragg peak of a Al_2O_3 polycrystal. (b) and (c) Powder-averaged intensity as a function of Q of empty measurements at E_i = 300 meV. (b) With the Soller collimator (green) and the rectangular collimator (blue). (c) With the Soller collimator when the aperture of the upstream beam narrower was 20 mm (width) × 48 mm (height) (blue), 48 mm (width) × 20 mm (height) (green), and 20 mm (width) × 20 mm (height) (red).

sensitive ^{3}He detectors to cover effectively a wide solid angle. However, this kind of detector tends to cause pile-up when it detects strong neutron counts [4]. To mitigate the problem, we consider using a new detector electronics module, called NEUNET-C [5]. This electronics module can analyze pulse width of the signal as well as pulse height, and we expect it can filter out pile-up signals. Then, we performed a preliminary test measurement by applying a prototype of NEUNET-C. The result was promising. We will carry out the test again to evaluate the effect of the filtering in more detail next year.

Utilities: The cooling water supplying ports and helium gas recovering ports of 4SEASONS are placed on the floor. This position is inconvenient for the use of sample environment devices, because the hatch for the sample environment devices is located on the shielding house and is far from the ports. To eliminate the inconvenience, in FY2021, we added a utility rack hosting ports of water and helium gas on the shielding house (Fig. 3).

Figure 3. Utility rack of cooling water and helium gas recovering lines added on the shielding house.

Acknowledgements

We thank K. Inoue and W. Kambara for their support and advice. The on-beam test of NEUNET-C was performed with the help of S. Sato. The instrumentation works described here were supported by the engineers of the Neutron Science Section and the Technology Development Section of the MLF.

References

[1] R. Kajimoto et al., J. Phys. Soc. Jpn. **80**, SB025 (2011).
[2] T. Nakatani et al., JPS Conf. Proc. **8**, 036013 (2015).
[3] M. Nakamura et al. JPS Conf. Proc. **8**, 036011 (2015).
[4] D. Raspino et al., 2015 IEEE Nuclear Science Symposium and Medical Imaging Conference, doi: 10.1109/NSSMIC.2015.7581915.
[5] S. Sato et al., EPJ Web of Conferences **231**, 05004 (2020).

R. Kajimoto[1], M. Nakamura[1], K. Kamazawa[2], Y. Inamura[1], K. Iida[2], K. Ikeuchi[2], and M. Ishikado[2]
[1]*Neutron Science Section, Materials and Life Science Division, J-PARC Center;* [2]*Neutron Science and Technology Center, CROSS*

Current Status of BL02 DNA in 2021

1. Introduction

DNA is a TOF type Si crystal analyzer backscattering spectrometer installed at the Japan Proton Accelerator Research Complex (J-PARC) spallation neutron source [1, 2]. DNA uses a pulse-shaping chopper to extract sharp pulsed neutrons from a strong but broad spectrum of the coupled moderator, which achieves μeV-order energy resolution in wide energy transfers of meV-order. Furthermore, the signal-to-noise ratio at DNA reaches ~10^5, which makes it possible to cover a variety of research fields with small scattering amplitudes or with small quantities of samples (of the order of milligrams).

The number of peer-reviewed papers from DNA in 2021 was 18, including 8 proceedings papers, which is double the average since 2017. BL02 was also used for one master thesis in 2021. In addition, Mr. Yuki Hirota, doctoral student from Setsunan University stayed at MLF as a fellow of advanced science for 3 months to analyze DNA data.

2. User Program in the periods 2020A and 2020B–2021A

In 2021, 33 (2020B–2021A) and 24 (2022A) General Proposals (GP) were submitted to BL02. 13 GP, and 5 GPs including 2 New User Promotions (NUP) were approved for 2020B–2021A and 2021B, respectively. The portion of approved beamtime from all requested beamtime was 38% for 2020B–2021A and 20% for 2021B. The competition rate was high: 2.75 and 4.8 for 2020B–2021A and 2021B, respectively. Additionally, 2 and 5 reserved proposals were also conducted in 2021A and 2021B, respectively.

Due to the pandemic situation, two experiments were conducted by BL02 staff without users. But two foreign groups could come to MLF for experiments with the relaxation of border restrictions. In addition, four General Proposal (Long Term) (hereafter LTP) Program, proposals ran at BL02 in 2021.

3. Beamline activities

Additional Si311 analyzer mirrors were installed at scattering angle (2θ) of $-150° < 2\theta < -126°$. Now, Si311 analyzers cover momentum transfer from 1.79 to 3.70 $Å^{-1}$. We also replaced the damaged Si111 analyzer mirrors at scattering angle (2θ) of $6° < 2\theta < 30°$.

At BL02, the superconducting magnet prepared in the MLF as the common-use equipment could not be used due to its radius (800 mm-ϕ) that was larger than our access-port flange (420 mm-ϕ). However, the DNA spectrometer potentially enables us to investigate a magnetic excitation with a small (~μeV) gap, that small gap and its magnetic field dependence are often essential for characterizing the quantum magnetic systems. To apply a magnetic field to samples, we have introduced a new superconducting magnet suitable for BL02 (Fig. 1). The new magnet is designed as follows: (1) The maximum magnetic field is 3.5 T, (2) The temperature range is 300 ~ 1.5 K, which comes down to 100 mK with the dilution refrigerator option, (3) The coils of the magnet are coated by B_4C tiles to reduce the background. Taking into account that the magnetic field of 1 T produces a change in energy about 60 μeV for $S = 1/2$ spin, the max field of 3.5 T will be enough to investigate the magnetic field dependence of such a μeV-order gap at DNA. Now, we are proceeding with the commissioning of this magnet, and plan to make it available with user experiments next year.

At BL02, aqueous solutions are often measured in pure Al and alloyed Al sample cells. Focusing on the interaction between the container and the aqueous solution, the corrosion susceptibility of Al and its alloys was investigated using various treatments and compared to other candidate materials with lower chemical reactivity [3]. QENS measurements of empty sample cells fabricated with these materials were also performed to evaluate their contribution to the QENS profile. This is expected to reduce the possibility that chemical interactions between the Al surface and the sample, promoted

Figure 1. Photographs of the superconducting magnet suitable for BL02. (a) whole view, (b) coils of magnet covered by B_4C tiles.

by corrosive materials or specific pH conditions, could compromise the integrity of the cell and interfere with QENS experiments.

As denoted in the introduction, BL02 are used in a variety of scientific fields, which requires various sample environments (SE's) including cryostat, furnace, magnet, vapor-control system, etc. To reduce background from various SE, we have developed oscillating radial collimators. Figure 2 shows the background with and without radial collimator for a 2K cryostat. The split elastic line at $E \sim \pm AQ^2$ is scattering from the wall of SE, which is eliminated with a radial collimator. We have two radial collimators with different blade lengths, 56 and 76 mm, which reduce background at $r > 47$ mm and 30 mm, respectively.

As the neutron source becomes more intense, the measurement time per sample becomes shorter and there is a high demand for automation of measurements. We are developing RABBIT, a rotating automatic sample changer that can install 20 samples. This will enable the effective measurement of a large number of samples and facilitate QENS experimental planning based on new ideas.

We have been working on the problem of N_2 beam monitor's aging for several years. By checking the pulse-height spectrum, we found that the peak shifted to the lower channel side, especially after radiation to strong neutron beam, suggesting decomposition of the converter gas. We plan to replace the converter gas CF_4 with another gas. In addition, in 2020, we found that the TOF spectrum was shifted when the beam monitor was measured at the sample position. To study these shifts in detail, we have developed new monitors to be used at the sample position. We successfully obtained the TOF spectrum with new monitors under various conditions. We are currently developing software that would allow these new monitors to be incorporated into DNA's data reduction.

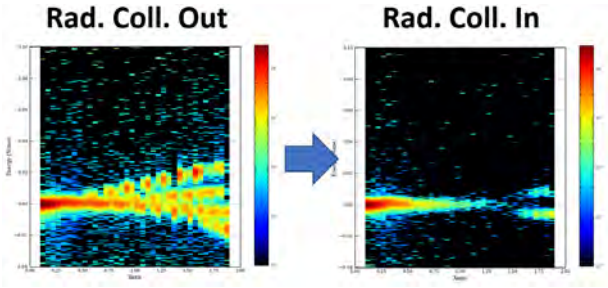

Figure 2. Background from the cryostat with and without radial collimator (Rad. Col.) on Q (horizontal)-E (vertical) map.

As for the software development, 4D mapping of $S(Q, \omega)$ by rotating a single crystal sample was performed for the first time at BL02 in 2020. We have modified the 4D $S(Q, \omega)$ visualization software D4mat so that it can be used with BL02. In addition, we tested kernel density estimation methods to improve the accuracy of the QENS fitting with MLF's Computational team. Although it still takes time, the kernel density estimation method still improves the error bar by half for preliminarily fits.

4. Other activities

To accommodate the increasing number of SE equipment, the floor around the BL02 hatch has been expanded.

5. Future plans

We will proceed with the further replacement of damaged Si111 analyzer mirrors. We will also replace the focusing mirror with one with higher reflectivity, which is expected to enhance the neutron beam flux by ~20%. At the same time, the jacket of the focusing mirror will be changed to a non-magnetic one, which is necessary for the use of the BL02 magnet.

References

[1] Kaoru SHIBATA et al., JPS Conference Proceedings, **8** (2015) 036022.
[2] Y. Kawakita et al., EPJ Web of Conferences **272** (2022) 02002.
[3] T. Tominaga et al., J. Appl. Cryst. **54** (2021) 1631.

Y. Kawakita[1], M. Matsuura[2], T. Yamada[2], T. Tominaga[2], H. Tamatsukuri[1], and H. Nakagawa[1,3]
[1]Neutron Science Section, Materials and Life Science Division, J-PARC Center; [2]Neutron Science and Technology Center, CROSS; [3]Materials Sciences Research Center, JAEA

IBARAKI Biological Crystal Diffractometer iBIX

1. Introduction

Neutron single-crystal diffraction is a powerful method for obtaining structural information, especially for light atoms. Because understanding the enzyme chemistry of proteins at the atomic level requires the visualization of hydrogen atoms at active sites and remote residues, cofactors, substrates, and water molecules, it is particularly important to obtain precise information on the positions of the hydrogen atoms in biological macromolecules. The complementary use of neutron diffraction data, which includes more information on hydrogen atoms, and X-ray diffraction data, which includes more information on non-hydrogen atoms (such as C, O, N, and S etc.), allows us to obtain structural information on all atoms in the protein. The IBARAKI biological crystal diffractometer, iBIX, is a high-performance TOF neutron single-crystal diffractometer [1, 2]. It is designed to elucidate the hydrogen atoms, protonation states, and hydration structures of biological macromolecules. In 2019, the iBIX diffractometer, equipped with 34 detectors, was available for user experiments on organic compound, biological macromolecules, and polymer samples, supported by the Frontier Research Center of Applied Atomic Sciences, Ibaraki University. The specifications of iBIX are shown in Table 1.

Table 1. Specifications of iBIX

Moderator	Coupled
Range of wavelength of incident neutron (Å)	0.7 ~ 4.0 (1st frame) 4.0 ~ 8.0 (2nd frame)
Neutron intensity (n/s/mm^2) (@1 MW)	0.7×10^6
L_1 (m)	40
L_2 (mm)	491
Solid angle of detectors (% for 4π str)	22.0
Detector covered region (deg.)	15.5 ~168.5
Detector size (mm^2)	133 × 133
Detectors pixel size (mm^2)	0.52 × 0.52
No. of detectors	34
Sample environment	Gas flow type cooling system by N_2 gas (~100 K)
	Heating system for polymer sample (~600 K)
	Tensile loading system for polymer sample (~200 N, ~90 mm, 1~1000 mm/sec)

2. Current status

In 2021, J-PARC was operated regularly at an accelerator power of 700 kW. We were able to collect a full data set of biological macromolecules for neutron structure analysis with around 2.0 Å resolution in less than one week by using the iBIX at the accelerator power of 700 kW. The maximum unit cell size was 135×135×135 Å^3. The typical crystal volume of the sample measured by the iBIX was around 1.0 mm^3.

4 test measurements for a J-PARC proposal (2021A: 1, 2021B: 3), 11 test measurements for a proposal of an innovative research project of the Ibaraki Neutron Beamline (2021A: 6, 2021B: 4) and 6 test measurements for a proposal of a leading research project of the Ibaraki Neutron Beamline (2021A: 3, 2021B: 3) were performed using the iBIX. And then, 6 proposals were moving on to the full data collection for neutron structure analysis.

3. Maintenance and development

Temperature control of the experimental hatch is important to constantly maintain detector sensitivity because the photomultiplier tube of our scintillator detectors is very sensitive to temperature change. The temperature control system with a water-cooled type air-conditioning package was installed in our experimental hatch as shown in Fig. 1. The total operation time of the water-cooled type air-conditioning package has already exceeded the service life. We replaced the water-cooled type air-conditioning package in FY2021.

Temperature change inside the experimental hatch was recorded for several days after the replacement of the air-conditioning package. From this result, we confirmed that it met the required performance specifics. The temperature control system is already available for user experiments. Several parts of the detectors also need replacement due to age deterioration. In FY2021, we replaced the encoder modules and read out modules of some detectors. The data reduction software "STARGazer" has also been updated continuously in order to become more user friendly.

4. Future plans

It has been over 10 years since the iBIX instrument was installed on the beamline, so some of the beamline instruments have been already replaced in the last few years due to age deterioration. One of the remaining instruments for replacement is the disk-chopper. The cumulative time of servomotor rotation has exceeded the service life. Next

year, we will replace the servomotor and the servo amplifier of the disk chopper. In order to enable remote access for the measurement, the measurement software of iBIX should be updated based on the standard instrument control software framework of the MLF, IROHA2.

In the near future, the accelerator power of J-PARC will increase to about 1 MW. iBIX should be available regularly for full data-set measurement of samples with a volume of less than 1 mm^3. However, the sample size is still large, and the measurement time is still long, especially for the users. We would like to reduce the difficulties of preparation of large crystal as much as possible. In other words, it is necessary to further improve the measurement efficiency of iBIX by developing the beamline instrument. We have started to consider the possibilities for improvement of the measurement efficiency. For example, installation of additional detectors, increase of beam divergence by insertion of a super mirror, changing the distance between the sample and detector surface, improvement of the chopper instrument, development of a high efficiency measurement method and so on. We will continue to develop both the software and the beamline instruments to improve the measurement efficiency and the accuracy of intensity data obtained from smaller protein samples in order to ensure that we have one of the highest performance single crystal neutron diffractometers for biomacromolecules in the world.

References

[1] I. Tanaka, K. Kusaka, T. Hosoya, N. Niimura, T. Ohhara, K. Kurihara, T. Yamada, Y. Ohnishi, K. Tomoyori and T. Yokoyama, Acta Cryst., D66 1194 (2010).

[2] K. Kusaka, T. Hosoya, T. Yamada, K. Tomoyori, T. Ohhara, M. Katagiri, K. Kurihara, I. Tanaka and N. Niimura, J. Synchrotron Rad., 20 994 (2013).

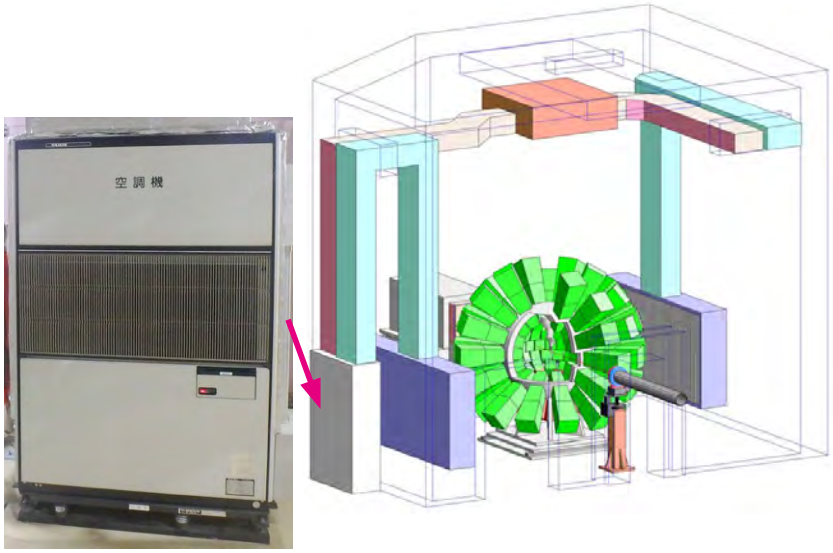

Figure 1. The temperature control system with the water-cooled type air-conditioning package.

K. Kusaka, T. Yamada, N. Yano, T. Hosoya, and I. Tanaka
Frontier Research Center for Applied Atomic Sciences, Ibaraki University

Development of a $LaBr_3$(Ce) Scintillator System for Detecting Prompt Gamma Rays at ANNRI

1. Introduction

Prompt gamma rays emitted from the neutron capture reactions can be used for the determination of elements contained in interesting samples and reaction rates of nuclei for the broad purpose of research in several scientific fields, such as geology, archaeology, earth science, industry, environmental science, astrophysics, and nuclear data [1-4]. Therefore, the intensive work to develop techniques for detecting gamma rays in higher counting rate and higher efficiency has continued for decades. However, background gamma rays (noise) emitting from the impurities contained in samples sometimes impede the quantification of gamma rays emitting from interesting elements (signals). Here, a lanthanum bromide ($LaBr_3$(Ce)) crystal is well known to have the features of high-energy resolution and light output within a short decay time. Thus, we have been developing a new gamma-ray spectrometer system using the $LaBr_3$(Ce) at the Accurate Neutron Nucleus Reaction Measurement Instrument (ANNRI) of the Materials and Life Science Experimental Facility at Japan Proton Accelerator Research Complex (J-PARC) [5, 6] to meet the expanding demands from the scientific fields for quantification of the gamma rays with better signal-to-noise ratio.

2. Set up and experiments

Figure 1 shows the photograph of the $LaBr_3$(Ce) scintillator system and a neutron beam duct made of carbon fiber. Inside this beam duct, air can be evacuated or purged by He-gas to prevent neutron scattering events. The samples are set inside the beam duct utilizing the sample holder made by Teflon. The $LaBr_3$(Ce) crystal size is 89 mm and 101.8 mm in thickness, which is covered by the shields to prevent the background gamma rays and neutrons B-doped polyethylene, Pb and LiF-doped polyethylene.

In 2021 and 2022, an experiment was performed to test the performance of the $LaBr_3$(Ce) scintillator system. The proton beam power was approximately 730 kW. All our samples had a shape of a pellet wrapped with a fluorinated ethylene propylene (FEP) film which is neutron-insensitive. A ^{204}Pb metal of 87% purity and 1.84 g in weight was used as a sample. In addition, ^{197}Au, C, and B samples were measured for energy calibration, estimation of the neutron scattering influence, and estimation of the incident neutrons.

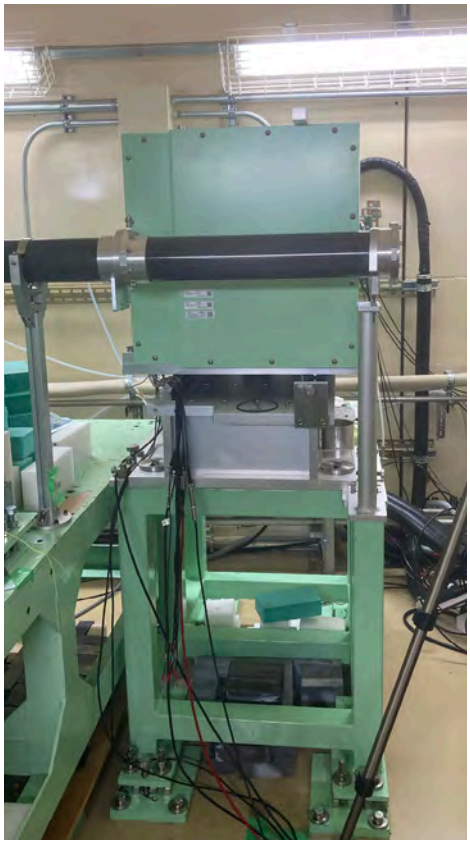

Figure 1. $LaBr_3$(Ce) scintillator system installed at ANNRI.

3. Results

Figure 2 shows the gamma-ray energy spectra for the ^{204}Pb sample obtained by the $LaBr_3$ scintillator system indicated by the red line and the energy spectrum obtained by the NaI(Tl) detector equipped at ANNRI for comparison (indicated by the black line) [7]. After calibrating the gamma-ray energies with ^{60}Co and the intrinsic ratio activity of the $LaBr_3$(Ce) scintillator, several gamma-ray peaks of ^{204}Pb were observed which the NaI(Tl) detector could not resolve.

4. Conclusion

We have tested the performance of the developing $LaBr_3$(Ce) scintillator system at ANNRI in J-PARC/MLF using an intense pulsed neutron beam. The result shows that the $LaBr_3$(Ce) scintillator system has a higher energy resolution using ^{204}Pb compared with that of the NaI(Tl) scintillator system at the ANNRI. The hereafter obtained data of the Carbon, ^{204}Pb, and blank samples will be used for data corrections as follows: the scattering

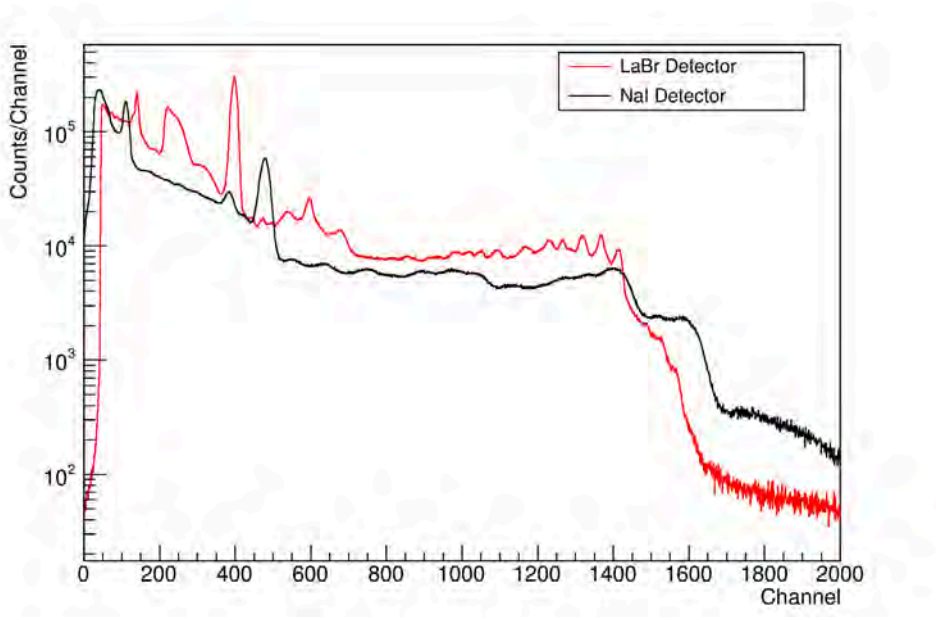

Figure 2. Pulse height spectra obtained with the $LaBr_3(Ce)$ (red line) and NaI scintillator (black line) systems.

component and the self-shielding effect in the samples. This analysis is now in progress.

This work was supported in part by Grants-in-Aid for Scientific Research (JP).

References

[1] Y. Toh, Y. Murakami, K. Furutaka, A. Kimura, M. Koizumi, K. Hara, T. Kin, S. Nakamura, H. Harada, Appl. Radiat. Isot., **70** 984 (2012).

[2] H. Harada, S. Goko, A. Kimura, M. Ohta, M. Oshima, F. Kitatani, Y. Toh, K. Furutaka, T. Kin, M. Koizumi, S. Nakamura, M. Igashira, T. Katabuchi, M. Mzumoto, T. Ohsaki, J. Hori, T. Fujii, K. Takamiya, J. Goto, Y. Kiyanagi, K. Kino, M. Furusaka, F. Hiraga, Y. Kamiyama, J. Korean Phys. Soc., **59** 1547 (2011).

[3] K. Kino, M. Furusaka, F. Hiraga, T. Kamiyama, Y. Kiyanagi, K. Furutaka, S. Goko, H. Harada, M. Harada, T. Kai, A. Kimura, T. Kin, F. Kitatani, M. Koizumi, F. Maekawa, S. Meigo, S. Nakamura, M. Ooi, M. Ohta, M. Oshima, Y. Toh, M. Igashira, T. Katabuchi, M. Mizumoto, Nucl. Instrum. Methods Phys. Res. A, **626** 58 (2011).

[4] Y. Toh, M, Ebihara, A. Kimura, S. Nakamura, H. Harada, K. Y. Hara, M. Koizumi, F. Kitatani, K.; Furutaka, Anal. Chem., **86** 12030 (2014).

[5] Y. Ikeda, Nucl. Instrum. Methods Phys. A, **600** 1 (2009).

[6] F. Maekawa, M. Harada, K. Oikawa, M. Teshigawara, T. Kai,T S. Meigo, M. Ooi, S. Sakamoto, H. Takeda, M. Futakawa, T. Kato, Y. Ikeda, N. Watanabe, T. Kamiyama, S. Torii, R. Kajimoto, M. Nakamura, Nucl. Instrum. Methods Phys. Res. A, **620** 159 (2010).

[7] M. Igashira, Y. Kiyanagi, M. Oshima, Nucl. Instrum. Methods Phys. Res. A, **600** 332 (2009).

M. Segawa, M. Maeda, Y. Toh, S. Endo, S. Nakamura, and A. Kimura
Nuclear Science and Engineering Center, JAEA

Status of Fundamental Physics Beamline BL05 (NOP) in 2021

1. Introduction

"Neutron Optics and Physics (NOP/ BL05)" at the MLF in J-PARC is a beamline for studies in the field of fundamental physics. The beamline is divided at the upstream into three branches, the so-called Polarized, Unpolarized, and Low-Divergence branches, used in different experiments in a parallel way [1, 2].

A neutron lifetime measurement is conducted at the Polarized beam branch with a spin flip chopper. Pulsed ultra-cold neutrons (UCNs) by a Doppler shifter are available at the Unpolarized beam branch. At the Low-Divergence beam branch, the search for an unknown intermediate force is performed by measuring neutron scattering with nano particles. The beamline is used also for R&D of optical elements and detectors.

2. Measurement of the neutron lifetime

The decay of neutrons is closely related to the mechanism of the synthesis of elements in the universe and to particle physics. The neutron lifetime has been measured in two ways: 1) by counting the incident neutrons and the protons from neutron beta decay (beam method) and 2) by storing UCNs in a container and determining the neutron lifetime according to the disappearing time (storage method). Currently, the lifetime determined via the former method is 888.0 ± 2.0 s, and that for the latter is 878.4 ± 0.5 s, with a difference of 9.5 s (4.6 σ) [3]. This discrepancy is called "neutron lifetime puzzle" and has remained unsolved for nearly 20 years. The smaller decays compared with the disappearance suggest that neutrons are lost owing to decay into dark matter or collisions with dark matter. In general, different methods are needed to validate the experimental results, as utilizing the same experimental methods may lead to the same mistakes. Using the polarization beam branch at NOP/BL05, an experiment was conducted via a different method, in which instead of protons, electrons were measured from the neutron beta decays. The first lifetime result was published in 2020 as $898 \pm 10\ (stat.)^{+15}_{-18}(syst.)$ s, which is consistent with both the beam and bottle methods [4]. Upgrade of the experiment is under way. In 2020, a spin-flip chopper (SFC), which shapes neutron beam into bunches, was replaced with a larger one (Fig.1). The intensity was increased by 3.2 times [5]. Commissioning began in 2021, and physics run for the neutron lifetime began after the SFC was tuned. So far, a statistical uncertainty achieved at 3 s, and another 100 days of beamtime brings it to 1 s. The largest source of systematic uncertainty is undefined background. Research is underway to resolve this background event.

3. Development of a neutron detector with highest spatial resolution with nuclear emulsion

Nuclear emulsion plates are used as detectors that can achieve high positional resolution in the fields of nuclear and particle physics. N. Naganawa of Nagoya University and colleagues developed an emulsion detector for neutrons that can achieve a positional resolution of <100 nm [6]. The emulsion detector consists of ^{10}B sputtered on a silicon substrate and coated with a fine-grained nuclear emulsion. After the development of the exposed detector, tracks from ^{10}B layer observed via an optical microscope could be reconstructed, and the starting points from the ^{10}B layer (reaction points) were obtained with higher resolutions (minimum of 10 nm).

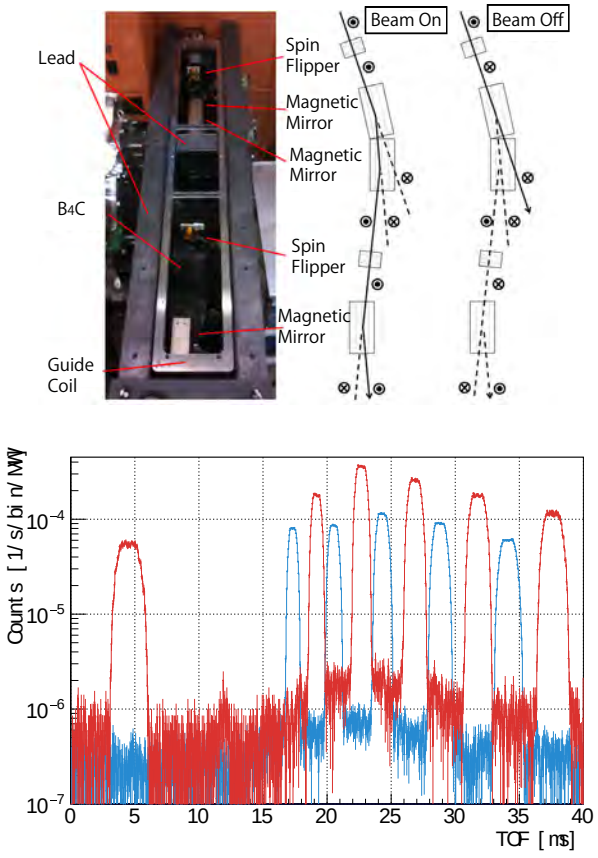

Figure 1. (Top) setup of the new SFC. (bottom) TOF spectra of neutron bunches, the blue and red lines indicate the old and new SFC, respectively [5].

This detector was developed to measure the quantized state of neutrons due to gravity and can also be applied to submicron neutron imaging. This detector was developed to measure the quantized state of neutrons due to gravity. By using gadolinium grating, we proved that inclusive spatial resolution of $0.56 \pm 0.8\ \mu m$ (Fig. 2) [7]. In a test of emulsion-based imaging, we successfully imaged a quartz crystal at J-PARC and captured a clear image of 30 μm gold wires in it [8].

4. Multilayer-type neutron interferometer

A neutron interferometer is a device that splits the wavefunction of a single neutron into two paths, superimposes them, and detects the potential difference between the two paths as a phase difference. It was put into practical use in the 1970s and it has contributed significantly to the development of quantum mechanics, e.g., the verification of spinors and the phase shift of matter waves due to gravity. Thus far, neutron interferometers have been cut out of silicon ingots, which could only use mono-energetic neutrons and were limited in size.

A multilayer-type neutron interferometer is expected to be a new device to overcome these limitations, and improve the sensitivity by using neutrons with longer wavelength and/or making the flight path longer. Especially with the time-of-flight (TOF) method, the time-dependent systematic uncertainty can be suppressed since the interference fringes are observed on the TOF spectrum.

We have demonstrated it with pulsed neutron at the low-divergence branch. The geometrical optics of the Jamin interferometer was constructed using a "beam splitting etalon" [5, 6], which is a high-precision

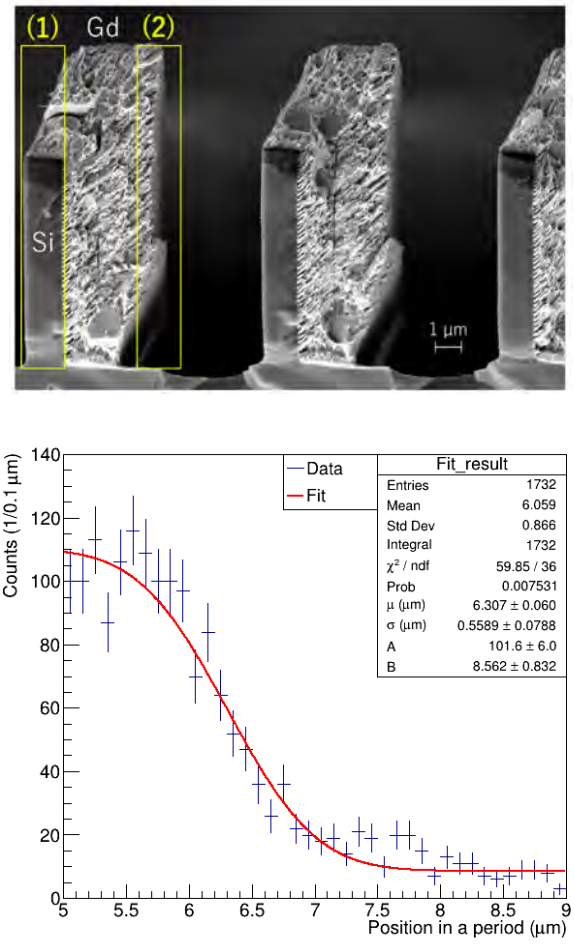

Figure 2. (Top) electron micrograph showing a cross section of a Gd grating that was manufactured by the same process as that used in this experiment. (Bottom) fit result of the distribution of neutrons around the Gd grating edge. The blue histogram data is an excerpt of the data. The red line shows the result of the least squares fit of error function to the data.

assembly of multilayer neutron mirrors on a quartz substrate. The anti-correlated moderations between the forward (O) beam and the deviated (H) beam on the TOF were clearly observed (top of Fig. 3) [11]. In case a path was covered by Cd beam stopper, the oscillation disappeared.

The beam width is 100 μm while the beam paths are 300 μm apart, so they are completely separated. When a material is placed in one path, the phase changes due to the refractive index of the material. Thus, we inserted a 300 μm thick Si into a beam path and observed phase shift of the interference fringes (bottom of Fig. 3). This can be applied to precise measurement of the scattering length of the nuclei.

References

[1] K. Mishima et al., Nucl. Instruments Methods Phys. Res. Sect. A, vol. 600, no. 1 (2009)342–345.
[2] K. Mishima, Hamon Neutron Netw. news,vol. 25, no. 2 (2015) 156–160.
[3] R.L. Workman et al., (Particle Data Group 2022), Prog. Theor. Exp. Phys. 2022, 083C01 (2022).
[4] K. Hirota et al., Prog. Theor. Exp. Phys. (2020) 123C02.
[5] G. Ichikawa et al., Proceedings of science, PoS (PANIC2021) 457.
[6] N. Naganawa et al., Eur. Phys. J. C 78, 11 (2018) 959.
[7] N. Muto et al., J. Instrum, 17 (2022) P07014.
[8] K. Hirota et al., J. Imaging 7 (2021) 4.
[9] M. Kitaguchi, et al., Phys, Rev. A 67, 033609 (2003).
[10] Y. Seki, et al., J. Phys. Soc. Jpn. 79, 124201 (2010).
[11] T. Fujiie et al., Annual Meeting of the Japanese Society of Neutron Science 2021, online.

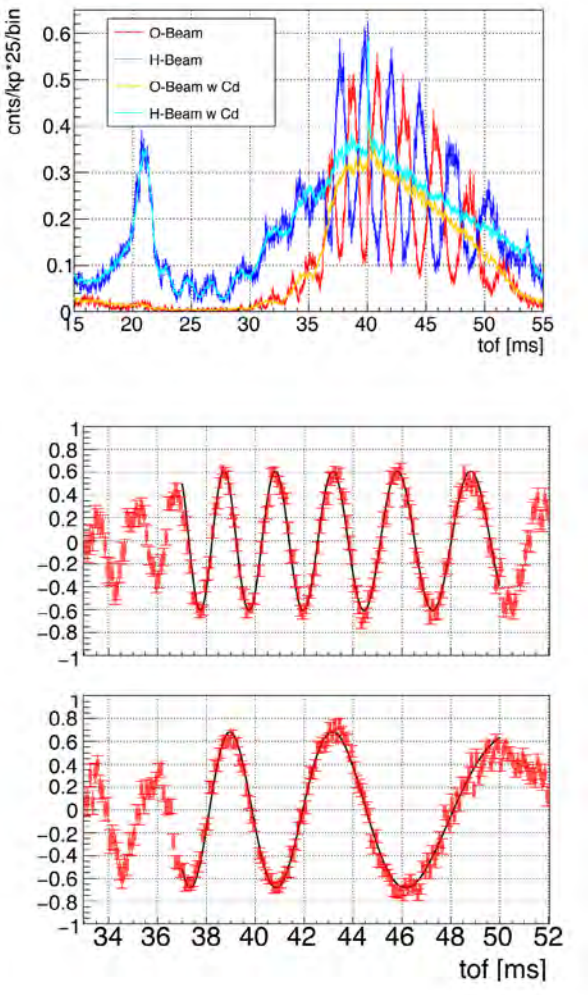

Figure 3. (Top) TOF spectra of the H beam (red) and the O beam (blue). The orange and cyan lines show them when the other path is covered. (Bottom) The interferometer fringes with a 300 μm thick Si in a path, and without.

K. Mishima[1,2] on behalf of NOP collaboration

[1]*Neutron Science Section, Materials and Life Science Division, J-PARC Center;* [2]*Institute of Materials Structure Science, KEK*

BL06: Commissioning Status of Village of Neutron Resonance Spin Echo Spectrometers (VIN ROSE)

1. Introduction

BL06 consists of two types of resonance neutron spin echo (NSE) spectrometers, which are a modulated intensity by zero effort (MIEZE) instrument and a neutron resonance spin echo (NRSE) instrument, which are under construction in collaboration between Kyoto University and The High Energy Accelerator Research Organization (KEK) since 2011.

NSE is a variety of inelastic and quasi-elastic neutron scattering methods with fine energy resolution [1]. Because the energy resolution of the energy transfer measurement is not limited by the energy spectrum of the incoming neutrons in the NSE technique, a moderately (10–15% FWHM) monochromatic neutron beam can be acceptable. In addition, the intermediate scattering function can be directly derived by NSE, so that the method is suitable for investigating slow relaxation dynamics in condensed matter, and high-intensity and high-energy-resolution NSE spectrometers have been developed [2].

By using neutron resonance spin flippers (RSFs), which enable us to replace large magnetic precession fields with low guide fields, downsizing and adjacence of the two spectrometers has become possible [3].

In this report, the status of the MIEZE and NRSE spectrometers at BL06 in FY2021 is summarized.

2. Commissioning status at BL06 in FY2021

The user program has started partially with the MIEZE spectrometer since the 2017B proposal round. At the NRSE spectrometer, used for fine-energy resolution, devices, such as two-dimensional ellipsoidal neutron-focusing mirrors [4], are still under commissioning.

The main scientific highlights of BL06 achieved in FY2021 are (i) investigations of MIEZE signals from a thin monolayer with specular reflection and (ii) studies of ellipsoidal focusing mirrors for the NRSE spectrometers, which are described in the following sections in detail.

3. Investigations of MIEZE signals from a thin monolayer with specular reflection

In this study, the MIEZE method is applied to observe dynamics at the surface and the interface in a thin monolayer. It had been thought that it would be very difficult to separate inelastic or quasielastic neutron scattering components from specular reflection due to the limitation of the scattering cross-section area in the reflection geometry. At MLF J-PARC, the pulsed neutron beam is generated by accelerated short-pulse protons, so that the wavelengths of the neutrons can be determined with very narrow wavelength distribution via the time-of-flight (TOF) method. Moreover, the angular distribution of the MIEZE spectrometer is significantly better than in the conventional neutron spin echo spectrometers. In Fig. 1, the observed normalized intermediate scattering function, S_{qt}, from specular reflection of a carbon monolayer on a silicon substrate is shown. In the experiment, the neutron incident angle is fixed, and the wavelength is decoded by the TOF method. As a result, S_{qt} is evaluated with different Q and different t, since $Q \propto 1/\lambda$ and $t \propto \lambda^3$ in this case. Clear reductions of S_{qt} can be observed, which suggests excitation modes rather than diffusion modes. Similar phenomena have been reported with helium atom scattering, however, the findings have not been verified by neutron scattering. We will explore these phenomena further by making use of flexible sample environments with neutrons.

4. Studies of ellipsoidal focusing mirrors for the NRSE spectrometers

This ellipsoidal neutron-focusing supermirror is essential for high-resolution NRSE spectrometers, which can correct the optical path difference. We have developed and tested 900 mm long ellipsoidal focusing $m = 5$ supermirrors with 2.5 m focal length. In FY2021, the mirrors were tested at the NRSE beam line with the MIEZE condition to investigate the possibility of focusing TOF-MIEZE method. We successfully identified time-of-flight MIEZE (TOF-MIEZE) signals for neutrons elastically scattered at the sample under a focused geometry using the supermirrors. The effective frequency of the TOF-MIEZE signal was 108 kHz. The Fourier time range was covered from 0.48 to 5.3 ns using the TOF method with neutron wavelengths from 0.65 to 1.45 nm. The result has been summarized in ref. [5].

5. Summary

In this report, the activities of BL06 VIN ROSE in FY2021 were summarized. The two achievements were introduced, i.e., the investigations of MIEZE signals from a thin monolayer with specular reflection, which is currently only possible with J-PARC, and studies of ellipsoi-

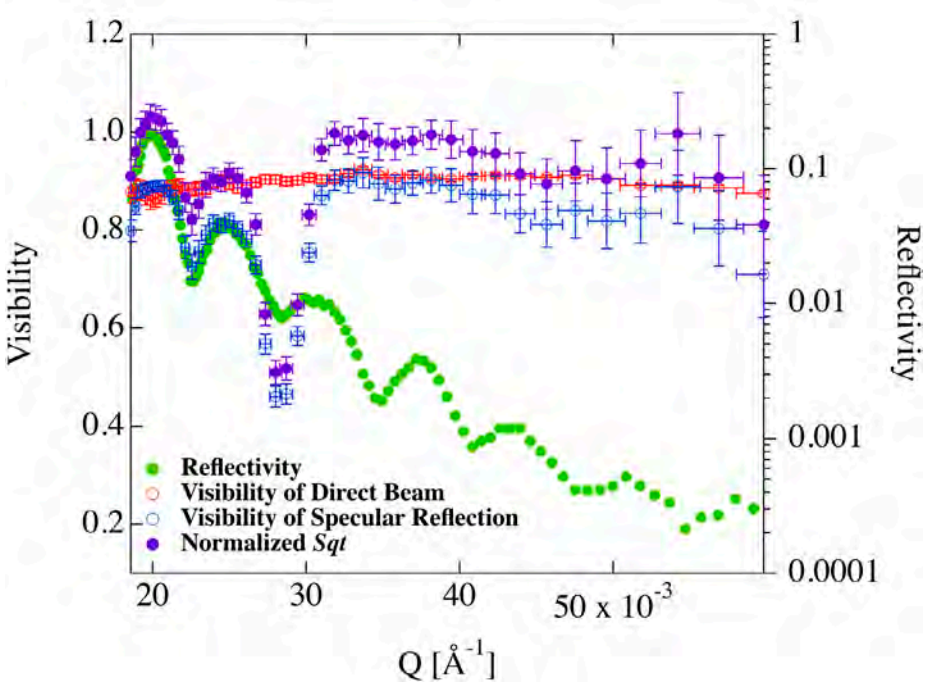

Figure 1. Tentative results of the normalized intermediate scattering function and related data obtained by 100 kHz MIEZE signals from neutron specular reflection in a carbon monolayer on a silicon substrate. The left-hand ordinate represents the visibility of the MIEZE signals, and the right-hand ordinate displays reflectivity.

dal focusing mirrors for the NRSE spectrometers, which is a necessary step to advance the development of the NRSE spectrometer.

References

[1] F. Mezei ed., Neutron Spin Echo, Lecture Notes in Physics, (Springer, Berlin) **128**, (1982).
[2] B. Farago et al., *Neutron News* **26**, (2015) 15.
[3] M. Hino et al., *Physics Procedia* **136-141**, (2013) 136.
[4] T. Hosobata, M. Hino, H. Yoshinaga, T. Kawai, H. Endo, Y. Yamagata, N. L. Yamada, S. Takeda, *JPS Conf. Proc.* **22**, (2018) 011010.
[5] F. Funama et al., *JPS Conf. Proc.* **33**, (2021) 011088.

H. Endo[1,2], M. Hino[3], T. Oda[4], N. L. Yamada[5], H. Seto[1,2], and Y. Kawabata[3]
[1]Neutron Science Division, Institute of Materials Structure Science, KEK; [2]Neutron Science Section, Materials and Life Science Division, J-PARC Center; [3]Institute for Integrated Radiation and Nuclear Science, Kyoto University; [4]The Institute for Solid State Physics, The University of Tokyo; [5]Center for Integrative Quantum Beam Science, Institute of Materials Structure Science, KEK

BL08: Verification of Sample Temperatures Using a High-Temperature Sample Stick for Cryofurnace

1. Introduction

In FY2021, the cryofurnace was installed in BL08 Super High Resolution Powder Diffractometer, SuperHRPD [1, 2]. The commissioning test was reported in the MLF Annual Report 2020 [3]. This cryofurnace can be used with a low-temperature sample stick for measurements in the 4 K–300 K range and a high-temperature sample stick for the 300 K–800 K range. In measurements below 300 K, the introduction of exchange gas into the sample chamber controls its atmosphere, so that sample temperature irregularities are not a cause for concern. The high-temperature sample stick has double radiation shielding around the sample. The exchange gas in the sample chamber must be evacuated to create a vacuum, partly to protect the cold head, and the sample temperature is controlled by a heater attached to the top of the sample holder. However, since temperature is controlled by heat conduction through the sample holder, the temperature irregularities are an issue due to the vertical length of the sample holder. Therefore, the sample temperature was verified using the structural phase transition of barium titanate, $BaTiO_3$.

2. Temperature verification experiment

As a powder sample, $BaTiO_3$ manufactured by Sigma-Aldrich Co. LLC with a particle size < 2.0 μm and a purity of 99.5% was used, and the sample holder was a standard 6 mm diameter vanadium-nickel alloy holder. Neutron powder diffraction measurements were performed in the temperature range of 273 K–285 K and 388 K–403 K to take advantage of the structural phase transition of $BaTiO_3$ above room temperature (Fig. 1 [4]). Temperature changes were performed by an increase path, and the sample space was under vacuum condition with a high-temperature sample stick. The accelerator power at the time of measurement was approximately 700 kW, and sufficient statistical data to compare peak profiles could be obtained in 30 minutes per measurement.

3. Discussion

The temperature dependence of the diffraction peaks around 280 K and 400 K are plotted in Fig. 2. (a) and (b) show a marked change in peak shape indicating a structural phase transition around 280 K. This is considered to indicate the phase transition from the orthorhombic phase to the tetragonal phase shown in Fig. 1. Similarly, in (c) and (d), a change in the peak shape indicating a phase transition to the cubic phase is seen around 400 K. The transition temperatures evaluated from the dielectric constants were ~280 K and ~400 K, respectively, it can be assumed that the sample temperature approximately reflects the temperature of the stick sensor.

Although the statistics were somewhat insufficient, a crystal structure refinement by Rietveld analysis was performed. The software Z-Rietveld (Ver. 1.1.11) [5, 6] was used for the analysis. The analytical profile near the transition temperature is shown in Fig. 3. At 285.6 K, the analysis with the coexistence of two phases, orthorhombic and tetragonal, showed good profile agreement. The analysis was also performed around 400 K, and a trend of coexistence of tetragonal and cubic crystals was

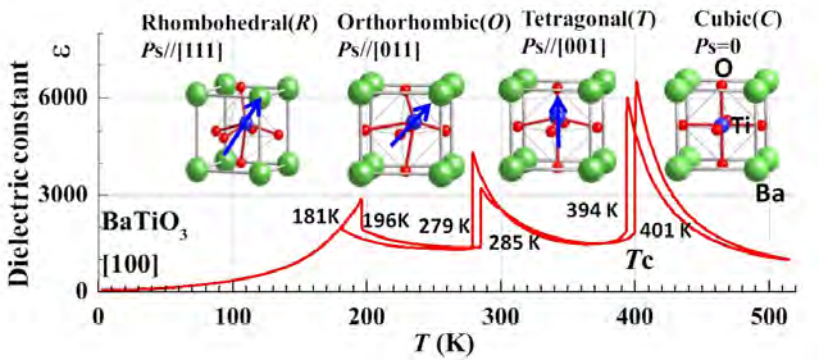

Figure 1. Change of dielectric permittivity of the $BaTiO_3$ single crystal with temperature. The schematics of Ti-displacement in the oxygen octahedron of the perovskite structure are also shown.

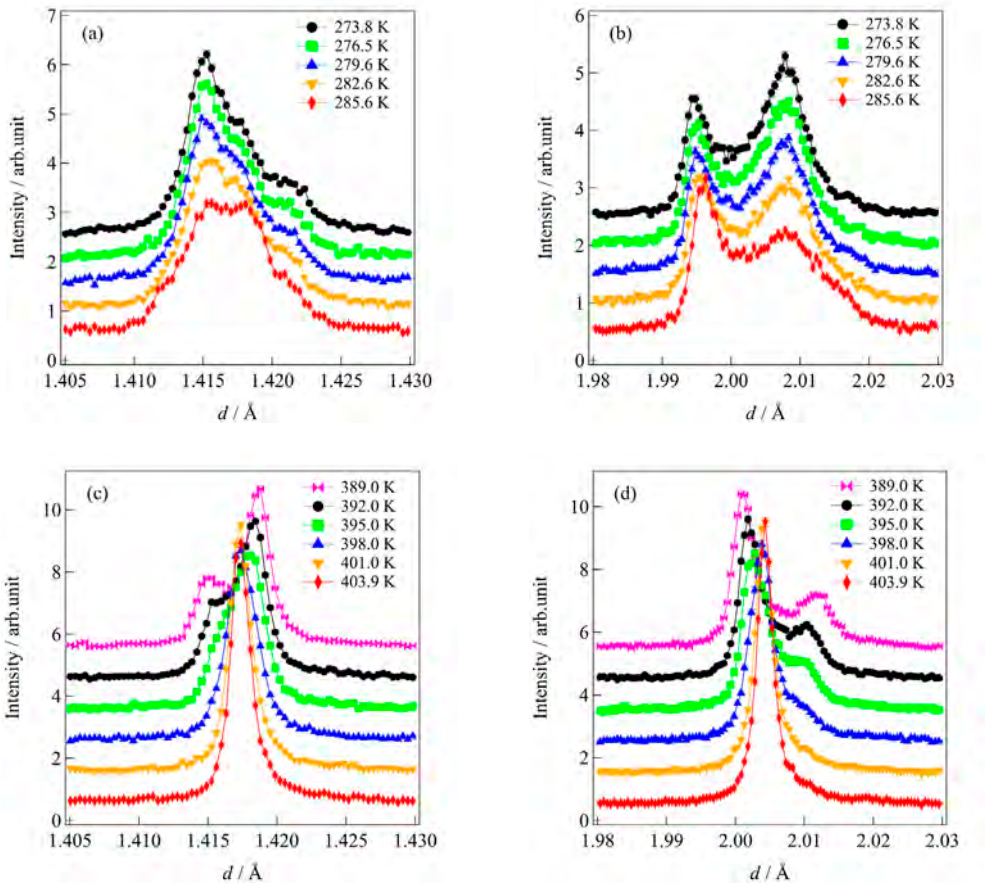

Figure 2. (a), (b) Temperature variation of the diffraction peak near 280 K. (c), (d) Temperature variation of the diffraction peak near 400 K. The displayed temperature is the value of the platinum resistance temperature sensor PT100 installed on the sample stick.

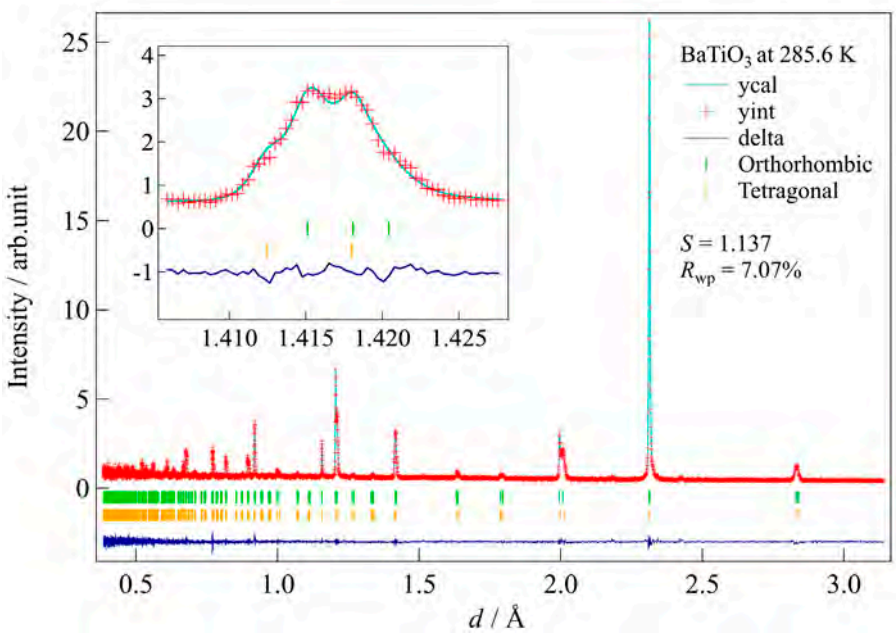

Figure 3. The Rietveld analysis results at 285.6 K. In this analysis, we obtained the result that the orthorhombic phase and tetragonal phase were mixed at a mass ratio of about 6:4.

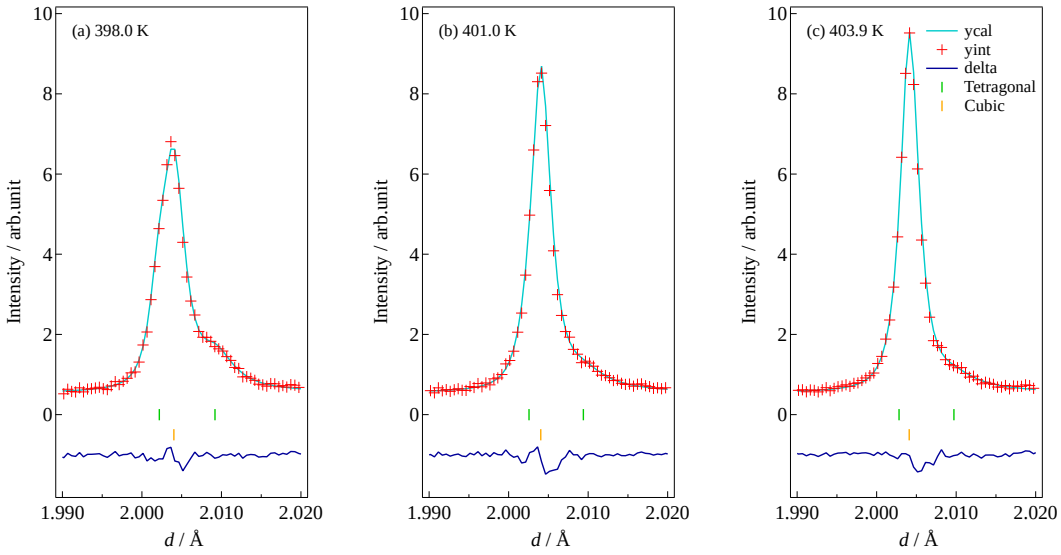

Figure 4. The Rietveld analysis results near the transition temperature 400 K. In those temperatures, a better fit was obtained by analyzing the coexistence of two phases, tetragonal and cubic.

observed at 398.0 K, 401.0 K, and 403.9 K (Fig. 4). In this series of measurements, it was not possible to determine whether the coexistence of these two phases was a characteristic of the sample during the phase transition process or due to temperature irregularities. In the future, it will be necessary to evaluate whether the coexistence is due to temperature irregularities or not by using an incident beam slit to check the differences in the profiles of the sample in the vertical direction.

4. Summary

The accuracy of the sample temperature above room temperature for cryofurnace was investigated using a high-temperature sample stick. The sample temperature assumed from the profile changes was found to follow the temperature of the sensor attached to the top of the sample holder. However, to evaluate the temperature irregularity of the sample itself, measurement using a slit is necessary, and we would like to conduct this in a future commissioning, including Rietveld analysis with data with higher statistics.

References

[1] S. Torii, M. Yonemura, T. Y. S. Panca Putra, et al., J. Phys. Soc. Jpn., SB020 SB020-1-4 (2011).
[2] S. Torii, M. Yonemura, Y. Ishikawa, et al., J. Phys.: Conf. Ser., 502 012052 (2014).
[3] S. Torii, M. Hagihala, K. Cho, et al., MLF Annual Report 2020, 94–95 (2021).
[4] A. P. Barranco, Ferroelectric Materials – Synthesis and Characterization, IntechOpen (2015)
[5] R. Oishi, M. Yonemura, Y. Nishimaki, et al., Nuclear Instruments and Methods, A600 94–96 (2009).
[6] R. Oishi-Tomiyasu, M. Yonemura, T. Morishima, et al., J. Appl. Cryst., 45 299–308 (2012).

S. Torii[1,2], S. Yamauchi[1,2], and K. Mori[1,2]
[1]*Neutron Science Section, Materials and Life Science Division, J-PARC Center;* [2]*Institute of Materials Structure Science, KEK*

BL10: NOBORU

1. Introduction

In FY 2021, twenty-one general-use proposals and two project-use proposals were carried out at NOBORU. Two long-term proposals were postponed due to the entry restriction for foreigners because of the COVID-19 pandemic. This year, in addition to the fixed-point observations that have been conducted every year, we started testing 90° diffraction experiments using a 1 mm radial collimator on long-term loan from BL19 (TAKUMI). Using this collimator, we plan to aim at mapping heterogeneous cultural heritage samples by neutron diffraction in a gauge volume of about 1 mm × 1 mm × 4 mm at NOBORU.

2. Experimental setup

Although NOBORU does not use a neutron guide tube, we can use neutrons of sufficient intensity over a wide wavelength band, since the standard sample position is 14 m from the moderator. The diffraction detector consists of 16 ^{3}He PSD tubes (Toshiba E6867-600) with dimensions of 60 cm length and 1/2-inch in diameter and nominal 10 MPa of gas pressure. The detector box is placed near the inner wall of the experiment room to obtain a flight path of approximately L_2 = 1.4 m. The incident beam path to 50 mm in front of the sample in the experiment room consists of NW50 flanged vacuum tubes covered with B_4C rubber sheet. At the end of the tube, i.e., at the location of the vacuum window, a 5 mm wide × 12 mm high aperture was temporarily made with B_4C rubber (this is considerably larger than the final aperture size we are aiming for). The 1 mm radial collimator was placed on the experiment table using a common laser marking. Powder samples were enclosed in a standard vanadium (V) holder (Taiyo Koko PV-06-F) with a 6 mm outside diameter and 0.1 mm wall thickness. In order to examine the capability to detect minor phases, we also used bulk steel (Fe-0.18C) previously measured by TAKUMI to see if the peaks of cementite (Fe_3C) were clearly visible.

3. Results

After starting the on-beam test, *x* and *z* scans were performed to center the sample using silicon (Si) sealed in a standard V holder with additional shielding materials as shown in Fig. 1. An example result of the *z* scan is shown in Fig. 2. Neutron counts in the range avoiding the Bragg peaks at 12.3 to 16.6 ms (hatched range in Fig. 2a) are integrated and are plotted as a green circle in Fig. 2b. The curve fitting allowed us to determine that *z* was centered at about −0.7 mm in this experimental

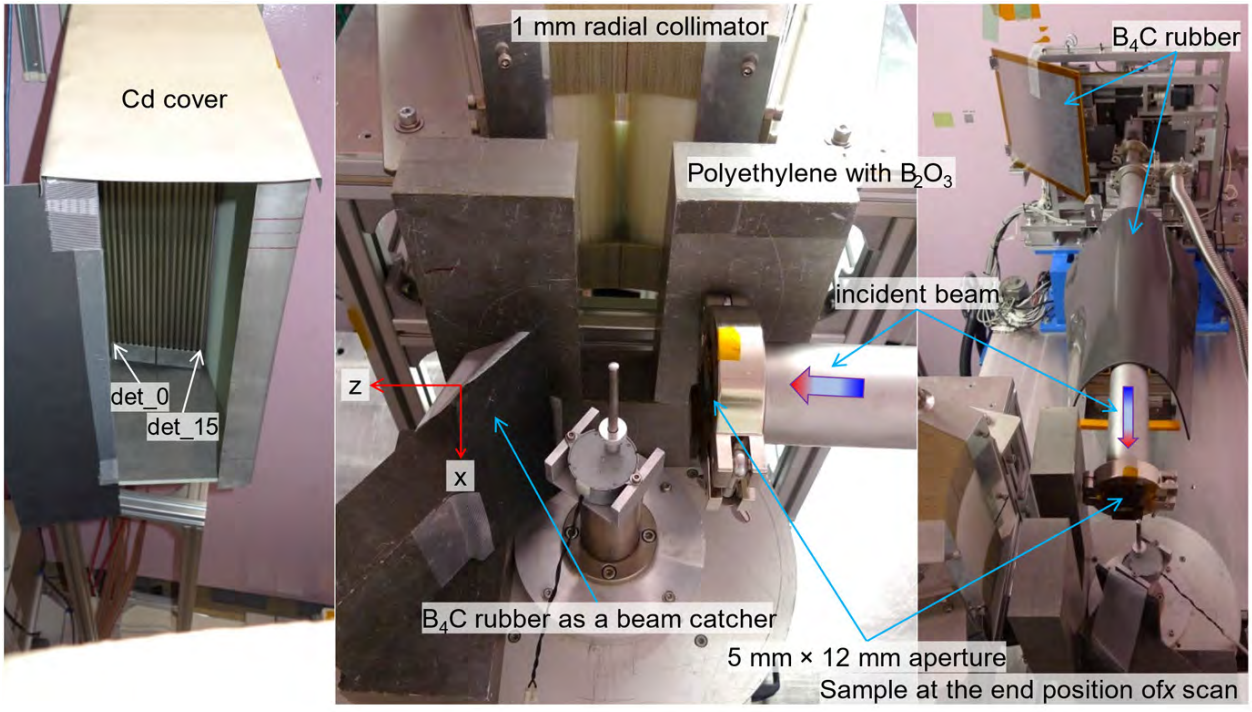

Figure 1. Experimental setup for the 90° diffraction experiment at NOBORU.

setup. The gauge volume width expected by the radial collimator is expressed in Fig. 2 as a horizontal grid, and the cut view of the ϕ6 mm sample holder is also inserted in this figure as a circle, with a 5 mm wide neutron beam path overlapping it. It can be seen that the volume of the holder in contact with the neutrons contrasts well with the background counts due to incoherent scattering from V.

Figures 3a and 3b show the diffraction patterns of bulk steel for each PSD without and with time-focus correction, respectively. The area circled in blue square appears to have peaks that were not detected, except for this bulk steel. These peaks were not included in TAKUMI's measurement data, but were comparable to the peak intensity of Fe_3C in these data. Further verification of this is needed.

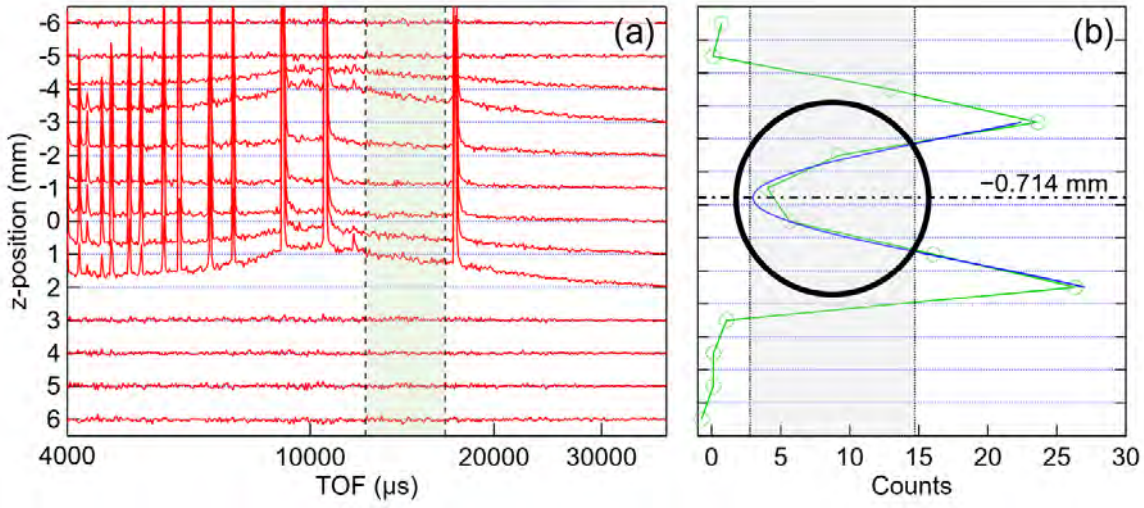

Figure 2. Diffraction patterns of Si sealed in a standard V holder. Z-position was moved in 1 mm intervals.

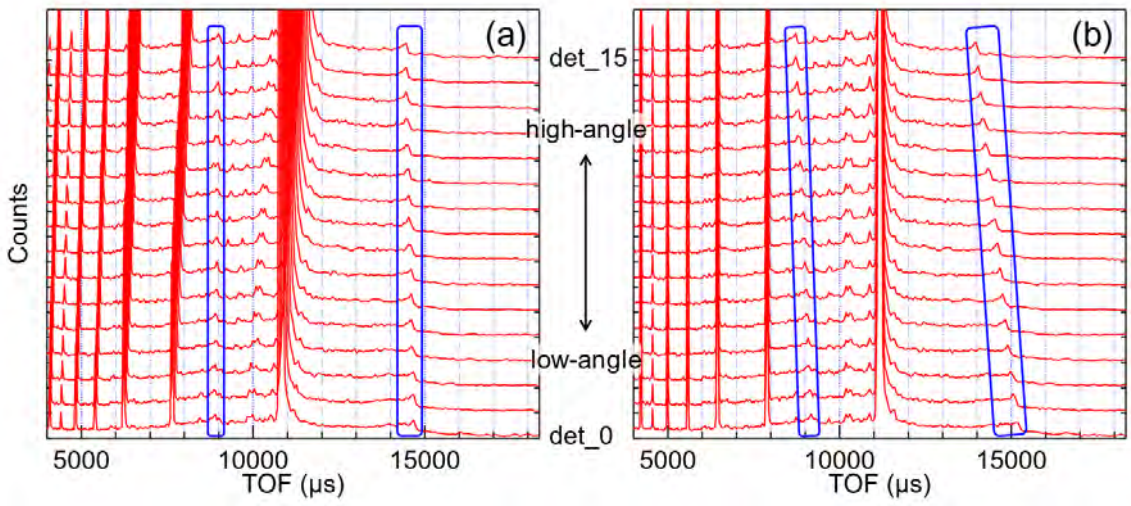

Figure 3. Diffraction patterns of bulk steel for each PSD without time-focus correction (a) and with time-focus correction (b).

K. Oikawa and Y. Tsuchkawa
Neutron Science Section, Materials and Life Science Division, J-PARC Center

Recent Developments at BL11 PLANET

1. Introduction

This year, the following devices and software were installed:

i) Automatic sample changer and its remote-control system
ii) Radial collimators with a field of view of 0.8 mm
iii) Automatic sample positioning command for the experiments using PE presses
iv) Software to mask unwanted Diamond Bragg spots in the data taken with anvils or sample containers made of single crystal diamonds

The details are shown below.

2. Automatic sample changer and its remote-control system

At PLANET, ambient-pressure data are collected by placing a sample in a vanadium can (Taiyo Koko Co. Ltd) on the six-axis press. So far, when several samples were measured successively each one had to be replaced by hand. Since the typical exposure time for one measurement is about 3 to 6 hours, the continuous measurements of several samples late at night have exhausted the beamline staffs. The automatic sample changer has been developed to improve this situation (Fig. 1). It consists of a motorized stage and a frame for attaching cans. Five cans can be attached to the frame at maximum and each can is remotely positioned at the center of the six-axis press in the precision of 0.1 mm by shifting the frame. By using a stage control command newly added to Experimental Scheduler (device control and data acquisition software), a series of sample data acquisition is possible by making the batch sequence.

3. Radial collimators with a field of view of 0.8 mm

With the increase in the beam power at the MLF, the use of a smaller sample and resulting experiments at a higher pressure became possible. Related to this, the necessity for reducing the diffraction gauge volume is increasing. This year, radial collimators with a field of view of 0.8 mm along the incident beam direction are developed for the experiments using Paris-Edinburgh (PE) presses or diamond anvil cells. Figure 2 shows the efficacy of the collimators. The intensities of the Diamond Bragg peaks are significantly reduced while maintaining sample intensity, which enables more precise structure analysis at higher pressures.

4. Automatic sample positioning command for PE presses

Since the pandemic of COVID-19, many proxy experiments have been conducted at PLANET. Currently, almost all high-pressure devices can be controlled via Experimental Scheduler at PLANET; thus, a proxy experiment is not difficult to conduct. Among them, the PE press is the most frequently used device because of its easy sampling and high reproducibility in pressure

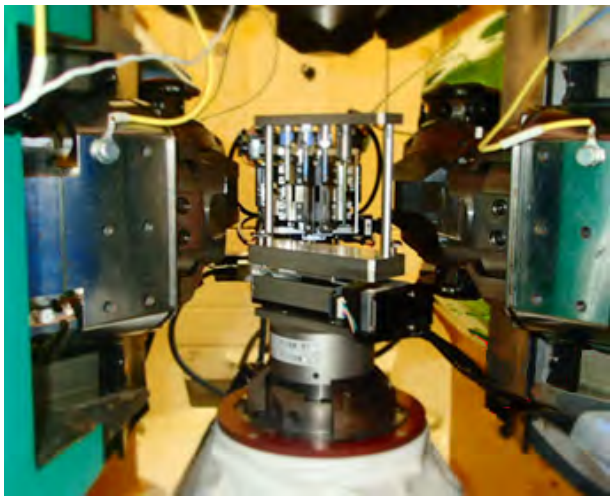

Figure 1. Photo of the automatic sample changer mounted on a six-axis press.

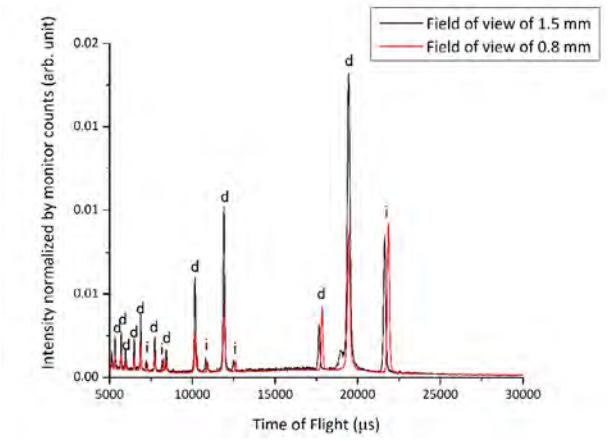

Figure 2. Comparison of data of ice VII compressed with a nanopolycrystalline diamond anvil cell using radial collimators with a field of view of 1.5 mm (black) and 0.8 mm (red). " i " and " d " denote Bragg peaks from ice VII and diamond anvils, respectively (courtesy of Dr. Komatsu).

generation. However, fully automatic experiments were still difficult to conduct because the sample drifts from the diffraction gauge volume during compression and the sample position must be readjusted after each compression. To achieve it, the automatic sample positioning command is implemented in Experimental Scheduler. It consists of three basic processes: i) scan the sample position along x, y, z or θ axis, ii) fit the obtained scan profiles by a Gaussian function and find the optimum position, and iii) move the sample to the optimum position. By using this command, all data collection at high pressures is completed once the target loads, scanning axis/range and data acquisition condition are input in Experimental Scheduler as a list.

5. Software to mask unwanted Diamond Bragg spots in the data taken with anvils or sample containers made of single crystal diamonds

With the increase in beam power, structure analyses of crystalline samples using diamond anvil cells or liquid samples using single-crystal diamond sample containers became realistic. Previous feasibility tests, however, demonstrated strong contamination of Bragg spots from single-crystal diamonds. The source of the scattering is spatially too close to the sample to eliminate them with radial collimators; thus, we tried to mask the Bragg spots in data reduction.

Figure 3 shows an example of data taken with a diamond anvil cell. In the detector map, Laue patterns of diamonds are clearly observed. Thus, we took a measure to remove them by estimating all the expected positions from the refined UB matrixes of diamond crystals.

The software has the following functions:

i) Pick up spot's positions in the selected area (and TOF region) and store them in the list.
ii) Find (and refine) UB matrixes from the positions in the list.
iii) Calculate all the expected positions on the basis of the refined UB matrixes and store the regions to be masked in a mask file.

In addition to the diamond Bragg spots, it is known that the incident beam impinged on the sample partly loses its intensity at specific wavelengths due to the Bragg reflection of a diamond in front of the sample (the so-called "Diamond Dips"). This also causes a systematic reduction in scattering intensities from the sample at the corresponding wavelengths. Thus, the software also has the following function:

iv) Calculate the expected TOF regions of "Diamond Dip" and store them in the mask file.

By using a mask file made by this software, more accurate scattering intensity of the sample is obtainable.

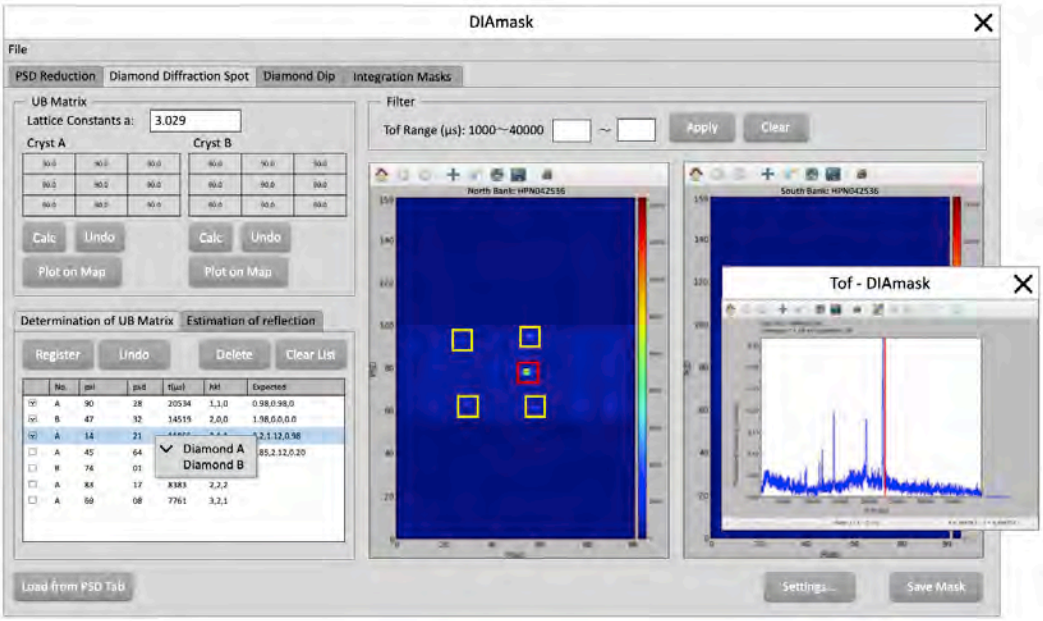

Figure 3. Newly developed software for removing the effects of single crystal diamonds.

T. Hattori[1], A. Sano-Furukawa[1], S. Machida[2], J. Abe[2], K. Funakoshi[2], and N. Okazaki[2]
[1]Neutron Science Section, Materials and Life Science Division, J-PARC Center; [2]Neutron Science and Technology Center, CROSS

High Resolution Chopper Spectrometer HRC

1. Introduction

The High Resolution Chopper Spectrometer (HRC) is being operated at BL12 in MLF under the S-type project of IMSS, KEK and the IRT project of ISSP, the University of Tokyo, in order to study dynamics in condensed matter, especially in a wide range of correlated electron systems. The activities of the HRC in FY2021 are summarized in this report.

2. Instrumentations

The 1 K refrigerator on HRC is a ^{3}He gas circulation type one, where the lowest temperature was 0.6 K in the best case. Recently, the lowest temperature destabilized and became 2 K, the volume of the ^{3}He gas decreased. We cleaned the circulation system of the ^{3}He gas and added more ^{3}He gas, but the situation did not improve. For this reason, we decided not to use it for the general user program. An investigation of the cause revealed an anomalous gas flow rate in the heat exchanger in the cold head caused by a leak in the ^{3}He exhaust line. The heat exchanger was remanufactured and replaced and cooling down to 0.6 K was confirmed.

Since it was decided not to use the 1 K refrigerator for experiments during the repair period, instead, Heliox (^{3}He gas sorption type refrigerator with minimum achievable temperature 0.3 K), which had been stored for a long time, was started up and commissioned to conduct low temperature experiments on the S-type project.

Information on ^{3}He gas sorption type refrigerators was collected and reviewed by cryogenic engineers and instrument staffs of HRC and POLANO, and specifications were developed for a higher performance refrigerator than Heliox. We plan to place a manufacture order for it next fiscal year.

The 4 K GM (Gifford-McMahon) refrigerator is the most frequently used refrigerator in experiments on HRC and has been in operation for more than 24,000 hours in total, and has exceeded 10,000 hours since the last maintenance, so scheduled maintenance was performed.

A cryofurnace (T = 4 - 800 K) was manufactured and delivered (Fig. 1), and the experiment control program YUI was modified to accommodate it. We plan to perform the commissioning next fiscal year.

As reported last year, T0#2 (the second machine of the T0 chopper) is currently running and T0#1 is stored. We performed maintenance work for T0#1.

In January 2019, the Fermi chopper became out of control because of a touch-down in the magnetic levitation system of the rotor. This Fermi chopper was replaced by a spare one. Last year, to repair the Fermi chopper, the damaged touch-down bearing was replaced by a new one. However, this did not restore the stable rotation because of a loss of the balance of the rotor. This year, further work was performed to improve the balance, and the repair was completed.

The wave shape of the 25 Hz timing signal input to the Fermi chopper is disturbed by noise from the T0 chopper control system, causing a problem that disrupts the control of the Fermi chopper and needs to be addressed.

The circuit of the T0 chopper control board was developed by a KEK engineer in the past, and some information has not been made public. In advancing maintenance, the control algorithm was investigated.

In the development of the Fermi chopper, a feasibility of gadolinium as a shielding plate for the slit package was examined. Material strengths were measured, and gadolinium film formation tests were conducted for the thickness of gadolinium of 0.02 mm and 0.5 mm on aluminum. It has been confirmed that it was possible to deposit 0.02 mm and 0.5 mm of gadolinium layer on both sides of aluminum foil and thin sheet.

Figure 1. Cryofurnace delivered to HRC in March 2022.

A scheduled maintenance of the cryopump in the vacuum scattering chamber and an overhaul of the turbomolecular pump in the Fermi chopper were performed.

The computational environment has been developed and maintained by ISSP, but from this fiscal year, a KENS engineer will maintain the parts related to DAQ MW common to KENS. ISSP will continue to be in charge of the part related to YUI and HANA.

The servers related to DAQ MW and storage will be migrated to virtual servers according to the plan in KENS. The servers related to YUI and HANA will also be migrated to virtual servers, but it will be necessary to cope with the termination of the support of the operating system and the version up of python in the future.

3. Scientific results

Complex magnetic phase diagram in the non-centrosymmetric compound $CePtSi_3$ was determined with magnetization measurements [1]. We plan to perform experiments on HRC using a single crystal sample to elucidate magnetic fluctuations unique to this system under the influence of antisymmetric spin-orbit interaction. Crystalline electric field level scheme in the non-centrosymmetric $CeRhSi_3$ and $CeIrSi_3$ was determined, an emergence mechanism of superconductivity was discussed in relation to the wavefunction of the ground state of f-electrons in crystalline electric field [2,3]. Spin gap was observed in sodium superoxide NaO_2, where O_2^- is a magnetic ion, it was found that this system shows the spin-Peierls transition [4]. Antiferromagnetic Kitaev interaction in $Na_2Co_2TeO_6$ was investigated [5, 6]. Using the results of one experiment (2019B0350), the two groups wrote their own papers.

References

[1] D. Ueta et al., J. Phys. Soc. Jpn. 90 (2021) 064712.
[2] D. Ueta et al., J. Phys. Soc. Jpn. 90 (2021) 104706.
[3] D. Ueta et al., MLF Annual Report 2021 (this issue).
[4] M. Miyajima et al., Phys. Rev. B 104, L140402 (2021).
[5] G. Lin et al., Nat. Commun. 12, 5559 (2021).
[6] C. Kim et al., J. Phys.: Condens. Matter 34, 045802 (2022).

S. Itoh[1,2], T. Masuda[3,2], T. Yokoo[1,2], T. Nakajima[3], S. Asai[3], H. Saito[3], D. Ueta[1,2], D. Kawana[3], R. Sugiura[3], T. Asami[3], T. Seya[1,2], S. Yamauchi[1,2], S. Torii[1,2], Y. Ihata[4], and H. Tanino[1,2]

[1]Neutron Science Section, Materials and Life Science Division, J-PARC Center; [2]Institute of Materials Structure Science, KEK; [3]The Institute for Solid State Physics, The University of Tokyo; [4]Technology Development Section, Materials and Life Science Division, J-PARC Center

BL14 AMATERAS

1. Introduction

AMATERAS is a cold-neutron disk-chopper spectrometer for studies on dynamical properties of atomic, molecular and magnetic systems from cold to sub-thermal energy range with high efficiency and flexible resolution [1, 2]. Due to the world pandemic since 2020, the instrument group carried out remote experiments for foreign users in JFY2021. We hosted graduate students for a short period as Fellows of Advanced Science and Internship of JAEA. Furthermore, in order to reduce staff workload and to relax the excessive competition for beamtime, we have upgraded some components of the instrument in recent years.

2. User program, outreach activities and outcomes

The number of general proposals (short-term) submitted to the 2020B+2021A and 2021B periods were 35 (accepted: 7, reserved: 27, not approved: 1) and 47 (accepted: 7, reserved: 35, not approved: 5), respectively. Consequently, eight experiments from the 2020B+2021A proposals and nine experiments from the 2021B proposals, including some "reserved" ones, were carried out in JFY2021. Japanese users carried out their experiments on-site, while foreign users were not yet able to visit the facility because of travel restrictions due to the Covid-19 pandemic since 2020. Thus, the instrument group members carried out these six experiments remotely. In addition to the general (short-term) proposals, one general (long-term) proposal and three project research proposals were also carried out. As a recent trend in the research field, the number of proposals on magnetism and strongly correlated electron systems is continuously increasing. Actually, only one proposal approved in the 2021B term is for the energy materials and the 16 other proposals are related to magnetism and strongly correlated electron systems.

In this fiscal year, 13 refereed papers related to scientific research at AMATERAS and one proceedings paper on instrumentation were published. AMATERAS hosted some students this fiscal year: Mr. Ryo Murasaki, a doctoral student from Tohoku University, and Ms. Rika Inoue, a master course student from Ochanomizu University, as Fellow of Advanced Science and Mr. Pharit Piyawongwatthana, a doctoral student from Tohoku University, based on Internship of JAEA.

3. Instrument-related upgrades

Recently, we have upgraded some components to increase the efficiency of experiments. Following the upgrade of the controlling system on the vacuum scattering chamber in 2020, we extended the neutron guide tube by ~50 cm at a section between the monochromating chopper and the window of the vacuum scattering chamber (Fig. 1) in JFY2021. It is expected that the neutron intensity, especially for the low-energy region, increases by extending guide mirrors to this section and further downstream. We removed a B_4C collimator, which has been placed between the monochromating chopper and the vacuum scattering chamber (Fig. 2(a)), and then installed a guide jacket made of stainless steel and a guide mirror (Fig. 2(b)). Its alignment was done after the installation (Figs. 2(c) and 2(d)). This extension increased neutron intensity by more than 20% at the low energy region, as shown in Fig. 3. We will compare the intensity to the simulation result.

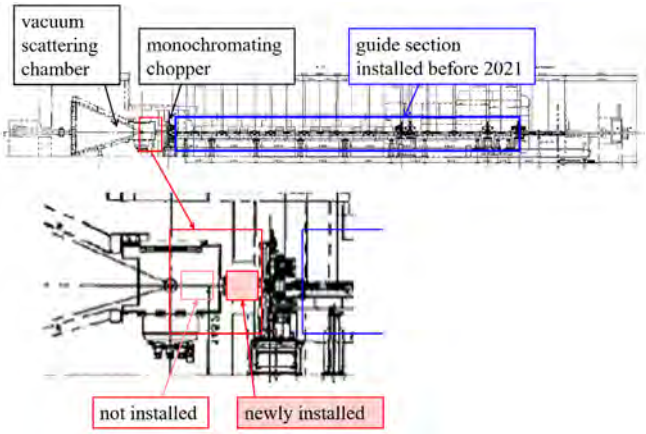

Figure 1. Beam transport of AMATERAS.

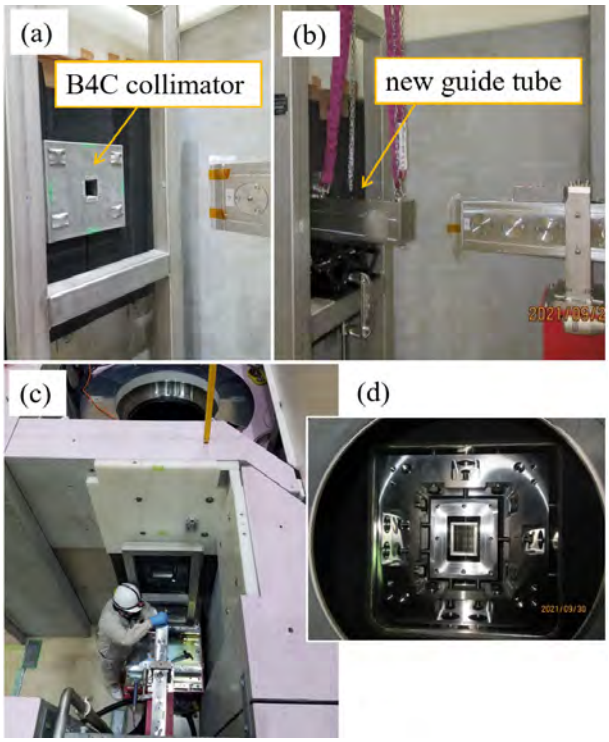

Figure 2. Installation of an additional guide tube. (a) B4C collimator that has been placed before. (b) Newly installed guide tube. (c) Alignment of the guide mirror. (d) New guide tube and jacket viewed from downstream.

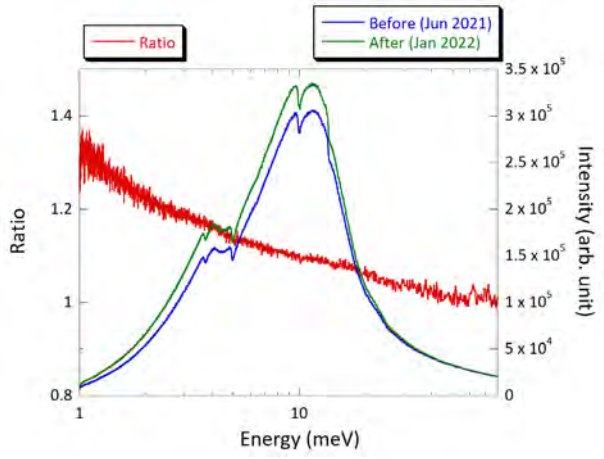

Figure 3. Beam intensity as a function of the incident neutron energy and its comparison of before and after the extension of the guide mirror.

4. Future plans

We will continue with the further upgrades and automation of components, which are important to save time to change the experimental configuration and to reduce our workload. We have purchased a new cryogen-free top-loading cryofurnace in JFY2021. We will commission this equipment next year, aiming to install it for users' experiments. We also plan to fully automate the pumping system of the vacuum scattering chamber.

References

[1] K. Nakajima et al., J. Phys. Soc. Jpn. **80** SB028 (2011).
[2] K. Nakajima, RADIOISOTOPES **66** 101 (2017).

S. Ohira-Kawamura[1], M. Kofu[1], N. Murai[1], Y. Inamura[1], D. Wakai[2], and K. Nakajima[3]
[1]*Neutron Science Section, Materials and Life Science Division, J-PARC Center;* [2]*NAT Corporation;* [3]*Material Science Research Center*

Upgrading TAIKAN

1. Introduction

The small and wide angle neutron scattering instrument TAIKAN (BL15) has been developed and upgraded at J-PARC to analyze precisely and efficiently the microstructures or hierarchical structures of substances in various scientific fields with a 1-MW spallation neutron source [1]. In FY2020, it was upgraded further to perform long-term stable measurement, humidity control measurement, and sample exchange measurement.

2. Upgrading for long-term stable measurement

The detector system of TAIKAN is composed of 5 detector banks: small-, middle-, high-, ultra-small-angle, and backward detector banks. The number of ^{3}He tubes is 912, 720, 400, and 80 for the small-, middle-, high-angle, and backward detector banks, respectively, or 2,112 in total. The installation ratios of the ^{3}He tubes are 100, 100, 76, and 100% for the small-, middle-, high-angle, and backward detector banks, respectively, and the overall average is 94%.

The gas pressure of these detectors is basically 6 atm, but 32 detectors in the center of the small-angle detector bank and 80 detectors in the backward detector bank were replaced in FY2019 with 20 atm gas pressure detectors for high efficiency measurements.

However, radiation damage was observed in the detectors of the small-angle detector bank, so the additive gas for the 64 detectors in the central part was replaced from CF_4 to N_2 to extend their service life.

3. Upgrading for humidity control measurement and sample exchange measurement

A humidity control system was developed (Fig. 1). The system is capable of controlling dew point with an accuracy of ±0.2°C for dew points ranging from -15 to 81°C. The flow rate is 0.05 ~ 3 L/min. The accuracy in gas mixing is within ±1 %. The pressure is 1 atm. The system can achieve automatic and quick humidity changes and continuous H_2O-D_2O composition changes because it has a two-temperature method humidity generator. Two types of sample cells are available for the system. They are a single-sample cell and a multiple-sample cell. The former cell is designed for temperature and humidity stability and fast changes in humidity. The latter cell is designed for automatic exchange of seven samples.

A sample exchanger with Peltier cooling elements was also developed (Fig. 2). The sample exchanger can be installed in three units of nine samples, each of which can be independently temperature-controlled in the range of 20 ~ 80°C.

4. Future prospects

The installation of long-life detectors will lead to stable instrument operation. In addition, the development of the humidity control system and the Peltier-type sample exchanger will be effective for the measurement of fuel cell materials, soft matter, and biomatter, and is expected to further promote uses in these research fields.

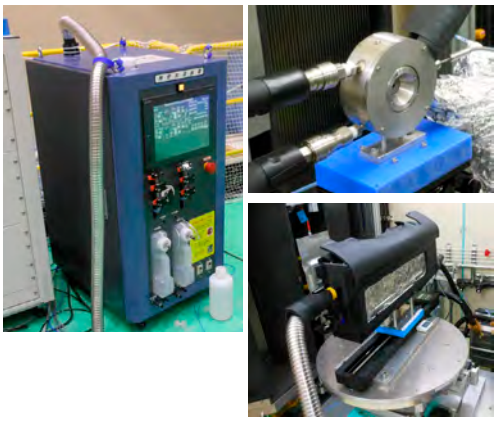

Figure 1. A humidity control system: (left) humidity generator, (upper right) single-sample cell, (lower right) multiple-sample cell.

Figure 2. A Peltier-type sample exchanger.

Reference

[1] S. Takata, J. Suzuki, T. Shinohara, T. Oku, T. Tominaga, K. Ohishi, H. Iwase, T. Nakatani, Y. Inamura, T. Ito, K. Suzuya, K. Aizawa, M. Arai, T. Otomo and M. Sugiyama, JPS Conf. Proc., **8** 036020 (2015).

J. Suzuki[1], S. Takata[2], K. Ohishi[1], H. Iwase[1], Y. Kawamura[1], K. Hiroi[2], T. Morikawa[1], and M. Ueda[1]
[1]Neutron Science and Technology Center, CROSS; [2]Neutron Science Section, Materials and Life Science Division, J-PARC Center

Renewal of Optical Components for Multi Incident-angle Neutron Reflectometry

1. Introduction

Neutron reflectometry (NR) is very useful for investigations of structures of surfaces and buried interfaces composed of soft materials. SOFIA is a horizontal-type neutron reflectometer constructed at Beamline 16 (BL16) of the Materials and Life Science Experimental Facility (MLF) of the Japan Proton Accelerator Research Complex (J-PARC) [1, 2]. Due to the high-flux beam of J-PARC, less than one hour is needed for taking a full *Q*-range data and only a few seconds for a limited *Q*-range data in the case of a sample with 3 inches (76 mm) in diameter; even though the beam power is still one-third of the planned value, 1 MW. However, several hours are still needed for a small sample, such as 10 mm × 10 mm, which is a typical size of a sample for X-ray reflectometry.

For the further upgrade of the SOFIA reflectometer, we have developed an elliptical focusing mirror to illuminate a sample with a neutron beam with a large beam divergence. So far, we have developed focusing super-mirrors [3–5]. The latest mirror is capable of focusing neutrons with a width of 0.13 mm in full width at half maximum (FWHM). This mirror has already been installed in the SOFIA and opened for users as reported last year.

Furthermore, we have a plan to realize a multi-incident neutron reflectometry (MI-NR) at the SOFIA by applying focusing mirrors, in which neutrons are transported by two different paths and converged at a sample position with different incident angles (Fig. 1). This method enables us to measure a Q-region from the total reflection at low-Q to the measurable high-Q limit of a typical sample at a time without any angle scan required for a conventional NR experiment [6]. To accept the neutron beams with two different paths by two detectors independently, we installed last year a compact detector utilizing a flat-panel multi-anode-type photomultiplier tube (FRP) with the detection area of 48 × 48 mm^2 [7, 8]. This year, we installed optical components for MI-NR: two disk choppers to change the repetition rate of neutron pulses of each neutron path independently; a rough focusing guide to transport neutron images at the chopper positions to the positions of virtual sources for fine focusing as follows.

2. Disk choppers

So far, the SOFIA employed double frame mode with a chopper rotation speed of 12.5 Hz (half of the neutron pulses generated at the source) to extend the

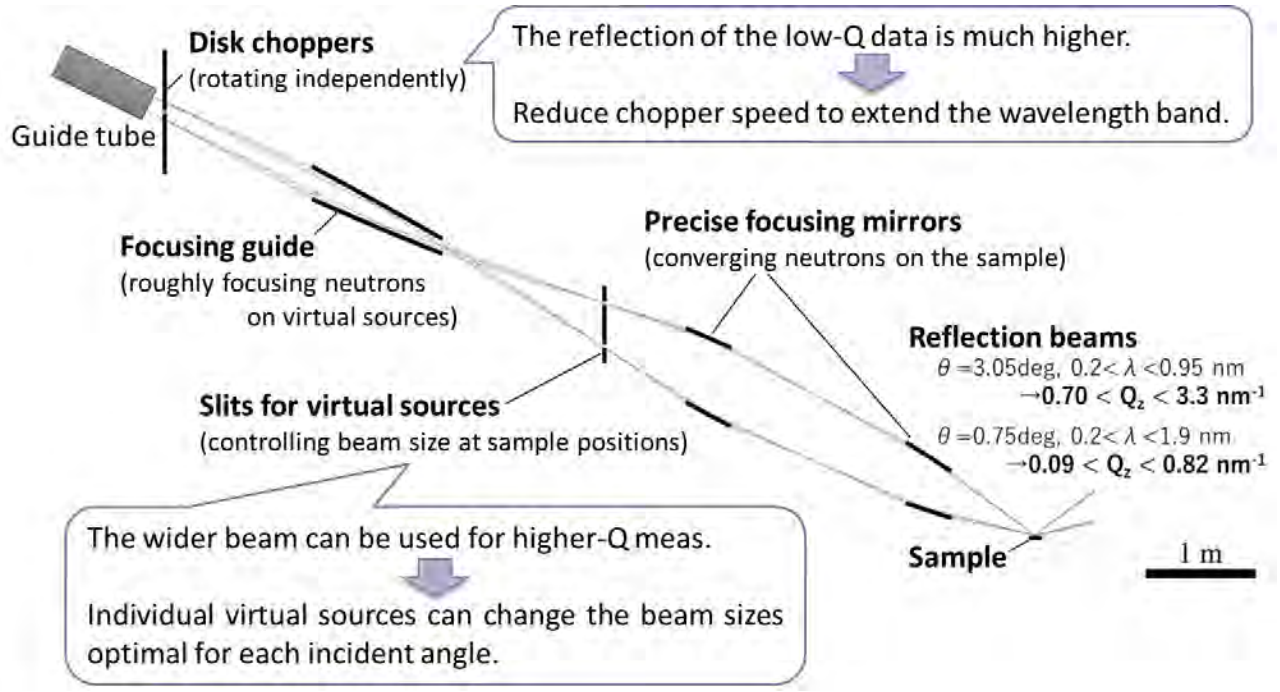

Figure 1. Design of optics for realizing MI-NR at the SOFIA. This year, disk choppers and a focusing guide were installed.

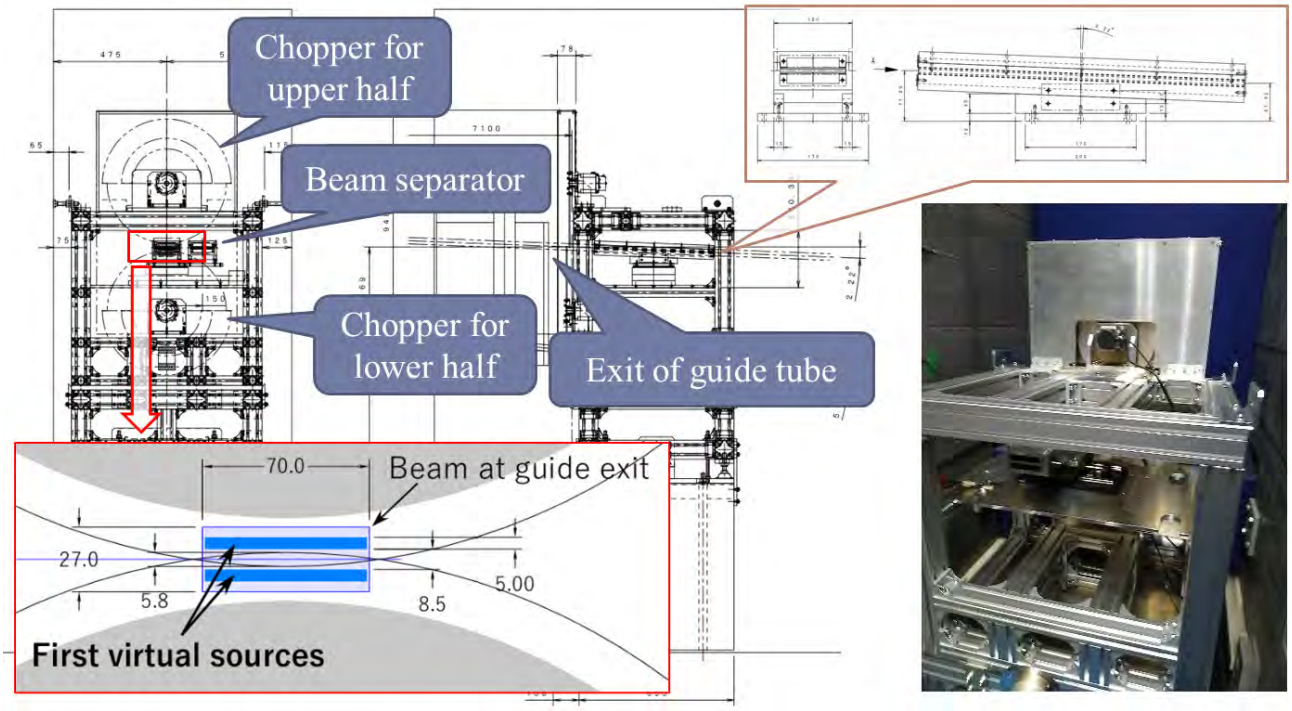

Figure 2. Double chopper system for MI-NR. The upper half and lower half of the beam at the guide exit are independently chopped by the upper and lower choppers, respectively.

Q-range by using a wider wavelength band. This enables us to perform time-slicing measurements with wider *Q*-region without any incident-angle scan. However, the *Q*-region is still limited even with the double frame mode due to the limitation of the wavelength band, and the neutron flux is reduced by a half because every other neutron pulse is cut by the chopper. With taking the merit and demerit of the double frame mode mentioned above, the MI-NR at the SOFIA reflectometer is going to be realized by the combination of the higher flux beam at 25 Hz for higher incident-angle and wider wavelength band beam at 12.5 Hz for lower incident-angle. It should be noted here that the longer exposure time is required for the measurement at higher incident-angle because of lower reflectivity. Therefore, the reduction of the flux due to the double frame mode at the lower incident-angle has no effect on the total measurement time because it is limited by the statistic at the higher incident-angle.

To realize the combination of the two beams above, two disk choppers were installed at the exit of the guide tube as shown in the Fig. 2. The choppers were made of circular aluminum plates with thickness of 4 mm, and Gd_2O_3 was painted on them to stop neutrons by the choppers. As two beams with different tilt angle, 2.22° and 5.71°, are acceptable at the SOFIA, the choppers have two windows: one is at the edge to realize the MI-NR at the 2.22° beam, and the other at the middle of the disk to cut the beam with the tilt angle of 5.71° to illuminate free-liquid surface with high incident-angle.

3. Focusing guide tube

As mentioned above, the upper and lower half parts of the 2.22° beam are separately cut by the two disk choppers, in which the repetition rate can be controlled to be 25 or 12.5 Hz independently. The focusing guide is to transport the two beams at the chopper position to the virtual sources 4500 mm from the choppers: one is for a lower incident angle and the other is for a higher one. As mentioned before, a shorter exposure time is generally required for a lower angle. Therefore, the repetition rate for the lower angle can be reduced to extend the measurable *Q*-region down to the total reflection region in exchange for less flux.

For this purpose, a focusing guide was installed at the middle of the choppers and virtual sources. The guide is 1300 mm in length and equips 3Qc supermirrors inside, in which the shapes of the top and bottom sizes are ellipses with foci at the upper and lower half of the beam at the chopper position and lower and upper exit at the virtual sources, respectively. Note here that a separator was placed to avoid the cross talk of the

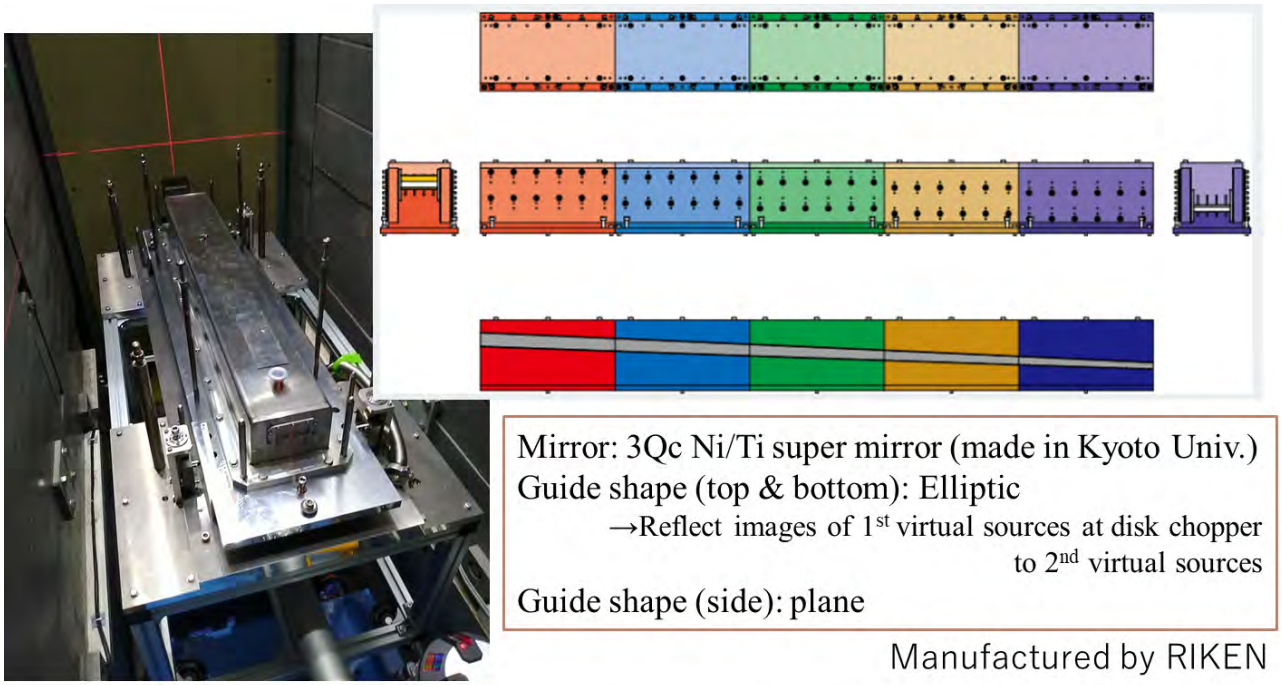

Figure 3. Focusing guide for MI-NR. Top and bottom mirrors of the guide focus the images of 1st virtual sources at the chopper to the 2nd virtual sources at the positions of slits.

two beams after the chopper, in which an iron plate was placed at the center to cut fast neutrons and two 2.5Qc supermirrors on glasses were positioned on the top and bottom sides of the iron plate to guide neutrons.

4. Future plans

The disk choppers and focusing guide installed in this year can transport neutron beams having different repetition rate at the virtual sources position. Next year, a slit system with two apertures to make virtual sources with the optimized gaps depending on the incident angle and sample size is going to be installed. In addition, a set of precise focusing mirrors to transport neutrons from the virtual sources to a sample position with different incident angles is also to be installed. A set of FRP detectors developed last year is to be used to count the neutrons reflected on the sample separately. After these planned upgrades are installedcompleted next year, hopefully, the first MI-NR measurement will be demonstrated.

References

[1] N. L. Yamada *et. al.*, *Euro. Phys. J. Plus*, **44** (2011) 9424.
[2] K. Mitamura *et. al.*, *Polymer J.*, **45** (2013) 100.
[3] S. Takeda *et. al.*, *Opt. Express*, **24** (2016) 12478–12488.
[4] T. Hosobata *et. al.*, *Opt. Express*, **25** (2017) 20012–20024.
[5] T. Hosobata *et. al.*, *Opt. Express*, **27** (2019) 26807–26820.
[6] N. L. Yamada *et. al.*, *J. Appl. Crystallogr.*, **53** (2020) 1462–1470.
[7] S. Satoh, *Plasma Fusion Res.* **13** (2018) 3–6.
[8] F. Nemoto *et. al.*, *Nucl. Instrum. Methods Phys. Res. Sect. A*, **1040** (2022) 166988.

N. L. Yamada[1,2], T. Hosobata[3], and M. Hino[4]
[1]Neutron Science Section, Materials and Life Science Division, J-PARC Center; [2]Institute of Materials Structure Science, KEK; [3]RIKEN Center for Advanced Photonics, RIKEN; [4]Institute for Integrated Radiation and Nuclear Science, Kyoto University

Current Status of SHARAKU: Polarized Neutron Reflectometer

1. Introduction

SHARAKU is a neutron reflectometer (NR) installed at BL17 in the Materials and Life Science Facility (MLF) of J-PARC to investigate the nanometric structure of surface and interfaces in a sample with spin-polarized neutrons. It has been employed for the structure analysis of thin films in various research fields, such as soft matters and magnetism. In this fiscal year, we developed a Helmholtz coil to allow the polarized neutron reflectometry (PNR) measurement in a weak magnetic field and a deep learning technique to accelerate the data acquisition in the experiment.

2. PNR in weak magnetic field

PNR is a non-destructive method for characterizing interface and surface structures in magnetic thin films. From the start-up period to the present, SHARAKU has been used to measure PNR data of various magnetic thin films under a strong magnetic field environment, i.e., from 5 mT to 6.5 T, and many results have been produced. On the other hand, the need for magnetic structure research under weak magnetic field conditions has been increasing in recent years, especially in spintronics device research, and a weak magnetic field environment near 2 mT is indispensable. For example, 90° interlayer coupling pseudo-antiferromagnetic films have been actively studied as high-speed, energy-saving magnetic recording media and high-sensitivity sensors in the GHz region. Such devices work by generating magnetic wall movement, magnetic reversal, and magnetic rotation in a weak magnetic field, which is the operating magnetic field. However, the magnetic domain, which is the heart of the device, is difficult to observe with non-neutron probes due to its complex stacking structure [1]. When conducting weak-field experiments, the conventionally used electro-magnet (1 T or lower) in BL17 contains an iron core as a pole piece, and because of its history, the magnetic field uniformity cannot be maintained in the weak-field region and a residual magnetic field exists, making it difficult to use the magnet as either a sample field or a polarized neutron field. In response to this necessity, a weak-field sample environment was fabricated and commissioned. This report introduces the apparatus and describes the polarization performance.

Figure 1 shows a schematic figure of the weak-field sample environment. The magnetic field in the sample position is generated by Helmholtz coils (HC), which generate magnetic field lines perpendicular to the direction of incoming and outgoing neutrons, and a pair of parallel plate magnets (PM1, PM2) and solenoid coils (B1, B2), which are auxiliary magnets, are placed on both sides of HC, connecting the magnetic field to the permanent guide field in BL17. The designed applied magnetic field to the sample is 0.5 to 10 mT. A heat sink is attached to the coil surface for air cooling, and a protective frame exists to cover the heat sink. The coil temperature is designed to be less than 48°C. The design is supposed to prevent the risk of fire accident or burns from human contact. Furthermore, it is equipped with a safety interlock that automatically shuts down the power supply in the event of electrical leakage or coil overheating. A GM 4 K type cryostat can also be mounted, allowing experiments from 4 K to room temperature. Figure 2 shows the polarization state |P1·P2| of the neutron beam at 0.9 mT using the HC magnet, which is the product of the polarization ratios, P1 and P2, for the polarizers in front of the samples and detectors, respectively. The result indicates

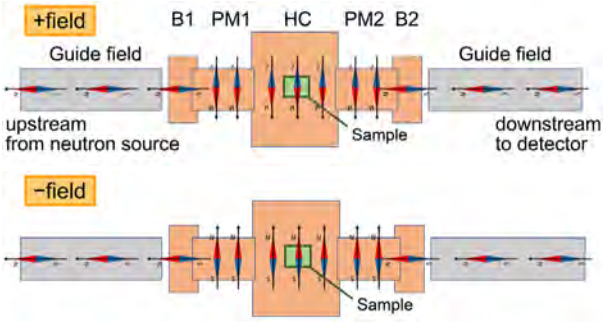

Figure 1. Schematic figure of field connection.

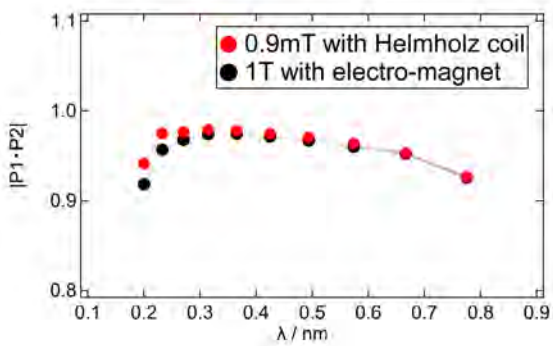

Figure 2. Comparison of polarization states in magnetic fields of 0.9 mT and 1 T.

that |P1·P2| is 92% or higher in neutron wavelength from 0.22 nm to 0.77 nm. Compared to |P1·P2| in a 1 T magnetic field in an electro-magnet, the performance is confirmed to be comparable to the existing sample environment. This polarization is also confirmed to be almost unchanged from 0.25 to 6.2 mT. This system is available for user experiments.

3. Deep learning for noise reduction

Because of the limitation of the beamtime in neutron experiment facilities, it has been demanded to shorten the measurement time. However, the reduction in the acquisition time introduces a large statistical noise in the obtained data, resulting in a false structure information from the data analysis. A deep learning technique was developed as a novel method for accelerating the data acquisition without compromising the accuracy of the data analysis [2]. The removal of the statistical noise from the NR data taken in a short acquisition time reduces the measurement time in the NR experiment. Here, we developed a convolutional neural network (CNN) for NR and demonstrated the accurate data analysis for the NR data which was obtained in a ten-time shorter measurement time compared with the conventional experiment.

A neural network with hidden layers consisting of one-dimensional convolution, batch normalization, and rectified linear unit was used for supervised deep learning. The data set for the training was generated by the neutron event simulator developed for SHARAKU. More than 200000 layered structures were generated, then the theoretical NR profile was calculated and the experimental NR data with a short acquisition time was simulated for each structure as the supervising and input data for deep learning. The blue circles in Fig. 3 show the experimental data in a 20-fold shorter acquisition time compared with a conventional experiment. On the other hand, the green curve in Fig. 3 indicates the data obtained by a longer acquisition time, indicating the low noise in the NR data. Comparing them, the

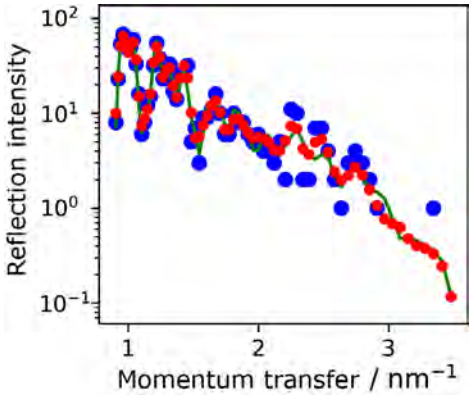

Figure 3. Statistical noise in the NR data obtained in a short measurement time (blue circles) is removed by the deep learning-based technique. The resultant NR data (red) is in good agreement with the ideal data without statistical noise (green curve).

NR data points taken in the short acquisition time are scattered by the large statistical noise. The red circles in Fig. 3 were obtained by removing the noise component from the NR data taken in the short time (blue data in Fig. 3) by data processing with the deep learning. The processed data is in good agreement with the NR data without noise (green curve). This indicates that the deep learning-based noise reduction method enables the reduction of the measurement time by over 10 times without a loss of the accuracy of the experimental data.

This method will considerably improve the time resolution in an *operando* measurement to examine the time evolution of the interface structure. Moreover, it will allow state-of-the-art methods which require unrealistic beamtime in conventional instruments [3]. This noise reduction function based on deep learning will be implemented in the analysis web application for SHARAKU and it would open a new horizon in surface/interface science.

References

[1] Y. Zhong et al, *AIP Advances*, **10**, 015323 (2020).
[2] H. Aoki et al, *Sci. Rep.*, **11**, 22711 (2021).
[3] H. Aoki et al, *Langmuir*, **37**, 196 (2021).

H. Aoki[1,2], T. Hanashima[3], K. Soyama[4], D. Yamazaki[5], N. Miyata[3], K. Akutsu[3], and S. Kasai[3]
[1]Neutron Science Section, Materials and Life Science Division, J-PARC Center; [2]Institute of Materials Structure Science, KEK; [3]Neutron Science and Technology Center, CROSS; [4]Administration and Operations Support Division, J-PARC Center; [5]Neutron Instrumentation Section, Materials and Life Science Division, J-PARC Center

Status of SENJU 2021

1. Introduction

SENJU is a TOF single-crystal neutron diffractometer designed for precise crystal and magnetic structure analyses under multiple extreme environments, such as low-temperature, high-pressure, and magnetic-field, as well as for taking diffraction intensities of small single crystals with a volume of less than 1.0 mm^3 down to 0.1 mm^3 [1]. Since the operation of SENJU started in 2012, our instrument group has carried out continuous commissioning and upgrades.

In 2021, we developed a sample stick with an automatic sample changer, an automatic data-processing wizard for the STARGazer-Online, and a multi-crystal data processing method. In addition, we also report on the purposes of the instrument beam-time for SENJU.

2. Development of a sample stick with an automatic sample changer

Selecting a good quality sample crystal is one of the most crucial points for single-crystal neutron diffraction measurement. Screening of single crystals is often carried out to find a good quality single crystal, but it takes a long time and requires human resources to change the sample. We developed a sample stick with an automatic sample changer to achieve the sample screening automatically. The sample stick has five aluminum sample trays to set candidate crystals for measurement. The trays are arranged along the vertical direction and can move in upper and lower directions. The distance between the two trays is 50 mm, and only one of the trays is in the direct beam. The movement of trays is controlled by using the IROHA2 system. Suppose a SENJU user has several candidates of crystal for measurement. In that case, the user can find the most qualified single crystal by setting the crystals in the trays and performing sequential diffraction measurements using the sample stick.

3. Automatic data processing wizard for the STARGazer-Online

STARGazer-Online is a data processing application for SENJU, which works on several types of web browsers (Chrome, Safari, and Firefox). The application is made from several functional components, and SENJU users have to execute each component in the correct order to process the SENJU diffraction data correctly. So, for beginners of the single-crystal diffraction technique, using STARGazer-Online has been a complicated task. To solve this problem, we developed an automatic data processing wizard for the STARGazer-Online.

This wizard requires only specific information for each experiment, such as run numbers, sample environment device, and minimum *d*-spacing. The wizard automatically determines the cell parameters and UB matrix, integrates Bragg peak intensities, and outputs reflection files available for some structure refinement software such as JANA2006 and SHELXL. After determining cell parameters and UB matrix refinement, the user can verify whether the data processing proceeds appropriately. After the intensity integration, the obtained intensity distribution of the Bragg reflection is displayed as a summary. The wizard makes the SENJU data processing more accessible. We expect the users to iterate the data processing more comfortably and find the optimal data processing conditions for their diffraction data to produce high-quality structural refinement.

4. Development of a multi-crystal data processing method

One of the severe problems in single-crystal neutron diffraction is the sample volume. The time required for data collection at SENJU is expressed as "measurement time per crystal orientation" times "number of orientations," where the "measurement time per crystal orientation" is determined by the incident beam intensity and sample volume. Therefore, to measure small samples in the limited beam time without increasing the direct beam intensity or sample volume, reducing the "number of orientations" is essential. To achieve this purpose, we investigated the multi-crystal measurement, in other words, the simultaneous diffraction measurement of multiple single-crystal samples. By measuring several crystals simultaneously, data for different orientations can be obtained at once, which is expected to reduce the overall measurement time.

One of the essential points in the multi-crystal measurement is determining the UB matrix for every single crystal, and we tried the "auto two-Bragg indexing method" proposed by T. Sakakura [2]. This method requires the cell parameters and proceeds as follows:

1. Find Bragg peaks from the raw data and calculate the scattering vector in the reciprocal space for each Bragg peak.
2. Calculate the absolute length of each scattering vector and assign the presumable index estimated from the cell parameters.

3. Select any two peaks and calculate the UB matrix by the two-Bragg method.
4. Calculate the indexes of other peaks by the UB matrix. The matrix is accepted if reasonable indexes are assigned to peaks above the threshold. If not, the matrix is rejected.
5. Remove the indexed peaks and repeat processes 3 and 4 till all peaks are indexed.

We tested this method with ruby crystals. We measured diffraction data with three ruby crystals and six ruby crystals. The crystals' size was ϕ1.0 mm, and the measurement time was 1 hour for both conditions. The auto two-Bragg indexing method worked well for both diffraction data, and suitable UB matrices for all ruby crystals were successfully obtained.

The integration intensities of the Bragg peaks and structure refinement following the UB matrices determination worked well for the three crystals data, while the influence of peak overlapping became unignorable for the six crystals data. The next challenge is the intensity integration of the overlapping Bragg peaks, and we are now testing some methods.

5. Use of the instrument beam time

In 2021, the instrument beam time was used mainly for measurements of standard samples, and a vanadium-nickel alloy for calibration of the detector efficiency.

References

[1] T. Ohhara et al., J. Appl. Cryst., 49 120 (2016)
[2] T. Sakakura, CrSJ meeting (2019)

T.Ohhara[1], R. Kiyanagi[1], A. Nakao[2], K. Munakata[2], Y. Ishikawa[2], K. Moriyama[2], I. Tamura[1], and K. Kaneko[1]
[1]*Neutron Science Section, Materials and Life Science Division, J-PARC Center;* [2]*Neutron Science and Technology Center, CROSS*

Engineering Material Diffractometer TAKUMI

1. Introduction

TAKUMI is a neutron diffractometer dedicated for research in engineering materials sciences, which was installed at Beamline 19 in the MLF of J-PARC. Careful analysis of the Bragg peaks in a neutron diffraction pattern can reveal important structural details of a sample material, such as internal stresses, phase conditions, dislocations, texture, etc. Experiments in TAKUMI vary from internal strain mapping in engineering components, microstructural evolutions during deformations of structural or functional materials at various temperatures, microstructural evolutions during manufacturing (thermo-mechanical) processes, to texture analyses of engineering materials.

2. User program and publications

In FY2021, 28 general-use programs, 1 long-term program and 1 project-use program were successfully conducted on TAKUMI. Note that due to the effects of the COVID-19 restrictions, 7 experiments were performed by beamline staff on behalf of users. The statistics about the experimental types and the sample materials of the experiments conducted during FY2021 are summarized in Fig. 1. More than 60% of the beamtime was occupied by in-situ measurement during a loading test. On the other hand, 24% of the beamtime was used for strain mapping experiments for internal strain (stress) analysis of mechanical parts. Iron and steel, because of their importance as structural materials, accounted for 41% of the total samples. Summarizing the percentages for light metals (Al-, Mg- and Ti-based alloys, 19%) and metals and alloys (Ni-based superalloy, high-entropy alloys and other alloys, 32%), 91% of the beamtime was used for experiments with metallic material samples. In contrast, the percentage of experiments with non-metallic samples (rocks and ceramics) was only 5%.

Thanks to the efforts of the users and the collaborators, 20 papers and 1 proceedings paper using the data measured at TAKUMI have been published in FY2021. The statistics on experimental types and sample materials used in papers published during FY2021 are summarized in Fig. 2. In addition, the data were also used in 1 doctoral thesis and 1 master's thesis. Some highlights of the papers are introduced below:

(a) "**Stacking fault driven phase transformation in CrCoNi medium entropy alloy**", by Haiyan He, *et al*. [1]. A bulk *fcc*-to-*hcp* phase transformation in CrCoNi medium entropy alloy at 15 K under tensile loading was revealed by in-situ loading study with neutron diffraction.

(b) "**Quantifying internal strains, stresses, and dislocation density in additively manufactured AlSi10Mg during loading-unloading-reloading deformation**", by Xingxing Zhang, *et al*. [2]. In-situ neutron diffraction is employed to explore the residual strains, stresses, and dislocation density in the AlSi10Mg alloy manufactured via laser powder bed fusion during loading-unloading-reloading deformation.

(c) "**Effect of deformation-induced martensitic transformation on nonuniform deformation of metastable austenitic steel**" by Wenqi Mao, *et al*. [3]. A digital image correlation technique combined with in-situ neutron diffraction was used for the first time to investigate the Portevin–Le–Chatelier (PLC) behavior in an Fe–24Ni–0.3C steel.

(d) "**Analysis of residual stress in steel bar processed by cold drawing and straightening**", by Satoru Nishida, *et al*. [4]. The internal residual stress distributions in a free-cutting steel bar processed by cold drawing and straightening were investigated by neutron diffraction technique.

3. Upgrades and maintenances

The following upgrades and maintenance were performed to make TAKUMI more user-friendly and more stable in FY2021:

(1) The use of a new sample chamber developed for low-temperature deformation tests began on a trial basis. More rapid temperature changes and simplified sample exchange were realized by this chamber.

(2) The lighting in the radiation shielding chamber and the camera system for observing the sample were updated. These allow more accurate sample positioning.

(3) Some of the detector electronics and the DAQ electronics, which had aged due to more than 10 years of operation, were updated.

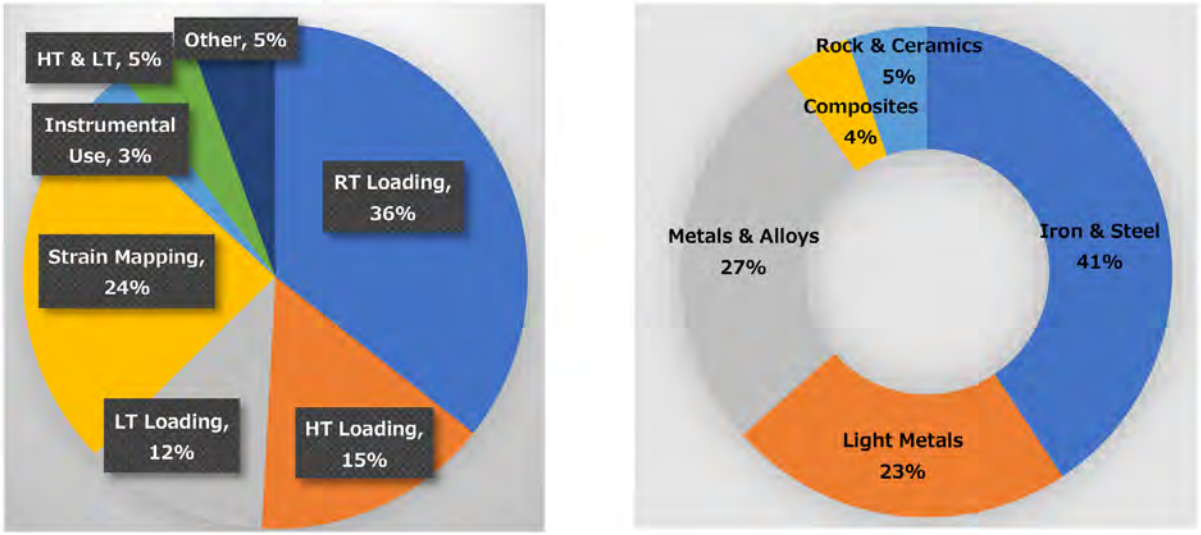

Figure 1. The statistics of (a) the kinds of experiment which were conducted at TAKUMI and (b) the kinds of material used in these experiments in FY2021. The percentages shown indicate the beamtime (in days).

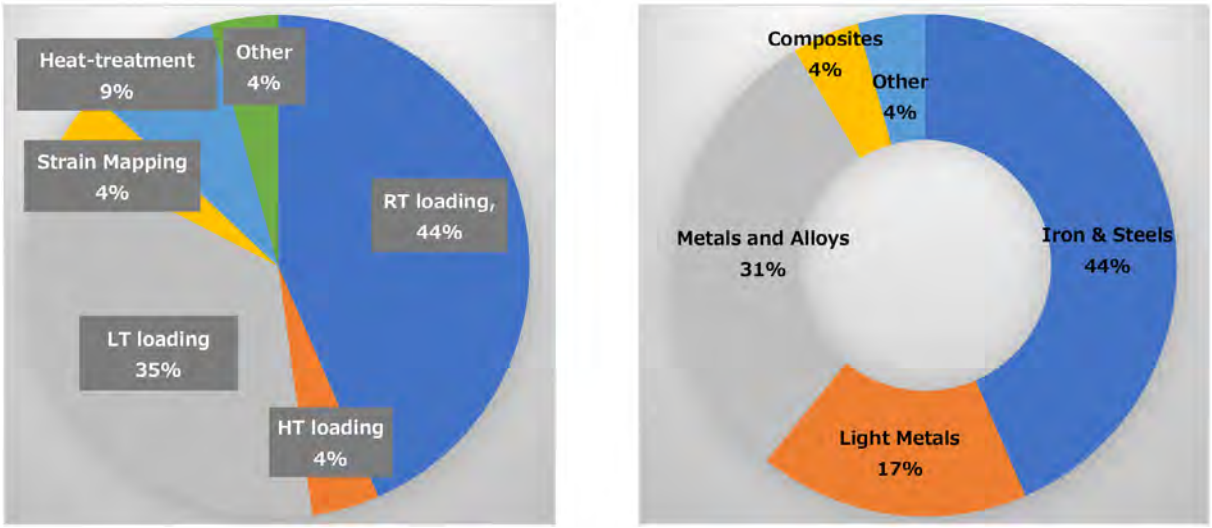

Figure 2. Statistics on (a) the types of experiments performed at TAKUMI and (b) the types of materials used in those experiments for papers using TAKUMI published during FY2021. The percentages shown indicate the beamtime (in days).

References

[1] H. He, M. Naeem, F. Zhang, Y. Zhao, S. Harjo, T. Kawasaki, B. Wang, X. Wu, S. Lan, Z. Wu, W. Yin, Y. Wu, Z. Lu, J-J. Kai, C-T. Liu, X-L. Wang, *Nano Letters*, **21**, 1419-1426 (2021).

[2] X. Zhang, H. Andrä, S. Harjo, W. Gong, T. Kawasaki, A. Lutz, M. Lahres, *Materials & Design*, **198**, 109339 (2021).

[3] W. Mao, W. Gong, T. Kawasaki, S. Harjo, *Materials Science and Engineering*: A, **837**, 142758 (2021).

[4] S. Nishida, S. Nishino, M. Sekine, Y. Oka, S. Harjo, T. Kawasaki, H. Suzuki, Y. Morii and Y. Ishii, *Materials Transactions*, **62**, 667-674 (2021).

T. Kawasaki[1], W. Gong[1], W. Mao[1], S. Harjo[1], and K. Aizawa[2]

[1]*Neutron Science Section, Materials and Life Science Division, J-PARC Center;* [2]*Materials and Life Science Division, J-PARC Center*

The Current Status of the Versatile Neutron Diffractometer, iMATERIA

1. Introduction

Ibaraki Prefecture, local government of Japan's area where the J-PARC sites are located, has decided to build a versatile neutron diffractometer (IBARAKI Materials Design Diffractometer, iMATERIA [1]) (fig. 1) to promote industrial applications for the neutron beam in J-PARC. iMATERIA is planned to be a high-throughput diffractometer that could be used by materials engineers and scientists in their materials development work, including chemical analytical instruments.

The applications of neutron diffraction in materials science are (1) to do structural analyses of newly developed materials, (2) to clarify the correlation between structures and properties (functions), and (3) to clarify the relation between structural changes and improvements of functions, especially for practical materials. A diffractometer with super high resolution is not required to achieve those goals. The match of features like intermediate resolution around $\Delta d/d = 0.15\%$, high intensity and wide d coverage is more important.

This diffractometer is designed to look at a decoupled-poisoned liquid hydrogen moderator (36 mm, off-centered) (BL20), and it has an incident flight path (L1) of 26.5 m, with three wavelength selection disk-choppers and straight neutron guides with a total length of 14.0 m. The instrumental parameters are listed in Table 1. There are four detector banks, including a low-angle and small-angle scattering detector bank. The angular coverage of each detector bank is also shown in Table 1. The rotation speeds for the disk-choppers are the same, with a pulse repetition rate of 25 Hz for the most applications (SF mode). In this case, the diffractometer covers $0.18 < d$ (Å) < 2.5 with $\Delta d/d = 0.16\%$ and covers $2.5 < d$ (Å) < 800 at three detector banks of 90-degree, low-angle and small-angle with gradually changing resolution. When the speed of the wavelength selection disk-choppers is reduced to 12.5 Hz (DF mode), we can access a wider d-range, $0.18 < d$ (Å) < 5 with $\Delta d/d = 0.16\%$, and $5 < d$ (Å) < 800 with gradually changing resolution with doubled measurement time compared to the SF mode.

2. Current status

All of the four banks, high-resolution bank (BS bank), special environment bank (90-degree bank), low-angle bank and small-angle bank, are operational. It takes about 5 minutes (in DF mode) to obtain 'Rietveld-quality' data in the BS bank at 700 kW beam power for about 1 g of standard oxide samples.

Figure 2 shows a typical Rietveld refinement pattern for $LiCoO_2$ sample, cathode material for lithium-ion battery (LIB), at the BS bank by the multi-bank analysis function of Z-Rietveld software [2]. It takes 20 min

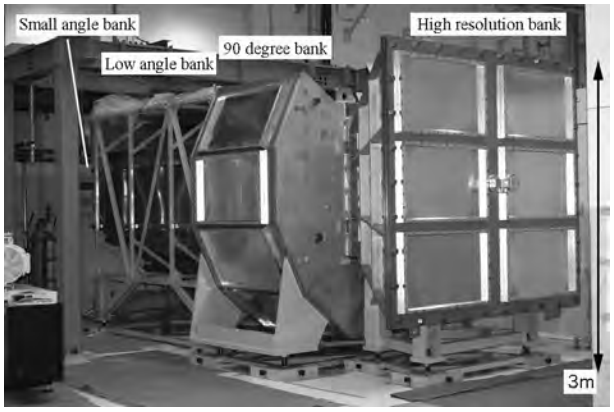

Figure 1. IBARAKI Materials Design Diffractometer, iMATERIA without detector for each bank and instrument shielding. The BS bank, 90-degree bank, and low-angle bank, can be seen from right to left. The small-angle detector bank, which is not shown in the picture, is situated in the low-angle vacuum chamber (left-hand side of the picture).

Table 1. Instrumental parameters of iMATERIA. L2 is the scattered flight path. The d-range (q-range) for each bank is the maximum value for 2-measurement mode.

L1	26.5 m	
Guide length		Total 14 m (3section)
Position of Disk choppers		7.5 m (double)
		11.25 m (single)
		18.75 m (single)
High	2θ	$150^\circ \le 2\theta \le 175$
Resolution	L2	2.0 – 2.3 m
Bank	d-range	$0.09 \le d\ (A^\circ) \le 5.0^\circ$
Special	2θ	$80^\circ \le 2\theta \le 100^\circ$
Environment	L2	1.5 m
Bank	d-range	$0.127 \le d\ (A^\circ) \le 7.2$
Low	2θ	$10^\circ \le 2\theta \le 40^\circ$
Angle	L2	1.2 – 4.5 m
Bank	d-range	$0.37 \le d\ (A^\circ) \le 58$
Small	2θ	$0.7^\circ \le 2\theta \le 5^\circ$
Angle	L2	4.5 m
Bank	q-range	$0.007 \le q\ (A^{\circ -1}) \le 0.6$

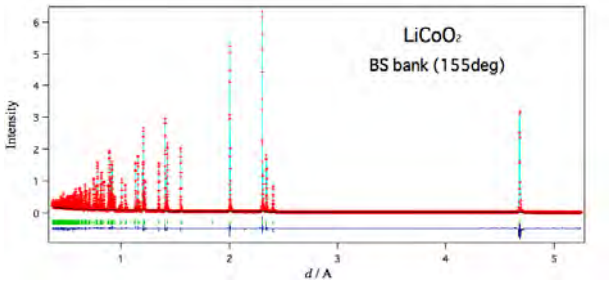

Figure 2. Rietveld refinement pattern for $LiCoO_2$ at the BS bank of iMATERIA.

in DF mode to collect the available Rietveld data, due to the high neutron absorption cross section for natural Li (σ_s^{Nat} = 70 barn).

3. Sample environments

The automatic sample changer is the most important sample environment for high-throughput ex-periments. Our automatic sample changer [3] consists of a sample storage, elevating system of two lines, two sets of pre-vacuum chambers and a sample sorting system. We can handle more than 600 samples continuously at room temperature (RT) without breaking the vacuum of the sample chamber.

The vanadium-furnace (~900°C), the gas flow furnace (~1000°C), and the 4 K and 1 K cryostats are ready for experiments.

The rapid heating/quenching furnace with automatic sample changer (RT – 1273 K with heating speed 10 K/s and cooling speed >20 K/s) [4] and the universal deformation testing machine (max loading 50 kN with RT – 1273 K) [5] are available for texture measurements.

The in-operando charge and discharge measurement system for LIB with a sample changer is available in cylindrical, coin and laminated types of batteries.

4. Development of multiscale measurement method for fuel cell materials

We have developed a new glass slit (fig. 3) for multi-scale measurement. This slit makes it possible to simultaneously measure small-angle scattering and wide-angle diffraction to obtain structural information.

We also have measured the battery materials using the developed technology and clarified their structural parameters. [6] This method will enable multi-scale measurements of electrolyte and electrode materials from crystal structure to nano-level structure, which is necessary for improving solid fuel cell performance.

Figure 3. The newly developed glass slit.

References

[1] T. Ishigaki, et al., Nucl. Instr. Meth. Phys. Res. A 600 (2009) 189-191.
[2] R. Oishi, et. al., Nucl. Instr. Meth. Phys. Res. A 600 (2009) 94-96.
[3] A. Hoshikawa, et al., J. Phys.: Conf. Ser. 251 (2010) 012083.
[4] Y. Onuki, et. al., Metall. Mat. Trans. A. 50 (2019) 4977-4986.
[5] Y. Onuki, et. al., Quantum Beam Sci., 4 (2020) 31.
[6] H. Takahashi., Prepare for publication.

T. Ishigaki and A. Hoshikawa
Frontier Research Center for Applied Nuclear Sciences, Ibaraki University

Status of the High Intensity Total Diffractometer (BL21, NOVA)

1. Introduction

Total scattering is a powerful technique to analyze non-crystalline structure in materials with atomic Pair Distribution Function (PDF). NOVA was designed to perform total scattering and is the most intense powder diffractometer with reasonable resolution ($\Delta d/d \sim 0.5$ %) in J-PARC. It is easy to adapt NOVA to a wide variety of fields: liquids, glass, local disordered crystalline, magnetic structure of long lattice constant and so on.

2. Installation of ^{3}He cryostat

Since the introduction of the radial collimator (NOVARC) [1], which is effective in reducing background from sample environment (SE) equipment, NOVA has been expanding the use of common SE ones managed by the SE team. In 2021, we installed the ^{3}He cryostat (common SE equipment) and implemented the linkage system between EPICS control and the IROHA2 sequence server.

As for the control system, the ^{3}He cryostat is controlled by a PLC manufactured by Keyence Co. With the cooperation of Mr. Y. Yamauchi (NAT) and Mr. R. Takahashi (JAEA) in the SE team, Mr. Y. Yasu (KEK) constructed a system that controls the PLC via the EPICS GUI tool (CSS GUI), which is commonly used in accelerator control software, and an online monitor for temperature using Grafana GUI software (Fig. 1). The measurement sequence is automatically controlled by sending commands from the IROHA2 sequence server to the EPICS through a façade (Fig. 2).

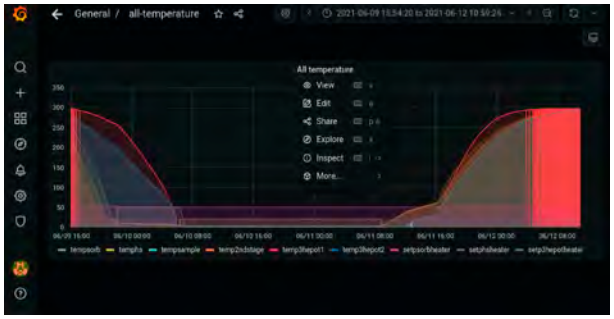

Figure 1. Temperature logging with Grafana GUI software.

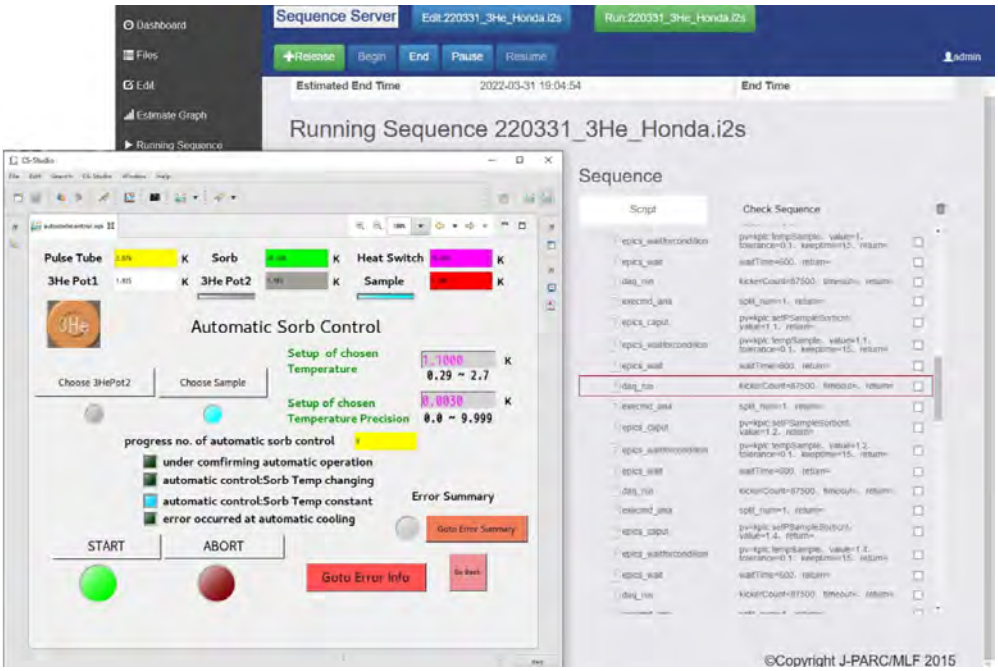

Figure 2. Automatic measurement sequence with IROHA2 sequence server and CSS GUI.

Using these systems, we performed neutron diffraction experiments using ErF_3, which has an antiferromagnetic phase transition at T_N = 1.05 K and shows a non-collinear magnetic structure [2]. The powder sample was provided by BL08. Figure 3(a) shows the scattering profile of the 10-minute measurement, Fig. 3(b) indicates the temperature dependence of the integrated intensity of the magnetic scattering Bragg peak 100 (d~6.4 Å), which reflects the antiferromagnetic magnetic structure, and Fig. 3(c) exhibits the temperature dependence of the diffraction profiles. The temperature is that of the sample stage.

We observed that the integrated intensity of the magnetic scattering peak below the transition temperature increased order parametrically with temperature cooling. From the results, we confirmed that the ^{3}He cryostat experiment was feasible for NOVA.

We have also prepared the manuals for EPICS (User's Guide for Control, Monitoring, and Archive System) and the one for the ^{3}He cryostat experiment at NOVA. Furthermore, the experiment with these systems installed at BL02 was successfully completed.

Acknowledgement

We would like to thank Mr. H. Maya for his technical support in operating NOVA. The operation and developments of NOVA was performed under the S1-type program (2019S06) approved by the Neutron Scattering Program Advisory Committee of IMSS, KEK.

References

[1] K. Ikeda et al., MLF Annual Report 2017, 110-111.
[2] K. Kramer et al., Eur. J. Solid State Inorg. Chem. 33, 273 (1996).

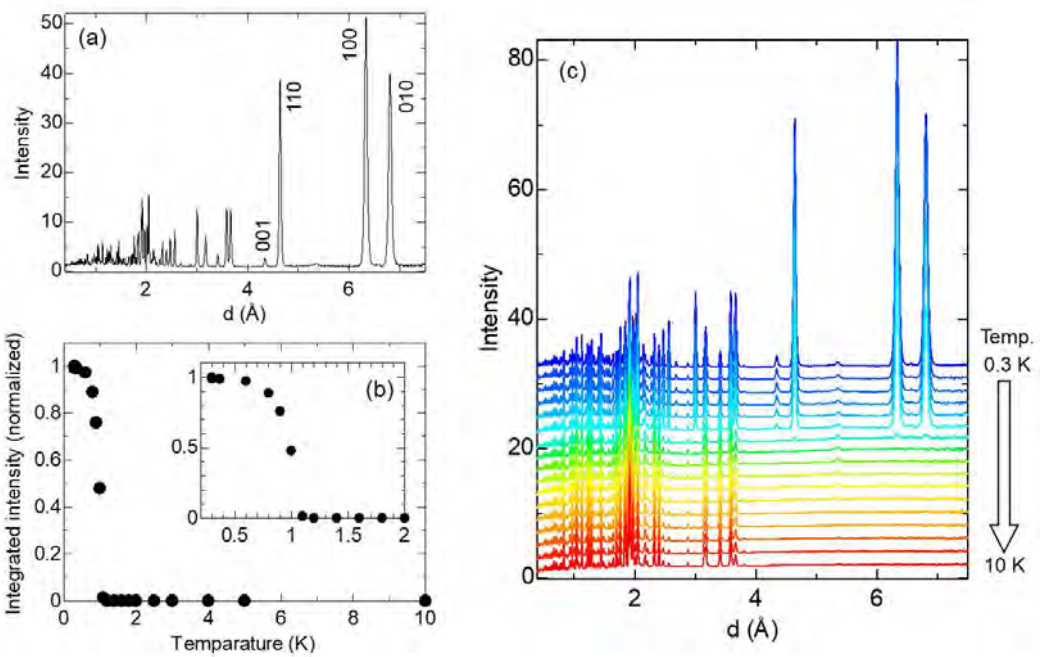

Figure 3. (a) 10-minute measurement profile of ErF_3 at the lowest temperature, (b) temperature dependence of integrated intensity of 100 magnetic scattering peaks, and (c) temperature dependence of the diffraction profiles.

T. Honda[1,2,3], K. Ikeda[1,2,3], T. Otomo[1,2,3,4], H. Ohshita[1,2], and M. Tsunoda[4]

[1]Institute of Materials Structure Science, KEK; [2]Neutron Science Section, Materials and Life Science Division, J-PARC Center; [3]Department Materials Structure Science, The Graduate University for Advanced Studies, SOKENDAI; [4]Graduate School of Science and Engineering, Ibaraki University

Current Status of the Energy-Resolved Neutron Imaging System RADEN

1. Introduction

The Energy-resolved neutron imaging system "RADEN", installed at beamline BL22 in the MLF of J-PARC, is a dedicated instrument for wavelength/energy-dependent neutron imaging experiments, which utilizes fully the short-pulsed neutron's nature [1]. A variety of imaging experiments have been conducted at RADEN, such as Bragg-edge imaging, neutron resonance absorption imaging, and polarized pulsed neutron imaging, in addition to the conventional neutron imaging. RADEN started the user operation in 2015, and after that, about 40 user programs have been conducted every year. In this report, the results of the technical development and remarkable application studies conducted at RADEN are described.

2. Energy-selective imaging by fast-gate image intensifier system

A neutron imaging detector system consisting of a CMOS camera and an optical image intensifier (I.I.) has been developed for a neutron energy/wavelength selective imaging [2]. The fast gate operation of the optical I.I., which opened or closed the electronic shutter very quickly by an external trigger signal, was utilized to select neutron energy/wavelength by amplifying the incident light from the scintillator during a given Time-of-flight (ToF) period. The output light signal from the I.I. was accumulated by the CMOS sensor, and an image, which had information only from the selected neutron energy/wavelength, was created (see Fig. 1). Because the delay and the width of the timing gate was controlled by applying a pulsed electric signal to I.I. using a digital delay generator, neutron energy selection could be done in an easier and quicker way compared with that by using the chopper system. Moreover, it is beneficial that this system allows to easily adjust the field of view and the spatial resolution suitable to the object and that exposure time needed to obtain one image is very short in comparison with the counting type image detectors. However, when spectral analysis with fine energy/wavelength resolution is required, the use of counting type detectors is more suitable than this camera system. Because the accessible energy resolution of this system is relatively coarse (around 1%), scanning the delay of the timing gate is needed to obtain spectra.

As application of this system, we have visualized iced and liquid water distributions by neutron energy selective imaging [2]. In our previous work, we conducted spectral analysis by using event type detector position by position [3], but we obtained images at two different neutron energies and divided their transmission images to produce an image to identify iced and liquid water distribution in this work. The resulting images are shown in Fig. 2. The exposure time was effectively decreased, and a large field of view could be realized.

3. Application study: visualizing water distribution in a driving fuel cell

The water visualization in a fuel cell used in the Fuel Cell Electric Vehicle (FCEV) has been conducted under the FC-Platform program supported by NEDO. A commercial full-size single fuel cell installed in the second generation TOYOTA MIRAI was used for the experiment. In order to carry out the operation of the fuel cell inside the shielding of RADEN beamline and to conduct in-operando imaging experiments, we have prepared a

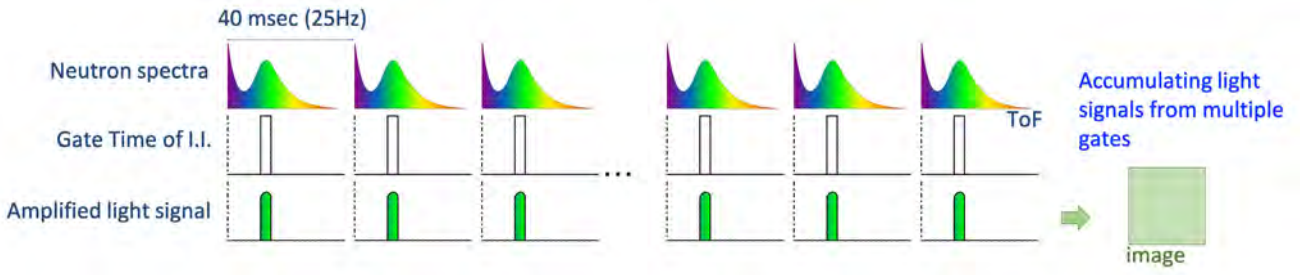

Figure 1. A schematic illustration of energy/wavelength selective neutron imaging using an optical I.I. with fast gate function. By means of the time gate, synchronized with the neutron pulse generation, it is possible to amplify the incident light from the scintillator screen only a given ToF and produce an image of selected neutron energy.

special equipment. At first, RADEN was equipped with a gas-supply system, a hydrogen dilution unit with nitrogen gas generator, hydrogen gas monitors, and leak detectors as safety devices. A fuel cell operation kit and a load unit were brought from the automobile company. And then, constraint plates for the cell assembly were designed by taking into account the neutron transmittance. These works were all done under the collaboration with several automobile companies.

Figure 3a shows the experimental setup of the fuel cell assembly. The cell was operated along the practical test procedure for the fuel cell of FCEV, and the load performance test was conducted. The neutron imaging experiments were performed by using a camera type detector system consisting of a CMOS camera and an optical I.I.. The exposure time was 1 sec, and it was repeated 300 times. The distribution image of generated water was derived by dividing an image obtained during the cell operation with that of a dried cell. The results of the load performance test clearly indicated different water distribution as load conditions. In addition, the amount of observed water was very little, and the shape of the channel was not observed clearly (Fig. 3b).

4. Summary

RADEN is used in various fields, not only scientific but also industrial, and its application has been spreading widely. The RADEN group continues the development works on devices and on imaging techniques and demonstration studies so as to promote user programs from broader fields.

References

[1] T. Shinohoara et al., Rev. Sci. Instrum., **91**, 043302 (2020).

[2] K. Isegawa et al., Nuclear Inst. and Methods in Physics Research, A **1040**, 167260 (2022).

[3] Y. Higuchi et al., Phys. Chem. Chem. Phys., **23**, 1062 (2021).

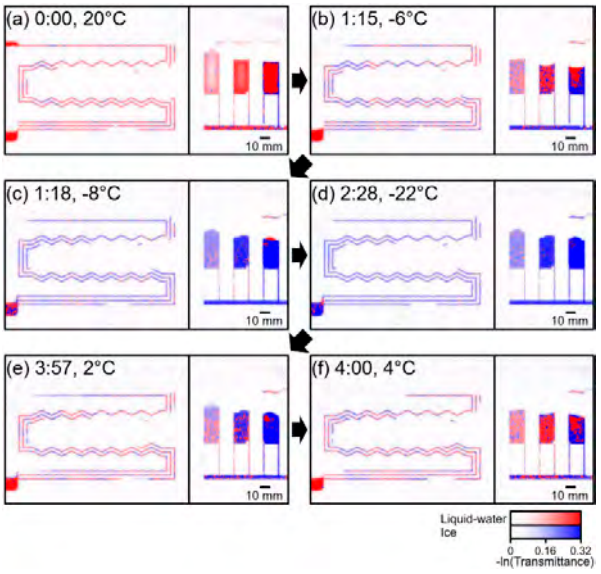

Figure 2. Example of visualization of iced and liquid water distribution by using energy selective neutron imaging [2]. Liquid water is represented with red color and iced water is indicated with blue.

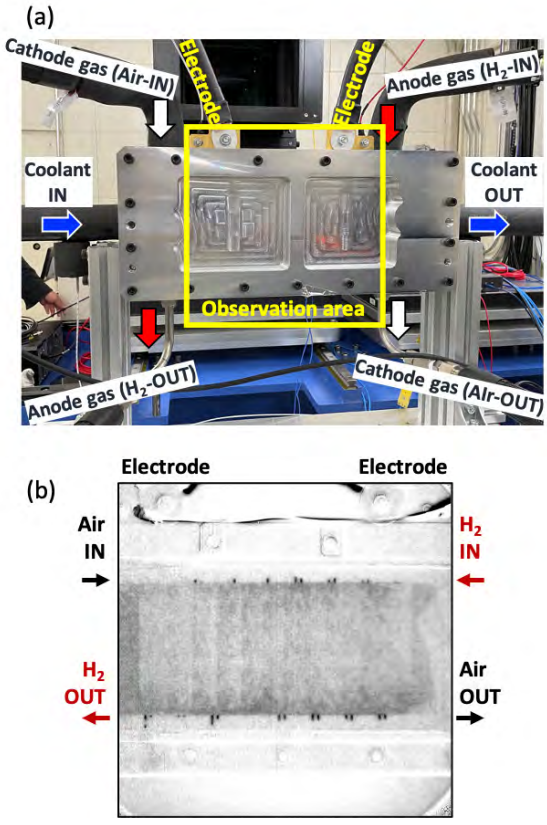

Figure 3. Neutron imaging experiment of the commercial fuel cell used in FCEV. (a) A photograph of the experimental setup of cell assembly. (b) A water distribution image obtained by neutron imaging.

T. Shinohara[1], T. Kai[1], K. Oikawa[1], Y. Tsuchikawa[1], K. Isegawa[1], K. Hiroi[1], Y. Su[2], H. Hayashida[3], J. D. Parker[3], Y. Matsumoto[3], and Y. Kiyanagi[4]

[1]Neutron Science Section, Materials and Life Science Division, J-PARC Center; [2]Technology Development Section, Materials and Life Science Division, J-PARC Center; [3]Neutron Science and Technology Center, CROSS; [4]Hokkaido University

Polarized Neutron Spectrometer POLANO

1. Introduction

POLANO is a direct geometry chopper spectrometer with middle energy and spatial resolution. For the purpose of high-efficient polarization experiments in inelastic scattering technique, the POLANO was optimized for high transfer energy (HTE) polarization analysis [1–3]. The POLANO opened to a part of user program since 2019 with only unpolarized neutron experiment. Some of the unique techniques and ideas of time-of-flight (tof) method with a so-called event recording data acquisition processes came up. The omega-rotation measurement is one of the excellent ways which enables us to measure entire four-dimensional momentum Q (q_x, q_y, q_z) and energy E spaces. POLANO can also be available to measure the inelastic signals with the multi-Ei technique, though this is not new technique but resulting event recording system of the tof method. Utilizing the above-mentioned technique, a reasonable quality of data is being obtained, and scientific results (articles) will be generated using the POLANO spectrometer.

We also made significant efforts to develop and install polarization devices, including magnetic and related devices in order to realize the HTE polarization. The HTE polarization can be realized by combining SEOP (spin exchange optical pumping) ^{3}He gas spin filter with 5.5 Qc bending mirror analyzer, as explained in the following section. However, even with this technique, the utilized neutron energy is restricted up to around Ef = 45 meV for out-going analyzed neutron energy (final neutron energy) by the reflecting capability of the mirrors. But our final goal for HTE is 100 meV beyond the reactor-based neutron polarization energy.

2. Polarization and magnetic devices

As reported last year, the safety assessment for the laser system and the magnetic device (Helmholtz-coils) has been completed. After addressing some of the issues raised, those devices were installed in the beamline, and test experiments have been performed.

1) SEOP polarizer system:

POLANO is using ^{3}He gas filter known as SEOP system for a polarizer. SEOP system used as a polarizer in POLANO has been under development for a long time. We were making efforts to realize a higher performance device for rather high energy neutron.

The evaluated figure of merit P^2T (P: polarization of ^{3}He spins, T: transmission of neutrons) was optimized for 100 meV neutron energy with the result of 30 atm・cm for ^{3}He gas. The glass cell containing ^{3}He and other gases was originally made in-house using GE180 glass material and reached 80% of ^{3}He spin polarization. Finally, the system has been installed on the beamline for practical use. Figure 1 shows the setup of the SEOP system on the POLANO beamline. A black box containing optical and laser devices in addition to the ^{3}He cell is the main component for the polarizer. The SEOP box and the newly installed straight collimator made of B_4C neutron absorber are on a trestle with vertical driving mechanism, which enables us to swap polarization and unpolarization experiments easily.

2) Magnetic system:

Another crucial item is the magnetic field. The magnetic field is essential for defining quantization axis and keeping the neutron spin polarization as a guide field.

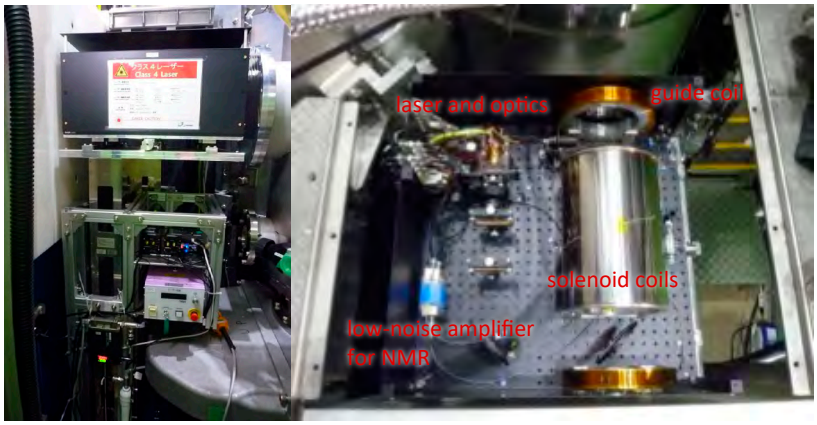

Figure 1. Left: Newly installed setup of the SEOP system. Neutron direct beam goes through the black box (SEOP box), where a glass cell for the ^{3}He gas filter is positioned. Right: The suite of magnets including SEOP ^{3}He polarizer and other optical devices.

Also, indispensable for controlling the spin directions and flipping the spins at a certain position. POLANO's whole magnetic system is composed of several devices like 1) SEOP system (combination of a solenoid coil and two convergence coils), 2) guide field at the entrance of the vacuum chamber made of neodymium boron permanent magnet, 3) asymmetric Helmholtz coils (HC) at the sample position, 4) fan-shaped magnet after the sample, then 5) analyzer mirror (yoke). A development of the HC system and innovative design of the fan magnet can be a key to the entire magnetic system of POLANO. As shown in Fig. 2, the final tests of the HC on the POLANO beamline were carried out. In Fig. 2 on the left, the calculated magnetic field by the set of magnetic devices (analyzer mirror not included) and the actually measured field by 3-dimensional Gauss meter are compared. Both are in good agreement though the ambient magnetic conditions are different.

The HC and its control system were also tested on the beamline. The new design of the installed HC can apply the magnetic field with 20–30 Gauss to any direction in the horizontal plane by adjusting the current of three horizontal coils (H1, H2, and H3) (Fig. 3, left). The magnetic field at sample position yielded by individual coils was measured with changing the current for the coils (Fig. 3 right). Based on these validation test results a remote controlling system was produced, which will allow us to change the conditions and check the status via the YUI program, the main program controlling all devices.

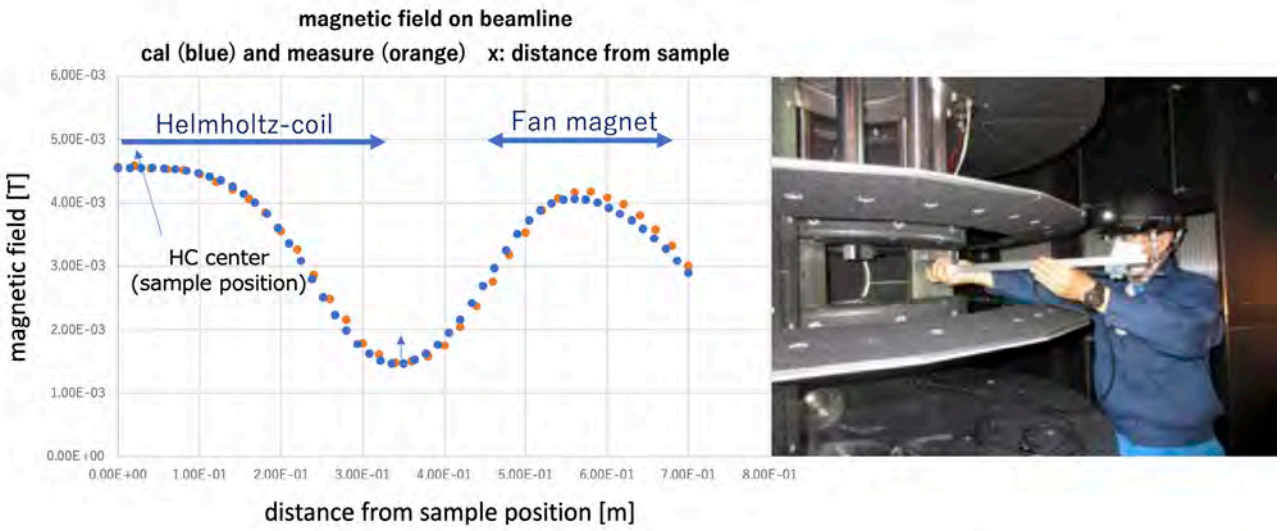

Figure 2. Newly designed fan-shaped magnet. Left: The measured and evaluated magnetic field at each position on the beamline. Right: The magnetic test in the beamline.

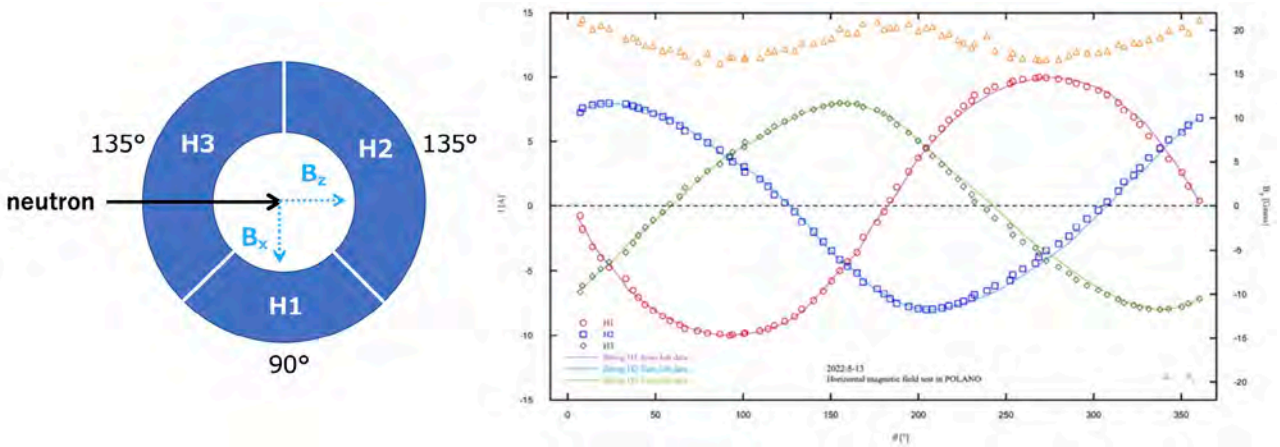

Figure 3. Helmholtz coils and evaluated electric current for maximizing the magnetic field on every scattering direction.

3. Fermi chopper issue

Fermi chopper is one of the key devices used for monochromatizing incoming neutron energies. But last year, we had a very serious and unexplained trouble on the Fermi chopper. The control on phasing was lost because of rotation signal failure. Since we use optical sensors for detecting the rotation, all the circuits, including the sensors, were renewed and the electrical board was re-designed. We also updated the payload (rotor) with all new design. This new rotor has been optimized to gain more neutron flux but is losing some of the energy resolution. Still, the problem has not yet been resolved, and we will continue to work toward a solution.

4. In summary

In this year we have made significant efforts to refurbish and optimize the devices for the upcoming polarization experiments. Now the POLANO is almost ready to launch a polarization experiment via on beam test at MLF beamline BL23. In addition to beam commissioning, developments and updating devices and methods are indispensable to realize spherical polarimetry with pulse neutron beam. In particular, the R&D of new devices, such as a spin flipper after the sample, high polarization ^{3}He filter, and large solid angle SEOP analyzer for the future HTE polarization.

References

[1] T. Yokoo, et al., EPJ Web of Conferences, **83** 03018 (2015).
[2] T. Yokoo, et al., AIP conference proceedings, **1969** 050001 (2018).
[3] MDPI Books, Quantum Beam Science 162 (2019).

T. Yokoo[1,2], N. Kaneko[1,2], D. Ueta[1,2], S. Itoh[1,2], S. Yamauchi[1,2], K. Hayashi[1], T. Ino[1,2], and M. Fujita[3]
[1]Institute of Materials Structure Science, KEK; [2]Neutron Science Section, Materials and Life Science Division, J-PARC Center; [3]Institute for Materials Research, Tohoku University

Sample Environment at the MLF

1. Introduction

The MLF sample environment (SE) team provides the sample environment equipment that is shared for use among the MLF beamlines, the so-called BL-common equipment. The equipment is upgraded according to users' demands. The equipment that can produce extreme sample conditions is also developed.

2. Cryogenics and magnets

We have five pieces of the BL-common cryogenic equipment. In JFY2021, (1) the superconducting magnet was operated for 11 experiments, (2) the ^{4}He cryostat for 8 experiments, (3) the ^{3}He cryostat for 10 experiments, (4) the ^{3}He-^{4}He dilution refrigerator (DR) insert for 12 experiments and (5) the Gifford-McMahon cryofurnace for 2 experiments, including instrument proposals. The equipment was in use for 198 days in total.

The DR was used on SHARAKU (BL17) for the first time, combined with the superconducting magnet. To use the DR on SHARAKU, the metal flexible line that connects the gas handling system with the DR insert (Fig. 1) had to be extended from the original length of 3 m because there was no room to place the gas handling system near the DR insert, which was inserted in the magnet in the shielding hutch of SHARAKU. The length of the metal flexible line was optimized to be 5 m through test experiments and the attainable lowest temperature at the length condition was almost the same as the original one.

The ^{3}He cryostat was used on NOVA (BL21) for the first time. On NOVA, the height of the top flange of the vacuum chamber from the beam center is 250 mm higher than the MLF standard. Therefore, an extension was added in the outer vacuum chamber, the radiation shields and the sample stage of the ^{3}He cryostat to adjust the height (Fig. 2). There was no change in the attainable lowest temperature, 0.3 K, by the extension although the cooling time from room temperature to the lowest temperature was extended from 19 to 25 hours.

Temperature control of the ^{4}He cryostat of POLANO (BL23) was significantly improved by precisely controlling temperatures of two heaters in the cryostat. Figure 3 shows the result of the temperature control of the cryostat from 5 to 250 K. Below 50 K, the temperature at the sample position was controlled within the accuracy of ±0.04 K.

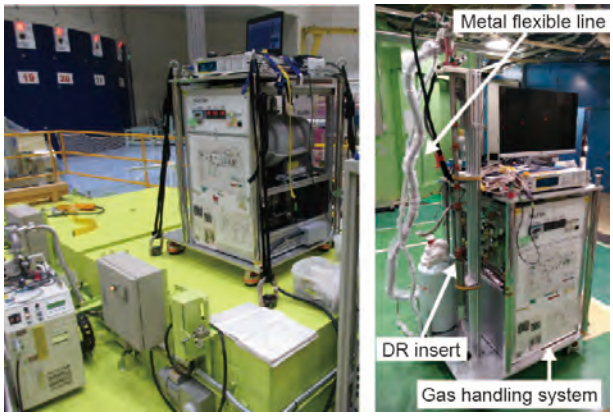

Figure 1. Left: the gas handling system of the DR on the shielding hutch of SHARAKU. Right: the DR system composed of the DR insert, the gas handling system, and the metal flexible line.

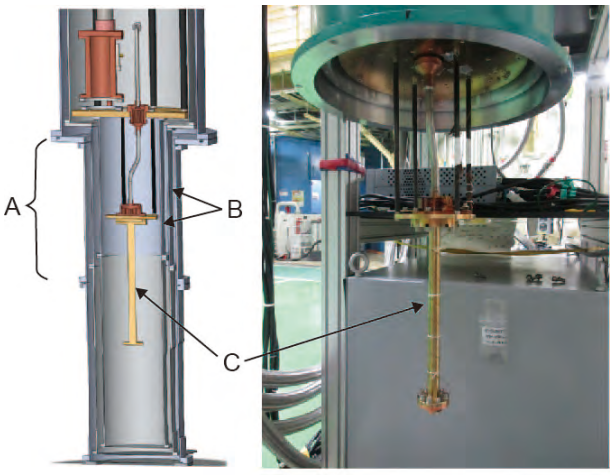

Figure 2. Extension of the outer vacuum chamber (A), the radiation shields (B), and the sample stage (C).

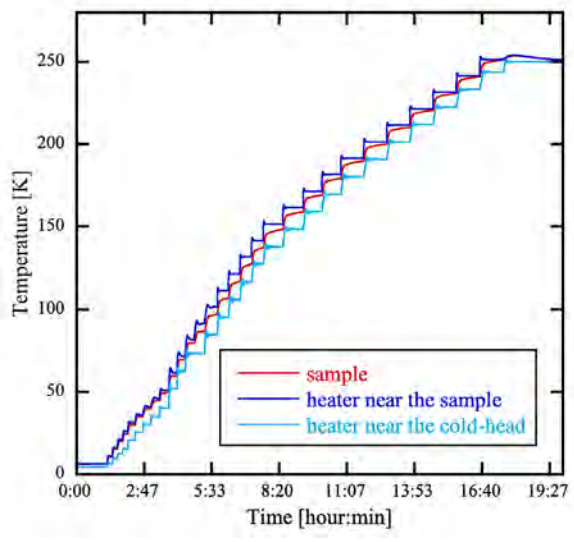

Figure 3. Temperature control of the ^{4}He cryostat of POLANO from 5 to 250 K.

3. Low and high temperatures

The exact temperature at the sample position of the cryofurnace of SuperHRPD (BL08) was examined in the range from 181 to 401 K, by observing the phase transition of a $BaTiO_3$ single crystal. It was verified from the study that the temperature at the heater was the same as that at the sample position.

4. High temperatures

We installed a remote monitoring system for the niobium furnace and received an approval for its use from the MLF equipment safety team in JFY2020. This remote monitoring system was used for the users' experiment on SENJU (BL18) for the first time in JFY2021 (Fig. 4). According to the MLF regulations, the user and/or staff should be present at all times to monitor the furnace for abnormal behavior or fault. However, the installation of the monitoring system released the users and/or staff from the monitoring task throughout the experiment.

5. A pulsed magnet system

In JFY2021, a new coil was developed to obtain pulsed magnetic fields of up to 35 T higher than the previous maximum magnetic field of 30 T. The coil is wound with 1 × 1.5 mm rectangular wire, which is made of a high-tensile strength Cu–Ag alloy (Fig. 5). It has inner and outer diameters of 14 and 50 mm, respectively, with the axial length of 21 mm. The inductance and resistance of the coil, immersed in liquid nitrogen, have been measured using an LCR meter (3522–50, HIOKI) at 100 Hz and a mΩ Hi-Tester (3540, HIOKI), respectively. The measured inductance and the resistance at 77 K are 369 μH and 60 mΩ, respectively. Subsequently, neutron scattering experiments using the pulsed magnet system was performed at NOBORU (BL10). Figure 6 shows the example of the output waveform of the coil. The coil produces 35 T with 6.6 kA at 18.1 kJ charged energy of the capacitor of the power supply.

6. Humidity

In JFY2021, we developed a vapor generator that allows us to control the D_2O/H_2O composition of the vapor continuously. The humidity generator was initially designed for use in the small and wide-angle neutron scattering instrument, TAIKAN (BL15), and neutron reflectometer, SHARAKU. We have constructed the gas flow system based on two concepts: precise and stable humidity generation and compositional changes due to gas mixing. Key features of the system are two saturators and four mass flow controllers, which help generate D_2O and H_2O vapors independently and quickly. The system makes possible small-angle neutron scattering and neutron reflectivity measurements under relative humidity of up to 85% within a temperature range of 25 °C to 85 °C.

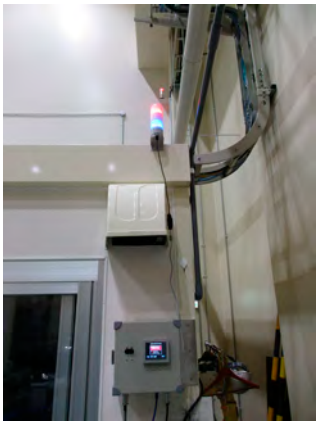

Figure 4. Remote monitoring system, used for high temperature experiment on SENJU.

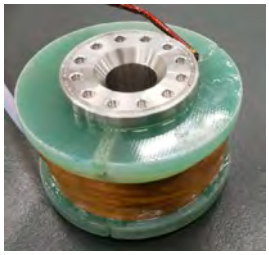

Figure 5. The coil that can generate a high pulsed magnetic field of up to 35 T.

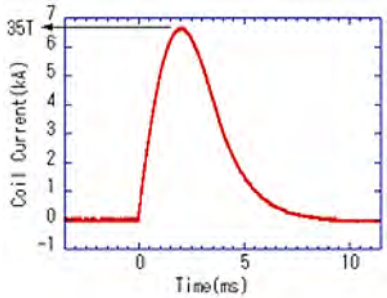

Figure 6. Example of the output waveform of the coil.

R. Takahashi[1], M. Ishikado[2], Y. Yamauchi[3], S. Ohira-Kawamura[1,4], M. Nakamura[3], H. Arima-Osonoi[2], S. Takata[1,4], Y. Su[1], S. Zhang[2], T. Morikawa[2], K. Ohuchi[2], S. Yamauchi[4,5], Y. Sakaguchi[2], M. Watanabe[1], and T. Oku[1]

[1]*Technology Development Section, Materials and Life Science Division, J-PARC Center;* [2]*Neutron Science and Technology Center, CROSS;* [3]*NAT Corporation;* [4]*Neutron Science Section, Materials and Life Science Division, J-PARC Center;* [5]*Institute of Materials Structure Science, High Energy Accelerator Research Organization (KEK)*

Development of Circuit Boards for Optical/Electrical Conversion

1. Introduction

We are developing a two-dimensional neutron detector system using helium-3 gas as a neutron converter [1, 2]. In the detector system, the electric charges generated by the nuclear reaction between neutrons and helium-3 are collected using a detector element. The signals from the detector element are amplified, shaped, and discriminated, and then calculated as the incident position of the neutrons. Various electronic circuits are used in this signal processing, and the electronic circuit components used in signal processing boards are usually discontinued after several years. A new signal processing board was developed to support the discontinuation of the components. In the development process, the signal processing board was also upgraded to increase signal processing speed, etc.

2. System design

Figure 1 shows a schematic of the two-dimensional neutron detector system under development. The blue frame in Fig. 1 depicts the developed signal processing boards. The developed board determines the neutron incident position from the X- and Y-axis signals output from the application specific integrated circuits (ASICs) used in the detector system. The optical signal transmission system mounted on the board is used to transmit the neutron incident position to the data acquisition system. This system can transmit signals over long distances of several kilometers by using optical fibers that are not affected by electrical noises. The developed board uses state-of-the-art field-programmable gate arrays (FPGAs) for digital signal processing, such as determining the position of the incident neutrons. The implemented FPGAs have a finer fabrication process and higher integration than the FPGAs currently in use. As a result, the processing speed is more than twice as fast and the number of logic elements is more than 2.5 times greater, while the power consumption of the FPGA alone is reduced by 70%.

Figure 2 shows photographs of the present and developed E/O converter boards. The present detector system uses two boards for signal processing, one for the x-axis and the other for the y-axis. The developed board uses the latest FPGA to process 128 channels each of x-axis and y-axis, for a total of 256 channels of signal processing on a single board. In addition, the number of optical fibers used is also reduced by using only one board, although optical fibers are currently used for signal transmission in each axis. The reduction in the number of boards enables the omission or shortening of signal wiring, which is expected to reduce electrical

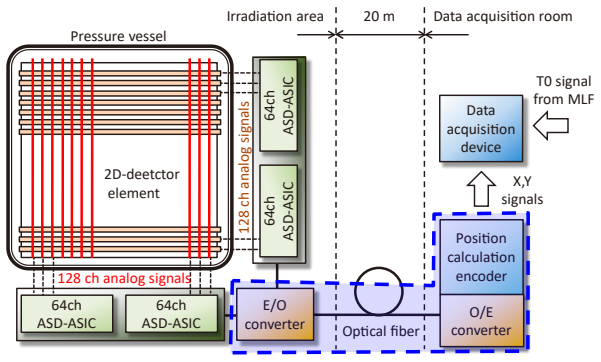

Figure 1. Schematic of a two-dimensional neutron detector system. The blue frame depicts the developed signal processing boards.

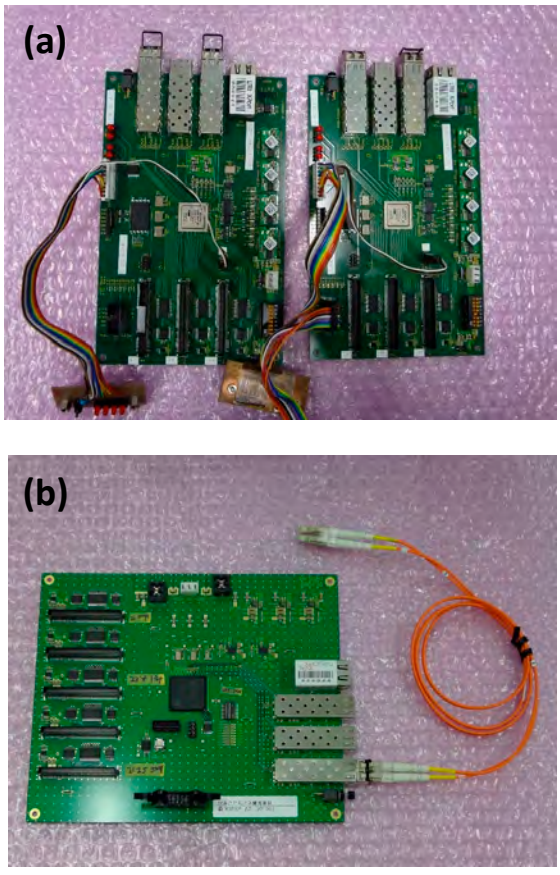

Figure 2. Photograph of (a) present and (b) developed E/O converter boards.

noise and signal delays. Also, since the number of components used is reduced, reliability can be expected to improve in terms of preventing failures at connections and the increased durability of individual components.

3. Operation test

The evaluation tests of the developed board were conducted using a test signal generation module and a real-time data display module. These modules were also created specifically for the development of a gas-based two-dimensional neutron detector system. The test signal generation module can generate detector-simulated signals and is capable of outputting simulated signals at any desired generation cycle and time interval.

The pulse pair resolution was measured by inputting two test-signal pulses into the developed board with varying time intervals and counting the number of pulses output from the board. The measured results are shown in Fig. 3. The horizontal and vertical axes show the time interval of the input double pulse and the measured counting loss, respectively. It can be seen that the counting loss increases from 0.41 μs as the time interval decreases. The developed board can discriminate input signals with time intervals over 0.41 μs.

Figure 4 shows the results of evaluating the counting rate capabilities by inputting periodic test-signal pulses into the developed board with varying frequencies. The horizontal axis shows the frequency of the input test signal, and the vertical axis shows the measured counts and counting losses. It can be seen that the counting loss increases from 1.27 MHz as the frequency increases. The developed board has linearity in counting rate up to 1.27 MHz.

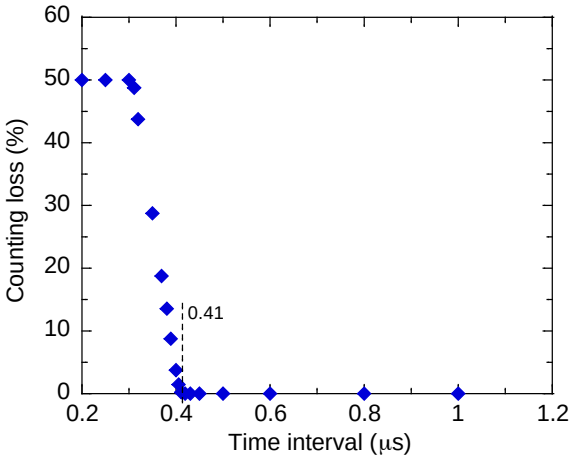

Figure 3. Counting losses of the developed board as a function of time interval of double pulses.

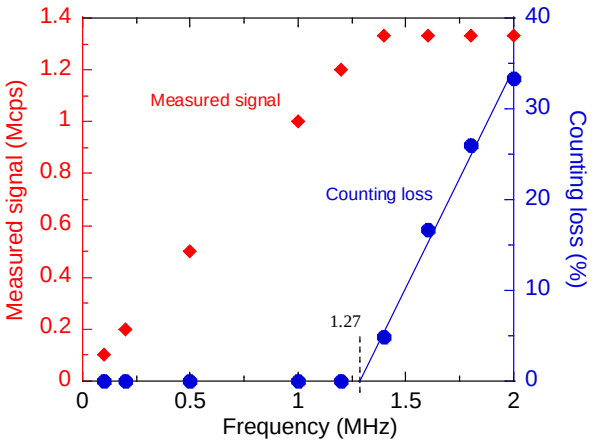

Figure 4. Measured signals of developed board as a function of the frequency of the continuous test pulse, and calculated counting losses.

4. Summary

We developed a signal processing board with optical signal transmission. The developed boards work well and can acquire two-dimensional neutron images in real time with a counting rate of more than 1.27 MHz and a pulse-pair resolution of less than 0.5 ns. This fast response is an essential characteristic for the two-dimensional neutron detector system that measures high-intensity pulsed neutrons.

References

[1] K. Toh et al., Nucl. Inst. and Meth. Phys. Res. A, **726** 169 (2013).

[2] K. Toh et al., J. Instrum., **9** C11019 (2014).

K. Toh, T. Nakamura, and K. Sakasai

Neutron Instrumentation Section, Materials and Life Science Division, J-PARC Center

Activities for Remote Access at MLF

1. Introduction

At MLF, it has been in high demand a way for remote access from outside of the J-PARC site for both users and staffs in order to control the experimental instruments devices and to monitor the status. To do measurement using neutrons at MLF, internal staffs and users must perform many tasks nearby a beamline instrument in the experimental hall, for example sample preparations, decisions concerning users' experimental conditions and operation of instruments devices suitable for the measurement. After a measurement starts with the required conditions, users and staffs start monitoring the progress in experiments to avoid accidents and to decide the next condition for their scientific purpose. Monitoring from outside of the experimental hall, especially, is in high demand because users and staffs need not stay long time nearby instruments during the measuring process.

Our MLF computing group provided *IROHA2* which is a software system to control various devices installed in instruments and to implement step-by-step device controls on a given schedule using web interface through a network [1]. Internal staffs can use the *IROHA2* system to watch and control at their office room far from the experimental hall. However, for security issues, it is not easy to access *IROHA2* directly on the internal servers in the J-PARC site through the internet. Therefore, we built an additional server on the DMZ area of J-PARC LAN (JLAN) and we added new functions to *IROHA2* to put only status information into the server for monitoring from outside. This remote monitoring system has been working well and now has provided to many staffs a routine access to *IROHA2*.

On the other hand, data handling is another issue. Recently, the amount of data produced from beamlines at MLF has become much larger with the increasing neutron source intensity and the expanding number of measurements with various conditions. It is difficult for users to handle such huge data, for example to take it back to users' laboratory to analyze them on their own computing resource. Though many users want to utilize the computing resources at MLF, which are larger than users' ones, for data handling, our computing group could not cope with their overwhelming demands.

2. Design

The recent COVID-19 pandemic situation, however, strongly focused our attention on these issues. To avoid crowds near the beamlines and to carry out experiments which users could not attend due to the COVID-19 situation, the remote access methods are required much more than before. The MLF computing group, therefore, has decided to produce a guideline and a model system for methods to control instrument devices and to analyze measured data from the internet, shown in Fig. 1. Almost all instrument devices and data processing

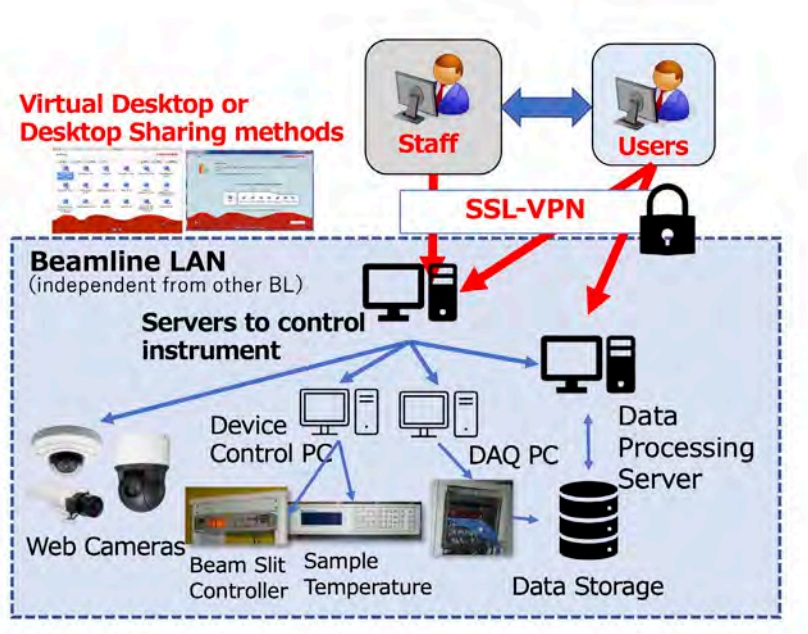

Figure 1. The proposed model for remote access using SSL-VPN and virtual desktop system.

servers are placed on JLAN, which has strong security protection against unauthorized access. To gain access to these servers from the internet, users and staffs must connect to servers inside JLAN through secure path by means of SSL-VPN (JLAN SSL-VPN), which is managed by the J-PARC Information System section. If users execute their own experiment from the internet in real time, staffs must take care of various security issues, for example, security incidents in the information system and handling mechanical devices. The MLF, therefore, prepares some check sheets for incidents and requires users to confirm them. However, there was no proper use of these full remote experiments this year because it is not easy for staffs to leave a full control of the instruments to users.

After all, the MLF computing group has constructed and serviced for users only the remote desktop environment system to process and analyze measured data, as shown in Fig. 2, and the automated processing and synchronization of data with users.

3. Developments

Users at some beamlines need desktop environments for processing measured data. They can install desktop environments for processing by themselves, but installations of those environments are complicated for most users. Additionally, the environments often require updating programs and maintaining system modules. These tasks, unrelated to the processing and analysis, often make users feel uncomfortable. Therefore, we decided to construct simpler desktop environments, which can be used easily for processing by users. New environments will be installed on JLAN and users can gain access to them *via* JLAN SSL-VPN. On the other hand, we must take care of the network security. JLAN is the main network in J-PARC. It is designed not only for office use but also for instruments control, so unlimited access to all networks cannot be permitted. For that reason, we adopted the *NoMachine Cloud Server* (*Cloud Server*) system [2]. Environments which are used by users are isolated from JLAN. With this configuration,

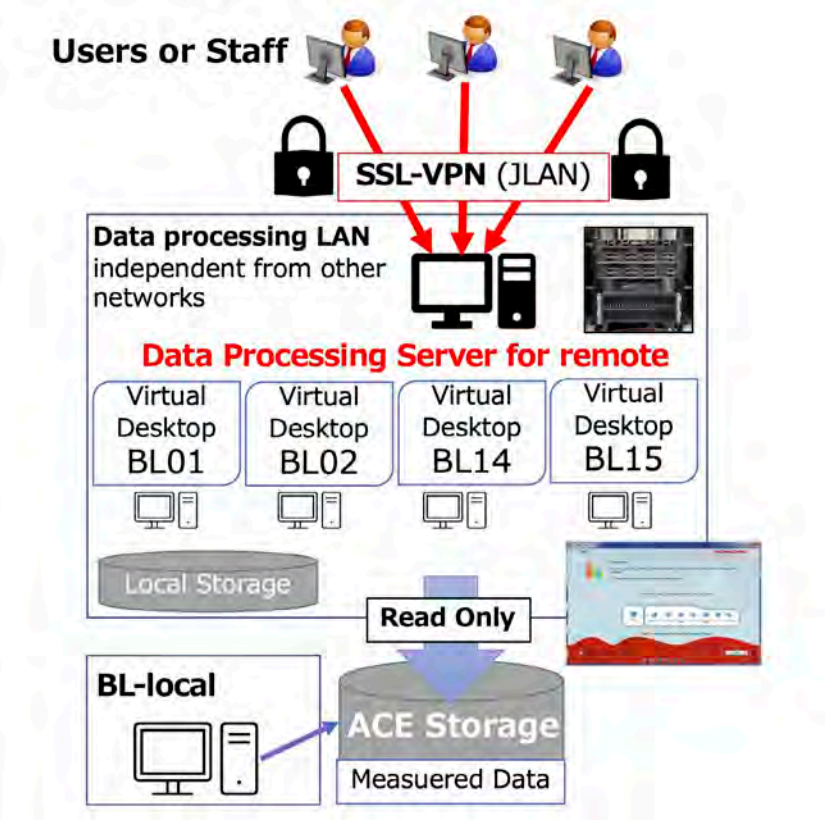

Figure 2. The structure of the remote desktop environment system for data processing services for users.

we can control user activities on the network. In the system, *Cloud Server* works as a portal for users, and the users connect to the *NoMachine Workstation* (*Workstation*) systems through the *Cloud Server* (Fig. 3). Desktop environments for users have been installed on PCs that have already *Workstation* installed. The user connects to the *Cloud Server* and initially is required to provide authentication. After the authentication is verified, the user can select authorized desktop environments only and connect to one of them. The user processes the measured data on the selected environment, which has been prepared by the MLF staff. We have decided to achieve this scheme with virtualization, and we have prepared a virtualization host machine and virtual machines for the *NoMachine* systems. In addition, users can use the MLF central storage system, named *ACE* storage, so they process the data seamlessly with the MLF beamlines.

Additionally, we introduced another way for processing. In some situations, automatic data processing is suitable for remote measurements. This scheme is very simple, as shown in Fig. 4. At the beamline, data is processed by each measurement automatically and the results are copied to the location which is bound to *Google Drive*. *Google Drive* synchronizes files among related folders on different systems. As a result, the files in the beamline folder will be copied to the user's PC. If distant users participate in the experiment, all folders will be synchronized in the same way. This scheme is more useful for routine processing, but the remote desktop is better when using manual processing. This scheme has resolved the sharing data problem between beamline and users' place. It needs to be solved to send measured data and/or processed data to users' working environments at their own places.

4. Results and future plans

NoMachine is a lightweight remote desktop. Unfortunately, JLAN SSL-VPN is too slow to use the remote desktop stably. This is the most critical problem. Connecting to JLAN with SSL-VPN is very complicated. It

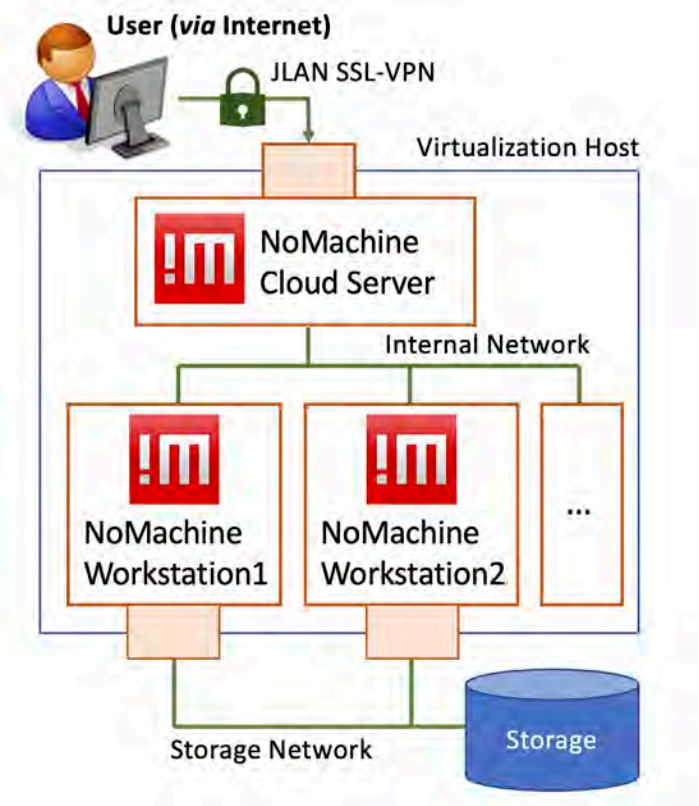

Figure 3. The technical structure of the remote desktop environment system for data processing using *NoMachine*.

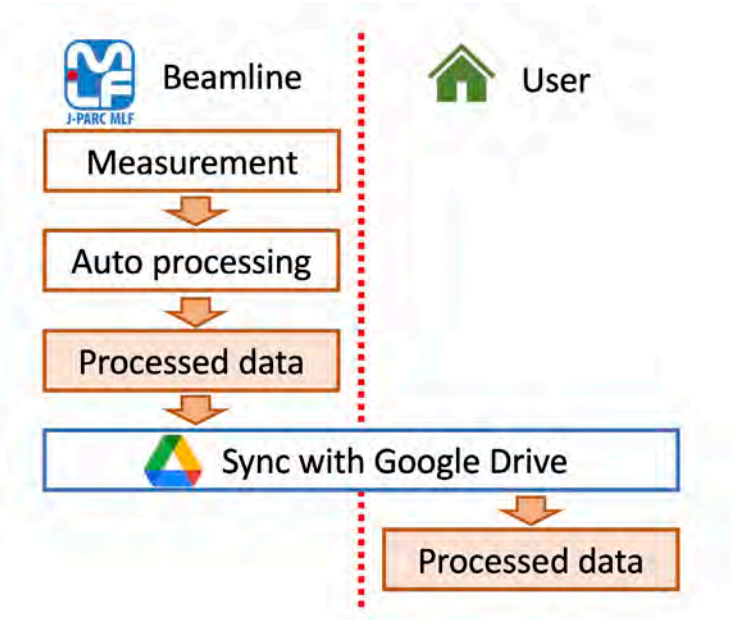

Figure 4. The scheme of the process to deliver processed data to users.

has been pointed out that the connection method is inconvenient and unstable. So, we must improve the network connection stability as soon as possible. However, these network equipment problems are difficult to solve immediately for procurement and configuration work. Now, we consider the option to migrate the system to cloud platforms, for example, Amazon Web Services (AWS), Google Cloud Platform (GCP) and so on. We have some accounting procedural issues, but we think it is technically viable.

In this implementation, we set up the specified environment for each beamline. But independent environment is inefficient with resource usage and human workload. We will investigate the environments on each beamline and will develop a common environment as much as possible. In the common environment, analysis programs will be specified by beamline. On the other hand, data transfer is a problem of remote analysis. We have developed a simple data transfer with Google Drive as described. Data synchronization, such as Google Drive, may be one of the solutions. We will investigate and improve the synchronization ways.

5. Summary

We proposed a schematic model for remote access at MLF and produced the remote desktop environment system for data processing and analysis. We've already started the remote desktop service to users on a small scale at several beamlines. However, there are many problems with the access speed via JLAN SSL-VPN, system operations by us and so on. In order to make our system's operations more efficient for users, for example using cloud services, we will continue with the improvements in the remote access environment.

References

[1] T. Nakatani, *et al.*, JPS Conference Proceedings, **8**, 036013, 2015.
[2] https://www.nomachine.com

Y. Inamura[1] and N. Okazaki[2]
[1]*Neutron Science Section, Materials and Life Science Division, J-PARC Center;* [2]*Neutron Science and Technology Center, CROSS*

Muon Science

Muon Section Overview

1. Commenced production of the third muon production target

In response to the remarks by the Muon Advisory Committee (MAC) and the International Advisory Committee (IAC) of J-PARC, the Muon Section received a budget for the production of a new muon target in FY2021. This is to reduce the current risk of operating without a spare target as a result of the unexpected failure of target Unit #1 in FY 2019, which was replaced with a spare (Unit #2). The project will be carried out over a period of two years, with the target storage container to be fabricated in the first year and the rotating target body in the second year. This is because it is necessary to reexamine the applicability of the Hot Isostatic Pressing (HIP) technique in advance, which is the key to target fabrication.

In the meantime, the rotating feeder unit was replaced as part of the maintenance in the summer shutdown period. It is recommended to replace it every two years, considering the wear and tear on the bearings. This was the first time since the rotating target itself has been replaced, and the work was carried out after careful preparation (see Fig. 1). However, a turbulence in the motor torque was confirmed during the test operation after the work, and it was presumed to have been caused by misalignment of the joint connecting the target rotation shaft and the drive shaft on the vacuum side.

To resolve this problem, another adjustment was attempted near the end of the maintenance period. However, subsequent beam operations revealed that the situation had not improved, suggesting that the connection accuracy between the rotating shaft and motor shaft was inadequate due to manual work. Therefore, it was decided to replace the flexible joint for the connection with one that has a higher tolerance for shaft misalignment during the next maintenance period, and the model selection and testing proceeded.

2. Construction of the H-Line

H-line is a new beamline under construction since FY2012 in Experimental Hall No.1 of the MLF building. It is a general-purpose beamline that can deliver both positive and negative muons and it has branches to two experimental areas named H1 and H2. The designed surface muon flux reaches 108 muons/s with a proton beam power of 1 MW owing to a large acceptance (108 mSr) capture solenoid and other beamline magnets with a large aperture.

As for the beamline to H1, the installation of cooling water piping and power cables progressed during the summer shutdown period, and was almost completed by the end of November. In addition, the review of facility modifications, including those for MUSE, by the Nuclear Regulation Authority (NRA), which had been delayed due to COVID-19 during this period, was finally completed and operation permission was granted. After prior approvals from JAEA and the surrounding municipalities, the beam commissioning started in January 2022. During beam commissioning, a large positron/electron background existed because the DC separator had not yet been installed. Although this made beam commissioning difficult, the commissioning team was

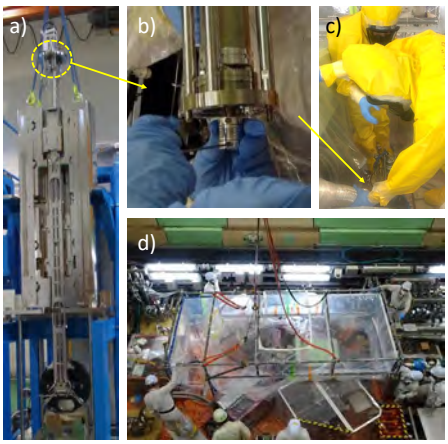

Figure 1. Rotating muon target (a) and its rotation feed through with a flexible joint (b). A snapshot of the target maintenance work (c) which was conducted within a greenhouse setup in the M2 area (d).

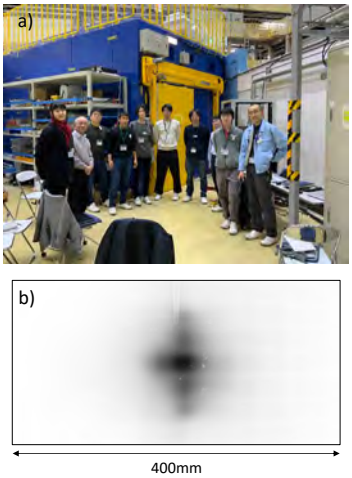

Figure 2. The H1-commissioning team headed by T. Yamazaki (a), and the muon beam profile measured by an imaging plate at the exit to the H1 area (b).

able to measure the beam intensity, profile, and momentum of the surface muons (see Fig. 2). The beam intensity of negative muons at several momenta was also measured.

3. Renovation of the beam kicker system on the S-Line

The S line is designed and built mainly for surface muon beams, and the beam kicker system allows muon experiments to be performed simultaneously in two areas, S1 and S2, by splitting a double pulse into two single pulses. The stable operation of the kicker device is very important as S2 begins operation in 2021.

The kicker device has encountered several problems since the start of the S-Line operation in 2017. One of these is the failure of the MARX board, which continues to occur several times a year. Since the failure was found to be caused by a certain component, the replacement of all 384 components on the MARX board was carried out during the summer shutdown period before the full-scale simultaneous operation of the S1 and S2 areas began.

Drastic measures were also taken during the summer shutdown period to address another issue: the location of the kicker power supply. The kicker power supply was installed inside the concrete shielding of the S-Line to reduce the potential impact of noise generated by the electric field kicker on the experimental equipment. Therefore, the concrete shield had to be opened and replaced every time a MARX board failed, making the work extensive and difficult. To resolve this issue, the kicker power supply unit was relocated to the fourth floor of the power supply yard to facilitate access during repairs (see Fig. 3). Upon the completion of the relocation work,

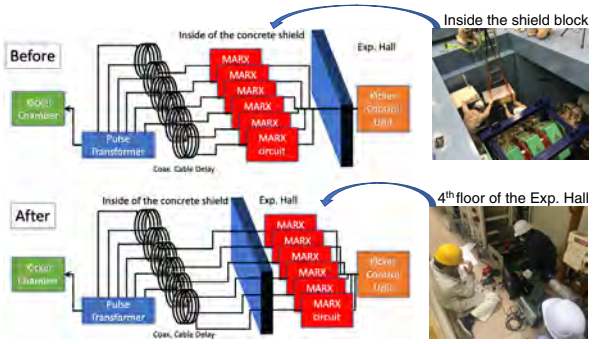

Figure 3. A schematic illustration of the beam kicker system before and after the relocation of the power supply.

the entire system was confirmed to be operational under the required specifications. Since then, although the MARX board failed due to a cause other than the replaced component, operation could be resumed within a maximum of half a day after detecting the failure, a significant improvement over the previous situation in which it took up to seven days to resume operation.

4. Laser system for Ultra-slow muon

Ultra-low velocity muons can be produced by resonant photoionization of thermal muonium from hot W-foil targets. In particular, a high-energy pulsed coherent Lyman-α light source is one of the most critical elements for efficient generation of ultra-low-velocity muons. Due to its high photon energy, the vacuum ultraviolet light causes degradation of optical materials over time. In addition, photochemical reactions that occur between vacuum ultraviolet light and residual gases (mainly hydrogen and carbon) that cannot be evacuated by turbo molecular pumps in vacuum cause degradation of the performance of the Lyman-α steering mirror. Degradation of the optics leads to a loss of ultra-slow muon yield and beam downtime for optics replacement. In addition, the surface of the mirror becomes noticeably cloudy when the same area is continuously irradiated with Lyman-α light for an extended period of time.

This year, we introduced a drive mechanism that changes the laser reflection position of the mirrors for vacuum ultraviolet light and restores the reflectivity of the two mirrors. This device adds a mirror displacement function to the mirror mounts that can adjust the horizontal angle and vertical tilt of the mirrors. The mirror mount located upstream has a rotation stage to rotate a 50 mmϕ circular mirror and a linear-motion stage (30 mm stroke). The mirror mount on the downstream side uses a 50 mm square cylindrical mirror, which allows horizontal and vertical motion. These stages have built-in encoders that record the movement history of the mirror positions, allowing the laser reflective surface to be set to the unirradiated area when the reflectivity of the mirror decreases. The new mirror steering and displacement device enables the mirror irradiation position to be adjusted by remote control without opening the vacuum chamber to the atmosphere.

R. Kadono[1,2], K. Shimomura[1,2], A. Koda[1,2], P. Strasser[1,2], T. Yamazaki[1,2], S. Kanda[1,2], S. Takeshita[1,2], I. Umegaki[1,2], Y. Ikedo[1,2], Y. Kobayashi[1,2], J. Nakamura[1,2], T. Yuasa[1,2], N. Kawamura[1,2], Y. Oishi[1,2], Y. Nagatani[1,2], S. Matoba[1,2], S. Nishimura[1,2], S. K. Dey[1,2], W. Higemoto[2,3], and T. U. Ito[2,3]

[1]*Institute of Materials Structure Science, KEK;* [2]*Muon Science Section, Materials and Life Science Division, J-PARC Center;* [3]*Advanced Science Research Center, JAEA*

Present Status of the Muon-Beam Source

The muon production target and the frontend part of each muon beamline are located in the M2 tunnel, downstream of the primary beamline, as shown in Fig. 1. This area is under a high radiation field due to the secondary particles generated by the muon target, and its operation is a key to the stable and safe operation of the whole MLF facility containing not only MUSE but also JSNS. The activation effect in the devices and radioisotopes, especially tritium, becomes more serious with every passing year. We are accumulating the know-how for the full-year 1 MW operation.

1 Muon production target

In FY2019, the rotating target was replaced with a new one due to trouble in the 1st rotating target. The 2nd target had been operated without any essential troubles before the summer maintenance period in 2021.

1.1 The 3rd target preparation

The replacement of the target was unexpected and we had to use the spare one as the 2nd. Thus, preparing the new spare target became an urgent issue and a top priority task for the muon section. In FY2021, we started the preparation work under a several-year plan. If the present target fails, we have to stop the muon facility operations. Thus, MAC, the Muon Advisory Committee, strongly recommended preparing the 3rd target as early as possible. To answer this, owing to the budgetary support of the J-PARC center and IMSS, the fabrication schedule was brought forward, and the 3rd target will be ready by the end of the next fiscal year. In FY2021, test pieces of cooling-water pipes buried in the target assembly by hot isostatic pressing were fabricated (Fig. 2). The same parts were used in the 1st and the 2nd target, but the detailed knowledge had been lost due to the retirement of the artisan employed by the manufacturer. In FY2022, the main body of the target assembly will be fabricated.

The details are reported separately [1].

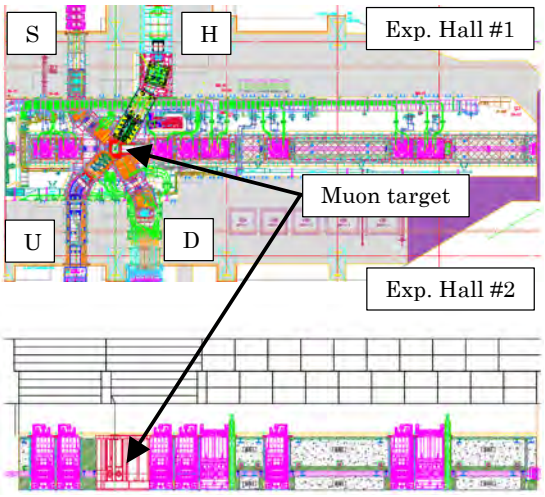

Figure 1. The horizontal (upper) and the vertical sectional view (lower) of the M2 tunnel. The proton beam is transported through the tunnel from the left side to the right side of the neutron target.

1.2 Replacement of the rotation feed-thru

The rotating shaft of the target assembly is connected to the motor out of the beamline vacuum through the rotation feed-thru. The lifetime of the feed-thru is determined by the total number of rotations and it has to be replaced every two years. Thus, we planned the replacement work for the maintenance period of 2021 as annual work. The replacement work created a high risk with the possibility of internal exposure due to the tritium from the muon target. The work was well prepared according to the safety review and conducted smoothly in the summer of 2021. However, after the replacement, we found turbulence in the motor torque in the off-beam rotating test. Finally, the reason for the turbulence was determined to be due to the misalignment of the feed-thru, and we re-adjusted it near the end of the maintenance period. However, these works did not solve the problem and the rotating torque was still unstable, even in the beam operation. The beam stoppages of the MLF occurred by the interlocking of the motor torque a few times, and thus we changed the interlock policy slightly to avoid disturbing the MLF operation. The temporary value of the interlock still has a safety margin, but this is not a healthy situation.

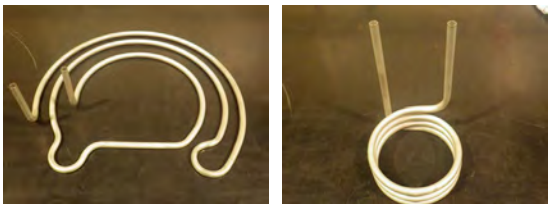

Figure 2. Test pieces of cooling water pipes to be buried in the target assembly.

The rotation feed-thru is connected with the rotating shaft of the target with the coupling. The allowable eccentricity of the center axes between the feed-thru and the shaft is 0.2 mm, and this high-level accuracy becomes hard to achieve in the maintenance in the M2 tunnel because the work has to wear rad-hard equipment such as an airline mask and vinyl anorak suit to prevent internal exposure by tritium.

We prepared a new coupling whose allowable eccentricity is sufficiently high and will replace the present one with it in the maintenance period of 2022.

We also consider developing a long-lived motor feed-thru. The lifetime of the motor feed-thru is determined by the bearing, and we will be able to replace it with a reliable one even in the high radiation field.

The details are reported separately [1, 2].

1.3 Collaboration with the PSI

At the beginning of the MLF operation in 2008, we adopted the fixed target [3]: the proton beams were irradiated onto the center of the 2 cm thick graphite disk surrounded by a water-cooled frame. However, the fixed target was expected to break within one year due to the accumulated radiation damage around the center of the disk. Thus, the rotating target was developed based on the original one developed at the Paul Scherrer Institute (PSI) in Switzerland. But it was known that the bearings that supported the rotating shaft had a short lifetime and could cause malfunction within a short period, less than a year.

We developed the rotating target for MLF J-PARC with bearings using radiation hard tungsten disulfide solid lubricant (Fig. 3). This J-PARC version of the rotating target achieved stable continuous operation for five years from 2014 to 2019. The 1st rotating target was unexpectedly replaced due to the trouble in the coupling connecting the motor feed-thru and not in the bearing. Thus, the lifetime of the bearing could be longer than five years. The 2nd rotating target succeeded in continuously receiving a 0.83 MW beam up to the present while the beam intensity has gradually increased. This solid-lubricant bearing was also adopted at the PSI and had achieved stable continuous operation over a period of one year, the best result after a long period of several bearing failures at the PSI.

We hope to keep this relationship with the PSI not only for the target but also for other things like the beamline, experimental techniques, and so on.

1.4 Long-term storage of spent targets

The original plan to store the spent target was made for the fixed target whose lifetime was less than a year. Thus, dozens of the spent targets were expected to be stored by reducing their volumes. The scenario of the volume reduction was constructed to cut the target rod by a dedicated device in the hot cell. However, the spent target is expected to be highly activated and such work will pose a high risk. We have completed a rotating target that has a much longer lifetime and does not need high volume reduction. Therefore, we will start to reconsider the long-term storage of the spent targets.

Figure 3. Solid-lubricant bearing used in the MLF J-PARC.

2 Secondary beamlines

The frontend magnets of all the secondary beamlines are placed surrounding the target chamber. Historically, the D-line magnets and the S-line ones were placed at the start of the MLF operation in 2008. Then, the U-line magnets, US1 and US2, were facilitated in 2009. And lastly, the frontend magnets in the H line, HS1 and HB1, were installed in 2012 before the activation in the working area became serious. Since then, the H line construction has been continued and finally completed in FY2021 up to the H1 area [4].

As well as the U line, the H line uses a large aperture solenoid for the frontend magnet to increase the acceptance of the muon beam. The leakage field of the solenoid on the proton beam line is not negligible and the BL product is expected to reach about 0.01 Tm. The proton beam is kicked by about 1 mrad to the vertical direction at the maximum excitation of HS1. This drift is compensated by the steering magnets located downstream of the muon target. The auto-feedback program that reads the current of HS1 and sets the current of the steering magnets has been developed by extending the existing system for the U line. The program is developed and operated by the 3NBT group of the neutron source section.

References

[1] S. Matoba *et al.*, *ibid.*
[2] Y. Kobayashi *et al.*, *ibid.*
[3] S. Makimura *et al.*, Proc. of Sci. 369 (2020) 124.
[4] T. Yamazaki *et al.*, *ibid.*

N. Kawamura[1,2], S. Matoba[1,2], Y. Kobayashi[1,2], and A. Koda[1,2]
[1]*Muon Science Section, Materials and Life Science Division, J-PARC;* [2]*Muon Science Laboratory, High Energy Accelerator Research Organization (KEK)*

Beam Commissioning at D1/2 Areas

1. Introduction

The D line of MLF MUSE has a long superconducting solenoid, which can provide positive and negative decay muons from a few MeV/c to 120 MeV/c in addition to surface muons. The primary proton beam energy of the MLF is as high as 3 GeV, resulting in a high negative muon yield. In particular, thanks to the recent increase in beam power, the world's highest intensity negative muon beams are available. Using this high-intensity negative muon beam, various experimental applications have been developed, such as nondestructive elemental analysis using negative muon characteristic X-rays and negative muon spin rotation/relaxation. In this report, we report the current status of the negative muon beam commissioning at the D line.

In experimental area D1, negative muon spin relaxation measurements can be performed using polarized high intensity negative muons. Recently, several results have been obtained by the negative muon spin relaxation method. However, further commissioning is required to perform more precise experiments with a variety of samples. Here we report on the tuning of a single bunch beam using a kicker system.

2. Kicker system and its operation at the D line

The MLF provides double bunch beams with a 25 Hz period. Each bunch has a width of 100 ns and a bunch spacing of 600 ns. The D line has a kicker system at the branch section to the D1 and D2 areas, which can be operated to provide single bunch beams (and, with appropriate adjustments, single bunch beams to both D1 and D2 areas simultaneously).

The branch consists of two switchyard magnets (DSY1 and DSY2, the so-called bending magnets), two kicker magnets (DKKR1 and DKKR2), and septum magnets (DSPTM1 and DSPTM2) that direct the muon beam toward areas D1 and D2 (Fig. 1).

As an example, we explain how to operate the system for negative muons. If the kicker is not excited, the trajectory of the negative muon beam is slightly bent toward the D2 by the DSY1 and 2, directed to the entrance of the DSPTM2, and further guided by DSPTM2 toward the D2 area properly (Fig. 1(a), here we call this a mainstream beam). When the second bunch passes through DKKR1 and 2, the kicker is excited with the appropriate voltage and timing, and only the second bunch is bent toward the DSPTM1 and directed to the D1 area (Fig. 1(b), here we call this a tributary beam). Since DKKR is unipolar, the kicker must be operated against the double bunch beam fed to the D2 area (and vice versa for positive muons).

3. Tuning of delay timing for the kicker trigger

In order to operate the kicker accurately, the delay timing of the trigger that excites the kicker must be adjusted to match the beam of the 2nd (or 1st) bunch. To make this adjustment, two detectors consisting of a 5 mm thick 75 mm square scintillator and a photomultiplier tube were installed in the D1 area (Fig. 2). For a muon

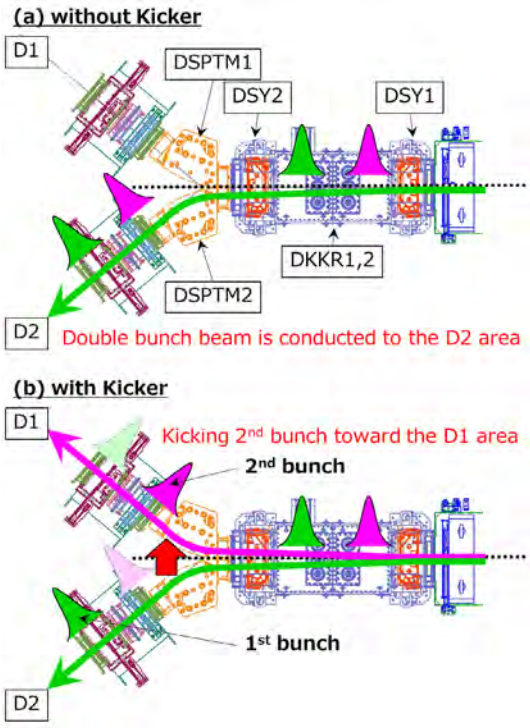

Figure 1. Schematic view of the branch section with the kicker system and its operation (a) without and (b) with kicker excitation for negative muons.

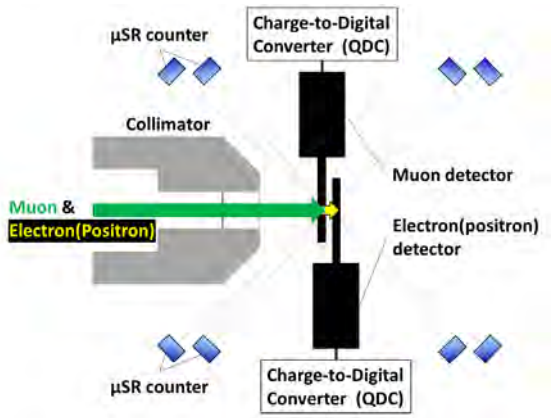

Figure 2. Detector configuration at the D1 area.

beam with a momentum of about 30 MeV/c, all muons stop at the scintillator of the detector installed upstream and cannot pass through. Therefore, the downstream detector can only detect signals from electrons/positrons. The signals from each detector were input to a charge-to-digital converter (QDC), and the integrated intensity was obtained.

Figure 3(a) shows the bunch structure, timing of the muon beam, and kicker excitation waveform. Figure 3(b) shows the timing of the gate signal used to observe each signal. Figures 3(c) to (f) show the simulation results of the positive and negative muon beam intensity observed in the D1 area as a function of the delay time for the kicker trigger. The simulations were obtained by performing convolution integration of the kicker waveform and muon (and electron/positron) pulses.

In the case of positive muons, the mainstream is the beam guided to the D1 area without kicker operation, and the tributary beam is the beam kicked to the D2 area by the kicker. Therefore, the signal in the D1 area changes as shown in Fig. 3(c) (1st bunch) and Fig. 3(d) (2nd bunch). On the other hand, in the case of a negative muon, the mainstream is the beam led to the D2 area without kicker operation, and the tributary beam is the beam kicked to D1. Since the beam intensity is not observed at D1 on the tributary side unless the beam is kicked, the signal changes as shown in Fig. 3(e) (1st bunch) and Fig. 3(f) (2nd bunch).

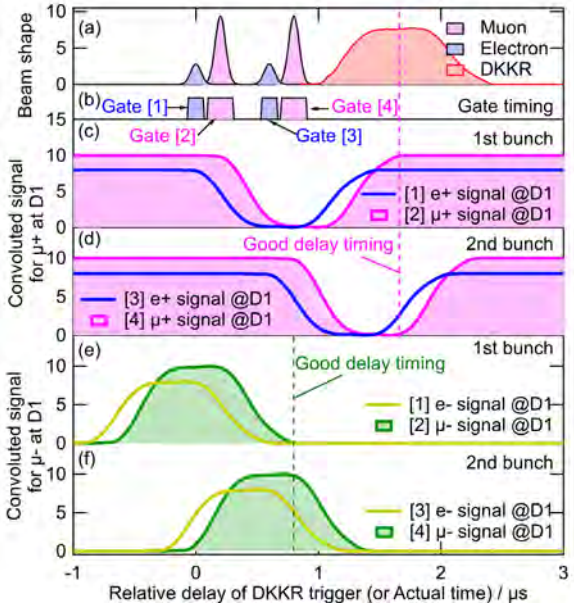

Figure 3. Simulated intensity of positive/negative muon signal observed at the D1 area with DKKR excited.

The observed delay time dependence of the signal intensities in each bunch of the surface (positive) muons (Fig. 4(P-a) and (P-b)) and decay (negative) muons of 30 MeV/c (Fig. 4(N-a) and (N-b)) at the D1 area is shown. Also, the shown values in the figure are the arrival times of the respective beams (versus the delay time) obtained from the derivative curves of the signal intensity.

For the positive muon signals in Figs. 4(P-a) and 4(P-b), the obtained data correspond to the signal after 1 μs in the Figs. 3(c) and 3(d). In Fig. 4(P-b) which shows the intensity of the 2nd bunch, there is an increase in the positron signal intensity around the time when the 1st bunch muon arrives (100.1 μs), but this is a background signal because decaying positrons from the positive muon that stopped in the upstream muon detector were injected into the downstream positron detector. From this result, it is clear that the optimal delay timing for triggering is approximately 100.28 μs in order to excite the kicker at the timing for delivering the complete 1st bunch and kicking the 2nd bunch completely.

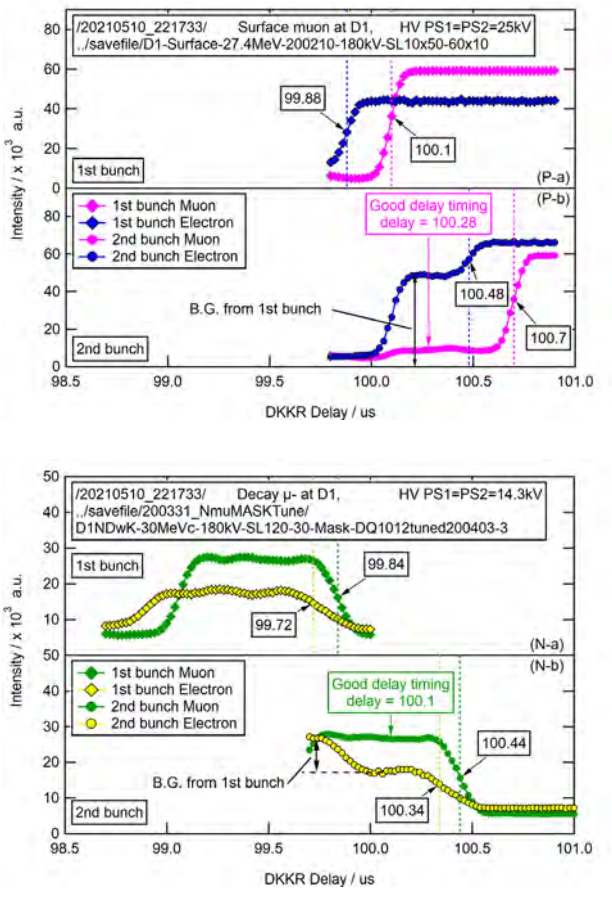

Figure 4. Observed intensities at D1 under operation of DKKR. (P-a) surface (positive) muon gated at 1st bunch, (P-b) 2nd bunch. (N-a) Decay (negative) muon gated at 1st bunch, (N-b) 2nd bunch.

Next, measurements were performed for negative muons, and the results are shown in Figs. 4(N-a) and 4(N-b). As with the positive muon case, an increase due to the signal of decay electrons stopping at the upstream muon detector (and injecting into the downstream electron detector) is observed around 99.8 μs in the electron detector at the 2nd bunch. For negative muons, the optimum condition is that only the 2nd bunch is delivered to the D1 area. The figure shows that a kicker trigger delay time of approximately 100.1 μs is optimal. However, these delay times may vary depending on the accelerator operating conditions, so adjustments should be made on a case-by-case basis.

4. Summary

We reported the tuning method to obtain a single bunch beam for the D1 area by setting the kicker trigger delay appropriately for the double bunch beam provided by the MLF, and the results. The tuning results showed that 100.28 μs was appropriate for the surface (positive) muon and 100.1 μs for the decay (negative) muon.

S. Takeshita[1,2], P. Strasser[1,2], A. Koda[1,2], W. Higemoto[2,3], I. Umegaki[1,2], M. Tampo[1,2], S. Doiuchi[1,2], A. Hashimoto[1,2], N. Kawamura[1,2], and K. Shimomura[1,2]

[1]Muon Science Laboratory, Institute of Materials Structure Science, KEK; [2]Muon Science Section, Materials and Life Science Division, J-PARC Center; [3]Advanced Science Research Center, Sector of Nuclear Science Research, JAEA

Current Status of μSR Experiment at D1

At the D-line, muons are delivered to the D1 and/or the D2. At the D1-area, the μSR spectrometer is installed as a main and fixed instrument. Since high momentum muon, surface muon, and negatively charged muon are available at the D1, all type of μSR measurements, except for the ultra-slow μSR, can be carried out. In particular, unique sample environments, such as very low temperature, high pressure *etc.* were possible to carry out only at the D1. Figure 1 shows the μSR spectrometer with the dilution refrigerator and the fly-past chamber. Here, we report recent accuracy improvement of the μSR measurement.

Positron energy selected μSR at D1

The positive muon decays into positron and two neutrinos with a mean lifetime of 2.197μs. This positron is emitted in a certain direction with a certain energy. As shown in Fig. 2, the asymmetry factor depends on the positron energy and the lower energy positron possesses a lower asymmetry factor. Therefore, by cutting low-energy positrons, we can obtain higher asymmetry factor as total.

The total accuracy depends on the number of counting positron N and total asymmetry A. To cut the low-energy positron, a copper plate was placed in front of the positron counters as absorber, and we investigated the optimal thickness for the copper plate. Figure 3 shows the copper plate mounted at the D1 spectrometer. As a beam window, 60 mm in diameter hole was opened at the copper plate. As a sample, another copper plate with a thickness of 0.5 mm was placed at the center of the spectrometer. We used single pulse of 4 MeV surface muon and muon was roughly stopped at the center of the sample plate in depth. We applied 20G of transverse field to measure the asymmetry factor. As figure of merit (FOM), we defined NA^2 and FOM maximization thickness

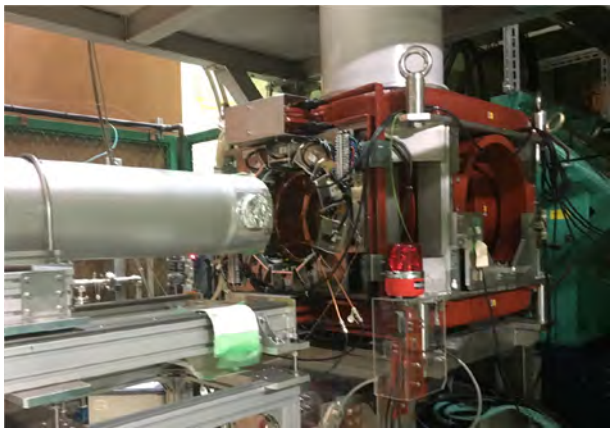

Figure 1. μSR spectrometer with the dilution refrigerator and the fly-past chamber at the D1.

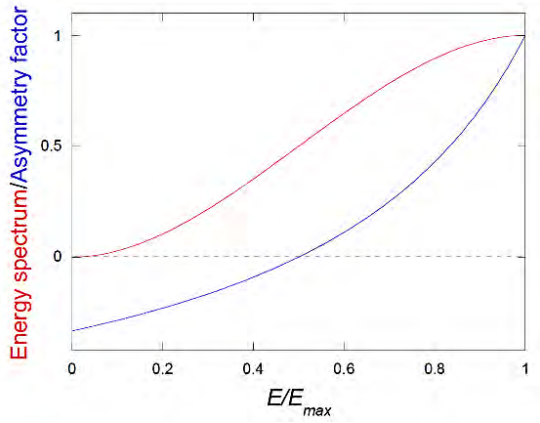

Figure 2. Positron/electron energy dependence of energy spectrum (red) and asymmetry factor (blue).

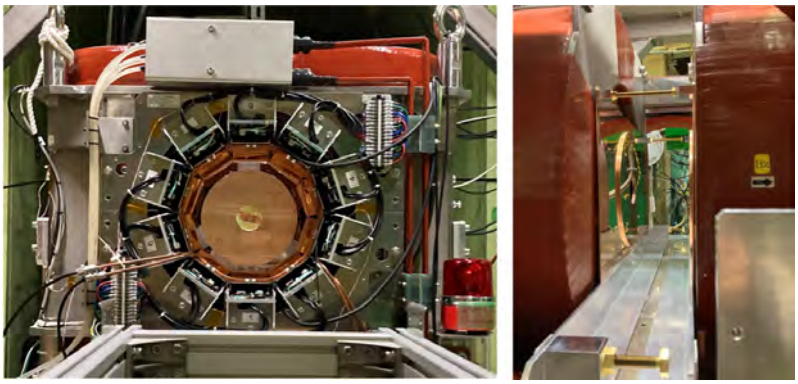

Figure 3. D1 μSR spectrometer with the copper plate which is located in front of the positron detector.

of the copper plate was investigated.

Figure 4 (a) shows the copper plate thickness dependence on the asymmetry factor. The asymmetry factor gradually increases with increasing the copper plate thickness and becomes ~0.29 with a copper plate thickness of 6 mm. Meanwhile, the counting rate is also dependent on the copper plate thickness and gradually decreases with increasing thickness, as shown in Fig.4(b). At 6 mm, the count rate roughly becomes half of that without copper plate.

FOM is shown in Fig. 4 (c). FOM reaches a maximum at 3 mm thickness. This fact indicates that the most efficient measurement can be carried out with a copper plate of 3 mm thickness. Of course, this value also depends on the thickness and density of the sample, sample holder and chamber. We note that this situation must be the same for the negative muon.

In summary, to maximize the μSR accuracy, we put copper plate and found that 3 mm thickness of the copper was the best value at D1.

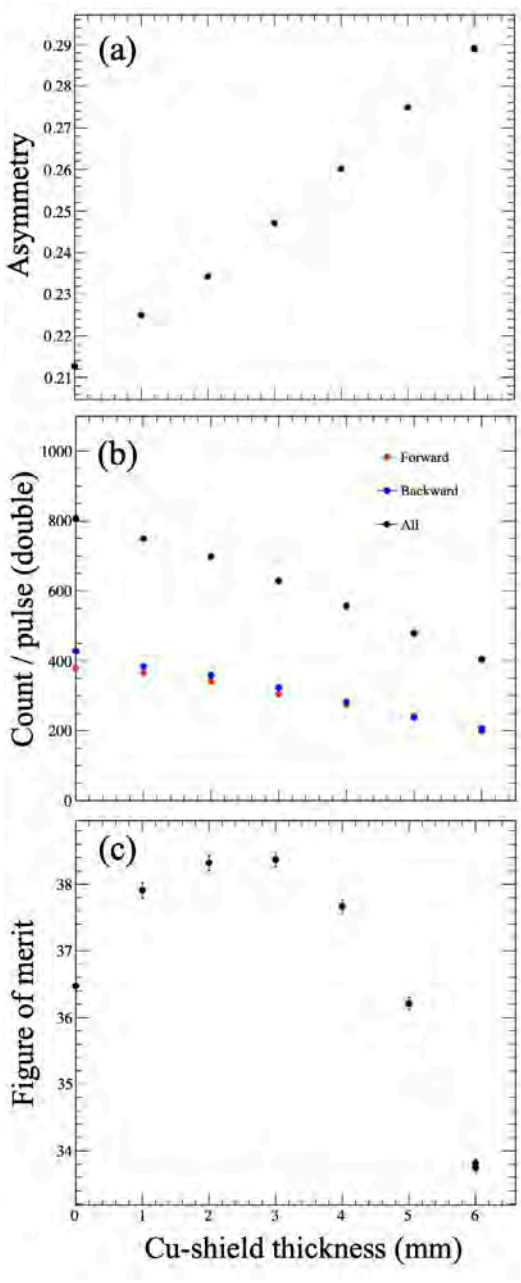

Figure 4. Copper plate thickness dependence on (a) asymmetry, (b) count per pulse and (c) figure of merit.

W. Higemoto[1,2,3] and S. Nishimiura[2,4]

[1]*Advanced Science Research Center, Japan Atomic Energy Agency;* [2]*Muon Section, Materials and Life Science Facility Division, J-PARC Center;* [3]*Department of Physics, Tokyo Institute of Technology;* [4]*Muon Science Laboratory, Institute of Materials Structure Science, High Energy Accelerator Research Organization (KEK)*

Development of D2 (Muonic X-ray Element Analysis) Instrument and Sample Environment

The D2 experimental area is actively used for variable experiments with positive and negative decay muons. This is because the D2 experimental area basically is a space of about 4 m × 4.5 m, allowing users to bring in their own equipment or chambers needed to realize their experiments. This has led to the publication of remarkable results in several fundamental physics experiments in FY2021 [1–4]. In addition, the soft errors induced in semiconductors by muon irradiation were studied, and their characteristics were clarified in comparison with those of neutrons [5]. This work is expected to contribute to the construction of effective evaluation and countermeasure technologies against soft errors caused by environmental radiation, and to lead to the creation of safe, secure, and reliable semiconductor devices.

On the other hand, in recent years, elemental analysis with muonic x-rays has been one of the most popular experiments at D2 experimental area. This kind of experiments requires a suitable sample chamber and germanium (Ge) semiconductor detectors. In fact, a lot of elemental analysis with muonic x-ray has been conducted on archaeological objects with historical and scientific value [6], meteorites [7, 8], and lithium-ion batteries [9] with remarkable results. Furthermore, it is desired to obtain fine data within shorter time in order to perform effectively larger numbers of interesting research programs in limited beam time. Therefore, the development of the sample environment and the addition of detectors are essential to this background.

The major progress of the D2 experimental area in FY2021 was the modification of the sample chamber for elemental analysis muonic x-ray, the so-called hemispherical chamber, to make up to 10 ports available for detectors (Fig. 1). There are three types of ports with different diameters: ϕ76.3 mm (6 ports), ϕ165.2 mm (2 ports), and ϕ60.5 mm (2 ports). Different detectors can be installed according to the size of the end cap of each detector (Table 1). In particular, ports 1-5 can be used with a Ge detector for low energy (LEGe), and ports 6-7 can be equipped with a Ge detector with a thicker end cap (MGe), which are for detecting muonic x-rays with energies below 300 keV. While ports 8-9 can fit into a multi-pixel detector, LEGe can also be mounted using a conversion flange to match the diameter size (Fig. 2). In addition, there are two upper ports 10-11 to install a decay counter or a smaller detector (e.g., a non-refrigerant detector requiring no liquid N_2 tank such as a silicon drift detector SDD).

The hemispheric chamber was modified so that seven Ge semiconductor detectors could be mounted, and various elemental analysis experiments were conducted using these detectors in FY2021. As an example, the following elemental analysis experiments were conducted in FY2021:

[2021B0321] Detection of metallic Li deposition in a lithium-ion battery with muonic x-rays

[2021B0356] Evaluation of activation by negative muons

[2014MS01] Elemental analysis of inkstick on inkstone surface

[2021MS01] Elemental analysis of gold coins from the

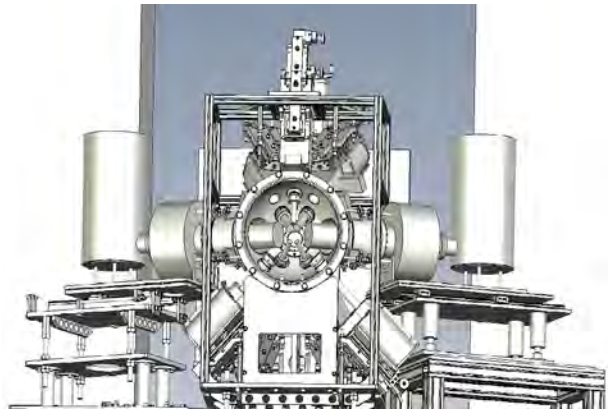

Figure 1. Illustration of Hemispheric chamber with seven Ge semiconductor detectors and multi-pixel Ge detectors on the left and right sides.

Table 1. Diameter of the ports (additional flange) and detectors frequently used at each port.

Port	Diameter (flange)	Main purpose
1-5	76.3 (20) mm	LEGe
6-7	76.3 (25) mm	MGe
8-9	165.2 mm	Multi-pixel Ge detectors
10-11	60.5 mm	Decay counter, SDD

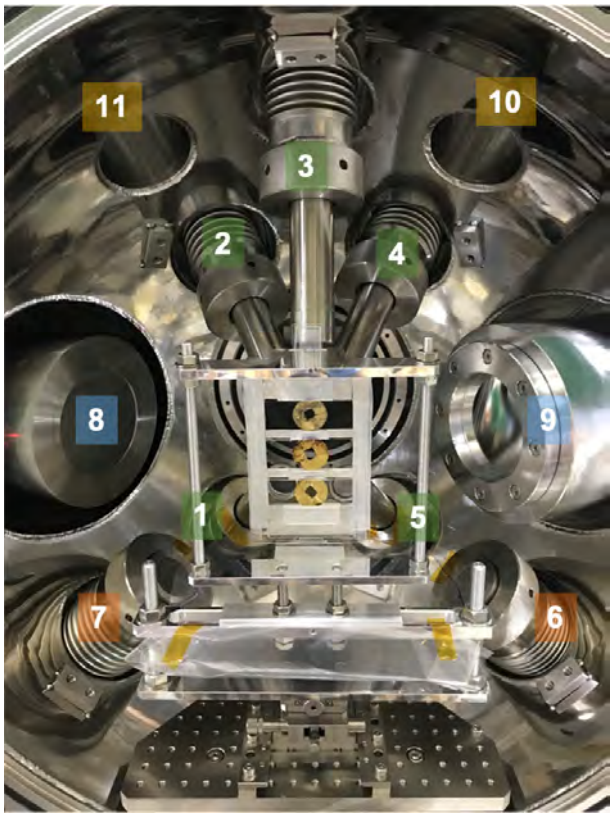

Figure 2. Photo of Hemispheric chamber in the view from downstream of the beam. Gold coins are set at a sample position. Ge semiconductor detectors and multi-pixel detectors are equipped at Port 1 - 7, and Port 8 - 9, respectively. Ports 10 - 11 can be used for decay counters and other detectors.

(a)

Port No.	1	2	3
θ	-36.202	36.202	72
ϕ	204.998	204.998	180
Port no.	4	5	6
θ	36.202	-36.202	-43.55
ϕ	155.002	155.002	108.082
Port no.	7	8	9
θ	-43.55	0	0
ϕ	251.918	245	115

(b)

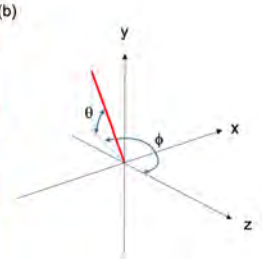

Figure 3. (a) Angles at each port in the Hemispheric chamber. (b) When the direction of the beam (from upstream to down-stream) is defined as z-axis, ϕ and θ are an angle from the z-axis in the horizontal plane (xy plane) and an elevation angle from vertical axis (y).

Shuri Castle in Okinawa

Other than elemental analysis, the hemispherical chamber was also used for experiments, such as muon transmission imaging and muon fusion.

Lastly, it is noted that elemental analysis was performed on the return samples from Ryugu by Hayabusa 2 program at D2 experimental area [10], although their special sample chamber covered with copper was used instead of the hemispherical chamber.

In FY2021, three new low-energy semiconductor Ge detectors (LEGe) have become ready for experiments. Next year, we expect to have further fruitful research programs in elemental analysis using muonic x-rays.

Acknowledgments

The development of the sample environment that we showed here was conducted as a part of "integration of arts and sciences" research program promoted by the KEK IMSS MSL. It was also supported by the JSPS Grant-in-Aid for Scientific Research on Innovative Areas "Toward new frontiers: Encounter and synergy of state-of-the-art astronomical detectors and exotic quantum beams". The authors appreciate the cooperation of Mr. Shogo Doiuchi, Dr. Akiko Hashimoto, Mr. Yudai Ishikake, and other members of the Negative Muon Group. The design and production of the hemispherical chamber and the detector adding were managed with great diligence by Dr. Tampo.

References

[1] T. Okumura et al., Phys. Rev. Lett. 127, 053001(2021).
[2] S. Nishimura et al., Physical Review A, 104, L020801 (2021).
[3] K. Okutsu et al., Fusion Engineering and Design, 170, 112712 (2021).
[4] T. Yamashita et al., Fusion Engineering and Design, 169, 112580 (2021).
[5] T. Kato et al., IEEE Transactions on Nuclear Science 68, 7, 1436-1444 (2021).
[6] K. Shimada-Takaura et al., Journal of Natural Medicines, 75(3), 532-539 (2021).
[7] K. Terada et al., Scientific Reports, 9, 1, (2019).
[8] K. Terada et al., Scientific Reports, 7, 15478 (2017).
[9] I. Umegaki et al., Analytical Chemistry, 92, 8192-8200 (2020).
[10] http://j-parc.jp/c/topics/2021/07/15000718.html

I. Umegaki, M. Tampo, Y. Miyake
Muon Science Laboratory, Institute of Materials Structure Science, KEK

Beamline Magnets and Power Supplies

Replacement of DB2 Coils and Status of Updating the MPS program for the Muon Target

1. Introduction

The bending magnet DB2 is installed in the decay muon beamline (D-line) at the Materials and Life Science Facility (MLF) of J-PARC. The existing DB2 is a dipole magnet, and over 40 years have passed since its production. Therefore, we planned to exchange the degraded coils with new ones within three years. In 2021, the final year of the three-year plan [1, 2], we exchanged the coils and measured the magnetic field with a Hall probe to compare the magnetic field measurements before and after the coil replacement.

Furthermore, in the MLF operation in January 2022, it was discovered that the torque in the rotation mechanism of the muon target was not constant, which was a problem. The MPS program for the muon target needed to be updated because of a hunting phenomenon that occurred due to the abnormal rotation torque in the muon target motor, resulting in a malfunction in the rotation indicator of the muon target display in the MLF control room. It also caused the torque monitoring interlock program for the muon rotating target to stop working as a Machine Protection System (MPS). Here, we report the causes of these troubles and how they were dealt with.

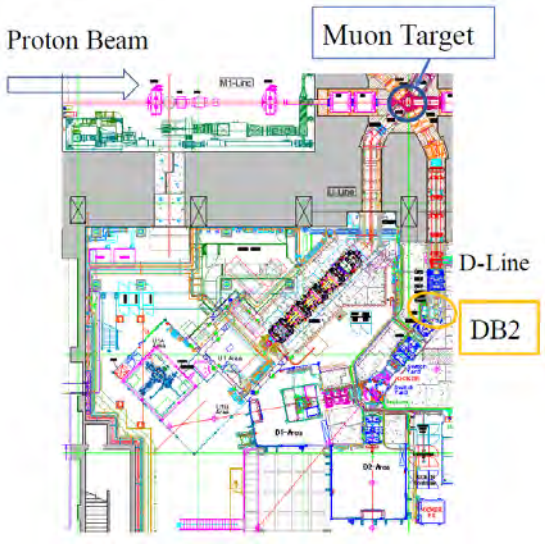

Figure 1. Decay muon beamline (D-line).

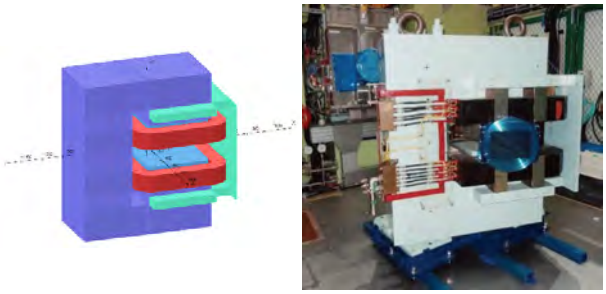

Figure 2. DB2 analysis model (left) and existing bending magnet (right).

2. Replacement of the DB2 coils

As shown in Fig. 1, the bending magnet DB2 deflects the beam by and directs the muons to the downstream experimental areas. As more than 40 years have passed since DB2 was manufactured, there were some concerns about the coil insulation degradation, so the whole process from hollow conductor selection to coil replacement was carried out according to a three-year plan.

We calculated the field of DB2 with a 3-dimensional field analysis program (OPERA-3d). The analysis model and actual DB2 are shown in Fig. 2.

The coil replacement work was carried out by removing the end-guard and then dividing DB2 into upper and lower sections using a crane in the MLF. Figure 3 shows DB2 after the coil replacement.

Performance tests and magnetic field measurements were carried out after the coil replacement was completed. Table 1 shows the results of the performance

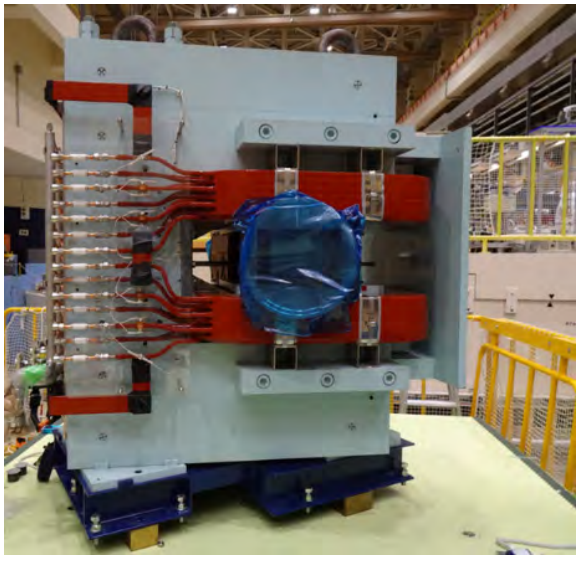

Figure 3. DB2 after the coil replacement.

inspection at the current rating of the existing power supply (400 A). It was confirmed that the measured and calculated values generally agreed with each other. We also measured the excitation curve at the pole center, and the magnetic field along the beam axis at ±250 mm from a reference point at the pole edge as shown in Fig. 4. Figure 5 shows the measured excitation curve, the magnetic field according to Ampere's law, and the calculated values obtained from the OPERA-3d model. It can be observed that the measured values are in good agreement with the calculated values. Figure 6 shows the magnetic field along the beam axis. Discrepancies were observed at the fringe field, possibly due to the misalignment of the magnet and the beam duct. Assuming that the duct was misaligned by 10 mm in the beam direction, the results were in good agreement with those measured with the old coils.

When we replaced the coils, the number of cooling water channels of the new coils was increased from 3 to 6 channels per coil to enable the transport of high-momentum muons up to 250 MeV/c. Table 2 shows the calculated temperature rise of the cooling water with an applied current value of 510 A, which is required to transport muons of 250 MeV/c. In J-PARC, the operational conditions for cooling water are defined as a flow velocity of less than 2 m/s and a temperature rise of less than 25°C. The temperature rise of the cooling water in the old coils would exceed this last condition, whereas

Table 1. Results of the performance inspection.

	Calculation	Measurement
Current [A]	400	400
Voltage [V]	43	44.9
Inductance [H]	0.204	0.299 (120 Hz)
Resistance [Ω]	0.1146	0.1051
Magnetic field [T]	0.599	0.598
Number of water channels [channels/coil]	12	12
Pressure drop [MPa]	0.1	0.1
Water flow [L/min]	21	21
Flow velocity [m/s]	0.87	0.87
Temperature rise of cooling water Δt [°C]	12.5	10

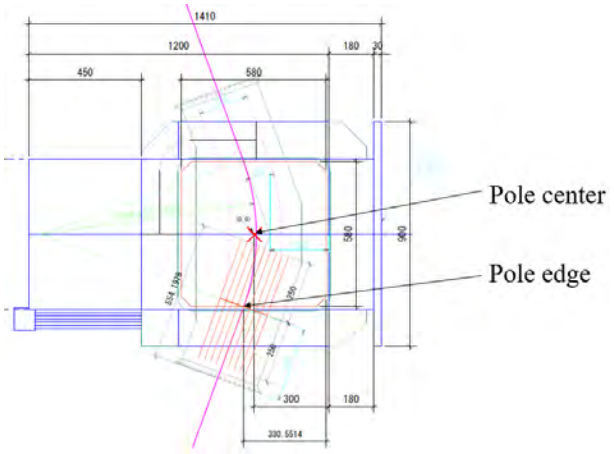

Figure 4. Reference point for magnetic field measurements.

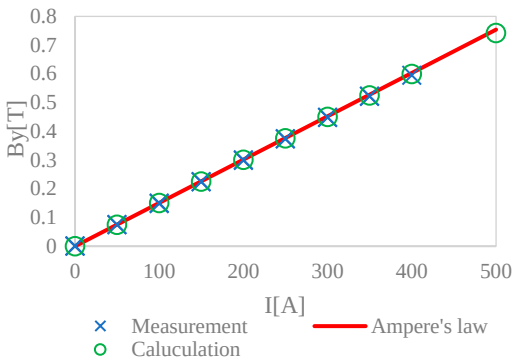

Figure 5. Excitation curve at the pole center.

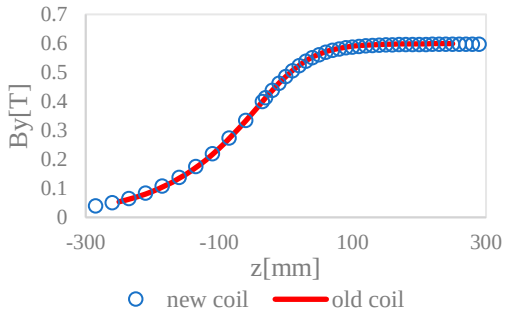

Figure 6. Magnetic field measurements.

Table 2. Calculation of transport 250 MeV/c muon

	Old coil	New coil
Cross section of hollow conductor	□12×12 -□6×6	□12×12 -Ø6.5
Cross section [mm^2]	108	110.8
Resistance (20 °C) [Ω]	0.1176	0.1146
Number of water channels [channels/coil]	6	12
Pressure drop [MPa]	0.1	0.1
Water flow [L/min]	15	21
Flow velocity [m/s]	1.26	0.88
Current [A]	510	510
Temperature rise of cooling water Δt [°C]	29	20

the new coils meet the requirements, indicating that they can be used at J-PARC.

3. Status of updating the MPS program for the Muon target

3.1 Display for the muon target in the MLF control room

Figure 7 shows the display for the muon rotating target in the MLF control room. When a hunting phenomenon occurred in the motor torque for the rotation of the muon target, the indicator lamp for the reverse rotation was blinking. According to the specifications, the reverse rotation indicator lamp must stay the same until the rotation has stopped. This indicated that there were some problems with the muon target rotation display system. Furthermore, since the graph that logs the torque values of the motor for the muon rotating target in the MLF control room showed torque fluctuation, also referred as hunting, with intense amplitudes, it was predicted that these two matters were related. Figure 8 shows a graph of the torque values for the muon target rotation motor.

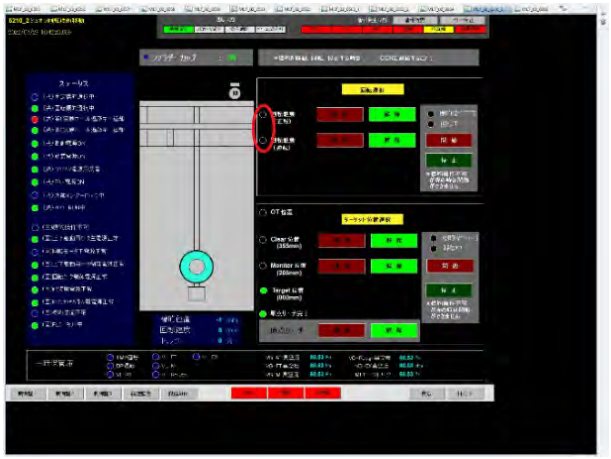

Figure 7. Display for the muon target in the MLF control room.

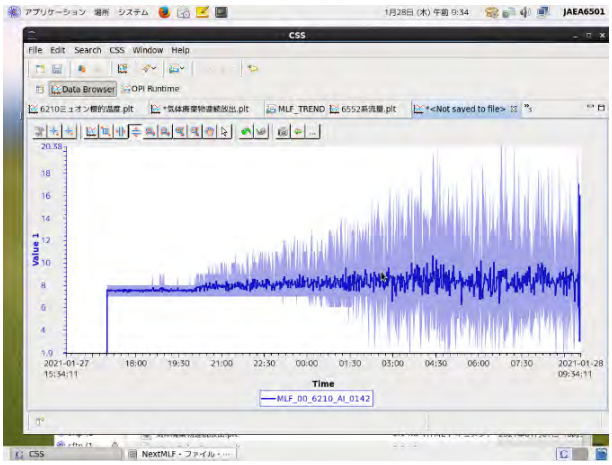

Figure 8. Graph of torque values for the muon target rotation motor showing hunting behavior.

3.2 Cause of failure for the MPS of the muon target

The control system for the muon target, including the muon target rotation control function, is installed in MLF experimental hall No. 2. This control system is used for the MPS of the muon target, and it seemed to be the main cause of the current problems [3].

In order to stop the rotation of the muon target safely, because of some mechanical resistances occurring in the rotation mechanism of the muon target, a MPS interlock fault is generated when the torque value of the muon target rotation motor exceeds a set threshold value. Initially, to prevent false MPS alarms due to electrical noise, the MPS signal was not generated immediately after an increase of the torque value, but only when the value increased continuously for one second. But with this method, if the torque value repeats intermittent increase and decrease within one second above the threshold, like in the case mentioned above of intense torque fluctuation such as hunting, a MPS signal cannot be generated. Figure 9 shows a comparison of two cases with and without MPS interlock fault generation when the torque threshold at which the MPS alarm occurs is set at 8% of the motor rated output ratio. The figure shows that the MPS alarm will not be generated unless the torque value exceeds the MPS threshold value for a consecutive period of time.

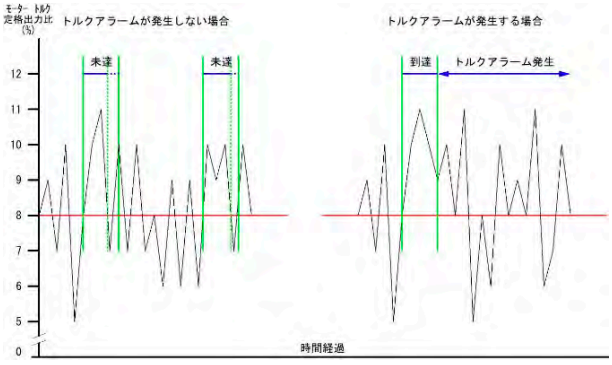

Figure 9. Comparison of the cases with (left) and without (right) MPS alarm generation.

3.3 Malfunction of the rotation indicator lamp

The reason for the wrong blinking of the lamp indicating the muon target reverse rotation was almost the same. In the case of the indicator lamp, the direction of rotation was obtained from the polarity of the torque value. Two timers were also used in the circuit for detecting normal and reverse rotation. The amplitude of the torque values was so intense that it quickly changed polarity, and it became impossible to detect the direction of rotation of the muon target, thus resulting in incorrect blinking of the indicator lamp.

3.4 Temporary and future measures

As a temporary measure, the timer was removed from the MPS alarm generation and detection of the rotation direction circuits. The MPS program was modified to immediately generate a MPS alarm when the instantaneous torque value exceeds the threshold. However, to avoid malfunction due to noise, the MPS threshold was set to 25% of the motor rated output. For the circuit that detects the direction of rotation of the muon target, the method of detecting the polarity from the torque value was changed to a method that detects states of the operation switch on the control panel.

Further, when the muon target was rotated in the reverse direction, the torque value of the rotation motor was higher than that in the normal direction, resulting in a certain tendency for the muon target to be unstable. In the MLF operation so far, in order to make the wear of the rotation mechanism and bearings uniform, the normal and reverse rotation operation were alternately used every few months. However, normal rotation only will be used for the time being.

4. Summary

A three-year plan from hollow conductor selection to coil replacement was established, and this year, the final year, coil replacement and magnetic field measurements were carried out. In the performance inspection after the coil retrofit, it was confirmed that each parameter was in general in agreement with the calculated values. The results obtained from the magnetic field measurements did not agree with the old coils at the fringe field, but assuming a misalignment of the magnet and the beam duct, the results agree well with the old coils. Furthermore, the number of cooling channels was increased, and the magnet was upgraded to be able to transport high-momentum muons (≤ 250 MeV/c). The DB2 dipole magnet with the new coils was reinstalled in the beamline and is now operating smoothly without the need of re-tuning the muon beam optics.

The update of the MPS program for muon target became necessary because of a hunting phenomenon that occurred in the torque value of the motor for the rotation of the muon rotating target, which resulted in a serious problem in generating MPS alarm for the muon target in FY2021. Although temporary measures have been taken to continue the operation, it is necessary to optimize the MPS program in the future in order to cope with the occurrence of hunting, as well as to determine the parameter settings of the motor, which is likely causing torque fluctuation such as hunting.

5. Acknowledgements

We are grateful to Dr. Y. Irie and Mr. R. Shimizu for helpful discussions and technical support during the magnetic field measurements. We would like also to thank Dr. Y. Bessho for his continuous support.

References

[1] T. Yuasa and Y. Kobayashi et al., Muon Beamlines and Control System, KEK-MSL REPORT 2020, KEK Progress Report 2021-6 (December 2021), 9-11.

[2] H. Fujimori and T. Yuasa et al., Muon Beamlines and Target Control System, KEK-MSL REPORT 2019, KEK Progress Report 2020-4 (October 2020), 13-15.

[3] Y. Kobayashi and S. Makimura et al., CONSTRUCTION OF CONTROL SYSTEM FOR MUON ROTATING TARGET AT J-PARC, The 8th Annual Meeting of Particle Accelerator Society of Japan, August 1-3, 2011, Epochal Tsukuba, 559-563. (in Japanese).

T. Yuasa[1,2], Y. Kobayashi[1,2], H. Fujimori[1,2], S. Matoba[1,2], N. Kawamura[1,2], P. Strasser[1,2], Y. Ikedo[1,2], A. Koda[1,2], K. Sakai[3], A. Watanabe[4], S. Sakata[4], M. Meguro[4], K. Kawabata[4], and H. Sunagawa[4]

[1]Muon Science Laboratory, Institute of Materials Structure Science, KEK; [2]Muon Science Section, Materials and Life Science Division, J-PARC Center; [3]Japan Atomic Energy Agency, JAEA; [4]NAT Co., Ltd.

Commissioning of the Ultra-slow Muon Beamline in FY2021

1. Introduction

Muons play an active role in materials science as microscopic magnetic probes. In accelerator-based experiments, muons are obtained as decay products of pions, which are produced by irradiating a fixed target with a proton beam. Muons produced near the surface of a production target are called "surface muons."

Surface muon beams have been used since the mid-1980s in meson factories around the world. The near-perfect spin polarization, monochromaticity, and high intensity of the beams brought many results in materials science. However, their kinetic energy of 4 MeV requires a sufficiently thick sample or a degrader. The large spatial and energy spread of the beam has limited its use to bulk sample measurements.

To overcome the limitation of the implantation depth resolution of surface muons, the ultra-slow muon (USM) project by laser ionization of muonium is underway at J-PARC MLF MUSE. The surface muon beam delivered by the Super-Omega beamline irradiates a muonium production target, and muonium in a vacuum is dissociated by laser ionization. This method produces very slow muons with kinetic energy corresponding to the target temperature. Using the USM, unique experiments to selectively implant muons near interfaces in materials and depth-resolved muon spin spectroscopy are possible.

2. The USM beamline

The U1 facility consists of a surface muon beamline, muonium production target, optics for ionization laser, electrostatic lens for extraction, and transport optics. Figure 1 shows a layout of the transport optics. The beamline has two branches, U1A for USM-μSR and U1B for transmission muon microscope.

3. Present status and tasks

The Super-Omega beamline delivers the world's most intense pulsed surface muons. The total flux of the beam is on the order of 10^8 μ^+/s [1]. The typical USM flux is about 2×10^2 Hz after EB1 with the Lyman-α light's pulse energy of 5 μJ.

The parameters of the transport optics have been optimized by maximizing the USM counts at the microchannel plate (MCP) detector installed at F3. However, the total flux and the profile are essential for optimization. The detector at F3 has been operated with a single anode without position sensitivity. The beam profile was obtained by knife-edge scanning with movable slits [2].

The USM beam intensity needs to be increased for the start of the user programs. A detailed understanding and systematic optimization of the transport optics is essential for this purpose.

4. Progress in FY2021

In FY2021, the MCP detector at F3 was replaced by a delay-line detector (DLD). The MCP-DLD detects the position of a particle from the time difference by reading out both ends of the wires that collect the charge amplified by the MCP. Rapid profile measurements using the MCP-DLD made it possible to scan multiple parameters. A typical result on a two-dimensional scan of the MB currents and the EB voltages is shown in Fig. 2.

Figure 2 shows three regions of large yield, each corresponding to a different beam profile. Since a well-focused beam is better suited for smaller samples, it is

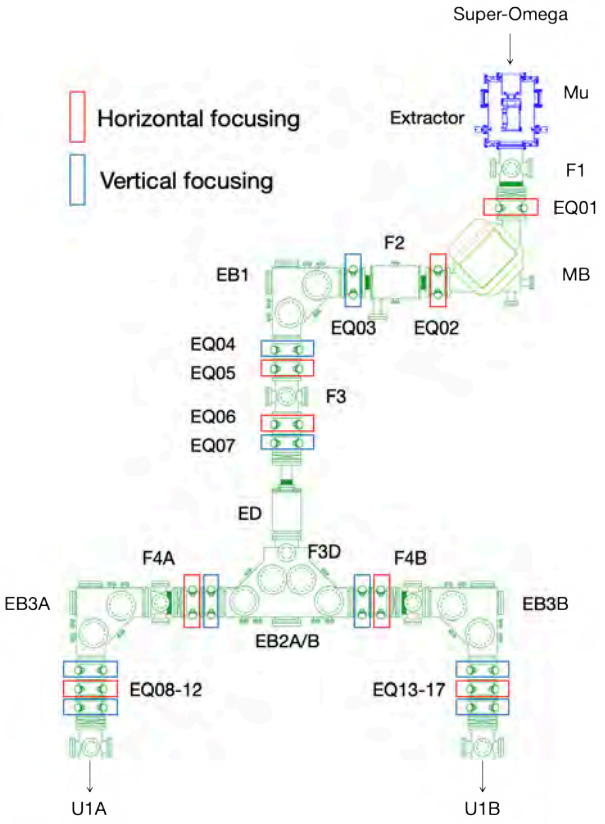

Figure 1. The USM beamline in the U1 area. USMs are obtained by laser ionization of muonium atoms produced at the target (Mu). The transport optics has electrostatic quadrupoles (EQ), the magnetic bend (MB) for momentum selection, the electric bends (EB) for energy selection, the electric deflector (ED) for beam destination switching, and detector ports (F).

beneficial to optimize the transport optics by taking the profile into account rather than simply using the yield as an indicator.

As a starting point, the transport optics were tuned using the Zone C setting shown in Fig. 2. The voltages of the five EQs from EQ01 to EQ05 were changed to search for conditions where the beam width becomes narrower. The results of comparing the profiles before and after the adjustment are shown in Fig. 3. The tuning shaped the beam width to a standard deviation of 1.8 mm (horizontal) and 1.6 mm (vertical). This beam profile is narrow enough compared to typical μSR samples.

In addition to the MB:EB scan, S2:S3 scans of the extraction electrodes [3], and two-dimensional scans of each EQ pair were performed to optimize the parameters. These measurements enabled systematic and efficient optimization of strongly correlated parameter pairs. The optimization method will be extended to higher dimensions to achieve a comprehensive understanding of transport optics.

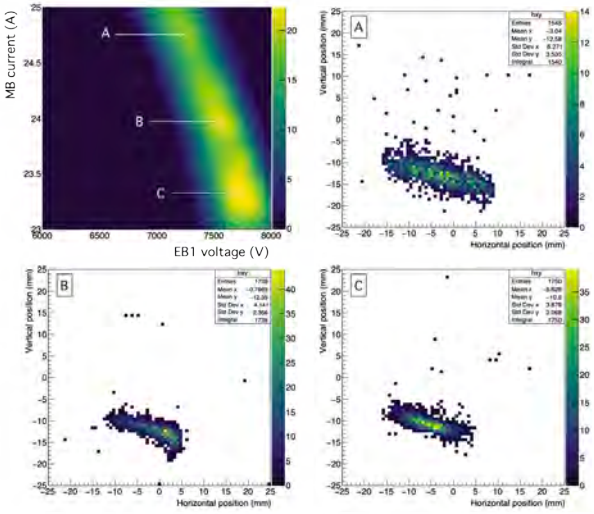

Figure 2. The result of yield and profile measurements from a two-dimensional grid scan of the magnetic and electric bends. The top left figure shows the yield, and the remaining three plots show the profile in zones A, B, and C, denoted in the top left.

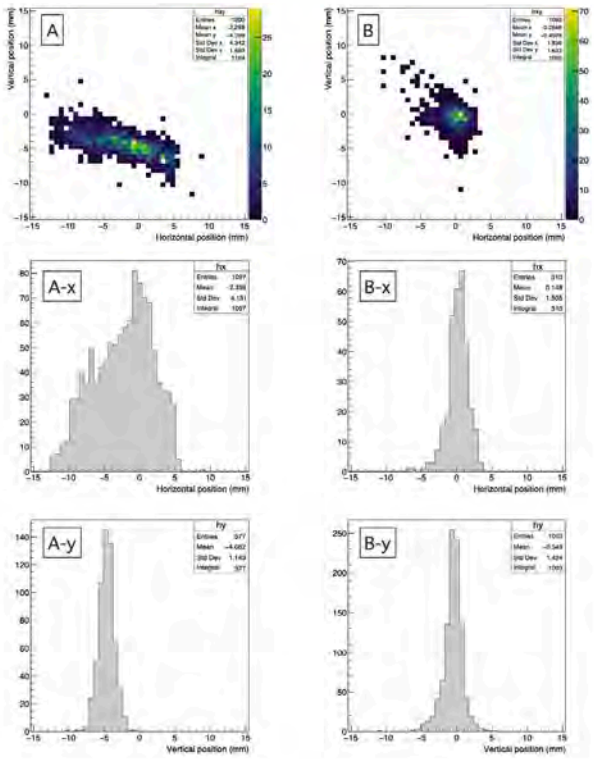

Figure 3. Comparison of beam profiles before and after adjustment. Group A corresponds to before adjustment, B to after. The projections were obtained using the bin that gives the largest yield and the four bins before and after it.

5. Summary and prospects

In the FY2021 commissioning, a method to optimize beam transport parameters using the MCP-DLD was established. From the next campaign, the USM intensity will be increased by improving the laser pulse energy and searching for a highly efficient muonium production target, aiming at the start of USM-μSR user programs.

References

[1] The total beam flux is 6.4 × 107 μ+/s at 212 kW. Y. Miyake et al., JPS Conf. Proc. 21 (2018) 011054.
[2] A. D. Pant et al., JPS Conf. Proc. 21 (2018) 011060.
[3] The extractor consists of four electrodes from S1 to S4, see P. Strasser et al., J. Phys.: Conf. Ser. 551 012065 (2014).

S. Kanda[1,2], T. Adachi[3], Y. Ikedo[1,2], Y. Oishi[1,2], and K. Shimomura[1,2]
[1]Muon Science Section, Materials and Life Science Division, J-PARC Center; [2]Institute of Materials Structure Science, KEK; [3]Nishina Center for Accelerator-Based Science, RIKEN

USM Commissioning at U1B area [J-PARC: 2021B0001]

The 5 MeV muon-cyclotron system has been constructed at the KEK Tsukuba campus, and was installed at the U1B area (see Fig. 1). The cyclotron is employed to accelerate the 30 keV ultraslow muon beam to 5 MeV for transmission muon microscopy (TμM). The TμM will visualize thick objects (>10 μm) in nanometer resolution. Quantum coherence of the ultra-slow muon beam, and deep-penetration power of the muon beam accelerated to 5 MeV will expand its capabilities.

1. Details of the muon cyclotron

The accelerated muon beam should have quite small energy dispersion ($\Delta E/E \sim 10^{-5}$) to reduce chromatic aberration of the object lens of the muon microscopy. To realize such a small energy dispersion, flat-top RF acceleration technology is employed, namely, not only the two main RF-cavities of 108 MHz (main Dee) but also a flat-top RF-cavities (flat top Dee) of 324 MHz are installed in the cyclotron (see Fig. 2).

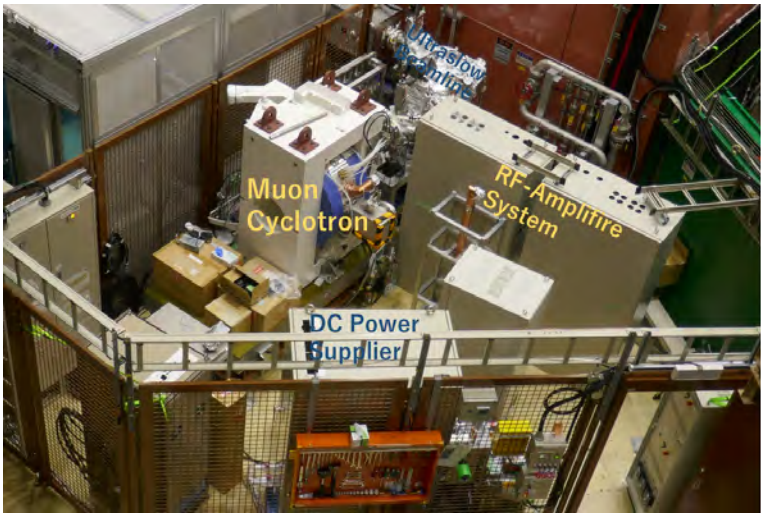

Figure 1. The 5 MeV muon-cyclotron system installed on the U1B area. The center block is the main body of the muon cyclotron, and the 2 cabinets are the 108 MHz/20 kW RF amplifier system including a low-level RF controller system.

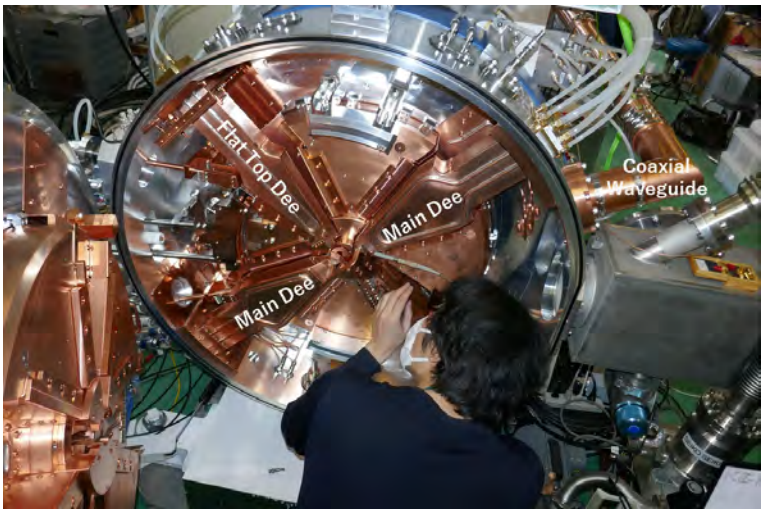

Figure 2. Internal structure of the 5 MeV muon-cyclotron. The ultraslow muon beam is injected at the center, and is accelerated by the Dees. The RF power is provided by the coaxial waveguide.

2. RF Controller and Power Amplifier

The cyclotron requires RF power of 108 MHz/20 kW to accelerate the muon beam to 5 MeV energy by less than 1μsec. It also requires 324 MHz RF less than 1 kW for flat-top acceleration. We constructed the low-level RF controlling system (Fig. 3) and the power RF amplifiers (Fig. 4). The low-level RF control system works to produce stable RF resonance in the cyclotron by driving the tuner of the cyclotron and controlling the amplitude and phase of the input RF powers. The controller consists of the fast A/D and D/A converters and FPGAs. Complex modulators and demodulators are used for a digitalized super heterodyne system.

The power RF amplifier consists of 16 RF-amplifiers of 1.5 kW and 16-way RF-combiner (Fig. 4). All systems, including the low-level RF controller except for the combiner, are stored into 2 cabinets.

At the next beam time from November 2022, the cyclotron system will be started to work.

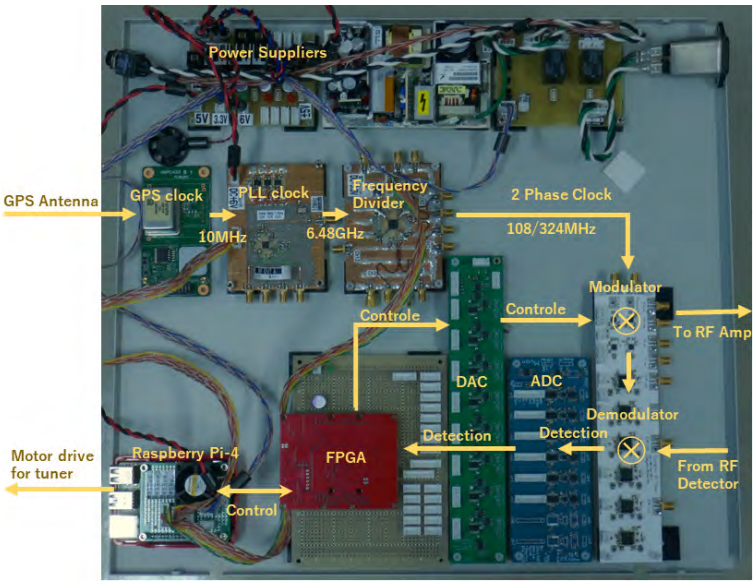

Figure 3. Low-level RF controller system.

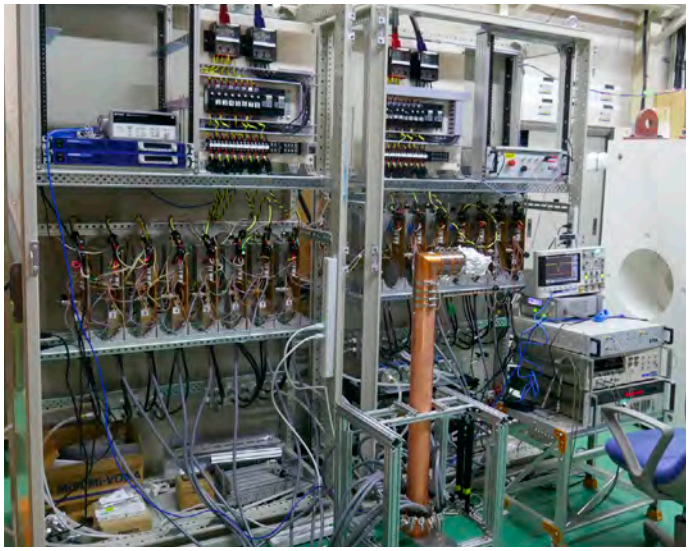

Figure 4. Internal structure of the 108 MHz / 20 kW RF Amplifier System. Panels of the cabinet are removed for tuning. The front pipe is the 16-way RF combiner.

Y. Nagatani[1], T. Yamazaki[1], J. Ohnishi[2], A. Goto[1], T. Yuasa[1], S. K. Dey[1], T. Adachi[1], and Y. Ikedo[1]
[1]*Muon Science Laboratory, Institute of Materials Structure Science, KEK;* [2]*Nishina Center, RIKEN*

The Progress of Laser System for Ultra-Slow Muon Generation

1. Introduction

Ultra-slow muons are attracting an increased attention as a probe for particle physics and material science. These ultra-slow muons are generated by stopping surface-muons in a target and ionizing the evaporated muonium by irradiating of coherent lights. To realize efficient ionization of muonium, vacuum ultraviolet (VUV) light (Lyman-α light) and coherent light with wavelengths shorter than 360 nm are required. So far, over 10 μJ Lyman-α light has been successfully generated and applied to ultra-slow muon generation. In this paper, we report on the additional equipment to keep stable irradiation of the Lyman-α light.

2. Problem in the reduction of Lyman-α light intensity

Ultra-slow muons can be generated by resonant optical ionization of thermal muonium from hot-W foil target. 122.09 nm (Lyman-α) and 355 nm coherent pulses are required for 1*s* to 2*p* state excitation and 2*p* to ionization, respectively. The high-energy pulsed coherent Lyman-α light source is one of the very important elements for the efficient generation of the ultra-slow muons. The design of the Lyman-α light source system is described in Ref. 1. More than 10 μJ Lyman-α pulse is stably generated in a krypton/argon mixture filled gas-cell by the methods of two-photon-resonant four-wave-mixing, which require 212.556 nm and 820 nm pulses. Vacuum ultraviolet light has high photon energy, which over time causes degradation of optical materials. In addition, photochemical reactions that occur between vacuum ultraviolet light and residual gaseous, mainly hydrogen and carbon that cannot be evacuated by a turbo molecular pump in a vacuum, cause performance degradation of Lyman-α steering mirrors. Degradation of the optics causes a decrease in the ultra-slow muon yield and beam downtime for optics replacement. This is a problem for future experiments.

The equipment setup of the Lyman-α light generation and propagation for the ultra-slow muon generation is shown in Fig. 1. Lyman-α light is generated in a gas cell and propagates through the lithium fluoride window, which is separating the gas and the ultrahigh vacuum. Inside the ultrahigh vacuum, a steering and a focusing mirrors are placed to control an irradiating position and beam shape.

Even in an ultrahigh vacuum of about 10^{-6} Pa, there are many light elements such as hydrogen and carbon as residual gases, so interaction with the Lyman-α light is inevitable. In the optical path, hydrocarbons are formed by ionization of the residual gas and deposited on the mirror surface with a certain probability. If this deposition of hydrocarbons continues for a long time, the reflectance decreases significantly due to scattering and absorption of Lyman-α light. If the same spot is continuously irradiated with Lyman-α light for a long period of time, cloudiness on the surface of the mirror is obviously observed. The photo of a clouded mirror is shown in Fig. 2. Each of the colored spots is a laser irradiated point accumulated over 3 weeks or a longer period. The performance degradation of the window and mirrors as a function of the irradiation time, as shown in Fig. 3. The fastest intensity reduction component is caused by Kr/Ar mixture degradation and it is recovered every 3 hours by automatic change of the mixture. The second reduction component is the degradation of transmittance at a gas cell window caused by color center. The intensity reduction is recovered by displacement of the window every 3 days. The residual intensity reduction component is degradation of the mirror reflectance. As you can see in Fig. 3, the intensity of Lyman-α after 8 days will be decreased to 50% of the maximum intensity when the mirror irradiation position is not changed.

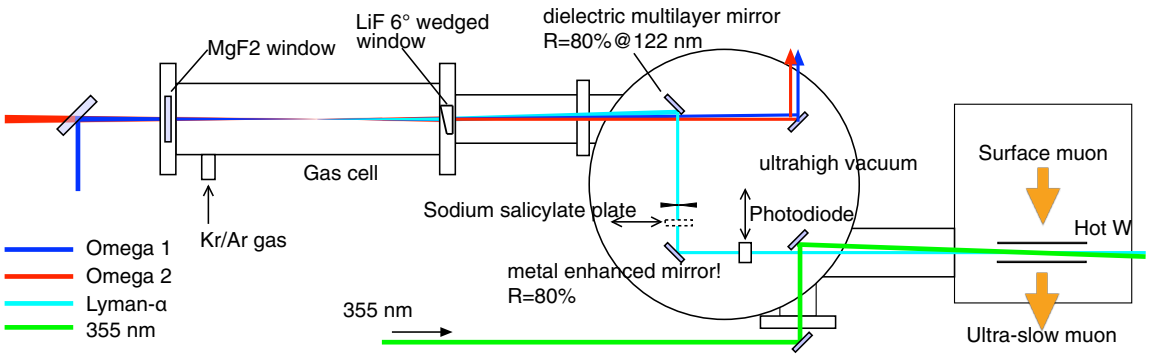

Figure 1. A schematic of Lyman-α generation and propagation setup for ultra-slow muon generation.

3. Mirror steering and displacement system

This year, we introduced a drive mechanism that can change the laser reflection position on the mirrors for vacuum ultraviolet light to recover the reflectivity of the two mirrors. The equipment adds a mirror displacement function to the mirror mount that can adjust the horizontal angle and vertical tilt of the mirror. The mirror mount located upstream has a rotation stage to rotate a ø50 mm circular shape mirror and a linear stage for translation (30 mm stroke). The mirror mount on the downstream side uses a 50 mm square shape cylindrical mirror, so horizontal and vertical translation stages were introduced. The installed mirror mounts are shown in Fig. 4. These stages are equipped with built-in encoders so that the movement history of the mirror position can be recorded, allowing the laser reflective surface to be set to the unirradiated area when the reflectivity of the mirror decreases. The new mirror steering and displacement system enables the mirror irradiation position adjustment by remote control without opening the vacuum chamber to the atmosphere.

4. Summary

A mirror steering and displacement system was introduced to maintain high intensity of the Lyman-α light, which directly affects the yield of ultra-slow muons.

The newly introduced mirror steering and displacement system significantly reduces the maintenance work and enables long-time ultra-slow muon experiments. However, the size of the steering mirror is finite, it will still be necessary to replace it with the vacuum chamber opened during beamtime. Since the frequency of mirror replacement is expected to increase as the Lyman-α intensity increases, we plan to remove hydrocarbons in the vacuum chamber using a NEG pump in order to extend the mirror's lifetime.

Acknowledgement

This work was carried out with Mr. K. Hosoya and Prof. S. Nakamura at Ibaraki Univ.

Reference

[1] N. Saito et al., Opt. Express, 24, 007566 (2016).

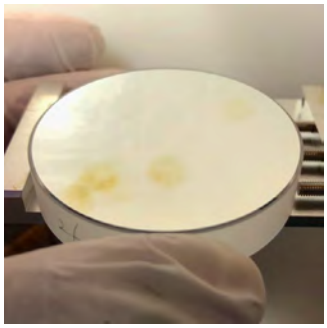

Figure 2. Typical degraded mirror. Several colored spots on the mirror surface are laser irradiated.

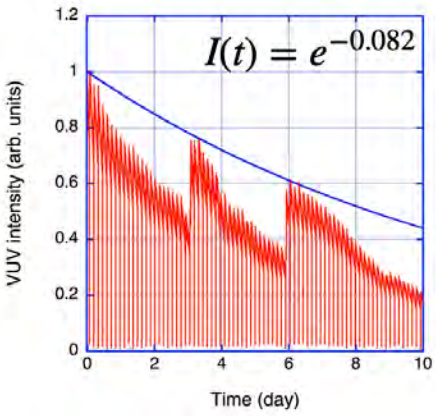

Figure 3. The typical time revolution of Lyman-a intensity.

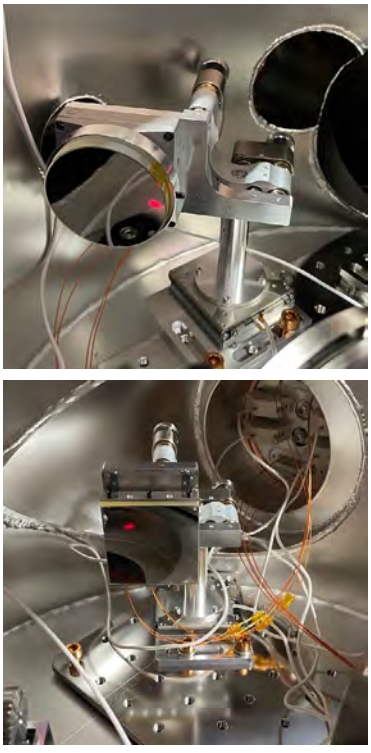

Figure 4. Installed motorized mirror mount with translation stages for steering and displacement of the VUV mirror.

Y. Oishi[1,2]

[1]*Muon Science Laboratory, Institute of Materials Structure Science, KEK;* [2]*Muon Science Section, Materials and Life Science Division, J-PARC Center*

Present Status of the S-line

The S line has been designed and constructed to mainly utilize surface muon beams, with a second planned experimental area, S2, starting its operation in 2021. The use of the kicker device allows double pulses to be used simultaneously as single pulses for the two areas currently in operation, S1 and S2. In this respect, a stable operation of the kicker device is very important.

The configuration of the kicker device and the previous troubles have been reported in earlier MSL reports [1]. The 600 V DC power supply failure, which had often occurred since the S line began operation in 2017, has not happened since the addition of smoothing capacitors in the summer of 2019. On the other hand, MARX board failures have continued to occur several times per year. Most of the failures were caused by damage to the charge current detecting resistor, and each time a failure occurred, the manufacturer replaced the resistor with a high-surge resistance resistor. Since the repaired boards have never failed again, we decided to replace the resistors on 384 MARX boards during the summer shutdown period of 2021, before the beginning of a full-scale simultaneous operation of S1 and S2. The work was performed by subcontracting staff. It took about 100 man-days over a period of about two months, with a maximum of three people per day who were relatively free for other maintenance work.

Another issue, the location of the kicker power supply unit, was also addressed during the summer shutdown period. Conventionally, the kicker power supply unit was installed inside the S-line concrete shielding. This was because it was unknown how much the noise generated by the electric field kicker would affect the experiment. However, with this method, whenever a MARX board failure occurred, the concrete shielding had to be opened and replaced, and this required waiting for the weekly maintenance day. Moreover, the work had to be done under very tight schedule, including checking the restoration of the shielding so as not to affect the operation resumption schedule. Therefore, we decided to relocate the kicker power supply unit to the fourth floor of the power supply yard. Originally, the kicker power supply unit had a coaxial cable delay line so that the reflected pulses would come after the muon data window, and the coaxial cables were wound on drums and installed in the concrete shielding. In the relocation work, the coaxial cables were unwound from the drums and connected to the kicker power supply unit on the fourth floor of the power supply yard through an independent cable rack to prevent noise from the electric field kicker operation from affecting other equipment.

In December, an engineer representing the manufacturer visited J-PARC MLF to conduct a comprehensive operation verification test and confirmed that there were no problems with the generated voltage waveforms. Unfortunately, there were times when the system had to be shut down due to the MARX board failure even after the maintenance works performed in the summer of 2021. However, there has never been a failure caused by damage to the charging current detection resistor, and all failures are now due to damage to the FETs. In addition, operation can be resumed up to half a day after a failure is detected, which is a significant improvement from the previous situation where it took up to seven days to resume operation. The manufacturer is currently investigating the cause of the FET failures and working on preventive countermeasures.

Reference

[1] K. M. Kojima et al., KEK Progress Report 2018-2 (2019) 16-17.

A. Koda, T. Yuasa, J.G. Nakamura, S. Nishimura, P. Strasser
Muon Science Laboratory, Institute of Materials Structure Science, KEK

Development of Sample Environment at the S1 Area – Reorganization of Electrical Systems –

The sample environment equipment for the μSR experiment receives its power supply from the S1 area experimental panel, which is the downstream distribution panel in the S1 area, to which various other pieces of equipment are connected. For example, "detectors and servers for μSR measurements" and "vacuum pumps for the beamline" are connected to the distribution panel. Although these devices were separated at the end breakers of the distribution board according to their respective characteristics, they were mixed up to one breaker upstream, according to the 2021 survey.

At the MLF, J-PARC, strict controls are generally in place to ensure electrical safety. One of the results of this is that the breakers of the distribution boards, which were installed according to the electrical safety application, ensure protective coordination based on their catalog specifications. It means that the downstream breakers have a faster time to operate, and in principle, the downstream breakers trip in sequence, so that the upstream breakers do not operate first. In practice, however, there are various transient phenomena, and the phenomenon of one upstream breaker tripping first can sometimes occur.

In this work, the electrical systems of the "sample environment equipment, which can be changed according to experimental conditions," and the "beamline vacuum pumps" were separated at one upstream breaker, as shown in Fig. 1. As a result, the vacuum system of the beamline is no longer affected by troubles during sample environment operation with user experiments.

The 2021 survey also revealed in this S1 area experimental panel that several cable taps and four other taps called JAERI taps (referred to as JTAP) were extended from the 15-A trip (AT) breakers and 20 AT breakers, respectively. The price of this JTAP was about 100,000 yen, which is expensive, but the cable and tap are solidly made and can be rolled on the floor at the MLF. The commonly distributed table taps, as the name suggests, are designed to be installed on tables, etc., and it is considered inappropriate to install cables and taps rolling on the floor from the standpoint of electrical safety. Although JTAPs are highly convenient at the MLF, they are not suitable for connecting loads that use large amounts of power. This is because the eight connection ports induce over-connection of the loads. Therefore, in this work, when large loads such as vacuum pumps and

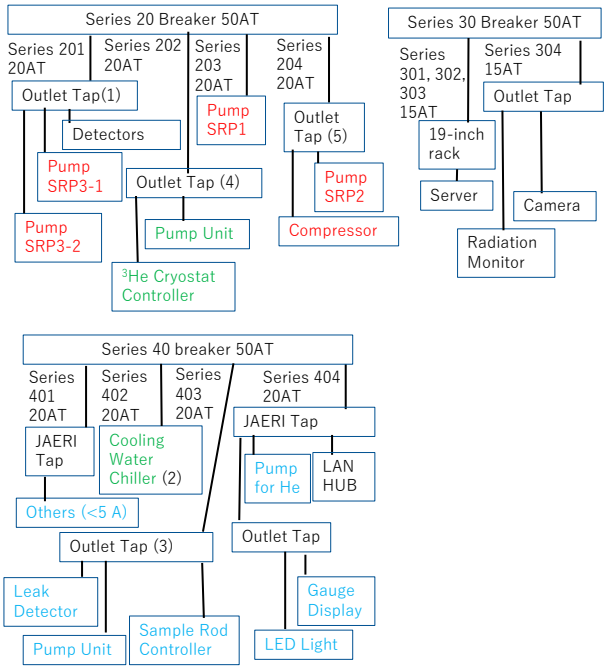

Figure 1. Electrical system diagram of the S1 area experimental panel, consisting of three series (20, 30 and 40) connecting to upstream breakers. The beamline vacuum pumps are shown in red letters. The blue and green letters indicate the sample environment equipment: the former is to be changed according to the experimental conditions, and the latter is to remain unchanged.

cooling water chillers were connected to the JTAP, the JTAP was removed and taps with a smaller number of connections were laid and organized for connection as shown in Fig. 1. At this time, in the wiring from the 20 AT breaker, a terminal block was installed and branched to connect two outlet taps, so that the load connected per outlet tap would not exceed 15 A. This is because the upper limit for use of the outlet taps is 15 A. If the outlet tap is directly connected to a 20 AT breaker, the upper limit of use would be 15 A.

Note that in this work four new cables were laid when reorganizing the electrical system (Fig. 2). The cables used were 2PNCT8sq-3C and 2PNCT2sq-3C, standard cables that are relatively soft and can be rolled on the floor. There was also an outlet installation on the 100 V 20 AT and 15 AT breakers, which was not an electrical work that required an application for use in accordance with the J-PARC Center Safety Management Regulations. An application for use is required for electrical works with a voltage exceeding 750 V for direct current and 600 V for alternating current, and for electrical works with a rated output exceeding 7.5 kW or 7.5 kVA or a rated current exceeding 30 A.

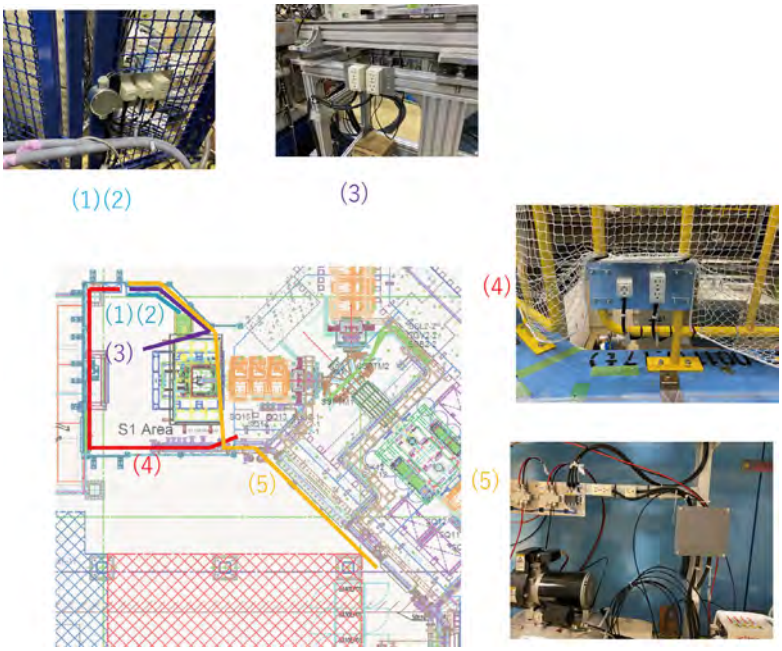

Figure 2. Cable installation and outlet taps from the S1 area experimental panel installed in this work. (1) to (5) numbers correspond to those shown in Fig. 1.

J. G. Nakamura[1,2], T. Yuasa[1,2], M. Meguro[3], S. Nishimura[1,2], and A. Koda[1,2]
[1]Muon Science Laboratory, Institute of Materials Structure Science, KEK; [2]Muon Science Section, Materials and Life Science Division, J-PARC Center; [3]NAT Corporation

H-Line Commissioning

The H-line is a muon beamline in the east #1 experimental hall of the MLF. It is a general-purpose beamline [1] that can generate both positive and negative muons. Its design intensity of surface muons reaches 10^8 muons/s with a proton beam power of 1 MW thanks to the large acceptance (108 mSr) of its capture solenoids and other beamline magnets with large apertures. The H-line has two branches named H1- and H2-area. The first branch (H1-area), where the hyperfine splitting measurement of muonium (MuSEUM experiment [2]) and search for a cLFV (charged Lepton Flavor Violation) process (DeeMe experiment [3]) are planned, has begun operation after the summer shutdown in FY2021. The second branch (H2-area) is under construction and aimed at experiments using a low emittance muon beam obtained by re-accelerating ultra-slow muons, such as the muon *g-2*/EDM experiment [4] and a transmission muon microscope (TμM) project.

The beam commissioning of the H-line has begun in January 2022. During the beam commissioning, large positron/electron background existed because the DC separator was not installed yet. It made the beam commissioning difficult, but we managed to measure beam intensity, profile, and momentum of surface muons. The beam intensities of negative muons at several momenta were also measured.

Figure 1 shows the setup to measure muon beam intensity. Decay positrons from the muon stopping target are measured using a pair of plastic scintillators. From the number of detected positrons (see Fig. 2) and detector acceptance estimated using a Geant4-based simulation [5], the preliminary result of surface muon beam intensity was estimated to be $(8.3 \pm 0.7) \times 10^7$ muon/s for 1 MW proton beam. This is about 75% of our expectations. We expect to recover the remaining 25% by modifying the power supplies of the muon capture solenoids. Due to the speculations of the power supplies, the rated currents cannot be applied now.

The momentum of surface muons was measured with almost the same setup as the intensity measurement. In the momentum measurement, a magnetic field of 23.85 G was applied to an aluminum target of various thicknesses. Due to the muon spin rotation in a magnetic field, the time spectrum of decay positrons showed wiggled structure. In Fig. 3, the beat amplitudes are plotted as a function of the thickness of the Al targets. The range of surface muons in Al was obtained by fitting this plot with an error function, and then we estimated the beam momentum to be 28.0 MeV/c (RMS 1.2 MeV/c), which was consistent with our expectation.

Figure 1. Setup of the beam intensity measurement.

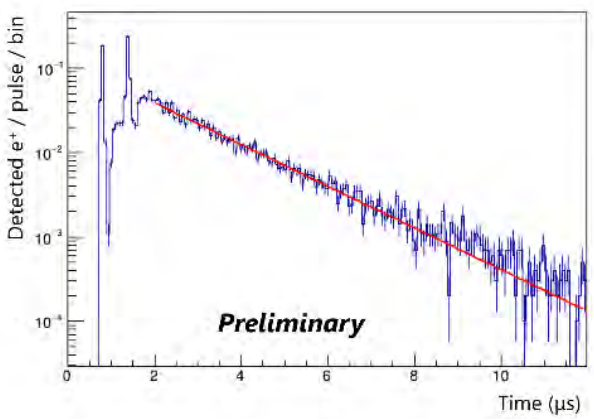

Figure 2. Time spectrum of decay positrons in the intensity measurement of surface muons.

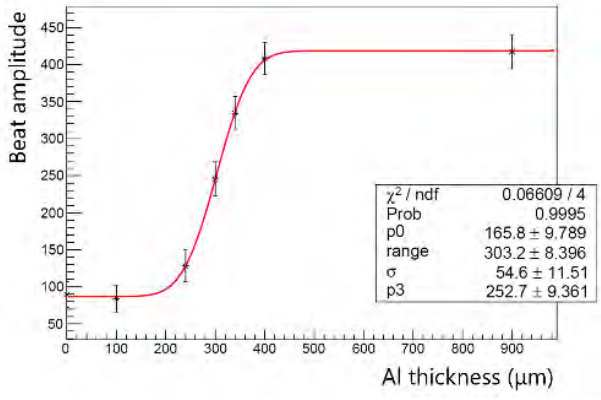

Figure 3. Muon range measurement to estimate surface muons.

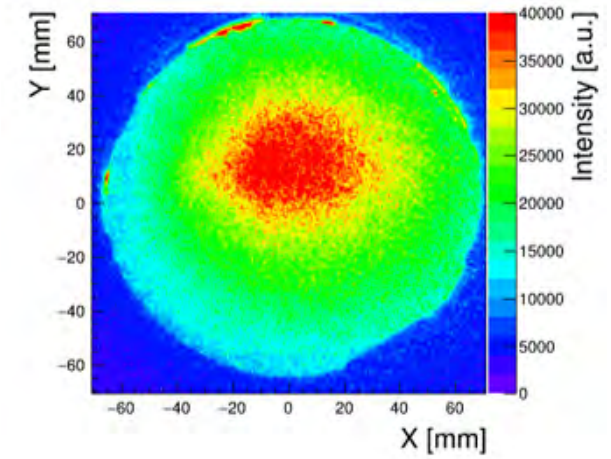

Figure 4. Typical beam profile of surface muons at the H1 area.

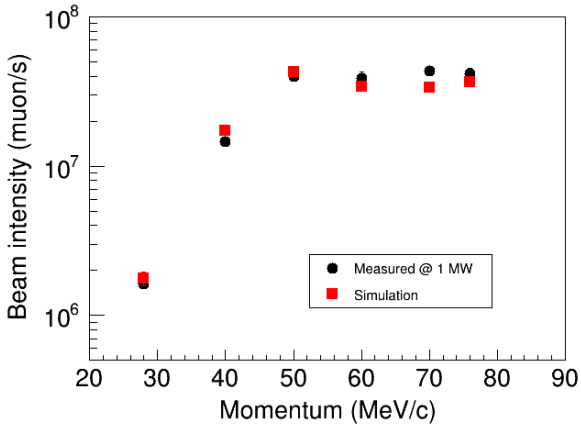

Figure 5. Negative muon yields at the H1-area.

The beam profile of surface muons was observed using a beam profile monitor developed by T. U. Ito (JAEA), *et al.* [6]. A typical beam profile at the H1 area is shown in Fig. 4 and its horizontal and vertical beam sizes are σ_x = 44 mm and σ_y = 24 mm, respectively.

The commissioning of negative muons was also conducted. Beam intensities of negative muons with several momentum setups are shown in Fig.5. The measured results have a good agreement with Geant4-based simulation of negative muons at the H1-area. Tthe plateau over 50 MeV/c is also due to the speculations of present power supplies of the capture solenoids. By modifying the power supplies, the capture solenoids can capture pions with higher momenta, resulting in more negative muons with higher momentum at the H1 area.

In the first beam commissioning at the H1-area, we measured beam intensity, momentum, and profile of surface muons and beam intensities of negative muons with several momentum setups. The commissioning has demonstrated that the beam performance of the H-line was almost as expected, given the present speculations of the power supplies of the capture solenoids. Next commissioning is planned after the modification of the power supplies and installation of a DC separator (Wien filter), both of which will be conducted in FY2022.

Acknowledgments

The authors are grateful to T. Ushizawa, S. Sugiyama, K. Hase, Y. Higashino, S. Kaneko, R. Tagawa, H. Tada, T. Mibe, and all members who joined the commissioning at the H1 area.

References

[1] N. Kawamura, *et al.*, Prog. Theor. Exp. Phys. **2018** (2018) 113G01.
[2] K. Shimomura, AIP conf. proc. **1382** (2011) 245.
[3] H. Natori, *et al.*, Nucl. Phys. B (Proc. Suppl.) **248-250** (2014) 52-57.
[4] T. Mibe, *et al.*, Chin. Phys. C **34** (2010) 745.
[5] S. Agostinelli, *et al.*, Nucl. Instrum. Methods Phys. Res. A **506** (2003) 250-303
[6] T.U. Ito, *et al.*, Nucl. Instrum. Methods Phys. Res. A **754** (2014) 1-9

T. Yamazaki[1,2] and N. Kawamura[1,2]

[1]Muon Science Section, Materials and Life Science Division, J-PARC Center; [2]Muon Science Laboratory, High-Energy Accelerator Research Organization (KEK-IMSS)

MLF Safety

Research Safety

1. Radiation safety

Maintenance of SAmple Radioactivity Evaluation program

SAmple Radioactivity Evaluation program (SARE) is continuously maintained to estimate the radioactivity of an irradiated sample for instrument groups. The estimation at all neutron beamlines can be performed by SARE. SARE is used to bring a sample away from controlled areas. In 2021, radioactivity production by negative muons and a mode irradiated by realistic neutron flux can be implemented.

Extension of the entry administration system

In 2021, the entry administration system of the controlled was extended to the entrance at the BL09 building and BL22 building. The system provides an entry to the experimental hall and an exit from it with a certification by an OSL badge (See Fig. 1).

Radiological license upgrade

Although the applications for radiological license upgrades in FY2020 were approved on April 28, 2020, the facility inspection was passed on January 27, 2022.

The following items were updated after the application approval in FY2020:

(1) Construction of a High momentum decay muon instrument (H-line).
(2) Change of the Accelerator experimental room followed by the construction of H-line.
(3) Extension of the Surface muon instrument (S-line).

The next application is prepared and is adjusted in cooperation with local governments and the nuclear regulatory agency. Recently, the licensing process time has increased and it is possible to apply for the new licensing only once a year.

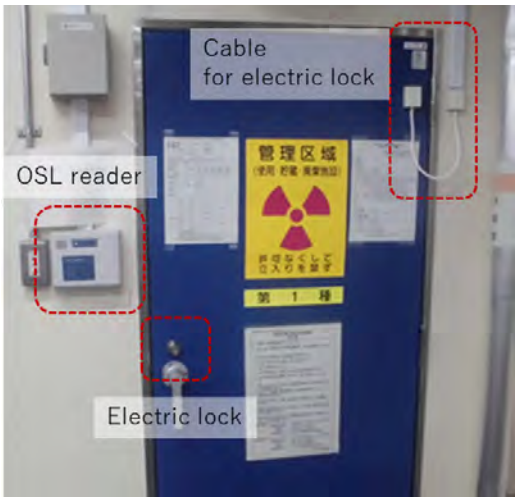

Figure 1. Electric lock and OSL reader authorizing the entry to the controlled area at the BL22 building.

2. Chemical safety

This year, due to space limitations, only statistics of the chemical safety check are shown in Fig. 2. Their number decreased due to the effect of the COVID-19 pandemic.

3. Crane safety

Also, this year, due to space limitations, only statistics of the crane usage are shown in Fig. 3. The usage was not affected by the COVID-19 pandemic.

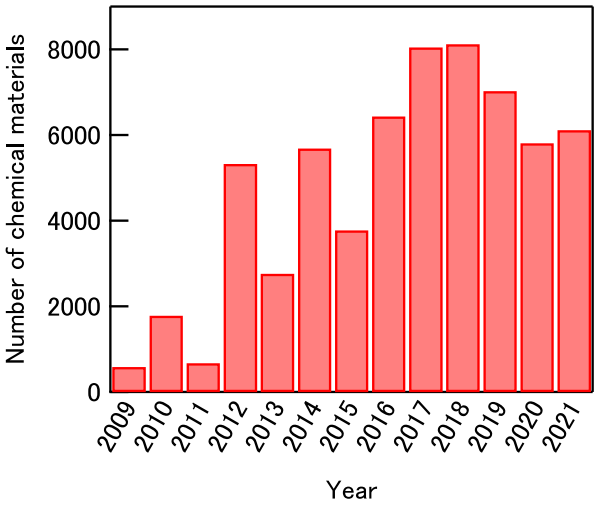

Figure 2. Trend of the amount of user-brought chemical materials for chemical safety check from the start of the MLF operation to the last year.

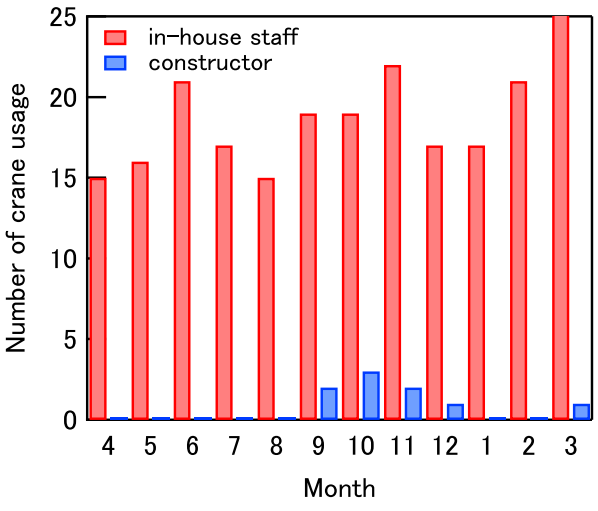

Figure 3. Trend of the total crane usage in one year.

4. COVID-19 pandemic measures

(1) General overview

As in the previous fiscal year, the MLF division handled the COVID-19 pandemic under the guidelines of the JAEA and KEK measures and the same measures were continued. As a result, no user infections occurred at the MLF and the beam time was operated as planned and there were no facility shutdowns due to the Covid pandemic.

As a record of specific efforts, photographs of a daily alcohol disinfection points are shown in Fig. 4, because it could not be included in last year's annual report due to space limitations. The number of times of disinfection per day was determined according to the frequency of entry to the point.

(2) Related matters

In response to the spread of Covid-19, we examined the safety of remote experiments, which are considered a new experimental method because users do not come to MLF. In particular, the items to consider are information security, equipment safety by re-mote control, and export control. The staff carried out a model experiment with overseas researchers, confirmed some problems, such as communication speed, and made plans to resolve them in the future.

(3) Next year

At the moment, the COVID-19 pandemic has not converged, so we will continue to take similar measures next year.

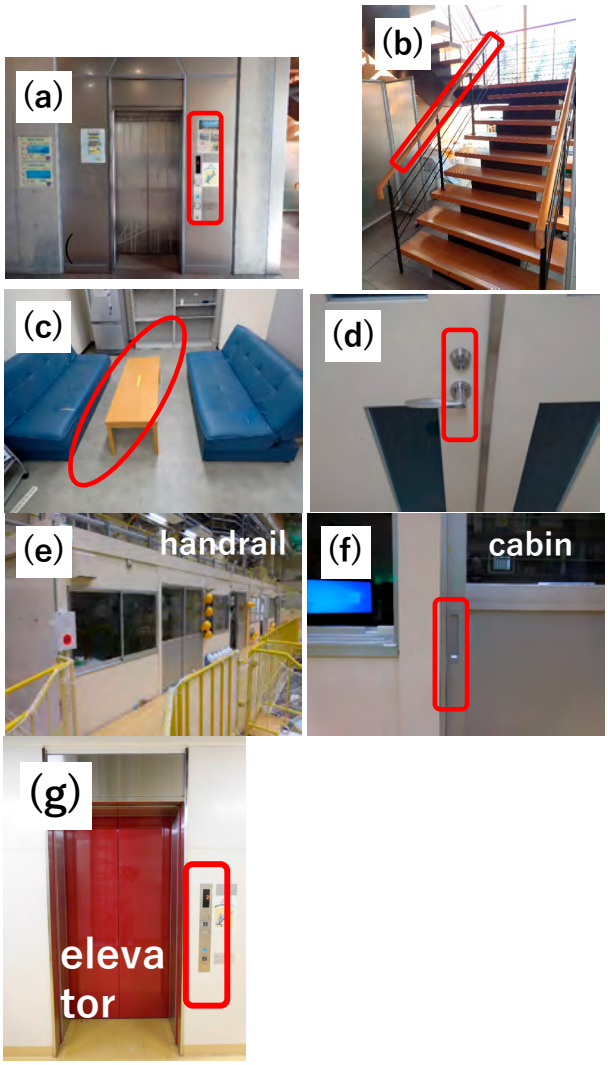

Figure 4. Alcohol disinfection points where MLF users enter: (a) entrance elevator, (b) upstairs to the experimental hall, (c), (d) user room. Frequency of (a) – (d) points: 4 times from 9:30-17:30, 1 time from 17:30-1:00 and 1 time from 1:00-9:30. (e) experimental hall handrail, (f) experimental hall cabin, (g) elevator in the MLF experimental hall. Frequency of (e) – (g) points: 1 time from 9:30-17:30.

M. Harada[1], M. Sekijima[1], H. Morikawa[1], K. Kawakami[2], Y. Watanabe[2], H. Tanaka[2], W. Kambara[2], H. Asai[2], T. Oku[2], K. Suzuya[3], N. Kawamura[4], Y. Sakaguchi[5], R. Takahashi[2], Y. Yamaguchi[5], K. Soyama[6], and K. Aizawa[6]

[1]Neutron Source Section, Materials and Life Science Division, J-PARC Center; [2]Technology Development Section, Materials and Life Science Division, J-PARC Center; [3]Neutron Science Section, Materials and Life Science Division, J-PARC Center; [4]Muon Science Section, Materials and Life Science Division, J-PARC Center; [5]Neutron Science and Technology Center, CROSS; [6]Materials and Life Science Division

MLF Operations in 2021

Beam Operation Status at the MLF

1. Overall

In Japanese Fiscal Year (JFY) 2021, the beam operation at the MLF started on April 1, 2021 and ended on March 31, 2022. In JFY2021, the beam operation started with a power of 600 kW with a double-bunch beam. After April 5, the beam power was increased from 600 kW to 700 kW. Due to the insufficient cooling power for the Radio Frequency (RF) cavity at the Rapid Cycling Synchrotron (RCS), the beam power was decreased to 600 kW in June. The beam period of 2021A was switched to 2021B on January 15, 2022. In the original beam operation plan determined in early April, the beam operation after the summer outage was planned to be resumed on November 21. Since the maintenance involves high risk, the radiation safety group was prohibited from carrying out simultaneously specific tasks, such as radiation works related to muon and neutron production targets, so the maintenance schedule was rearranged to be satisfied the requirement. It should be mentioned that such a requirement by radiation safety was only applied in 2021, which was not in 2022 by the decision of the safety group. Due to a long duration of a series of maintenance work, the beam operation after the outage was resumed on January 15, 2022.

The records of the beam power and the availability are shown in Fig. 1. We had planned to stop the operation during the national holidays from April 28 to May 10. After the national holidays, the beam operation continued up to the morning of July 15. Since insufficient cooling at the RCS RF cavity was expected, the beam power was limited to 600 kW after June 25. Eventually, the beam operation could continue up to July 15 as scheduled.

During the outage, the spent target #11 was replaced with a new target #14. During replacement, no significant issue was found on the target. Furthermore, since no severe damage was found on target #11, we decided to continue with the 700 kW beam operation after the outage. As the outage ended, the beam power was temporarily limited to 600 kW because the particle counter reading the beam current of the H0 beam dump at the RCS, which corrects the beam not to be injected into RCS, approached its limit. Through the accelerator study, we found that it was caused by the noise of the beam current monitor. After solving the noise of the beam monitor, we continued the 700 kW beam operation again after January 20.

In JFY2021, a high-intensity beam with a stable beam for users was carried out. Table 1 shows the scheduled time and availability in JFY2021. As shown in Table 1, a stable beam operation with 97% availability was achieved up to July 15 for 2021A. Eventually, the overall availability in JFY2021 was 96.0%.

The beam operation was stopped on several occasions due to minor failures. Typical causes of the beam stops with a duration longer than 3 hours are summarized in Table 2 and described below.

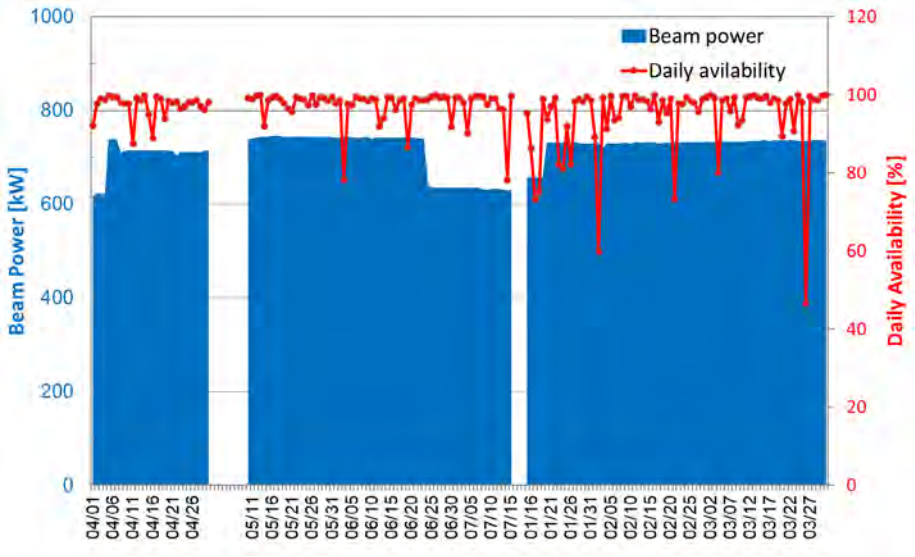

Figure 1. Beam power trend (blue line) at the MLF and availability per day (red line)

Table 1. Run cycle, scheduled time, actual beam time, and availability.

Run cycle	Duration	Scheduled time (h)	Beam time (h)	Availability (%)
86	Apr 1 – Apr 30	623	605	97.1
87	May 10 – July 15	1408	1,368	92.2
88	Jan 15 – Mar 31	1599	1,511	94.4
2021A	April 1 – July 15	2,031	1,973	97.2
2021B	Jan 15 – Mar 31	1,893	1,510	94.4
Overall	April 1 – March 31	3,924	3,483	96.0

Table 2. Events that stopped the beam with a duration longer than 3 hours.

Stop date	Cause of beam stop	Stop duration for each event [h]
June 3	LINAC klystron failure at HV1	5.2
June 19	LINAC klystron failure at HV4	3.2
July 14	LINAC RFQ power supply failure	5.2
January 16	RCS particles counts for H-0 beam dump	3.3
January 17	MLF water loop system failure	6.4
January 18	MLF water loop system failure	6.0
January 23	MLF water loop system failure	4.3
January 24	MLF water loop system failure	4.5
February 1 and 2	LINAC klystron failure at HV4	6.2
February 21	3NBT AC breaker failure	6.4
March 4	RCS charge exchange foil turning	4.7
March 26	LINAC klystron failure at HV4	12.9

2. Causes of the beam stop

LINAC:

During JFY2021, there were no shortages of water flow for the magnet at LINAC, which had been the main reason for beam stops before JFY2019. In JFY2021, we had four failures on the klystron providing the RF to the cavities.

3 GeV Rapid Cycling Synchrotron (RCS):

At the H0 beam dump, the beam current at the dump was close to being allowable, except when due to the noise of beam monitor. On March 4, due to the displacement of the charge exchange foil, the actual H0 beam was increased. To resume the beam operation, we tuned the foil position and the beam.

Beam transport from RCS to the MLF (3NBT) and MLF

The AC breaker for separation between the commercial electricity and the power supply of the bending magnet malfunctioned. Because the breaker has been used since the first day of the beam operation, we supposed that the cause of the failure was aging. Since we had a spare breaker, the stop duration was relatively short. If we did not have the spare, the beam operation would have had to be stopped for several months. We learned the importance of spare parts to maintain the high availability of the operation.

After the summer outage, the water loop systems for cooling the mercury target vessel and the proton beam window at the MLF failed four times during beam operation. The failures were caused by the presence of gas in the water loop, which exceeded the allowable pressure at the surge tanks.

S. Meigo
Neutron Source Section, Materials and Life Science Division, J-PARC Center

Users at the MLF

The MLF beam operation for FY2021 started on April 1 with a beam intensity of 600 kW, and then the beam intensity was increased to 700 kW on April 5. However, due to cooling capacity problems, the beam intensity was reduced to 600 kW in June. The problems were solved and the 700 kW operation was resumed on January 20. It should be noted that the overall availability reached 96%, achieving a very stable beam supply. The total number of users of the neutron and muon experimental facilities in FY2021 was 424, almost the same as in FY2019, due to the COVID-19 restrictions.

The trend for the number of users at the MLF since the start of the operations in FY2008 is summarized in Table 1 and Fig. 1.

Table 1. The number of domestic and foreign users by fiscal year.

	FY2008		FY2009		FY2010		FY2011		FY2012		FY2013		FY2014	
	Domestic Users	Foreign Users	Domestic Users	Foreign Users	Domestic Users	Foreign Users	Domestic Users	Foreign Users	Domestic Users	Foreign Users	Domestic Users	Foreign Users	Domestic Users	Foreign Users
Neutron	107		317		476		259		708		449		824	
	95	12	303	14	432	44	238	21	628	80	399	50	711	113
Muon	18		40		50		23		56		61		91	
	18	0	38	2	42	8	21	2	46	10	50	11	78	13

	FY2015		FY2016		FY2017		FY2018		FY2019		FY2020		FY2021	
	Domestic Users	Foreign Users	Domestic Users	Foreign Users	Domestic Users	Foreign Users	Domestic Users	Foreign Users	Domestic Users	Foreign Users	Domestic Users	Foreign Users	Domestic Users	Foreign Users
Neutron	559		852		927		965		940		489		307	
	476	83	744	108	742	185	789	176	827	113	448	41	257	50
Muon	69		99		179		161		138		92		117	
	59	10	83	16	149	30	146	15	127	11	88	4	112	5

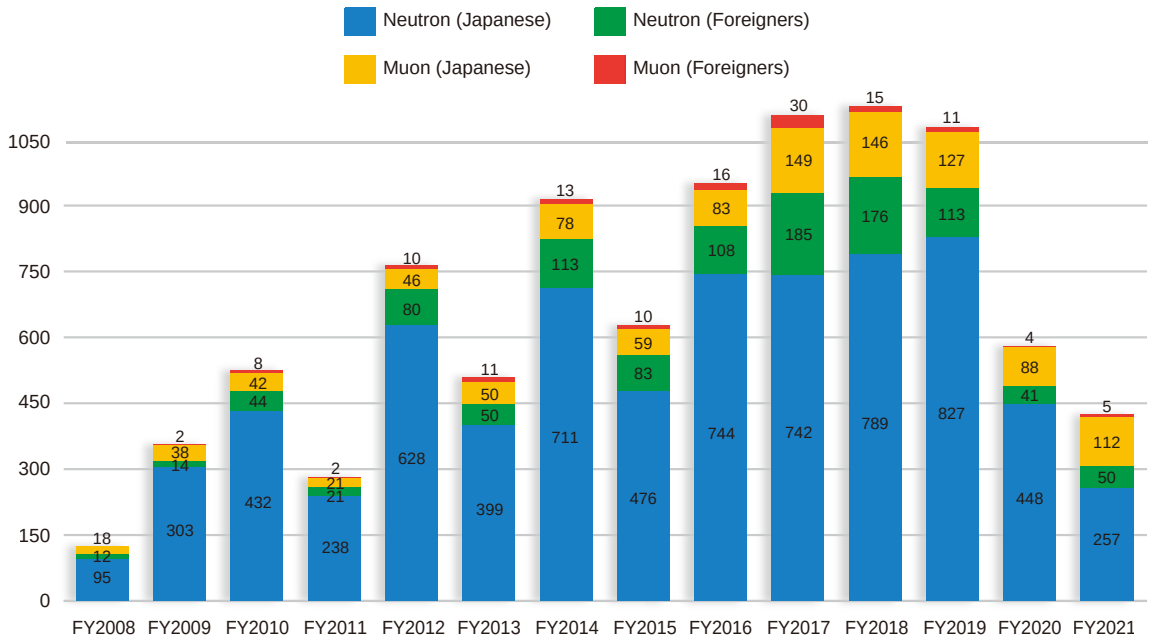

Figure 1. The number of domestic and foreign users by fiscal year.

MLF Proposals Summary – FY2021

The proposals for 2021A are not included in Table1. Due to the COVID-19 situation, 2020B and 2021A were combined into one proposal round. The operations period for the proposals for "2020B+2021A" was from December 2020 to July 2021. Therefore, the proposals for 2021A were included in the FY2020 data as they cannot be counted separately.

Table 1. Number of Proposals by Beamline

Beam-line	Instrument		2021B		Full Year			
			Submitted	Approved	Submitted		Approved	
			GU	GU	PU/S	IU	PU/S	IU
BL01	4D-Space Access Neutron Spectrometer - ***4SEASONS***		24(0)	8(0)	0	2	0	2
BL02	Biomolecular Dynamics Spectrometer - ***DNA***		26(2)	7(2)	2	3	2	3
BL03	IBARAKI Biological Crystal Diffractometer - ***iBIX***	(100–β)‡	3	3	0	0	0	0
		(β)†	1	1	45※	0	44※	0
BL04	Accurate Neutron-Nucleus Reaction Measurement Instrument - ***ANNRI***		10	5	2	1	2	1
BL05	Neutron Optics and Physics - ***NOP***		8	6	1	0	1	0
BL06	Village of Neutron Resonance Spin Echo Spectrometers - ***VIN ROSE***		2	2	1	0	1	0
BL08	Super High Resolution Powder Diffractometer - ***SuperHRPD***		9	5	1	0	1	0
BL09	Special Environment Neutron Powder Diffractometer - ***SPICA***		4	4	1	0	1	0
BL10	Neutron Beamline for Observation and Research Use - ***NOBORU***		16	4	2	1	2	1
BL11	High-Pressure Neutron Diffractometer - ***PLANET***		18(0)	7(0)	0	2	0	2
BL12	High Resolution Chopper Spectrometer - ***HRC***		7	4	1	0	1	0
BL14	Cold-Neutron Disk-Chopper Spectrometer - ***AMATERAS***		47	7	1	1	1	1
BL15	Small and Wide Angle Neutron Scattering Instrument - ***TAIKAN***		36(2)	12(2)	2	3	2	3
BL16	Soft Interface Analyzer - ***SOFIA***		17	5	0	1	0	1
BL17	Polarized Neutron Reflectometer - ***SHARAKU***		17(2)	10(2)	3	3	3	3
BL18	Extreme Environment Single Crystal Neutron Diffractometer - ***SENJU***		22(1)	7(1)	1	1	1	1
BL19	Engineering Materials Diffractometer - ***TAKUMI***		27	12	2	1	2	1
BL20	IBARAKI Materials Design Diffractometer - ***iMATERIA***	(100–β)‡	8	7	0	0	0	0
		(β)†	22	22	28	0	26	0
BL21	High Intensity Total Diffractometer - ***NOVA***		19	15	1	0	1	0
BL22	Energy Resolved Neutron Imaging System - ***RADEN***		19(2)	8(2)	0	2	0	2
BL23	Polarized Neutron Spectrometer - ***POLANO***		4	4	1	0	1	0
D1	Muon Spectrometer for Materials and Life Science Experiments - ***D1***		21(1)	10(0)	1	1	1	1
D2	Muon Spectrometer for Basic Science Experiments - ***D2***		11(4)	4(2)	1	1	1	1
S1	General purpose μSR spectrometer - ***ARTEMIS***		41(0)	18(0)	1	1	1	1
S2	Muonium Laser Physics Apparatus - ***S2***		0	0	0	1	0	1
U1A	Ultra Slow Muon Microscope - ***U1A***		0	0	0	1	0	1
U1B	Transmission Muon Microscope - ***U1B***		0	0	0	1	0	1
H1	High-intensity Muon Beam for General Use - ***H1***		0	0	0	1	0	1
Total			**439**	**197**	**89**	**28**	**86**	**28**

GU : General Use **PU :** Project Use or Ibaraki Pref. Project Use **S :** S-type Proposals **IU :** Instrument Group Use
† : baraki Pref. Exclusive Use Beamtime (β = 80%) **‡ :** J-PARC Center General Use Beamtime (100–β = 20%)
( ) : Proposal Numbers under the New User Promotion (BL01, BL02, BL11, BL15, BL17, BL18, BL22) or P-type proposals (D1,D2, S1) in GU
※ : Operations period is held twice per year (for each of the A and B periods), with only the yearly total shown above.
The actual total number of proposals in each beamline named in the table does not match the number shown in the "Total" cell, because some proposals are submitted or approved across multiple beamlines.

Table 2. Number of Long-Term Proposals by Fiscal Year

Fiscal Year	Submitted	Approved
2019	9	4
2020	13	3
2021	0	0

Due to the COVID-19 situation, no Long-Term Proposals were called for FY2021.

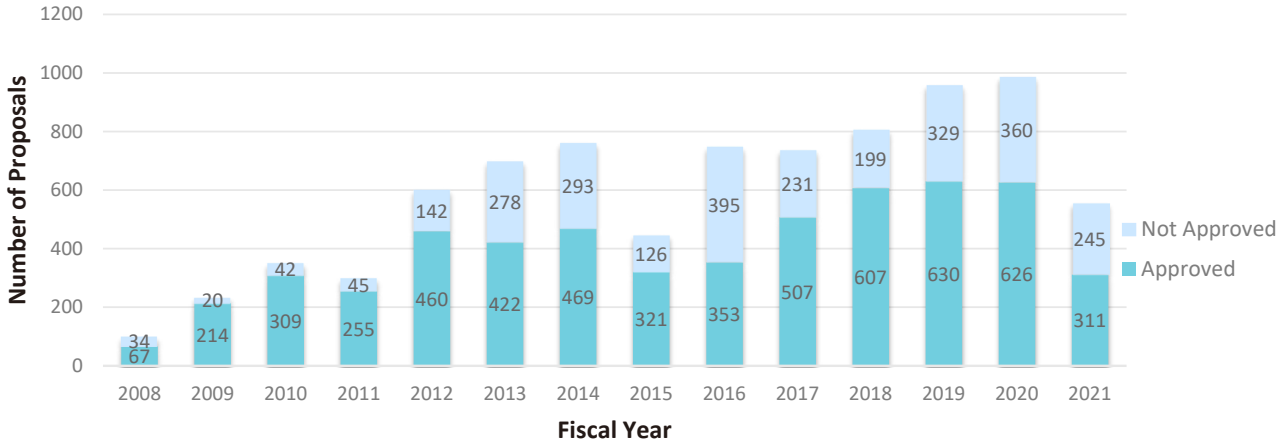

Figure 1. Number of MLF Proposals over Time

After publishing MLF Annual Report 2020, additional Fast Track Proposals and Urgent Proposals were approved. Therefore, the number of proposals of FY2020 was changed in Figure 1.

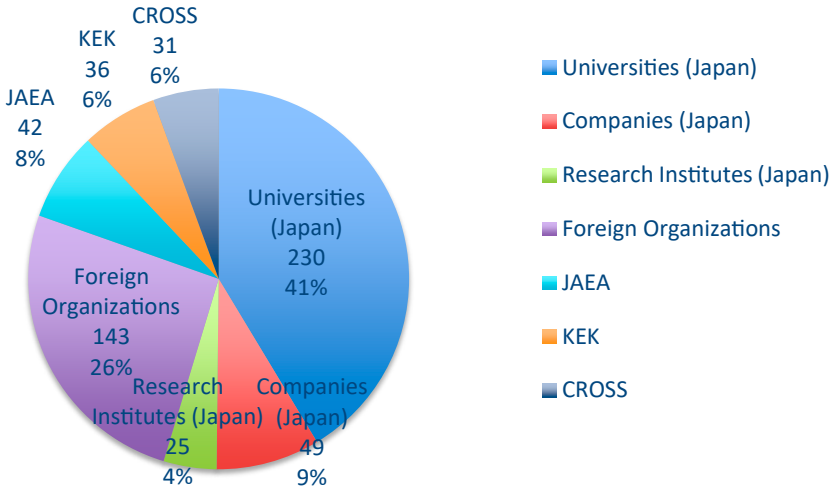

Figure 2. Origin of Submitted Proposals by Affiliation - FY2021

MLF Division Staff 2021

Toshiya Otomo (Head)
Kazuhiko Soyama (Deputy Head)
Kazuya Aizawa (Deputy Head)
Koichiro Shimomura (Deputy Head)
Eiichi Wakai
Kyoko Aizawa

Neutron Source Section

*: additional duties

<JAEA>

Katsuhiro Haga (Leader)
Kenji Sakai (Sub-Leader)
Makoto Teshigawara
Masahide Harada
Tomokazu Aso
Hiroyuki Kogawa
Hidetaka Kinoshita
Takashi Wakui
Motoki Ooi
Takashi Naoe
Masakazu Seki
Akira Shibata
Shiho Takamiya
Yuji Yamaguchi
Hui Liang
Toshiaki Uehara
Akihiko Watanabe
Hideki Muto
Akiyoshi Futakawa
Mitsuaki Sekijima
Yoshinori Kikuchi
Masakazu Nakamura
Hidemitsu Hosokawa
Atsushi Akutsu
Toshiyuki Yasuhara
Hiromi Inoue
Noriyuki Morikawa
Shigeto Tanaka
Shizuka Yoshinari
Midori Yamamoto
Rie Nemoto
Hiroshi Takada *
Shoichi Hasegawa *
Eiichi Wakai *
Shin-ichiro Meigo *
Kenichi Oikawa *
Tetsuya Kai *
Hiroyuki Uehara *

Neutron Science Section

*: additional duties

<JAEA>

Yukinobu Kawakita (Leader)
Mitsutaka Nakamura (Sub-Leader)
Kentaro Suzuya
Ryoichi Kajimoto
Takanori Hattori
Stefanus Harjo
Kenichi Oikawa
Takashi Ohhara
Takenao Shinohara
Hiroyuki Aoki
Tetsuya Kai
Seiko Kawamura
Shinichi Takata
Ryoji Kiyanagi
Kaoru Shibata
Asami Sano
Yasuhiro Inamura
Takuro Kawasaki
Maiko Kofu
Wu Gong
Kosuke Hiroi
Naoki Murai
Hiromu Tamatsukuri
Yusuke Tsuchikawa
Wenqi Mao
Kanae Ito
Kazuhisa Isegawa
Shigeki Uzuki
Yuki Hirota
Seiya Tanaka
Rintaro Nakabe
Ryo Murasaki
Rika Inoue
Tatsuya Kikuchi
Masashi Harada
Daigo Setoyama
Wataru Yoshimune
Takeshi Harada
Hideaki Isozaki
Keiichi Inoue
Misono Fujii
Naoko Shimizu
Toshiko Goto
Takeshi Yashiro
Hiroko Uchiki
Itaru Tamura *
Koji Kaneko *
Hiroshi Nakagawa *
Atsushi Moriai *
Satoshi Morooka *
Atsushi Kimura *

Shoji Nakamura *
Shunsuke Endo *
Yosuke Toh *
Mariko Segawa *
Masahide Harada *
Masao Watanabe *
Dai Yamazaki *
Kazuo Kurihara *
Tarou Tamada *
Yu Hirano *
Takeshi Hiromoto *
Fumiaki Kono *
Yuya Hanazono *

<KEK>

Testuya Yokoo (Sub-Leader)
Shinichi Ito
Hideki Seto
Toshiya Otomo *
Kazuhiro Mori
Takashi Kamiyama
Hitoshi Endo
Takashi Ino
Norifumi Yamada
Takashi Honda
Naokatsu Kaneko
Shuki Torii
Hidetoshi Oshita
Kaoru Taketani
Kenji Mishima
Hiroyuki Aoki *
Asami Sano *
Kazutaka Ikeda
Takashi Saito
Sara Yamauchi
Taichi Ueta
Go Ichikawa

Technology Development Section

*: additional duties

<JAEA>

Takayuki Oku (Leader)
Kazuyoshi Tatsumi
Masao Watanabe
Yuhua Su
Ryota Komine
Hiroyuki Hasemi
Takuya Okudaira
The Dang Vu
Wataru Kambara
Yoko Watanabe
Hideaki Takahashi
Ryuta Takahashi
Kazuhiro kawakami
Hiromichi Tanaka
Hiroyuki Asai
Yukiko Nagai
Kenji Sakai *
Tetsuya Kai *
Hiroyuki Kogawa *
Motoki Ooi *
Kentaro Suzuya *
Mitsutaka Nakamura *
Shinichi Takata *
Tatsuya Nakamura *
Yasuhiro Inamura *
Masahide Harada *
Tomokazu Aso *
Seiko Kawamura *
Rumi Shimizu *
Satoru Fujiwara *
Motoyasu Adachi *
Shigeki Arai *
Chie Shibazaki *

<KEK>

Tomohiro Seya
Setsuo Sato
Testuya Yokoo *
Shuki Torii *
Takashi Ino *
Naokatsu Kaneko *
Kaoru Taketani *
Naritoshi Kawamura *
Hiroshi Fujimori *
Shunsuke Makimura *

Neutron Instrumentation Section

*: additional duties

<JAEA>

Tatsuya Nakamura (Leader)
Kentaro Toh
Kaoru Sakasai
Ryuji Maruyama
Dai Yamazaki
Tomokatsu Koizumi
Yukio Hishinuma
Aoi Yanagi

Muon Science Section

*: additional duties

<KEK>

Ryosuke Kadono (Leader)
Naritoshi Kawamura (Sub-Leader)
Koichiro Shimomura *
Akihiro Koda
Patrick Strasser
Takayuki Yamazaki
Sotaro Kanda
Yutaka Ikedo
Yasuo Kobayashi
Junpei Nakamura
Takashiro Yuasa
Yasuhiro Miyake
Yu Oishi
Yukinori Nagatani
Shiro Matoba
Soshi Takeshita
Izumi Umegaki
Hiroaki Natori
Shoichiro Nisimura
Sourav Kumar Dey
Hiroshi Fujimori
Masatoshi Hiraishi
Hirotaka Okabe
Motonobu Tanpo
Taihei Adachi
Amba Datt Pant
Atsuko Irie
Hua Li
Shogo Doiuchi
Akiko Hashimoto
Yoshinori Ito

<JAEA>

Wataru Higemoto *
Takashi Ito *

CROSS Staff 2021

Director Mitsuhiro Shibayama

Science Coordinators

Shamoto Shinichi
Jun Sugiyama
Hibi Masaaki
Kazuhisa Kakurai
Midori Kamimura

Research & Development Division

*: additional duties

Jun-ichi Suzuki (Head)
Kenichi Funakoshi (Deputy Head)
Tsukasa Miyazaki * (Deputy Head)

<BL01 Group>
Kazuya Kamazawa (Leader)
Kazuki Iida
Kazuhiko Ikeuchi

<BL02 Group>
Masato Matsuura (Leader)
Takeshi Yamada
Taiki Tominaga

<BL11 Group>
Kenichi Funakoshi * (Leader)
Jun Abe
Shinichi Machida

<BL15 Group>
Kazuki Ohishi (Leader)
Jun-ichi Suzuki *
Hiroki Iwase
Yukihiko Kawamura

<BL17 Group>
Noboru Miyata (Leader)
Kazuhiro Akutsu
Takayasu Hanashima

<BL18 Group>
Akiko Nakao (Leader)
Koji Munakata
Yoshihisa Ishikawa

<BL22 Group>
Hirotoshi Hayashida (Leader)
Joseph Don Parker
Yoshihiro Matsumoto

<Technical Support Group>
Yoshifumi Sakaguchi (Leader)
Nobuo Okazaki (Leader)
Toshiaki Morikawa (Sub-Leader)
Koji Kiriyama *
Hiroshi Kira
Motoyuki Ishikado
Shuoyuan Zhang
Hiroshi Arima
Misaki Ueda
Keiichi Ohuchi
Masae Sahara
Yuukou Nojiri
Takayoshi Ito *
Satoshi Kasai
Kentaro Moriyama
Yuuki Nagai

Safety Division

*: additional duties

Mitsuhiro Shibayama * (Head)
Koji Kiriyama (Leader)
Tazuko Mizusawa *
Masae Sahara *
Yasuhiro Yamaguchi

Utilization Promotion Division

*: additional duties

Takashi Noma (Head)
Tsukasa Miyazaki * (Deputy Head)
Seiya Konishi (Leader)
Takayoshi Ito (Leader)
Toshiki Asai (Leader)
Miho Igarashi
Tomoko Ishikawa
Kaoru Ohuchi
Emi Goto
Tazuko Mizusawa
Nobuo Okazaki *
Rie Kurosawa *
Taeko Ishikawa
Kazuko Kanno
Hideyuki Niitsuma

Administration Division

Michihiko Murasawa (Head)
Takashi Hikita (Leader)
Junichi Sato (Leader)
Rei Ito (Leader)
Tomoko Sakuma
Mutsumi Shiraishi
Shinobu Matsumoto
Mami Uchida

Industrial Collaboration Promotion Division

*: additional duties

Tsukasa Miyazaki (Head)
Seiya Konishi (Leader)
Noboru Miyata *
Jun Abe *
Takeshi Yamada *
Yoshihiro Matsumoto *
Hiroki Iwase *

Ibaraki Neutron Beamline Staff in 2021

Ibaraki Prefectural Government

<Senior Director for Neutron Promotion>
Hironori Kodama

<Neutron Beamline Coordinator>
Michiko Konno
Tetsuroh Minemura

Ibaraki University *

* Trustee of the Beamline operations

<BL03 iBIX Group>
Katsuhiro Kusaka (Leader)
Taro Yamada
Naomine Yano
Ichiro Tanaka
Takaaki Hosoya

<BL20 iMATERIA Group>
TToru Ishigaki (Leader)
Satoshi Koizumi
Akinori Hoshikawa
Shigeo Sato
Yusuke Onuki
Yohei Noda
Tomoki Maeda
Takeshi Matsukawa

<Technical Support Group>
Junichi Hiroki
Tomoyuki Nakazawa
Mitsuyuki Fujii
Shinju Shibata
Takumi Inada

Proposals Review System, Committees and Meetings

Proposal Review System

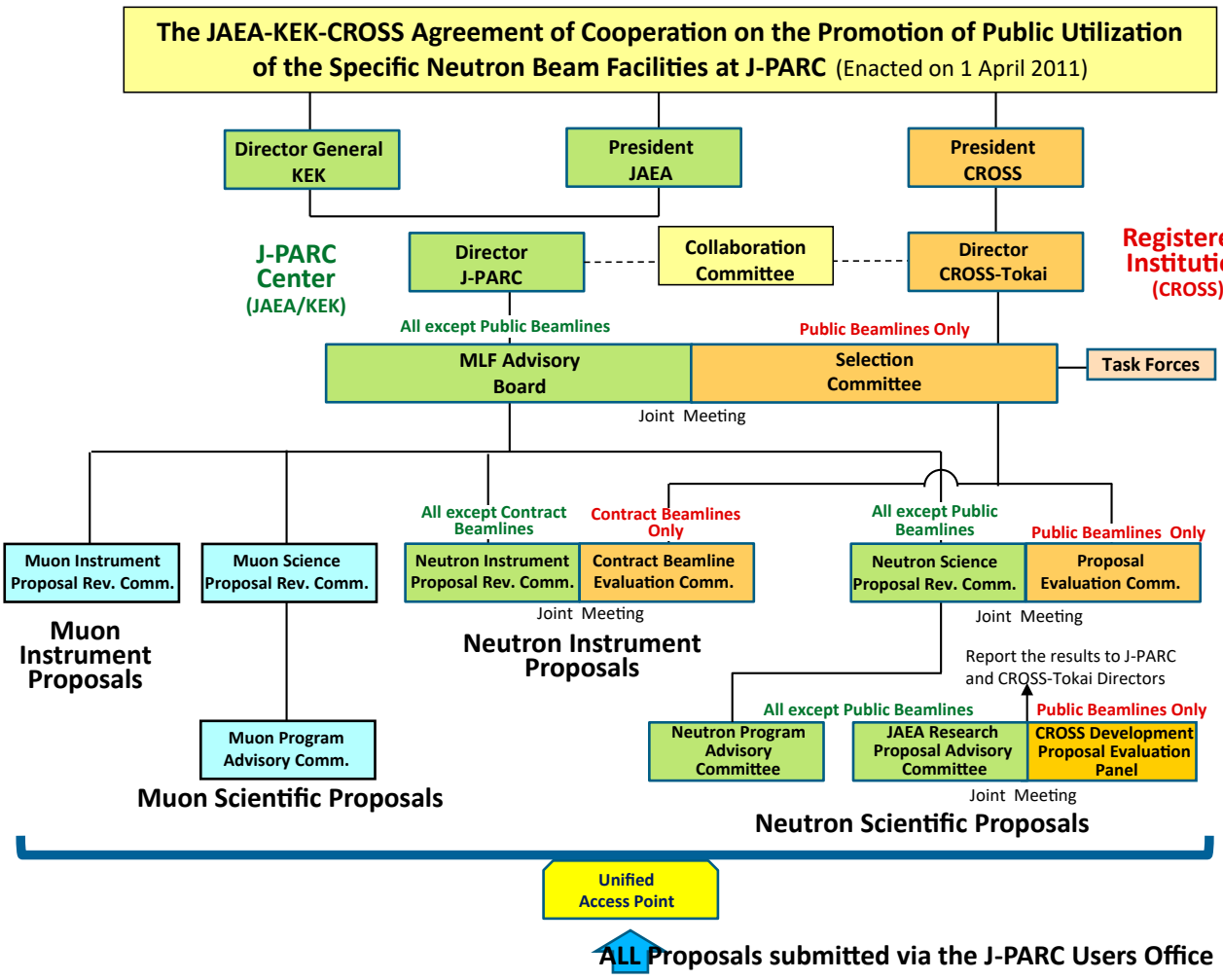

Figure 1. Proposals Review System Framework.

Materials and Life Science Facility Advisory Board

Tadashi Adachi	Sophia University
Kazuya Aizawa	Japan Atomic Energy Agency
Hiroshi Amitsuka	Hokkaido University
Taka-hisa Arima (chair)	The University of Tokyo
Masahiro Hino	Kyoto University
Shinich Itoh	High Energy Accelerator Research Organization
Yasuhiro Iye	Chubu University
Ryosuke Kadono	High Energy Accelerator Research Organization
Takashi Kamiyama	Hokkaido University
Yukinobu Kawakita	Japan Atomic Energy Agency
Hiroyuki Kishimoto	Sumitomo Rubber Industries, LTD.
Kenji Nakajima	Japan Atomic Energy Agency
Yoshie Otake	RIKEN
Toshiya Otomo	High Energy Accelerator Research Organization
Yoshiharu Sakurai	Japan Synchrotron Radiation Research Institute
Taku Sato	Tohoku University
Koichiro Shimomura	High Energy Accelerator Research Organization
Kazuhiko Soyama	Japan Atomic Energy Agency
Yoko Sugawara	Toyota Physical and Chemical Research Institute
Jun-ichi Suzuki	Comprehensive Research Organization for Science and Society
Atsushi Takahara	Kyushu University
Masayasu Takeda	Japan Atomic Energy Agency
Osamu Yamamuro	The University of Tokyo

Term: through March 31, 2023

Neutron Science Proposal Review Committee

Hiroshi Abe	National Defense Academy of Japan
Taka-hisa Arima (chair)	The University of Tokyo
Hiroyuki Kagi	The University of Tokyo
Ryosuke Kadono	High Energy Accelerator Research Organization
Yukinobu Kawakita	Japan Atomic Energy Agency
Masaaki Kitaguchi	Nagoya University
Takatsugu Masuda	The University of Tokyo
Tsukasa Miyazaki	Comprehensive Research Organization for Science and Society
Jun'ichiro Mizuki	Kwansei Gakuin University
Kenji Ohoyama	Ibaraki University
Toyotaka Osakabe	Japan Atomic Energy Agency
Toshiya Otomo	High Energy Accelerator Research Organization
Hideki Seto	High Energy Accelerator Research Organization
Naoya Torikai	Mie University
Noriyuki Tsuchida	University of Hyogo

Term: through September 30, 2021

Muon Science Proposal Review Committee

Tadashi Adachi	Sophia University
Kenta Amemiya	High Energy Accelerator Research Organization
Hidehito Asaoka	Japan Atomic Energy Agency
Toshiyuki Azuma	RIKEN
Katsuyuki Fukutani	The University of Tokyo
Wataru Higemoto	Japan Atomic Energy Agency
Adrian Hillier	Rutherford Appleton Laboratory
Katsuya Inoue	Hiroshima University
Shinichi Itoh	High Energy Accelerator Research Organization
Ryosuke Kadono	High Energy Accelerator Research Organization
Yukinobu Kawakita	Japan Atomic Energy Agency
Naritoshi Kawamura	High Energy Accelerator Research Organization
Yasushi Kino	Tohoku University
Akihiro Koda	High Energy Accelerator Research Organization
Takamitsu Kohzuma	Ibaraki University
Kenya Kubo (chair)	International Christian University
Roderick Macrae	Marian University
Tsutomu Mibe	High Energy Accelerator Research Organization

Yasuhiro Miyake	High Energy Accelerator Research Organization
Chihiro Ohmori	High Energy Accelerator Research Organization
Toshiya Otomo	High Energy Accelerator Research Organization
Hideki Seto	High Energy Accelerator Research Organization
Tatsushi Shima	Osaka University
Koichiro Shimomura	High Energy Accelerator Research Organization
Yoko Sugawara	Kitasato University
Jun Sugiyama	Comprehensive Research Organization for Science and Society
Masaaki Sugiyama	Kyoto University
Toshiyuki Takayanagi	Saitama University

Term: through March 31, 2021

Selection Committee

Tadashi Adachi	Sophia University
Hiroshi Amitsuka	Hokkaido University
Taka-hisa Arima (chair)	The University of Tokyo
Masahiro Hino	Kyoto University
Yasuhiro Iye	Japan Society for Promotion of Science
Takashi Kamiyama	Hokkaido University
Hiroyuki Kishimoto	Sumitomo Rubber Industries, LTD.
Yoshie Otake	RIKEN
Yoshiharu Sakurai	Japan Synchrotron Radiation Research Institute
Taku Sato	Tohoku University
Yoko Sugawara	Toyota Physical and Chemical Research Institute
Atsushi Takahara	Kyushu University
Osamu Yamamuro	The University of Tokyo

Term: through March 31, 2023

Proposal Evaluation Committee

Hiroshi Abe	National Defense Academy of Japan
Taka-hisa Arima (chair)	The University of Tokyo
Hiroyuki Kagi	The University of Tokyo
Masaaki Kitaguchi	Nagoya University
Takatsugu Masuda	The University of Tokyo
Tsukasa Miyazaki	Comprehensive Research Organization for Science and Society
Jun'ichiro Mizuki	Kwansei Gakuin University
Kenji Ohoyama	Ibaraki University
Toshiya Otomo	High Energy Accelerator Research Organization
Naoya Torikai	Mie University
Noriyuki Tsuchida	University of Hyogo

Term: through September 30, 2021

Neutron Advisory Committee (NAC)

NAC convened online on 10 and 17 February 2022.

Ken Anderson	Oak Ridge National Laboratory
Taka-hisa Arima	The University of Tokyo
Christiane Alba-Simionesco	Laboratoire Léon Brillouin
Bertrand Blau	Paul Scherrer Institut
Michael Dayton	Oak Ridge National Laboratory
Phillip King	Rutherford Appleton Laboratory
Toyohiko Kinoshita	Japan Synchrotron Radiation Research Institute
Guenter Muhrer	European Spallation Source
Yoshie Otake	RIKEN
Sungil Park	Korea Atomic Energy Research Institute
Jamie Schulz (chair)	Australian Nuclear Science and Technology Organization
Jon Taylor	European Spallation Source

Muon Advisory Committee (MAC)

MAC convened online on 2, 7, 14 and 21 February 2022.

Thomas Prokscha (chair)	Paul Scherrer Institut
Hiroshi Amitsuka	Hokkaido University
Klaus Kirch	ETH Zurich and Paul Scherrer Institut
Kenya Kubo	International Christian University
Andrew Macfarlane	The University of British Columbia
Martin Månsson	KTH Royal Institute of Technology
Nori Aoi	Osaka University
Tadayuki Takahashi	The University of Tokyo

Workshops, Conferences, Seminars and Schools in 2021

Conferences held jointly by J-PARC MLF and CROSS

2021 Meeting on J-PARC MLF Industrial Use
15-16 Jul. 2021, Online

Workshop with ANSTO on Mutual Cooperation in Field of Neutron Science
30 Jul. 2021, Online

2021 Z-Code Beginner Level Training Course
2-31 Aug. 2021, On-demand

2021 Z-Code Intermediate level Training Course
1 Dec. 2021-28 Feb. 2022, On-demand

2021 Quantum Beam Science Festa (The 13th MLF Symposium and the 39th PF Symposium)
7-9 Mar. 2022, Online

Screenshot of Quantum Beam Science Festa
(photo courtesy of J-PARC)

Conferences held by J-PARC MLF and other organizations

18th Korea-Japan Meeting on Neutron Science "Workshop on Neutron and Muon Methods for J-PARC MLF Users in Korea"
30 Apr. 2021, Online

Conferences held by KEK

第 5 回文理融合シンポジウム " 量子ビームで歴史を探る ー加速器が紡ぐ文理融合の地平ー "
9 Sep. 2021, Online

第 6 回文理融合シンポジウム " 量子ビームで歴史を探る ー加速器が紡ぐ文理融合の地平ー "
7-8 Jan. 2022, Online, Osaka University, Toyonaka

Workshops held by KEK

令和 3 年度物構研コロキウム　第 4 回 " 中性子で観る量子物質の準粒子構造 "
12 Jul. 2021, Online

令和 3 年度物構研コロキウム　第 5 回 " ミュオンは超伝導の研究にどう役立ってきてどう役立っていくか "
13 Sep. 2021, Online

Analysis of ordered/disordered structure in functional materials with high intensity neutron total scattering technique (BL21)
16 Nov. 2021, Online

Study on Cross-correlated Physics by Polarized Neutron Spectrometer, POLANO (BL23)
30 Nov. 2021, Online

Studies on Dynamics in Condensed Matters by using the High Resolution Chopper Spectrometer (BL12)
10 Dec. 2021, Online

Study on slow dynamics by the neutron resonance spin echo spectrometers VIN ROSE (BL06)
15 Dec. 2021, Online

Fundamental Physics with Pulsed Cold Neutrons (BL05)
16-17 Dec. 2021, Nagoya University, Nagoya

Workshop on Neutron Powder Diffraction using SuperHRPD (BL08)
17 Dec. 2021, Online

Workshop on Neutron Powder Diffraction using SPICA (BL09)
20 Dec. 2021, Online

2021 年度物構研コロキウム　第 9 回
“MLF 中性子回折・散乱装置による蓄電池材料研究の展開 ”
17 Jan. 2022, Online

Workshops and Seminars held by CROSS and other organizations

3rd Joint Workshop for Complementary Use of Synchrotron Radiation and Neutrons “Small-angle Neutron scattering measurement”
9 Apr. 2021, MLF, IBARAKI Quantum Beam Research Center, Tokai

Workshop on Battery Materials
10 Jun. 2021, Online

Workshop on Organic materials and Polymers
“ 有機・高分子材料への小角散乱解析法の展開 ”
（第 2 回）
3 Aug. 2021, Online

第 1 回中性子産業応用セミナー
13 and 27 Sep. 2021, Online

7th Symposium on the Collaborative Use of Large Research Institutions and the Super Computer
14 Sep. 2021, Online

2021 Neutron experiment technique training course
21 Oct. 2021, Online

CBI 研究機構 量子構造生命科学研究所 中性子産業利用推進協議会 生物・生体材料研究会 合同シンポジウム
“ 生体分子の動的挙動解析への挑戦 試料調整から解析まで ”
29 Oct. 2021 and 4 Mar. 2022, Online

The 25th CROSSroads Workshop
“ データ解析ソフトウェアの紹介 ”
15 Nov. 2021, Online

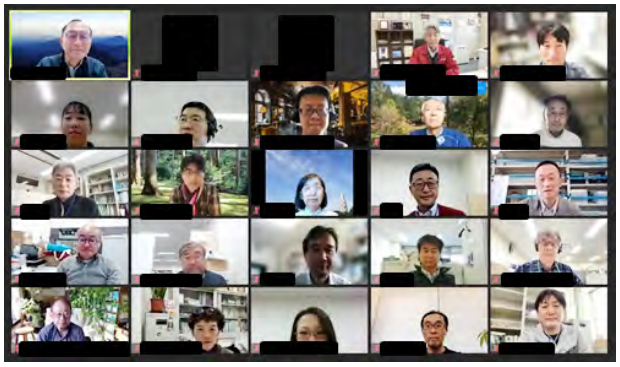

Screenshot of CROSSroads
(photo courtesy of CROSS)

4th Joint Workshop for Complementary Use of Synchrotron Radiation and Neutrons
“Neutron Powder Diffraction Measurement”
18 Nov. 2021, JRR-3, IBARAKI Quantum Beam Research Center, Tokai

Workshop on Organic materials and Polymers
“ 有機・高分子材料への小角散乱解析法の展開 ”（第 3 回）
25 Jan. 2022, Online

2021 年度 磁性材料研究会
16 Feb. 2022, Online

ものづくり基盤研究会
“ ー内部応力・ひずみ測定を様々な材料で考えるー ”
10 Mar. 2022, Online

2021 Workshop on Liquids and Amorphous Materials
11 Mar. 2022, Online

2021 Workshop on Structural Biology
“ タンパク質科学・構造生物学と創薬への展開 ”
15 Mar. 2022, Online

第 75 回 SPring-8 先端利用技術ワークショップ / 第 1 回放射光・中性子連携利用研究会
25 Mar. 2022, Online

Workshops and Seminars held by Ibaraki Neutron Beamline and other organizations

iBIX タンパク質構造研究会
20 Aug. 2021, Online

2021 1st Workshop on iMATERIA
23 Aug. 2021, Online

2021 2nd Workshop on iMATERIA
21 Sep. 2021, Online

2021 3rd Workshop on iMATERIA
1 Oct. 2021, Online

2021 4th Workshop on iMATERIA
21 Dec. 2021, Online

2021 5th Workshop on iMATERIA
11 Jan. 2022, Online

2021 年度 iBIX JAXA KEK 物構研 QST 合同タンパク質研究会
16 Feb. 2022, Online

2021 1st (29th) Workshop on iBIX
24 Feb. 2022, Online

2021 6th Workshop on iMATERIA
15 Mar. 2022 Online

Schools in 2021

Hello Science from J-PARC
"Seeing with Muons"
30 Jul. 2021, Online

Hello Science from J-PARC
"Neutrons for Finding Hydrogen"
29 Oct. 2021, IBARAKI Quantum Beam Research Center, Tokai

KEK-IINAS School The 5th Neutron and Muon School
6-9 Dec. 2021, Online

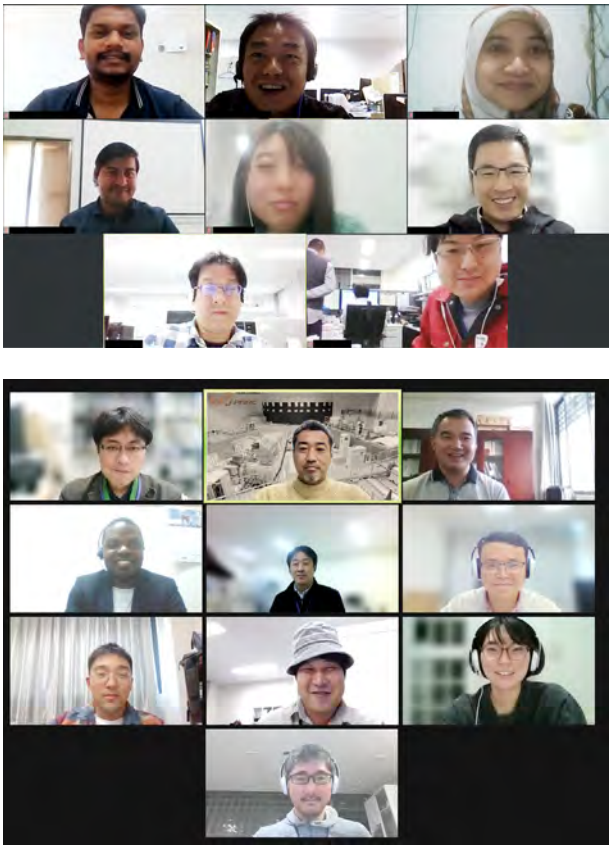

Screenshot of Neutron and Muon School
(photo courtesy of CROSS)

Hello Science from J-PARC
"Muon H Line Finally Starts Operation"
24 Dec. 2021, IBARAKI Quantum Beam Research Center, Tokai

Award List

Dept. of Chem Chair Award for the best B.Sc presentation, The University of Tokyo
Exploring hydrogen-ordered counter polymorph of ice IV by in-situ neutron/X-ray diffraction and Raman spectroscopy
H. Kobayashi (2022-03-25)

The JSNS Poster Prize
Measurement of Neutron Nuclear Scattering Length using Pulsed Neutron Interferometer
T. Fujiie (2021-12-02)

The JSNS Science Prize
Application and development of neutrons on soft matter science
H. Seto (2021-12-01)

The JSNS Technology Prize
Development of Metal Substrates for Neutron-focusing Supermirrors
T. Hosobata, Y. Yamagata (2021-12-01)

The FY2021 Research Award, The Crystallographic Society of Japan
Structural & Chemical Study of Molecular Crystals based on Precise Positions of Hydrogen Atoms by Single-crystal Neutron Diffraction
T. Ohhara (2021-11-20)

The 55th Paper Award, Japan Institute of Copper
Characterization of Precipitated Phase in Cu-Ni-Si Alloy by Small Angle X-ray Scattering, Small Angle Neutron Scettering and Atom Probe Tomography
H. Sasaki, S. Akiya, Y. Oba, M. Onuma, A. D. Giddings, T. Ohkubo (2021-10-23)

The 50th Young Scientist Presentation Award, The Japan Society of Applied Physics
Observation of spontaneous vortices in superconductor/ferromagnet nanocomposites
N. Teramachi, (2021-09-21)

MSJ Presentation Award for Student
Magnetization analysis of hollow Fe_3O_4 particles by polarized small angle neutron scattering
E. Nomura (2021-08-27)

SPSJ Publicity Award
Distinguishing Adsorbed and Deposited Ionomers in the Catalyst Layer of Polymer Electrolyte Fuel Cells using Contrast Variation Small-angle Neutron Scattering
M. Harada, S. Takata, H. Iwase, S. Kajiya, H. Kadoura, T. Kanaya (2021-08-18)

The First Prize in the Best Paper on Materials, Hong Kong Institution of Engineers
Cooperative deformation in high-entropy alloys at ultralow temperatures
M. Naeem (2020-12)

Kyushu Analytical Chemistry Award 2020
Mixing States and Properties of Reaction Fields for Binary Solvents Studied by Small-Angle Neutron Scattering
T. Takamuku (2020-11-06)

The 60th Harada Young Research Award, The Honda Memorial Foundation
金属積層造形における組織形成と特性制御への応用
K. Yamanaka (2020-07-03)

JSNS: The Japanese Society for Neutron Science
MSJ: The Magnetics Society of Japan
SPSJ: The Society of Polymer Science, Japan

MLF Publication 2021

1 W. Saito, K. Hayashi, Z. Huang, K. Sugimoto, K. Ohoyama, N. Happo, M. Harada, K. Oikawa, Y. Inamura, K. Hayashi, T. Miyazaki, Y. Miyazaki
Chemical-Pressure-Induced Point Defects Enable Low Thermal Conductivity for Mg_2Sn and Mg_2Si Single Crystals
ACS Appl. Energy Mater., **4** 5123-5131 (2021).

2 S. Uenuma, K. Endo, N. L. Yamada, H. Yokoyama, and K. Ito
Polymer Brush Formation Assisted by Hierarchical Self-Assembly of Topological Supramolecule
ACS Appl. Mater. Interfaces, **13** 60446-60453 (2021).

3 K. Nakashima, K. Onagi,Y. Kobayashi, T. Ishigaki, Y. Ishikawa, Y. Yoneda, S. Yin, M. Kakihana, T. Sekino
Stabilization of Size-Controlled $BaTiO_3$ Nanocubes via Precise Solvothermal Crystal Growth and Their Anomalous Surface Compositional Reconstruction
ACS Omega, **6** 9410 (2021).

4 M. Harada, S. Takata, H. Iwase, S. Kajiya, H. Kadoura, T. Kanaya
Distinguishing adsorbed and deposited ionomers in the catalyst layer of polymer electrolyte fuel cells using contrast variation small-angle neutron scattering
ACS Omega, **6** 15257-15263 (2021).

5 K. Chino
Multinetwork Elastomer Using Covalent Bond, Hydrogen Bond, and Clay Plane Bond
ACS Omega, **6** 31168-31176 (2021).

6 Q. Li, Z. Deng, Y. Onuki, W. Wang, L. Li, Q. Sun
In-plane low thermal expansion of NiTi via controlled cross rolling
Acta Mater., **204** 116506 (2021).

7 M. M. Nygård, Ø. S. Fjellvåg, M. H. Sørby, K. Sakaki, K. Ikeda, J. Armstrong, P. Vajeeston, W. A. Sławiński, H. Kim, A. Machida, Y. Nakamura, B. C.Hauback
The average and local structure of TiVCrNbDx (x = 0, 2.2, 8) from total scattering and neutron spectroscopy
Acta Mater., **205** 116496 (2021).

8 Q. Li, Y. Onuki, Q. Sun
Tailoring thermal expansion of shape memory alloys through designed reorientation deformation
Acta Mater., **218** 117201 (2021).

9 M. Naeem, H. He, S. Harjo, T. Kawasaki, W. Lin, J-J. Kai, Z. Wu, S. Lan, X-L. Wang
Temperature-dependent hardening contributions in CrFeCoNi high-entropy alloy
Acta Mater., **221** 117371 (2021).

10 M. Busi, N. Kalentics, M. Morgano, S. Griffiths, A. S. Tremsin, T. Shinohara, R. Logé, C. Leinenbach, M. Strobl
Nondestructive characterization of laser powder bed fusion parts with neutron Bragg edge imaging
Additive Manufacturing, **39** 101848 (2021).

11 A. S. Tremsin, Y. Gao, A. Makinde, H. Z. Bilheux, J. C. Bilheux, K. An, T. Shinohara, K. Oikawa
Monitoring residual strain relaxation and preferred grain orientation of additively manufactured Inconel 625 by in-situ neutron imaging
Additive Manufacturing, **46** 102130 (2021).

12 C. J. Brett, O. K. Forslund, E. Nocerino, L. P. Kreuzer, T. Widmann, L. Porcar, N. L. Yamada, N. Matsubara, M. Månsson, P. Müller-Buschbaum, L. D. Söderberg, S. V. Roth
Humidity-induced Nanoscale Restructuring in PEDOT:PSS and Cellulose reinforced Bio-based Organic Electronics
Adv. Electron. Mater., **7** 2100137 (2021).

13 M. Kawasaki, J.-K. Han, X. Liu, Y. Onuki, Y. O. Kuzminova, S. A. Evlashin, A. M. Pesin, A. P. Zhilyaev, K.-D. Liss
In-situ heating neutron- and X-ray diffraction analyses for revealing structural evolution during post-printing treatments of additive-manufactured 316L stainless steel
Adv. Eng. Mater., 2100968 (2021).

14 N. Hisano, T. Sakamaki, T. Ohashi, K. Funakoshi, Y. Higo, Y. Shibazaki, A. Suzuki
Elastic properties and structures of pyrope glass under high pressures
Am. Mineral., **106** 7 (2021).

15 S. Kumar, D. Saha, S. Takata, V.K. Aswal, H. Seto
Modifications in the nanoparticle-protein interactions for tuning the protein adsorption and controlling the stability of complexes
Appl. Phys. Lett., **118** 153701 (2021).

16 P. Wu, J. Song, X. Yu, Y. Wang, K. Xia, B. Hong, L. Zu, Y. Du, P. Vallobra, F. Liu, S. Torii, T. Kamiyama, Y. Xiong, W. Zhao
Evidence of Spin Reorientation and Anharmonicity in Kagome Ferromagnet Fe_3Sn_2
Appl. Phys. Lett., **119** 082401 (2021).

17 M. Naeem, H. Zhou, H. He, S. Harjo, T. Kawasaki, S. Lan, Z. Wu, Y. Zhu, X-L. Wang
Martensitic transformation in CrCoNi medium-entropy alloy at cryogenic temperature
Appl. Phys. Lett., **119** 131901 (2021).

18 R. Aggarwal, B. P. Lamichhane, M. H. Meylan, C. M. Wernsrich
An Investigation of Radial Basis Function Method for Strain Reconstruction by Energy-Resolved Neutron Imaging
Appl. Sci., **11** 391 (2021).

19 K. Ikeda, F. Fujisaki, T. Otomo, H. Ohshita, T. Honda, T. Kawamata, H. Arima, K. Sugiyama, H. Abe, H. Kim, K. Sakaki, Y. Nakamura, A. Machida, T. Sato, S. Takagi, S. Orimo
Generating Mechanism of Catalytic Effect for Hydrogen Absorption/Desorption Reactions in $NaAlH_4$–$TiCl_3$
Appl. Sci., **11** 8349 (2021).

20 H. Nakagawa, T. Saio, M. Nagao, R. Inoue, M. Sugiyama, S. Ajito, T. Tominaga, Y. Kawakita
Conformational dynamics of a multi-domain protein by neutron scattering and computational analysis
Biophys. J., **120** 3341-3354 (2021).

21 Y. Kameda, K. Tsutsui, Y. Amo, T. Usuki, K. Ikeda, T. Otomo
Direct Observation of Scattering Angle Dependence of the Inelasticity Effect on the Interference Term Obtained from Time-of-Flight Neutron Diffraction Experiments
Bull. Chem. Soc. Jpn., **94** 2800 (2021).

22 N. Nishi, J. Uchiyashiki, T. Oda, M. Hino, N. L. Yamada
Overscreening Induced by Ionic Adsorption at the Ionic Liquid/Electrode Interface Detected Using Neutron Reflectometry with a Rational Material Design
Bull. Chem. Soc. Jpn., **94** 2914-2918 (2021).

23 S. Klotz, B. Baptiste, T. Hattori, S.M. Feng, Ch. Jin, K. Béneut, J.M. Guigner, I. Estève

Synthesis and characterisation of a new graphitic C-S compound by high pressure decomposition of CS_2
Carbon, **185** 491-500 (2021).

24 S. Yamazoe, A. Yamamoto, S. Hosokawa, R. Fukuda, K. Hara, M. Nakamura, K. Kamazawa, T. Tsukuda, H. Yoshida, T. Tanaka
Identification of hydrogen species on Pt/Al_2O_3 by in situ inelastic neutron scattering and their reactivity with ethylene
Catal. Sci. Technol., **11** 116-123 (2021).

25 S. Behara, K. Ikeda, T. Thomas
Amphoteric behavior of Dy^{3+} in $Na_{0.5}Bi_{0.5}TiO_3$: neutron diffraction and Raman studies
Ceram. Int., **47** 12870 (2021).

26 K. Fukui, S. Iimura, J. Wang, T. Tada, T. Honda, K. Ikeda, T. Otomo, H. Hosono
Stabilization Factor of Anion-Excess Fluorite Phase for Fast Anion Conduction
Chem. Mater., **33** 1867-1874 (2021).

27 M. Nakamura, H. Watanabe, H. Akamatsu, K. Fujii, M. Yashima, G. Hasegawa, M. Inada, K. Hayashi, K. Maeda
Sn-Based Perovskite with a Wide Visible Light Absorption Band Assisted by Hydride Doping
Chem. Mater., **33** 3631-3638 (2021).

28 Y. Kitagawa, J. Ueda, K. Fujii, M. Yashima, S. Funahashi, T. Nakanishi, T. Takeda, N. Hirosaki, K. Hongo, R. Maezono, S. Tanabe
Site-Selective Eu^{3+} Luminescence in the Monoclinic Phase of $YSiO_2N$
Chem. Mater., **33** 8873-8885 (2021).

29 Y. Yano, T. Ono, T. Ohhara, Y. Hisaeda
Insights into Proton Dynamics in a Photofunctional Salt-Cocrystal Continuum: Single-Crystal X-ray, Neutron Diffraction, and Hirshfeld Atom Refinement
Chemistry - A European Journal, **27** 17802-17807 (2021).

30 T.-N. Lam, M.-Y. Luo, T. Kawasaki, S. Harjo, J. Jain, S.-Y. Lee, A.-C. Yeh, E.-W. Huang
Tensile Response of As-Cast CoCrFeNi and CoCrFeMnNi High-Entropy Alloys
Crystals, **12** 157 (2021).

31 T. Matsukawa, K. Iida, M. Nakamura, T. Ishigaki
Detection of hydroxyl and hydride functional groups in a ceria crystal under hydrogen reduction
CrystEngComm, **23** 2355-2359 (2021).

32 H. Yukawa, S. Watanabe, A. Suzuki, Y. Matsumoto, H. Araki, M. Mizuno, K. Sugita, W. Higemoto
Temperature dependence of hydrogen solubility and diffusivity in hydrogen permeable membrane of pd-cu alloy with b2-type crystal structure
Defect and Diffusion Forum, **407** 31 (2021).

33 T. Katabuchi, Y. Toh, M. Mizumoto, T. Saito, K. Terada, A. Kimura, S. Nakamura, H. Minghui, G. Rovira, M. Igashira
Discovery of a new low energy neutron resonance of ^{89}Y
Eur. Phys. J. A Hadron. Nucl., **57** 4 (2021).

34 Y. Fujii, T. Tominaga, D. Murakami, M. Tanaka, H. Seto
Local Dynamics of the Hydration Water and Poly(Methyl Methacrylate) Chains in PMMA Networks
Frontiers in Chemistry, **9** 728738 (2021).

35 T. Yamashita, K. Okutsu, Y. Kino, R. Nakashima, K. Miyashita, K. Yasuda, S. Okada, M. Sato, T. Oka, N. Kawamura, S. Kanda, K. Shimomura, P. Strasser, S. Takeshita, M. Tampo, S. Doiuchi, Y. Nagatani, H. Natori, S. Nishimura, A. D. Pant, Y. Miyake, K. Ishida
Time evolution calculation of muon catalysed fusion: Emission of recycling muons from a two-layer hydrogen film
Fusion Engineering and Design, **169** 11258 (2021).

36 K. Okutsu, T. Yamashita, Y. Kino, R. Nakashima, K. Miyashita, K. Yasuda, S. Okada, M. Sato, T. Oka, N. Kawamura, S. Kanda, K. Shimomura, P. Strasser, S. Takeshita, M. Tampo, S. Doiuchi, Y. Nagatani, H. Natori, S. Nishimura, A. D. Pant, Y. Miyake, K. Ishida
Design for detecting recycling muon after muon-catalyzed fusion reaction in solid hydrogen isotope target
Fusion Engineering and Design, **170** 112712 (2021).

37 N. Kawamura, S. Matoba, S. Makimura, M. Hara, Y. Hatano
Tritium behavior in isotropic graphite at room temperature
Fusion Engineering and Design, **172** 112801 (2021).

38 J. Tang, T. Katashima, X. Li, Y. Mitsukami, Y. Yokoyama, U.-i. Chung, M. Shibayama, T. Sakai
Effect of Nonlinear Elasticity on the Swelling Behaviors of Highly Swollen Polyelectrolyte Gels
Gels, **7** 25 (2021).

39 Y. Tsuji, M. Shibayama, X. Li
Neutralization and Salt Effect on the Structure and Mechanical Properties of Polyacrylic Acid Gels under Equivolume Conditions
Gels, **7** 69 (2021).

40 A. Sano-Furukawa, S. Kakizawa, C. Shito, T. Hattori, S. Machida, J. Abe, K. Funakoshi, H. Kagi
High-pressure and high-temperature neutron-diffraction experiments using Kawai-type multi-anvil assemblies
High Press. Res., **41** 65 (2021).

41 T. Okumura, T. Azuma, D. A. Bennett, P. Caradonna, I. Chiu, W. B. Doriese, M. S. Durkin, J. W. Fowler, J. D. Gard, T. Hashimoto, R. Hayakawa, G. C. Hilton, Y. Ichinohe, P. Indelicato, T. Isobe, S. Kanda, M. Katsuragawa, N. Kawamura, Y. Kino, K. Mine, Y. Miyake, K. M. Morgan, K. Ninomiya, H. Noda, G. C. O'Neil, S. Okada, K. Okutsu, T. Osawa, N. Paul, C. D. Reintsema, D. R. Schmidt, K. Shimomura, P. Strasser, H. Suda, D. S. Swetz, T. Takahashi, S. Takeda, S. Takeshita, H. Tatsuno, Y. Ueno, J. N. Ullom, S. Watanabe, S. Yamada
Dynamical Response of Transition-Edge Sensor Microcalorimeters to a Pulsed Charged-Particle Beam
IEEE Trans. Appl. Supercond., **31** 2101704 (2021).

42 H. Shishido, K. Nishimura, T. D. Vu, K. Aizawa, K. M. Kojima, T. Koyama, K. Oikawa, M. Harada, T. Oku, K. Soyama, S. Miyajima, M. Hidaka, S. Y. Suzuki, M. M. Tanaka, S. Kawamata, T. Ishida
High Spatial Resolution Neutron Transmission Imaging Using a Superconducting Two-Dimensional Detector
IEEE Trans. Appl. Supercond., **31** 2400505 (2021).

43 T. Oda, T. Arai, T. Furukawa, M. Shiraishi, Y. Sasajima
Electric-Field-Dependence Mechanism for Cosmic Ray Failure in Power Semiconductor Devices
IEEE Trans. Electron Devices, **68** 3505 (2021).

44 T. Kato, M. Tampo, S. Takeshita, H. Tanaka, H. Matsuyama, M. Hashimoto, Y. Miyake
Muon-Induced Single-Event Upsets in 20-nm SRAMs: Comparative Characterization with Neutrons and Alpha Particles
IEEE Trans. Nucl. Sci., **68** 1436 (2021).

45 S. Yamamoto, K. Ninomiya, N. Kawamura, T. Yabe, Y. Hirano
Three dimensional (3D) optical imaging system of muon beams using a silver activated zinc sulfide (ZnS(Ag)) sheet combined with a mirror
IEEE Trans. Nucl. Sci., **68** 2748 (2021).

46 Y. Iwamiya, M. Kawai, D. Nishio-Hamane, M. Shibayama, Z. Hiroi
Modern alchemy: Making "plastics" from paper
Ind. Eng. Chem. Res., **60** 355-360 (2021).

47 D. Urushihara, T. Asaka, K. Fukuda, M. Nakayama, Y. Nakahira, C.

Moriyoshi, Y. Kuroiwa, O. K. Forslund, N. Matsubara, M. Månsson, K. Papadopoulos, Y. Sassa, K. Ohishi, J. Sugiyama, Y. Matsushita, H. Sakurai
Structural Transition with a Sharp Change in the Electrical Resistivity and Spin-Orbit Mott Insulating State in a Rhenium Oxide, $Sr_3Re_2O_9$
Inorg. Chem., **60** 507 (2021).

48 S. Nakano, A. Sano-Furukawa, T. Hattori, S. Machida, K. Komatsu, H. Fujihisa, H. Yamawaki, Y. Gotoh, T. Kikegawa
Observation of dihydrogen bonds in high-pressure phases of ammonia borane by X-ray and neutron diffraction measurements
Inorg. Chem., **60** 3065-3073 (2021).

49 H. Kwon, E. Pietrasiak, T. Ohhara, A. Nakao, B. Chae, C.-C. Hwang, D. Jung, I.-C. Hwang, Y. H. Ko, K. Kim, E. Lee
Programmable Synthesis of Silver Wheels
Inorg. Chem., **60** 6403-6409 (2021).

50 K. Kimura, N. Yagi, S. Hasegawa, M. Hagihala, A. Miyake, M. Tokunaga, H. Cao, T. Masuda, T. Kimura
Coexistence of Magnetoelectric and Antiferroelectric-like Orders in $Mn_3Ta_2O_8$
Inorg. Chem., **60** 15078-15084 (2021).

51 Y. Zhang, J. Brorsson, T. Kamiyama, T. Saito, P. Erhart, A. E. C. Palmqvist
Investigating the Chemical Ordering in Quaternary Clathrate $Ba_8Al_xGa_{16-x}Ge_{30}$
Inorg. Chem., **60** 16977-16985 (2021).

52 S. Tajima, N. Ohba, A. Suzumura, S. Kajita
Synthesis and Ion-Transport Properties of $EuKGe_2O_6^-$, $Ca_3Fe_2Ge_3O_{12}^-$, and $BaCu_2Ge_2O_7$-Type Oxide-Ion Conductors
Inorg. Chem., **60** 17019-17032 (2021).

53 S. Nogami, K. Kadota, H. Uchiyama, H. Arima-Osonoi, H. Iwase, T. Tominaga, T. Yamada, S. Takata, M. Shibayama, Y. Tozuka
Structural changes in pH-responsive gelatin/hydroxypropyl methylcellulose phthalate blends aimed at drug-release systems
Int. J. Biol. Macromol., **190** 989 (2021).

54 X. X. Zhang, D. Knoop, H. Andrä, S. Harjo, T. Kawasaki, A. Lutz, M. Lahres
Multiscale constitutive modeling of additively manufactured Al-Si-Mg alloys based on measured phase stresses and dislocation density
Int. J. Plast., **140** 102972 (2021).

55 N. Ishida, T. Tajima, N. Kitamura, Y. Idemoto
Single-phase synthesis, average, electronic, and local structure and cathode properties of pyroxene type $LiFeSi_2O_6$
Ionics, **27** 925-933 (2021).

56 Y. Takayama, Y. Xu, T. Yoshida, H. Tanaka, Y. Onuki, S. Sato
Texture evolutions in aluminum and Al-3%Mg alloy subjected to shear deformation and subsequent annealing
IOP Conf. Ser. Mater. Sci. Eng., **1121** 12017 (2021).

57 N. Tsuchida, E. Ishimaru, M. Kawa
Role of Deformation-Induced Martensite in TRIP Effect of Metastable Austenitic Steels
ISIJ International, **61** 556-563 (2021).

58 N. Tsuchida, R. Ueji, T. Inoue
Effect of Temperature on Stress–Strain Curve in SUS316L Metastable Austenitic Stainless Steel Studied by In Situ Neutron Diffraction Experiments
ISIJ International, **61** 632-640 (2021).

59 S. Harjo, T. Kawasaki, N. Tsuchida, S. Morooka, W. Gong
Relation between Intergranular Stress of Austenite and Martensitic Transformation in TRIP Steels Revealed by Neutron Diffraction
ISIJ International, **61** 648-656 (2021).

60 H. Sato, M. Sato, Y. Su, T. Shinohara, T. Kamiyama
Improvement of Bragg-edge Neutron Transmission Imaging for Evaluating the Crystalline Phase Volume Fraction in Steel Composed of Ferrite and Austenite
ISIJ International, **61** 1584-1593 (2021).

61 R. Kataoka, M. Nozaki, T. Kimura, K. Sakaki, T. Kojima, K. Ikeda, T. *Otomo, N. Takeichi, A. Kamegawa*
Zirconium Hydride-Stabilized Yttrium Hydride (ZSY): Stabiliza- tion of a Face-Centered Cubic YH_3 Phase by Zr Substitution
J. Alloys. Compd., **851** 156071 (2021).

62 K. D. Liss, S. Harjo, T. Kawasaki, K. Aizawa, P. Xu
Anisotropic thermal lattice expansion and crystallographic structure of strontium aluminide within Al-10Sr alloy as measured by in-situ neutron diffraction
J. Alloys. Compd., **869** 159232 (2021).

63 K. Maruyama, S. Tanaka, S. Natori, I. Bizen, K. Amemiya, R. Kiyanagi, A. Nakao, K. Moriyama, Y. Ishikawa, Y. Amako, T. Iiyama, R. Futamura, S. Utsumi
Magnetic phase diagram of helimagnetic $Ba(Fe_{1-x}Sc_x)_{12}O_{19}(0 \leq x \leq 0.2)$ hexagonal ferrite
J. Alloys. Compd., **892** 162125 (2021).

64 X. X. Zhang, A. Lutz, H. Andrä, M. Lahres, W. Gong, S. Harjo, C. Emmelmann
Strain hardening behavior of additively manufactured and annealed AlSi3.5Mg2.5 alloy
J. Alloys. Compd., **898** 162890 (2021).

65 T. Okudaira, Y. Ueda, K. Hiroi, R. Motokawa, Y. Inamura, S. Takata, T. Oku, J. Suzuki, S. Takahashi, H. Endo, H. Iwase
Polarization analysis for small-angle neutron scattering with a ^3He spin filter at a pulsed neutron source
J. Appl. Crystallogr., **54** 1-9 (2021).

66 D. Miura, T. Kumada, Y. Sekine, R. Motokawa, H. Nakagawa, Y. Oba, T. Ohhara, S. Takata, K. Hiroi, T. Morikawa, Y. Kawamura, K. Ohishi, J. Suzuki, Y. Miyachi, T. Iwata
Development of spin-contrast-variation neutron powder diffractometry for extracting the structure factor of hydrogen atoms
J. Appl. Crystallogr., **54** 454-460 (2021).

67 M. Mizusawa, K. Sakurai
2D real space visualization of d values in polycrystalline bulk materials of different hardness
J. Appl. Crystallogr., **54** 597 (2021).

68 T. Tominaga, M. Sahara, Y. Kawakita, H. Nakagawa, T. Yamada
Evaluation of sample cell materials for aqueous solutions used in quasi-elastic neutron scattering measurements
J. Appl. Crystallogr., **54** 1631-1640 (2021).

69 H. Singh, V.K. Aswal
Tuning of micelle adsorption on nanoparticles by combination of surfactants
J. Appl. Phys., **129** 234703 (2021).

70 R. Maruyama, D. Yamazaki, H. Aoki, K. Akutsu-Suyama, T. Hanashima, N. Miyata, K. Soyama, T. Bigault, T. Saerbeck, P. Courtois
Improved performance of wide bandwidth neutron-spin polarizer due to ferromagnetic interlayer exchange coupling
J. Appl. Phys., **130** 083904 (2021).

71 J. G. Nakamura, Y. Kawakita, K. Shimomura, T. Suemasu
Hydrogen impurities in p-type semiconductors, GeS and GeTe
J. Appl. Phys., **130** 195701 (2021).

72 N. Sato, R. Yogo ,S. Yanaka, A. Martel, L. Porcar, K. Morishima, R. Inoue, T. Tominaga, T. Arimori, J. Takagi, M. Sugiyama, K. Kato

A feasibility study of inverse contrast-matching small-angle neutron scattering method combined with size exclusion chromatography using antibody interactions as model systems
J. Biochem., **169** 701-708 (2021).

73 E. Y. Kozhunova, V. Y. Rudyak, X. Li, M. Shibayama, G. S. Peters, O. V. Vyshivannaya, I. R. Nasimova, A. V. Chertovich
Microphase separation of stimuli-responsive interpenetrating network microgels investigated by scattering methods
J. Colloid Interface Sci., **597** 297 (2021).

74 H. Arima-Osonoi, K. Yamazaki, R. Simura, T. Sugawara, K. Yubuta, K. Sugiyama, A. Yoshiasa
Local structure investigations of Sn and Mn doped in β-Ga_2O_3 by X-ray absorption spectroscopy
J. Cryst. Growth, **570** 126223 (2021).

75 R. Yuge, S. Kuroshima, M. Tabuchi, K. Doumae, H. Shibuya
Charge Compensation Mechanism and Structural Change of Li- Rich Layered Oxide $Li_{1.23}Mn_{0.46}Fe_{0.15}Ni_{0.15}O_2$ Electrode during Charging and Discharging
J. Electrochem. Soc., **168** 040518 (2021).

76 N. V. Mdlovu, K.-S. Lin, M.-T. Weng, C.-C. Hsieh, Y.-S. Lin, M. J. C. Espinoza
In vitro intracellular studies of pH and thermo-triggered doxorubicin conjugated magnetic SBA-15 mesoporous nanocarriers for anticancer activity against hepatocellular carcinoma
J. Ind. Eng. Chem., **102** 1 (2021).

77 J. Koga, S. Ieki, A. Kimura, M. Kitaguchi, R. Kitahara, K. Mishima, N. Nagakura, T. Okudaira, H. Otono, H. M. Shimizu, N. Sumi, S. Takada, T. Tomita, T. Yamada, T. Yoshioka
Measurement of γ rays from ^{6}LiF tile as an inner wall of a neutron-decay detector
J. Instrum., **16** P02001 (2021).

78 S. Yamamoto, K. Ninomiya, N. Kawamura, Y. Hiran
Optical imaging of decayed positrons and muons with different collimators
J. Instrum., **16** P08062 (2021).

79 T. Yajima, Y. Hinuma, S. Hori, R. Iwasaki, R. Kanno, T. Ohhara, A. Nakao, K. Munakata, Z. Hiroi
Correlated Li-ion migration in the superionic conductor $Li_{10}GeP_2S_{12}$
J. Mater. Chem. A, **9** 11278-11284 (2021).

80 T. Kato, Y. Yamada, Y. Nishikawa, T. Otomo, H. Sato, S. Sato
Origins of peaks of graphitic and pyrrolic nitrogen in N1s X-ray photoelectron spectra of carbon materials: quaternary nitrogen, tertiary amine, or secondary amine?
J. Mater. Sci., **56** 15798–15811 (2021).

81 G. Yamamoto, A. Kyono, J. Abe, A. Sano-Furukawa, T. Hattori
Crystal structure of nesquehonite, $MgCO_3{\cdot}3H(D)_2O$ by neutron diffraction and effect of pH on structural formulas of nesquehonite
J. Mineral. Petrol. Sci., **116** 96 (2021).

82 Y. Mori, H. Kagi, S. Kakizawa, K. Komatsu, C. Shito, R. Iizuka-Oku, K. Aoki, T. Hattori, A. Sano-Furukawa, K. Funakoshi, H. Saitoh
Neutron diffraction study of hydrogen site occupancy in $Fe_{0.95}Si_{0.05}$ at 14.7 GPa and 800K.
J. Mineral. Petrol. Sci., **116** 309-313 (2021).

83 H. Abe
Phase variety in ionic liquids: Hydrogen bonding and molecular conformations
J. Mol. Liq., **332** 115189 (2021).

84 S. Hashimoto, K. Nakajima, T. Kikuchi, K. Kamazawa, K. Shibata, T. Yamada
Experimental analysis on dynamics of liquid molecules adjacent to particles in nanofluids
J. Mol. Liq., **342** 117580 (2021).

85 H. Abe, F. Nemoto, K. Hiroi, K. Ohishi, S. Takata
Spontaneous formations of nanoconfined water in ionic liquids by small-angle neutron scattering
J. Mol. Liq., **346** 117035 (2021).

86 K. Shimada-Takaura, K. Ninomiya, A. Sato, N. Ueda, M. Tampo, S. Takeshita, I. Umegaki, Y. Miyake, K. Takahashi
A novel challenge of nondestructive analysis on OGATA Koan's sealed medicine by muonic X-ray analysis
J. Nat. Med., **75** 532–539 (2021).

87 M. Arai, K. H. Andersen, D. N. Argyriou, W. Schweika, L. Zanini, S. Harjo, T. Kamiyama, M. Harada
The performance of neutron diffractometers at long and short pulse spallation sources: Comparison between ESS and J-PARC
J. Neutron Res., **23** 215-232 (2021).

88 H. Watanabe, N. Arai, E. Nozaki, J. Han, K. Fujii, K. Ikeda, T. Otomo, K. Ueno, K. Dokko, M. Watanabe, Y. Kameda, Y. Umebayashi
Local Structure of Li^+ in Super-concentrated Aqueous LiTFSA Solutions
J. Phys. Chem. B, **125** 7477 (2021).

89 Y. Kameda, M. Kowaguchi, K. Tsutsui, Y. Amo, T. Usuki, K. Ikeda, T. Otomo
Experimental Determination of Relationship between Intramolecular O-D Bond Length and Its Stretching Vibrational Frequency of D_2O Molecule in the Liquid State
J. Phys. Chem. B, **125** 11285-11291 (2021).

90 T. Takamuku, A. Tashiro, M. Kawano, M. Ando, A. Ogawa, K. Sadakane, H. Iwase, H. Shirota
Anion effects on the mixing states of 1-methyl-3-octylimidazolium tetrafluoroborate and bis(trifluoromethylsulfonyl)amide with methanol, acetonitrile, and dimethyl sulfoxide on the meso- and microscopic scales
J. Phys. Chem. B, **125** 13896-13907 (2021).

91 M. H. Petersen, N. Vernet, W. P. Gates, F. J. Villacorta, S. Ohira-Kawamura, Y. Kawakita, M. Arai, G. Kneller, H. N. Bordallo
Assessing diffusion relaxation of interlayer water in clay minerals using a minimalist three-parameter model
J. Phys. Chem. C, **125** 15085 (2021).

92 K. Ito, T. Yamada, A. Shinohara, S. Takata, Y. Kawakita
Dynamics of water in a catalyst layer of a fuel cell by quasielastic neutron scattering
J. Phys. Chem. C, **125** 21645 (2021).

93 P. Luo, Y. Zhai, J. B. Leao, M. Kofu, K. Nakajima, A. Faraone, Y Z
Neutron Spin–Echo Studies of the Structural Relaxation of Network Liquid $ZnCl_2$ at the Structure Factor Primary Peak and Prepeak
J. Phys. Chem. Lett., **12** 392-398 (2021).

94 N. Yamamoto, M. Kofu, K. Nakajima, H. Nakagawa, N. Shibayama
Freezable and Unfreezable Hydration Water: Distinct Contributions to Protein Dynamics Revealed by Neutron Scattering
J. Phys. Chem. Lett., **12** 2172 (2021).

95 L. J. Bannenberg, H. Schreuders, H. Kim, K. Sakaki, S. Hayashi, K. Ikeda, T. Otomo, K. Asano, B. Dam
Suppression of the Phase Coexistence of the fcc–fct Transition in Hafnium-Hydride Thin Films
J. Phys. Chem. Lett., **12** 10969-10974 (2021).

96 X. Wang, X, Tang, P. Zhang, Y. Wang, D. Gao, J. Liu, K. Hui, Y. Wang, Y. Wang, X. Dong, T. Hattori, A. Sano-Furukawa, K. Ikeda, P. Miao, X. Lin, M. Tang, Z. Zuo, H. Zheng, K. Li, H-k. Ma
Crystalline Fully Carboxylated Polyacetylene Obtained under High

Pressure as a Li-Ion Battery Anode Material
J. Phys. Chem. Lett., **12** 12055-12061 (2021).

97 M. Tabuchi, Y. Kobayashi
Appearance of pentavalent Fe ion as a result of a charge disproportionation in Fe-substituted Li_2MnO_3
J. Phys. Chem. Solids, **150** 109862 (2021).

98 K. Itoh, R. Yamada, J. Saida, K. Ikeda, T. Otomo
Atomic-level characterization of free volume in the structure of $Cu_{67}Zr_{33}$ amorphous alloy
J. Phys. Condens. Matter., **33** 274001 (2021).

99 H. K. Yoshida, H. Okabe, S. Takeshita, H. Luetkens, A. Koda, R. Kadono
μSR Study of Kapellasite-type Quantum Kagome Antiferromagnet $CaCu_3(OH)_6Cl_2 \cdot 0.6H_2O$
J. Physical Soc. Japan, **91** 013701 (2021).

100 S. Hosokawa, Y. Kawakita, L. Pusztai, K. Ikeda, T. Otomo
Detailed investigations on short- and intermediate-range structures of Ge-Se glasses near the stiffness transition composition
J. Physical Soc. Japan, **90** 024601 (2021).

101 M. Fujita, K. Ikeuchi, R. Kajimoto, M. Nakamura
Magnetic Excitations of $Sr_3Ir_2O_7$ Observed by Inelastic Neutron Scattering Technique
J. Physical Soc. Japan, 90 025001 (2021).

102 K. Kaneko, T. Kawasaki, A. Nakamura, K. Munakata, A. Nakao, T. Hanashima, R. Kiyanagi, T. Ohhara, M. Hedo, T. Nakama, Y. Ōnuki
Charge-Density-Wave Order and Multiple Magnetic Transitions in Divalent Europium Compound $EuAl_4$
J. Physical Soc. Japan, **90** 064704 (2021).

103 Y. Hwang, K. H. Lee, J.-H. Chung, K. Ikeuchi, V. O. Garlea, H. Yamauchi, M. Akatsu, S. Shamoto
Spin Wave Excitations in Honeycomb Antiferromagnet $MnTiO_3$
J. Physical Soc. Japan, **90** 064708 (2021).

104 D. Ueta, M. Yoshida, T. Kobuke, Y. Ikeda, T. Masuda, H. Yoshizawa
Complex Magnetic Phase Diagram in the Non-Centrosymmetric Compound $CePtSi_3$
J. Physical Soc. Japan, **90** 064712 (2021).

105 K. Matsubayashi, H. Okamura, T. Mizokawa, N. Katayama, A. Nakano, H. Sawa, T. Kaneko, T. Toriyama, T. Konishi, Y. Ohta, H. Arima, R. Yamanaka, A. Hisada, T. Okada, Y. Ikemoto, T. Moriwaki, K. Munakata, A. Nakao, M. Nohara, Y. Lu, H. Takagi, Y. Uwatoko
*Hybridization-Gap Formation and Superconductivity in the Pressure-Ind*uced Semimetallic Phase of the Excitonic Insulator Ta_2NiSe_5
J. Physical Soc. Japan, **90** 074706 (2021).

106 K. Kodama, T. Honda, H. Yamauchi, S. Shamoto, K. Ikeda, T. Otomo
Magnetic structure of short-range ordering in intermetallic antiferromagnet Mn_3RhSi
J. Physical Soc. Japan, **90** 074710 (2021).

107 Y. Nambu, S. Shamoto
Neutron Scattering Study on Yttrium Iron Garnet for Spintronics
J. Physical Soc. Japan, **90** 081002 (2021).

108 S. Shamoto, H. Yamauchi, K. Ikeuchi, M. K. Lee, L.-J. Chang, V. O. Garlea, I. Y. Hwang, K. H. Lee, J.-H. Chung
Spin-flop Phase in a Honeycomb Antiferromagnet $Mn_{0.84}Mg_{0.16}TiO_3$
J. Physical Soc. Japan, **90** 093703 (2021).

109 D. Ueta, T. Kobuke, H. Shibata, M. Yoshida, Y. Ikeda, S. Itoh, T. Yokoo, T. Masuda, H. Yoshizawa
Crystalline electric field level scheme in the non-centrosymmetric $CeRhSi_3$ and $CeIrSi_3$
J. Physical Soc. Japan, **90** 104706 (2021).

110 M. Fujita, T. Taniguchi, T. Wang, S. Torii, T. Kamiyama, K. Ohashi, T. Kawamata, T. Takamatsu, T. Adachi, M. Kato, Y. Koike
Reduction Annealing Effects on the Crystal Structure of T'-type $La_{1.8}Eu_{0.2}CuO_{4+\alpha-\delta}$
J. Physical Soc. Japan, **90** 105002 (2021).

111 D. Ueta, M. Yoshida, T. Kobuke, Y. Ikeda, A. Nakao, T. Moyoshi, K. Munakata, Y. Liu, T. Masuda, H. Yoshizawa
Oval-cycloidal Magnetic Structure with Phase-shift in the Non-centrosymmetric Tetragonal Compound $CePdSi_3$
J. Physical Soc. Japan, **90** 114702 (2021).

112 K. Nawa, Y. Imai, Y. Yamaji, H. Fujihara, W. Yamada, R. Takahashi, T. Hiraoka, M. Hagihala, S. Torii, T. Aoyama, T. Ohashi, Y. Shimizu, H. Gotou, M. Itoh, K. Ohgushi, T. J. Sato
Strongly Electron-Correlated Semimetal RuI_3 with a Layered Honeycomb Structure
J. Physical Soc. Japan, **90** 123703 (2021).

113 K. Iwasa, S. Nakazato, D. Hashimoto, M. Shiozawa, K. Kuwahara, H. Sagayama, S. Ohira-Kawamura, N. Murai, D. T. Adroja. A. M. Strydom
Magnetic excitations in chiral-structure phase of $Ce_3Ir_4Sn_{13}$
J. Physical Soc. Japan, **90** 124701 (2021).

114 Y. Idemoto, M. Ichiyama, N. Ishida, N. Kitamura
Structural and electronic properties of spinel type $Mg_{1+y}Co_{2-x-y}Mn_xO_4$ for cathode applications in magnesium rechargeable batteries
J. Power Sources, **482** 228920 (2021).

115 H. Yamada, N. Morimoto, H. Mukohara, T. Tojo, S. Yano, E. Magome, T. Morimura, R. Bekarevich, K. Mitsuishi
Concerted influence of microstructure and adsorbed water on lithium-ion conduction of $Li_{1.3}Al_{0.3}Ti_{1.7}(PO_4)_3$
J. Power Sources, **511** 230422 (2021).

116 N. Ishida, K. Kawagoe, N. Kitamura, J. Akimoto, Y. Idemoto
Average and local structure analysis of Na/Li ion-exchanged $Li_x(Mn,Ni,Ti)O_2$ using synchrotron X-ray and neutron sources
J. Solid State Chem., **25** 1319-1326 (2021).

117 J. Hendriks, N. O'Dell, A. Wills, A. Tremsin, C. Wensrich, T. Shinohara
Bayesian non-parametric Bragg-edge fitting for neutron transmission strain imaging
J. Strain Anal. Eng. Des., **56** 371-385 (2021).

118 K. Hirota, T. Ariga, M. Hino, G. Ichikawa, S. Kawasaki, M. Kitaguchi, K. Mishima, N. Muto, N. Naganawa, H. M. Shimizu
Neutron Imaging Using a Fine-Grained Nuclear Emulsion
J. Imaging, **7** 4 (2021).

119 K. Isegawa, D. Setoyama, H. Kimura, T. Shinohara
The First Application of a $Gd_3Al_2Ga_3O_{12}$:Ce Single-Crystal Scintillator to Neutron Radiography
J. Imaging, **7** 232 (2021).

120 S. Sasada, K. Hiroi, K. Osanai, T. Shinohara, K. Watanabe, A. Uritani
High-spatial-resolution measurement of magnetization distribution using polarized neutron imaging
Jpn. J. Appl. Phys., **60** 126003 (2021).

121 M. Yotsuzuka, T. Iijima, H. Iinuma, K. Inami, M. Otani, N. Kawamura, R. Kitamura, Y. Kondo, N. Saito, K. Shimomura, Y. Sue, Y. Nakazawa, K. Hasegawa, K. Futatsukawa, T. Mibe, Y. Miyake, T. Morishita, H. Yasuda, T. Yamazaki
Simulation of the Beam Commissioning Method for a Muon APF IH-DTL in the J-PARC Muon g – 2/EDM Experiment
JPS Conf. Proc., **33** 011040 (2021).

122 N. Kawamura on behalf of muon science section MLF J-PARC
Current Status of Muon Science Facility
JPS Conf. Proc., **33** 011052 (2021).

123 M. Ohta, A. Koda, C. Ohmori, Y. Yoshizawa, K. Ogura, Y. Miyake
Magnetic Field Dependence on Crystallization Process of FINEMET® Nano-crystalline Alloy Detected by μSR Method
JPS Conf. Proc., **33** 011053 (2021).

124 Y. Shoda, T. Igarashi, H. Yamashita, Y. Kitamura, S. Takata, K. Ohishi, D. Aoki, K. Tsunoda, H. Otsuka
Structural analysis of polybutadienes with urethane linkages by small-angle neutron scattering
JPS Conf. Proc., **33** 011054 (2021).

125 Y. Ishikawa, R. Kiyanagi, Y. Noda
Electrostatic Potential Mapping by Maximum Entropy Method based on Mott-Bethe relations
JPS Conf. Proc., **33** 011055 (2021).

126 N. Sumi, K. Hirota, G. Ichikawa, T. Ino, Y. Iwashita, S. Kajiwara, Y. Kato, M. Kitaguchi, K. Mishima, K. Morikawa, T. Mogi, H. Oide, H. Okabe, H. Otono, T. Shima, H. M. Shimizu, Y. Sugisawa, T. Tanabe, S. Yamashita, K. Yano, T. Yoshioka
Precise Neutron Lifetime Measurement Using Pulsed Neutron Beams at J-PARC
JPS Conf. Proc., **33** 011056 (2021).

127 M. Takahashi, R. Miyazaki, T. Kawasaki, S. Harjo
Phase Transitions and Atomic Ordering in Cu–Pd–Fe Ternary Alloys
JPS Conf. Proc, **33** 011057 (2021).

128 S. Itoh, T. Masuda, T. Yokoo, H. Yoshizawa, M. Soda, S. Asai, Y. Ikeda, S. Ibuka, M. Yoshida, T. Hawai, H. Saito, D. Kawana, R. Sugiura, T. Asami, Y. Ihata
Dynamical studies in condensed matter on High Resolution Chopper Spectrometer (HRC) – 2nd phase of HRC project –
JPS Conf. Proc., **33** 011058 (2021).

129 K. Kodama, T. Honda, K. Ikeda, S. Shamoto, T. Otomo
Magnetic Pair Distribution Function of Spin-glass System $Mn_{0.5}Fe_{0.5}TiO_3$
JPS Conf. Proc., **33** 011059 (2021).

130 K. Ohishi, Y. Kousaka, S. Iwasaki, J. Akimitsu, M. Pardo-Sainz, V. Laliena, J. Campo, M. Ohkuma, M. Mito
Small angle neutron scattering study near the critical field at low temperature in MnSi
JPS Conf. Proc., **33** 011060 (2021).

131 K. Maruyama, S. Tanaka, R. Kiyanagi, A. Nakao, K. Moriyama, Y. Ishikawa, S. Utsumi
Helimagnetism of $Ba(Fe_{1-x}Sc_x)_{12}O_{19}$ Studied by Magnetization Measurement and Neutron Diffraction
JPS Conf. Proc., **33** 011061 (2021).

132 K. Oikawa, S. Harjo, A. H. Pham, T. Kawasaki, S. Morito, Y. Kiyanagi, T. Shinohara, T. Kai, T. Ohba, M. Ito
Microstructure Distribution of Japanese Sword Cross Sections Analyzed by the Diffractometer TAKUMI at J-PARC
JPS Conf. Proc, **33** 011062 (2021).

133 T. Yamashita, S. Harjo, O. Umezawa, T. Kawasaki
Neutron Diffraction Mapping Measurement for Japanese Nails in the Ancient and Present Days
JPS Conf. Proc, **33** 011063 (2021).

134 T. Yamashita, S. Tomono, S. Morooka, S. Harjo, T. Kawasaki, T. Nameki, N. Koga, O. Umezawa
Stress Partitioning Behavior of Duplex Alloys Consisting of BCC and FCC Phases at Low Temperature
JPS Conf. Proc, **33** 011064 (2021).

135 D. Setoyama, H. Kimura, T. Shinohara, Y. Matsumoto
Non-Destructive 3D Neutron Imaging for Power Electronic Module
JPS Conf. Proc., **33** 011065 (2021).

136 A. Nakao, T. Moyoshi, K. Moriyama, T. Matsumura, K. Iba, S. Ohara, Y. Ishikawa, K. Munakata, T. Ohhara, R. Kiyanagi
Determination of Crystallographic Planes for a Polyhedral Single Crystal
JPS Conf. Proc., **33** 011067 (2021).

137 M. Matsuura, T. Yamada, T. Tominaga, M. Kobayashi, H. Nakagawa, Y. Kawakita
Position Dependency of the Scattered Intensity in the Time-of-flight Backscattering Spectrometer DNA
JPS Conf. Proc., **33** 011068 (2021).

138 S. Hosokawa, J. R. Stellhorn, Y. Onodera, S. Kohara, H. Tajiri, E. Magome, L. Pusztai, K. Ikeda, T. Otomo, M. Krbal, T. Wagner
Local- and Intermediate-Range Atomic Order in $Ga_2Ge_3Se_9$ Glass: Complementary Use of X-Rays and Neutrons
JPS Conf. Proc., **33** 011069 (2021).

139 S. Hosokawa, Y. Kawakita, J. R. Stellhorn, L. Pusztai, N. Blanc, N. Boudet, K. Ikeda, T. Otomo
Local- and Intermediate-Range Order in Room Temperature Superionic Conducting Ag-$GeSe_3$ Glasses
JPS Conf. Proc., **33** 011070 (2021).

140 Y. Kawakita, T. Kikuchi, S. Tahara, M. Nakamura, Y. Inamura, K. Maruyama, Y. Yamauchi, S. Ohira-Kawamura, K. Nakajima
Mode distribution analysis for superionic melt of CuI by coherent quasielastic neutron scattering
JPS Conf. Proc., **33** 011071 (2021).

141 K. Ninomiya, T. Kudo, A. Shinohara, M. Tampo, S. Takeshita, Y. Miyake, M. K. Kubo
Muonic X-ray Identification of Nuclear Materials Sealed in a Box
JPS Conf. Proc., **33** 011072 (2021).

142 Y. Miyazaki, S. Watanabe, M. Nakamura, A. Shibata, K. Nomura, T. Kai, J. D. Parker
Observation of Eu Adsorption Band in the CMPO/SiO_2–P Column by Neutron Resonance Absorption Imaging
JPS Conf. Proc., **33** 011073 (2021).

143 Y. Tsuchikawa, Y. Abe, Y. Ohishi, T. Kai, Y. Toh, M. Segawa, M. Maeda, A. Kimura, S. Nakamura, M. Harada, K. Oikawa, Y. Matsumoto, J. D. Parker, T. Shinohara, Y. Nagae, I. Sato
Feasibility study of PGAA for boride identification in simulated melted core materials
JPS Conf. Proc., **33** 011074 (2021).

144 Y. Abe, Y. Tsuchikawa, T. Kai, Y. Matsumoto, J. D. Parker, T. Shinohara, Y. Ohishi, T. Kamiyama, Y. Nagae, I. Sato
Visualization of the Boron Distribution in Core Material Melting and Relocation Specimen by Neutron Energy Resolving Method
JPS Conf. Proc., **33** 011075 (2021).

145 F. Kaneko, A. Radulescu, H. Iwase, S. Takata, M. Nishiura, Z. Hou
Application of simultaneous measurement system combining wide q-range small-angle neutron scattering and polarized Fourier transform infrared spectroscopy: Cocrystal of syndiotactic polystyrene with methyl benzoate
JPS Conf. Proc., **33** 011076 (2021).

146 F. Nemoto, N. L. Yamada, F. Takabatake, H. Seto
Installation of a Rheometer on Neutron Reflectometer SOFIA at J-PARC toward Rheo-NR and Observation for Crystallization Behavior of Cocoa Butter in Chocolate
JPS Conf. Proc., **33** 011077 (2021).

147 H. Iwase, R. Kawai, T. Yoshimura, S. Takata
Rheo-SANS study on shear thinning behavior of cationic gemini surfactant (12–2–12) in salt-free solution
JPS Conf. Proc., **33** 011078 (2021).

148 J. Kobayashi, Y. Kasama, W. Fujii, E. Tominaga, H. Iwase, H. Nanbu
Structural analysis of microemulsion formed from polymer surfactant polyglycerol esters in the manufacturing process
JPS Conf. Proc., **33** 011079 (2021).

149 M. Nakada, T. Yamada, K. Ikeda, T. Otomo
Static and Dynamic Structure Analysis of Intermediate Water on Polyvinyl Pyrrolidone Using Neutron Scattering
JPS Conf. Proc., **33** 011080 (2021).

150 M. Iguchi, Y. Fujii, K. Hori, F. Nemoto, N. Torikai
Thermal Stability and Interfacial Segregation for Polymer Thin Films Blended with a Homologue Having Different Tacticity
JPS Conf. Proc., **33** 011081 (2021).

151 T. Honda, G. Nishikawa, Y. Fujii, S. Inada, H. Iwase, N. Torikai
Adsorbed polymer effects on particle dispersion in polymeric matrix examined by SANS
JPS Conf. Proc., **33** 011082 (2021).

152 T. Tominaga, T. Yamada
Water dynamics of double-network polymers in a primally hierarchical structure
JPS Conf. Proc., **33** 011083 (2021).

153 T. Yamada, H. Arima, T. Hattori
Commissioning for QENS Experiments at Pressures Up to 200 MPa at MLF, J-PARC
JPS Conf. Proc., **33** 011084 (2021).

154 T. Yamada, T. Tominaga
In Situ Quasi-Elastic Neutron Scattering of Nafion Membrane with Water–Vapor Pressure Control System
JPS Conf. Proc., **33** 011085 (2021).

155 T. Tominaga, Y. Kawakita, H. Nakagawa, T. Yamada, K. Shibata
Quartz Cell for a Backscattering Spectrometer
JPS Conf. Proc., **33** 011086 (2021).

156 F. Funama, M. Hino, T. Oda, H. Endo, T. Hosobata, Y. Yamagata, S. Tasaki, Y. Kawabata
A study of Focusing TOF-MIEZE Spectrometer with Small-angle Neutron Scattering
JPS Conf. Proc., **33** 011088 (2021).

157 K. Nakajima, S. Ohira-Kawamura, M. Kofu, N. Murai, Y. Inamura, T. Kikuchi, D. Wakai
Recent update of AMATERAS: a cold-neutron disk-chopper spectrometer
JPS Conf. Proc., **33** 011089 (2021).

158 S. Imajo, Y. Iwashita, K. Mishima, M. Kitaguchi, H. M. Shimizu, T. Ino, S. Yamashita, K. Hirota, F. Goto, Y. Fuwa, R. Katayama
Ultracold Neutron Time Focusing Experiment and Performance Evaluation of an Improved UCN Rebuncher at J-PARC/MLF
JPS Conf. Proc., **33** 011091 (2021).

159 R. Maruyama, D. Yamazaki, K. Akutsu-Suyama, T. Hanashima, N. Miyata, H. Aoki, K. Soyama
Improvement in sputtering rate uniformity over large deposition area of large-scale ion beam sputtering system
JPS Conf. Proc., **33** 011092 (2021).

160 T. Tominaga, M. Sahara, Y. Kawakita, H. Nakagawa, N. Shimamoto
Corrosion of Aluminum-based Containers for Neutron Studies with Aqueous Samples under Low Temperatures
JPS Conf. Proc., **33** 011094 (2021).

161 T. Tominaga, M. Kobayashi, T. Yamada, M. Matsuura, Y. Kawakita, S. Kasai
Position-Encoded Automatic Cell Elevator for BL02, J-PARC MLF
JPS Conf. Proc., **33** 011095 (2021).

162 T. Okudaira, T. Oku, K. Sakai, K. Hiroi, T. Shinohara, T. Ino, H. Kira, H. Hayashida, J. Suzuki, K. Kakurai, K. Aizawa
A Neutron Depolarization Measurement of Single Crystal Fe by Using a ^{3}He Neutron Spin Filter and Magnetic Super-mirrors
JPS Conf. Proc., **33** 011096 (2021).

163 T. Nakamura, T. Kawasaki, K. Toh, S. Harjo, K. Sakasai, K. Aizawa
A Two-Dimensional Scintillation Neutron Detector for TAKUMI Diffractometer in J-PARC MLF
JPS Conf. Proc, **33** 011097 (2021).

164 Y. Sakaguchi, S. Kasai, K. Ohuchi, T. Morikawa, H. Iwase, M. Akamatsu, H. Sakai, A.-A. A. Simon, M. Mitkova, R. Takahashi
Recent development of the sample environment for light irradiation experiments at the Materials and Life Science Experimental Facility
JPS Conf. Proc., **33** 011100 (2021).

165 H. Nakagawa, Y. Yonetani, K. Nakajima, S. Ohira-Kawamura, T. Kikuchi, Y. Inamura, M. Kataoka, H. Kono
Sequence-dependent hydration water dynamics of dodecameric DNA
JPS Conf. Proc, **33** 011101 (2021).

166 T. Yoshioka, T. Aoyagi, Y. Fujita, Y. Honda, H. Ikeda, M. Ikeno, K. Kawagoe, T. Kishishita, T. Kohriki, T. Kume, S. Kurumida, M. Matama, T. Mibe, T. Murakami, K. Namba, S. Nishimura, N. Saito, O. Sasaki, T. Sata, N. Sato, Y. Sato, H. Sendai, S. Shirabe, M. Shoji, T. Suda, Y. Sue, T. Suehara, M. Tanaka, T. Takatomi, J. Tojo, K. Tsukada, Y. Tsusumi, T. Uchida, K. Ueno, T. Ushizawa, T. Yamanaka, H. Yasuda, and J-PARC muon g − 2/EDM Collaboration
Positron Tracking Detector for Muon g − 2/EDM Experiment at J-PARC
JPS Conf. Proc., **33** 011108 (2021).

167 K. Sakai, T. Oku, T. Okudaira, T. Kai, M. Harada, K. Hiroi, H. Hayashida, K. Kakurai, H. M. Simizu, K. Hirota, T. Yamamoto, T. Ino
Study of neutron–nuclear spin correlation term with a polarized Xe target
JPS Conf. Proc., **33** 011116 (2021).

168 K. Yano, Y. Makida, S. Makise, K. Mishima, H. Otono, N. Sumi, T. Yoshioka
Precise Neutron Lifetime Measurement: An Integration Test with a Gaseous and a Solenoidal Magnet
JPS Conf. Proc., **33** 011117 (2021).

169 M. Hiromoto, T. Hori, R. Kondo, S. Hara, T. Shima, R. Nakabe, N. OI, H. M. Shimizu, K. Hirota, M. Kitaguchi, C. C. Haddock, W. M. Snow, T. Yoshioka, K. Mishima, T. Ino
Proof-of-principle Experiment for the Study of a New Intermediate-range Interaction Using Coherent Neutron Scattering
JPS Conf. Proc., **33** 011118 (2021).

170 N. Yamamoto, M. Kitaguchi, H. M Shimizu, Y. Seki, K. Mishima
Development of Pulsed Neutron Interferometer
JPS Conf. Proc., **33** 011119 (2021).

171 N. Kawamura, R. Kitamura, H. Yasuda, M. Otani, Y. Nakazawa, H. Iinuma, T. Mibe
A New Approach for Mu − Mu Conversion Search
JPS Conf. Proc., **33** 011120 (2021).

172 C. Zhang, H. Hara, T. Hiraki, Y. Ikedo, Y. Imai, K. Ishida, S. Kamal, N. Kawamura, A. Koda, Y. Mao, T. Masuda, T. Mibe, Y. Miyake, Y. Miyamoto, Y. Oishi, M. Otani, P. Strasser, K. Shimomura, K. Suzuki, S. Uetake, T. Yamazaki, S. Yamamoto, K. Yoshimura, M. Yoshida
Simulation Study of Laser Ionization of Muonium by 1S-2S Excitation for the Muon g − 2/EDM Experiment at J-PARC
JPS Conf. Proc., **33** 011125 (2021).

173 H. Yasuda, H. Iinuma, N. Kawamura, R. Kitamura, Y. Kondo, T. Mibe, Y. Nakazawa, M. Otani, N. Saito, Y. Sue, Y. Takeuchi, T. Yamazaki, M.

Yotsuzuka
Development of Spin Flip Analysis for the J-PARC Muon g – 2/EDM Experiment
JPS Conf. Proc., **33** 011126 (2021).

174 Y. Nakazawa, H. Iinuma, Y. Iwashita, Y. Iwata, E. Cicek, M. Otani, N. Kawamura, R. Kitamura, Y. Kondo, N. Saito, Y. Sue, Y. Takeuchi, K. Hasegawa, N. Hayashizaki, T. Mibe, T. Morishita, H. Yasuda, T. Yamazaki, M. Yoshida, M. Yotsuzuka
Multipacting Simulations of Coaxial Coupler for IH-DTL Prototype in Muon Accelerator
JPS Conf. Proc., **33** 011128 (2021).

175 Y. Takeuchi, K. Futatsukawa, K. Hasegawa, N. Hayashizaki, H. Iinuma, T. Ito, Y. Iwashita, Y. Iwata, N. Kawamura, R. Kitamura, Y. Kondo, T. Mibe, T. Morishita, F. Naito, Y. Nakazawa, M. Otani, T. Yamazaki, N. Saito, Y. Sue, H. Yasuda, M. Yoshida
Error Studies for Muon Linac in the Muon g – 2/EDM Experiment at J-PARC
JPS Conf. Proc., **33** 011129 (2021).

176 N. Kawamura, S. Makimura, A. Koda, S. Matoba, Y. Kobayashi
Safety Measure Against Tritium in the MLF Muon Target
JPS Conf. Proc., **33** 011146 (2021).

177 K. Sakai, M. Ooi, K. Haga, T. Kai, T. Nakatani, Y. Kobayashi, A. Watanabe
Upgrade History and Present Status of the General Control System for the Materials and Life Science Experimental Facility at J-PARC
JPS Conf. Proc., **33** 011151 (2021).

178 H. Aoki, H. Ogawa, M. Takenaka
Neutron reflectometry tomography for imaging and depth structure analysis of thin films with in-plane inhomogeneity
Langmuir, **37** 196-203 (2021).

179 H. Iwase, M. Kubota, T. Itoh, T. Ogura, T. Ebina, H. Ohtani, K. Kurosaka, Y. Fukushima
Direct observation of the relationship between thixotropic behavior and shear-induced orientation of clay particles in synesthetic hectorite suspensions
Langmuir, **37** 6435–6441 (2021).

180 T. Miyazaki, N. Miyata, H. Arima-Osonoi, H. Kira, K. Ohuchi, S. Kasai, Y. Tsumura, H. Aoki
Layered Structure in the Crystalline Adsorption Layer and the Leaching Process of Poly(vinyl alcohol) Revealed by Neutron Reflectivity
Langmuir, **37** 9873-9882 (2021).

181 M. Akamatsu, K. Saito, H. Iwase, T. Ogura, K. Sakai, H. Sakai
Contrast variation small-angle neutron scattering study of solubilization of perfumes in cationic surfactant micelles
Langmuir, **37** 10770–10775 (2021).

182 M. Harada, M. Yamamoto, H. Iwase
Combined small-angle neutron scattering/small-angle X-ray scattering analysis for the characterization of silver nanoparticles prepared via photoreduction in water-in-oil microemulsions
Langmuir, **37** 13085 (2021).

183 A. Izumi, Y. Shudo, M. Shibayama, N. Miyata, T. Miyazaki, H. Aoki
In Situ Neutron Reflectometry Analysis of Interfacial Structure Formation between Phenolic Resin and Silica during Curing
Langmuir, **37** 13867-13872 (2021).

184 K. Shimokita, K. Yamamoto, N. Miyata, Y. Nakanishi, H. Ogawa, M. Takenaka, N. L. Yamada, T. Miyazaki
Investigation of Interfacial Water Accumulation between Polypropylene Thin Film and Si Substrate by Neutron Reflectivity
Langmuir, **37** 14550–14557 (2021).

185 H. Taneda, N. L. Yamada, F. Nemoto, Y. Minagawa, H. Matsuno, K. Tanaka
Modification of a Polymer Surface by Partial Swelling Using Non-solvents
Langmuir, **37** 14941–14949 (2021).

186 H. Ogawa, M. Takenaka, T. Miyazaki
Molecular Weight Effect on the Transition Processes of a Symmetric PS-b-P2VP during Spin-Coating
Macromolecules, **54** 1017 (2021).

187 Y. Kimura, S. Imai, M. Takenaka, T. Terashima
Amphiphilic random cyclocopolymers as versatile scaffolds for ring-functionalized and self-assembled materials
Macromolecules, **54** 3987 (2021).

188 K. Aizawa, W. Gong, S. Harjo, T. Kawasaki
Kink Deformation Dynamics of LPSO Alloy from the Experimental Viewpoint of Multilayer Structure Deformation
Magnesium 2021, 247-254 (2021).

189 X. X. Zhang, H. Andrä, S. Harjo, W. Gong, T. Kawasaki, A. Lutz, M. Lahres
Quantifying internal strains, stresses, and dislocation density in additively manufactured AlSi10Mg during loading-unloading-reloading deformation
Mater. Des., **198** 109339 (2021).

190 H. Saitoh, T. Sato, M. Tanikami, K. Ikeda, A. Machida, T. Watanuki, T. Taguchi, S. Yamamoto, T. Yamaki, S. Takagi, T. Otomo, S. Orimo
Hydrogen storage by earth-abundant metals, synthesis and characterization of $Al_3FeH_{3.9}$
Mater. Des., 109953 (2021).

191 S. Shamoto, M. K. Lee, Y. Fujimura, K. Kondo, T. U. Ito, K. Ikeuchi, S. Yasuda, L.-J. Chang
Gallium-effect in a lead-free solder for silver-sheathed superconducting tape
Mater. Res. Express, **8** 076303 (2021).

192 T. Yamashita, N. Koga, T. Kawasaki, S. Morooka, S. Tomono, O. Umezawa, S. Harjo
Work hardening behavior of dual phase copper–iron alloy at low temperature
Mater. Sci. Eng. A Struct. Mater., **819** 141509 (2021).

193 M. Kumagai, K. Akita, M. Kuroda, S. Harjo
In situ diffraction characterization on microstructure evolution in austenitic stainless steel during cyclic plastic deformation and its relation to the mechanical response
Mater. Sci. Eng. A Struct. Mater., **820** 141582 (2021).

194 Y. S. Kim, H. Chae, W. Woo, D. K. Kim, D. H. Lee, S. Harjo, T. Kawasaki, S. Y. Lee
Multiple deformation scheme in direct energy deposited CoCrNi medium entropy alloy at 210K
Mater. Sci. Eng. A Struct. Mater., **828** 142059 (2021).

195 W. Mao, W. Gong, T. Kawasaki, S. Harjo
Effect of deformation-induced martensitic transformation on non-uniform deformation of metastable austenitic steel
Mater. Sci. Eng. A Struct. Mater., **837** 142758 (2021).

196 Y. S. Kim, H. Chae, E.-W. Huang, J. Jain, S. Harjo, T. Kawasaki, S. I. Hong, S. Y. Lee
Microstructural Evolution and Mechanical Properties of Non-Equiatomic $(CoNi)_{74.66}Cr_{17}Fe_8C_{0.34}$ High-Entropy Alloy
Materials, **15** 1312 (2021).

197 Y. Onuki, T. Hirano, K. Umemura, S. Sato, T. Tomida
In Situ Neutron Diffraction Measurement during Bainite Transformation and Accompanying Carbon Enrichment in Austenite

at iMATERIA, J-PARC MLF
Materials Science Forum, **1016** 1079 (2021).

198 T. Naoe, H. Kinoshita, H. Kogawa, T. Wakui, E. Wakai, K. Haga, H. Takada
Effect of Gas Microbubble Injection and Narrow Channel Structure on Cavitation Damage in Mercury Target Vessel
Materials Science Forum, **1024** 111 (2021).

199 T. Wakui, E. Wakai, H. Kogawa, T. Naoe, K. Hanano, K. Haga, T. Shimada, K. Kanomata
New Design of High Power Mercury Target Vessel of J-PARC
Materials Science Forum, **1024** 145 (2021).

200 S. Nishida, S. Nishino, M. Sekine, Y. Oka, S. Harjo, T. Kawasaki, H. Suzuki, Y. Morii, Y. Ishii
Analysis of Residual Stress in Steel Bar Processed by Cold Drawing and Straightening
Mater. Trans., **62** 667-674 (2021).

201 T. Nakagawa, D. Heshiki, H. Higa, J. Kawakami, R. Kobayashi, N. Hanada, K. Ikeda, T. Otomo, H. Ofuchi, M. Ishida
Structural properties of (Ti, Zr)(Mn,Cr)$_2$M$_{0.1}$ (M=none, Fe, Co, Ni, and Cu) hydrogen storage alloys: Composition distribution and occupied site of doped element
Mater. Trans., **62** 899 (2021).

202 N. Koga, O. Umezawa, M. Yamamoto, T. Yamamoto, T. Yamashita, S. Morooka, T. Kawasaki, S. Harjo
Effect of Solute Carbon on the Characteristic Hardening of Steel at High Temperature
Metall. Mater. Trans. A Phys. Metall. Mater. Sci., **52** 897-901 (2021).

203 N. Tsuchida, S. Harjo
Enhancement of Uniform Elongation by Temperature Change during Tensile Deformation in a 0.2C TRIP Steel
Metals, **11** 2053 (2021).

204 K. J. Gi, B. J. Wung, P. J. Min, W. Wanchuck, H. Stefanus, L. Sunghak, K. H. Seop
Effect of the Difference in Strength of Hard and Soft Components on the Synergetic Strengthening of Layered Materials
Metals and Materials International, **27** 376-383 (2021).

205 L. Temleitner, T. Hattori, J. Abe, Y. Nakajima, L. Pusztai
Pressure Dependent Structure of Methanol-Water Mixtures up 1.2 GPa: Neutron Diffraction Experiments and Molecular Dynamics Simulations
Molecules, **26** 1218 (2021).

206 H. He, M. Naeem, F. Zhang, Y. Zhao, S. Harjo, T. Kawasaki, B. Wang, X. Wu, S. Lan, Z. Wu, W. Yin, Y. Wu, Z. Lu, J-J. Kai, C-T. Liu, X-L. Wang
Stacking Fault Driven Phase Transformation in CrCoNi Medium Entropy Alloy
Nano Lett., **21** 1419-1426 (2021).

207 S. Gao, T. Broux, S. Fujii, C. Tassel, K. Yamamoto, Y. Xiao, I. Oikawa, H. Takamura, H. Ubukata, Y. Watanabe, K. Fujii, M. Yashima, A. Kuwabara, Y. Uchimoto, H. Kageyama
Hydride-based antiperovskites with soft anionic sublattices as fast alkali ionic conductors
Nat. Commun., **12** 201 (2021).

208 R. Yamane, K. Komatsu, J. Gouchi, Y. Uwatoko, S. Machida, T. Hattori, H. Ito, H. Kagi
Experimental evidence for the existence of a second partially-ordered phase of ice VI
Nat. Commun., **12** 1129 (2021).

209 P. Park, K. Park, J. Oh, K. H. Lee, J. C. Leiner, H. Sim, T. Kim, J. Jeong, K. C. Rule, K. Kamazawa, K. Iida, T. G. Perring, H. Woo, S.-W. Cheong, M. E. Zhitomirsky, A. L. Chernyshev, J.-G. Park
Spin texture induced by non-magnetic doping and spin dynamics in 2D triangular lattice antiferromagnet h-Y(Mn,Al)O$_3$
Nat. Commun., **12** 2306 (2021).

210 S.-Q. Su, S.-Q. Wu, M. Hagihala, P. Miao, Z. Tan, S. Torii, T. Kamiyama, T. Xiao, Z. Wang, Z. Ouyang, Y. Miyazaki, M. Nakano, T. Nakanishi, J.-Q. Li, S. Kanegawa, O. Sato
Water-oriented magnetic anisotropy transition
Nat. Commun., ***12*** 2738 (2021).

211 R. Okuma, M. Kofu, S. Asai, M. Avdeev, A. Koda, H. Okabe, M. Hiraishi, S. Takeshita, K. M. Kojima, R. Kadono, T. Masuda, K. Nakajima, Z. Hiroi
Dimensional reduction by geometrical frustration in a cubic antiferromagnet composed of tetrahedral clusters
Nat. Commun., **12** 4382 (2021).

212 G. Lin, J. Jeong, Y. Wang, Q. Huang, T. Masuda, S. Asai, S. Itoh, G. Günther, M. Russina, Z. Lu, J. Sheng, L. Wang, C. Kim, J. Wang, G. Wang, Q. Ren, C. Xi, W. Tong, L. Ling, Z. Liu, L. Wu, J. Mei, H. Zhou, Z. Qu, J.-G. Park, Y. Wan, J. Ma
Field induced quantum spin disordered state in spin-1/2 honeycomb magnet Na$_2$Co$_2$TeO$_6$ with small Kitaev interaction
Nat. Commun., **12** 5559 (2021).

213 P. Hua, M. Xia, Y. Onuki, Q. Sun
Nanocomposite NiTi shape memory alloy with high strength and fatigue resistance
Nat. Nanotechnol., **16** 409-413 (2021).

214 K. Yamanaka, M. Mori, K. Yoshida, Y. Onuki, S. Sato, A. Chiba
Surface evolution and corrosion behaviour of Cu-doped carbide-reinforced martensitic steels in a sulfuric acid solution
npj Mater. Degrad., **5** 43 (2021).

215 Y. Tsuchikawa, T. Kai, Y. Abe, Y. Ohishi, Y. Sun, K. Oikawa, T. Nakatani, I. Sato
Measurement of Doppler broadening of prompt gamma-rays from various zirconium- and ferro-borons
Nucl. Instrum. Methods Phys. Res. A, **991** 164964 (2021).

216 B. Ma, M. Teshigawara, Y. Wakabayashi, M. Yan, T. Hashiguchi, Y. Yamagata, S. Wang, Y. Ikeda, Y. Otake
Optimization of a slab geometry type cold neutron moderator for RIKEN accelerator-driven compact neutron source
Nucl. Instrum. Methods Phys. Res. A, **995** 165079 (2021).

217 N. Teshima, M. Aoki, Y. Higashino, H. Ikeuchi, K. Komukai, D. Nagao, Y. Nakatsugawa, H. Natori, Y. Seiyaa, N. M. Truong, K. Yamamoto
Development of a multiwire proportional chamber with good tolerance to burst hits
Nucl. Instrum. Methods Phys. Res. A, **999** 165228 (2021).

218 M. Harada, M. Teshigawara, M. Ooi, K. Oikawa, H. Takada, Y. Ikeda
Experimental characterization of high-energy component in extracted pulsed neutrons at the J-PARC spallation neutron source
Nucl. Instrum. Methods Phys. Res. A, **1000** 165252 (2021).

219 D. Vu, H. Shishido, K. Aizawa, K. M. Kojima, T. Koyama, K. Oikawa, M. Harada, T. Oku, K. Soyama, S. Miyajima, M. Hidaka, S. Y. Suzuki, M. M. Tanaka A. Malins M. Machida, S. Kawamata, T. Ishida
Practical tests of neutron transmission imaging with a superconducting kinetic-inductance sensor
Nucl. Instrum. Methods Phys. Res. A, **1006** 165411 (2021).

220 A. S. Tremsin, H. Z. Bilheux, J. C. Bilheux, T. Shinohara, K. Oikawa, Y. Gao
Calibration and optimization of Bragg edge analysis in energy-resolved neutron imaging experiments
Nucl. Instrum. Methods Phys. Res. A, **1009** 165493 (2021).

221 F. Funama, S. Tasaki, M. Hino, T. Oda, H. Endo

Double-focusing geometry for phase correction in neutron resonance spin-echo spectroscopy
Nucl. Instrum. Methods Phys. Res. A, **1010** 165480 (2021).

222 A. D. Pant, K. Nagamine, E. Torikai, I. Shiraki, K. Shimomura, F. L. Pratt, H. Ariga-Miwa, K. Ishida, J. S. Schultz
Muonium response to low oxygen levels in haemoglobin and other biological aqueous solutions and potential application towards monitoring hypoxia
Nucl. Instrum. Methods Phys. Res. A, **1011** 165561 (2021).

223 T. Oda, H. Endo, H. Ohshita, T. Seya, Y. Yasu, T. Nakajima, M. Hino, Y. Kawabata
Phase correction method in a wide detector plane for MIEZE spectroscopy with pulsed neutron beams
Nucl. Instrum. Methods Phys. Res. A, **1012** 165616 (2021).

224 S. Yamamoto, K. Ninomiya, N. Kawamura, T. Yabe, Y. Hirano
Three-dimensional (3D) optical imaging of muon beam using a plastic scintillator plate in water
Nucl. Instrum. Methods Phys. Res. A, **1015** 165768 (2021).

225 D. Gao, X. Tang, X. Wang, X. Yang, P. Zhang, G. Chu, J. Han, T. Hattori, Y. Wang, X. Dong, H. Zheng, K. Li, H-k. Mao
Phase transition and chemical reactivity of 1H-tetrazole under high pressure up to 100 GPa
Phys. Chem. Chem. Phys., **23** 19503 (2021).

226 M. Kawano, K. Sadakane, H. Iwase, M. Matsugami, B. A. Marekha, A. Idrissi, T. Takamuku
Assessment of the UCST-type liquid-liquid phase separation mechanism of imidazolium-based ionic liquid, [C_8mim][TFSI], and 1,4-dioxane by SANS, NMR, IR, and MD simulations
Phys. Chem. Chem. Phys., **23** 24449-24463 (2021).

227 L. A. Ma, R. Palm, E. Nocerino, O. K. Forslund, N. Matsubara, S. P. Cottrell, K. Yokoyama, A. Koda, J. Sugiyama, Y. Sassa, M. Mansson, R. Younes
Na-ion mobility in P2-type $Na_{0.5}Mg_xNi_{0.17-x}Mn_{0.83}O_2$ ($0 \le x \le 0.07$) from electrochemical and muon spin relaxation studies
Phys. Chem. Chem. Phys., **23** 24478-24486 (2021).

228 S. Kanda, Y. Fukao, Y. Ikedo, K. Ishida, M. Iwasaki, D. Kawall, N. Kawamura, K. M. Kojima, N. Kurosawa, Y. Matsuda, T. Mibe, Y. Miyake, S. Nishimura, N. Saito, Y. Sato, S. Seo, K. Shimomura, P. Strasser, K. S. Tanaka, T. Tanaka, H. A. Torii, A. Toyoda, Y. Ueno
New precise spectroscopy of the hyperfine structure in muonium with a high-intensity pulsed muon beam
Phys. Lett. B, **815** 136154 (2021).

229 S. Nishimura, H. A. Torii, Y. Fukao, T. U. Ito, M. Iwasaki, S. Kanda, K. Kawagoe, D. Kawall, N. Kawamura, N. Kurosawa, Y. Matsuda, T. Mibe, Y. Miyake, N. Saito, K. Sasaki, Y. Sato, S. Seo, P. Strasser, T. Suehara, K. S. Tanaka, T. Tanaka, J. Tojo, A. Toyoda, Y. Ueno, T. Yamanaka, T. Yamazaki, H. Yasuda, T. Yoshioka, K. Shimomura
Rabi-oscillation spectroscopy of the hyperfine structure of muonium atoms
Phys. Rev. A, **104** L02080 (2021).

230 R. Kitamura, S. Bae, S. Choi, Y. Fukao, H. Iinuma, K. Ishida, N. Kawamura, B. Kim, Y. Kondo, T. Mibe, Y. Miyake, M. Otani, G. P. Razuvaev, N. Saito, K. Shimomura, P. Strasser
Development of negative muonium ion source for muon acceleration
Phys. Rev. Accel. Beams, **24** 33403 (2021).

231 P. Miao, Z. Tan, S. Lee, Y. Ishikawa, S. Torii, M. Yonemura, A. Koda, K. Komatsu, S. Machida, A. Sano-Furukawa, T. Hattori, X. Lin, K. Li, T. Mochiku, R. Kikuchi, C. Kawashima, H. Takahashi, Q. Huang, S. Itoh, R. Kadono, Y. Wang, F. Pan, K. Yamauchi, T. Kamiyama
Origin of magnetvolume effect in a cobaltite
Phys. Rev. B, **103** 094302 (2021).

232 J. Sugiyama, W. Higemoto, D. Andreica, O. K. Forslund, E. Nocerino, M. Månsson, Y. Sassa, R. Gupta, R. Khasanov, H. Ohta, H. Nakamura
Pressure dependence of ferromagnetic phase boundary in $BaVSe_3$ studied with high-pressure μ^+SR
Phys. Rev. B, **103** 104418 (2021).

233 Z. H. Zhu, J. Zhang, Z. F. Ding, C. Tan, C. S. Chen, Q. Wu, Y. X. Yang, O. O. Bernal, P.-C. Ho, G. D. Morris, A. Koda, A. D. Hillier, S. P. Cottrell, P. J. Baker, P. K. Biswas, J. Qian, X. Yao, D. E. MacLaughlin, L. Shu
Muon spin relaxation and fluctuating magnetism in the pseudogap phase of $YBa_2Cu_3O_y$
Phys. Rev. B, **103** 134426 (2021).

234 H. Okabe, M. Hiraishi, A. Koda, S. Takeshita, K. M. Kojima, I. Yamauchi, T. Ohsawa, N. Ohashi, H. Sato, R. Kadono
Local electronic structure of dilute hydrogen in β–MnO_2
Phys. Rev. B, **103** 155121 (2021).

235 T. Omi, Y. Watanabe, N. Abe, H. Sagayama, A. Nakao, K. Munakata, Y. Tokunaga, T. Arima
Antiferromagnetic-to-ferrimagnetic phase transition with large electric-polarization change in a frustrated polar magnet $CaBaCo_4O_7$
Phys. Rev. B, **103** 184412 (2021).

236 P. Wu, K. Xia, K. Peng, T. Honda, K. Ikeda, F. Liu, P. Vallobra, F. Fan, J. Song, D. Zhang, F. Yu, J. Ying, F. Zhu, T. Otomo, T. Kamiyama, W. Zhao
Strong anharmonicity in tin monosulfide evidenced by local distortion, high-energy optical phonons, and anharmonic potential
Phys. Rev. B, **103** 195204 (2021).

237 W. Chen, X. Li, Z. Hu, Z. Hu, L. Yue, R. Sutarto, F. He, K. Iida, K. Kamazawa, W. Yu, X. Lin, Y. Li
Spin-orbit phase behavior of $Na_2Co_2TeO_6$ at low temperatures
Phys. Rev. B, **103** L180404 (2021).

238 M. Hiraishi, K. M. Kojima, H. Okabe, A. Koda, R. Kadono, J. Wu, Y. Lu, H. Hosono
Anomalous diamagnetism of electride electrons in transition metal silicides
Phys. Rev. B, **103** L241101 (2021).

239 N. Higa, T. U. Ito, M. Yogi, T. Hattori, H. Sakai, S. Kambe, Z. Guguchia, W. Higemoto, M. Nakashima, Y. Homma, A. Nakamura, F. Honda, Y. Shimizu, D. Aoki, M. Kakihana, M. Hedo, T. Nakama, Y. Ōnuki, Y. Tokunaga
Critical slowing-down and field-dependent paramagnetic fluctuations in the skyrmion host EuPtSi: μSR and NMR studies
Phys. Rev. B, **104** 045145 (2021).

240 M. Matsuura, Y. Fujiwara, H. Moriwake, K. Ohara, Y. Kawakita
Microscopic dynamics of lithium diffusion in single crystal of the solid-state electrolyte La2/3–x$Li_{3x}TiO_3$ (x = 0.13) studied by quasielastic neutron scattering
Phys. Rev. B, **104** 094305 (2021).

241 Y. Shangguan, S. Bao, Z.-Y. Dong, Z. Cai, W. Wang, Z. Huang, Z. Ma, J. Liao, X. Zhao, R. Kajimoto, K. Iida, D. Voneshen, S.-L. Yu, J.-X. Li, J. Wen
Evidence for strong correlations at finite temperatures in the dimerized magnet $Na_2Cu_2TeO_6$
Phys. Rev. B, **104** 224430 (2021).

242 M. Miyajima, F. Astuti, T. Fukuda, M. Kodani, S. Iida, S. Asai, A. Matsuo, T. Masuda, K. Kindo, T. Hasegawa, T. C. Kobayashi, T. Nakano, I. Watanabe, T. Kambe
Spin-gap formation due to spin-Peierls instability in π-orbital-ordered NaO_2
Phys. Rev. B, **104** L140402 (2021).

243 W. Hong, L. Liu, C. Liu, X. Ma, A. Koda, X. Li, J. Song, W. Yang, J. Yang, P. Cheng, H. Zhang, W. Bao, X. Ma, D. Chen, K. Sun, W. Guo, H. Luo,

A. W. Sandvik, S. Li
Extreme Suppression of Antiferromagnetic Order and Critical Scaling in a Two-Dimensional Random Quantum Magnet
Phys. Rev. Lett., **126** 037201 (2021).

244 T. Okumura, T. Azuma, D. A. Bennett, P. Caradonna, I-H. Chiu, W. B. Doriese, M. S. Durkin, J. W. Fowler, J. D. Gard, T. Hashimoto, R. Hayakawa, G. C. Hilton, Y. Ichinohe, P. Indelicato, T. Isobe, S. Kanda, D. Kato, M. Katsuragawa, N. Kawamura, Y. Kino, K. M. Kubo, K. Mine, Y. Miyake, K. M. Morgan, K. Ninomiya, H. Noda, G. C. O'Neil, S. Okada, K. Okutsu, T. Osawa, N. Paul, C. D. Reintsema, D. R. Schmidt, K. Shimomura, P. Strasser, H. Suda, D. S. Swetz, T. Takahashi, S. Takeda, S. Takeshita, M. Tampo, H. Tatsuno, X.-M. Tong, Y. Ueno, J. N. Ullom, S. Watanabe, S. Yamada
Deexcitation Dynamics of Muonic Atoms Revealed by High-Precision Spectroscopy of Electronic K X rays
Phys. Rev. Lett., **127** 053001 (2021).

245 M. Nagao, E.G. Kelley, A. Faraone, M. Saito, Y. Yoda, M. Kurokuzu, S. Takata, M. Seto, P.D. Butler
Relationship between viscosity and acyl tail dynamics in lipid bilayers
Phys. Rev. Lett., **127** 078102 (2021).

246 K. Hagiwara, M. Ishikado, M. Horio, K. Koshiishi, S. Nakata, S. Ideta, K. Tanaka, K. Horiba, K. Ono, H. Kumigashira, T. Yoshida, S. Ishida, H. Eisaki, S. Shamoto, A. Fujimori
Superconducting gap and pseudogap in the surface states of the iron-based superconductor $PrFeAsO_{1-y}$ studied by angle-resolved photoemission spectroscopy
Phys. Rev. Research, **3** 043151 (2021).

247 Y. Hirano, S. Yamamoto, N. Kawamura, K. Ninomiya
Position distribution calculation of annihilation radiations and bremsstrahlung x rays in water during irradiation of positive muons: a Monte Carlo simulation study
Phys. Scr., **96** 025302 (2021).

248 O. K. Forslund, D. Andreica, H. Ohta, M. Imai, C. Michioka, K. Yoshimura, M. Månsson, J. Sugiyama
Co-existence of short- and long-range magnetic order in $LaCo_2P_2$
Phys. Scr., **96** 125864-1 (2021).

249 A. D. Pant, K. Ishida, N. Kawamura, S. Matoba, A. Koda, S. Nishimura, K. Shimomura
Study of muonium behavior in n-type silicon for generation of ultra cold muonium in vacuum
Physica B Condens. Matter., **613** 412997 (2021).

250 Y. Zhai, P. Luo, M. Nagao, K. Nakajima,T. Kikuchi,Y. Kawakita, P. A. Kienzle, Y Z, A. Faraone
Relevance of hydrogen bonded associates to the transport properties and nanoscale dynamics of liquid and supercooled 2-propanol
Phys. Chem. Chem. Phys.s, **23** 7220-7232 (2021).

251 T. Hayashida, Y. Uemura, K. Kimura, S. Matsuoka, M. Hagihala, S. Hirose, H. Morioka, T. Hasegawa, T. Kimura
Phase transition and domain formation in ferroaxial crystals
Phys. Rev. Mater., **5** 124409 (2021).

252 S. Shamoto, H. Yamauchi, K. Ikeuchi, R. Kajimoto, J. Ieda
Broken C_4 symmetry in the tetragonal state of uniaxial strained $BaCo_{0.9}Ni_{0.1}S_{1.9}$
Phys. Rev. Res., **3** 013169 (2021).

253 S. Hasegawa, S. Hayashida, S. Asai, M. Matsuura, Z. Igor, T. Masuda
Nontrivial temperature dependence of magnetic anisotropy in multiferroics $Ba_2MnGe_2O_7$
Phys. Rev. Res., **3** L032023 (2021).

254 T. Maeda, M. Kitagawa, A. Hotta
Degradation of thermoresponsive laponite/PEG-b-PLGA nanocomposite hydrogels controlled by blending PEG-b-PLGA di-block copolymers with different PLGA molecular weights
Polym. Degrad. Stab., **187** 109535 (2021).

255 S. Hiroshige, H. Minato, Y. Nishizawa, Y. Sasaki, T. Kureha, M. Shibayama, K. Uenishi, T. Takata, D. Suzuki
Temperature-dependent relationship between the structure and mechanical strength of volatile organic compound-free latex films prepared from poly(butyl acrylate-co-methyl methacrylate) microspheres
Polym. J., **53** 345 (2021).

256 J.-H. Hong, M. Totani, D. Kawaguchi, N. L. Yamada, H. Matsuno, K. Tanaka
Poly[oligo(2-ethyl-2-oxazoline) methacrylate] as a surface modifier for bioinertness
Polym. J., **53** 643-653 (2021).

257 G. Ichikawa, Y. Fuwa, T. Hasegawa, M. Hino, K. Hirota, T. Ino, Y. Iwashita, M. Kitaguchi, J. Koga, S. Matsuzaki, K. Mishima, T. Mogi, K. Morikawa, H. Okabe, H. Otono, Y. Seki, D. Sekiba, T. Shima, H. Shimizu, H. Shimizu, N. Sumi, H. Sumino, S. Yamashita, K. Yano, T. Yoshioka
Neutron lifetime experiment with pulsed cold neutrons at J-PARC
Pos. Proc. Sci. (PANIC2021), **457** (2021).

258 T. Mogi, T. Hasegawa, K. Hirota, G. Ichikawa, S. Ieki, T. Ino, Y. Iwashita, S. Kajiwara, Y. Kato, M. Kitaguchi, R. Kitahara, J. Koga, S. Makise, S. Matsuzaki, K. Mishima, K. Morikawa, N. Nagakura, H. Okabe, H. Otono, Y. Seki, D. Sekiba, T. Shima, H. E. Shimizu, H. M. Shimizu, Y. Sugisawa, N. Sumi, H. Sumino, T. Tanabe, T. Tomita, H. Uehara, T. Yamada, S. Yamashita, K. Yano, T. Yoshioka
Improvement of systematic uncertainties for the neutron lifetime experiment at J-PARC
Pos. Proc. Sci. (PANIC2021), **458** (2021).

259 S. Ishida, D. Kagerbauer, S. Holleis, K. Iida, K. Munakata, A. Nakao, A. Iyo, H. Ogino, K. Kawashima, M. Eisterer, H. Eisaki
Superconductivity-driven ferromagnetism and spin manipulation using vortices in the magnetic superconductor $EuRbFe_4As_4$
Proc. Natl. Acad. Sci. USA, **118** e2101101118 (2021).

260 K. Akutsu, M. Sahara, M. Ueda, T. Niizeki, M. Yoshii, T. Sugiyama, N. Eguchi, T. Wada
Development of new waterproof thin-layers for the magnetic alloy core: structural studies using neutron reflectometry
Proc. of the 18th Annual Meeting of Particle Accelerator Society of Japan, August 9-11, 2021, Takasaki, Japan, **600** (2021).

261 K. Haga, H. Kogawa, T. Naoe, T. Wakui, E. Wakai, M. Futakawa
Development of the high-power spallation neutron target of J-PARC
Proc. The 19th International Topical Meeting on Nuclear Reactor Thermal Hydraulics (NURETH-19), Log nr.: 3392 (2021).

262 K. S. Tanaka, M. Iwasaki, O. Kamigaito, S. Kanda, N. Kawamura, Y. Matsuda, T. Mibe, S. Nishimura, N. Saito, N. Sakamoto, S. Seo, K. Shimomura, P. Strasser, K. Suda, T. Tanaka, H. A. Torii, A. Toyoda, Y. Ueno, M. Yoshida
Development of microwave cavities for measurement of muonium hyperfine structure at J-PARC
Prog. Theor. Exp. Phys., **2021** 053C01 (2021).

263 Y. Onuki, S. Sato
In Situ Observation for Deformation-Induced Martensite Transformation during Tensile Deformation of SUS 304 Stainless Steel by Using Neutron Diffraction PART II: Transformation and Texture Formation Mechanisms
Quantum Beam Sci., **5** 6 (2021).

264 F. Grazzi, C. Cialdai, M. Manetti, M. Massi, M. P. Morigi, M. Bettuzzi, R. Brancaccio, F. Albertin, T. Shinohara, T. Kai, A. Fedrigo, A. Di Giovanni, F. Arneodo, R. Torres, O. Al-Ketan, J. Elhashemi, F.

Taccetti, L. Giuntini
A multi-technique tomography-based approach for non-invasive characterization of additive manufacturing components in view of vacuum/UHV applications: preliminary results
Rend. Lincei. Sci. Fis. Nat., (2021).

265 Y. Nishizawa, H. Minato, T. Inui, I. Saito, T. Kureha, M. Shibayama, T. Uchihashi, D. Suzuki
Nanostructure and thermoresponsiveness of poly(N-isopropyl methacrylamide)-based hydrogel microspheres prepared via aqueous free radical precipitation polymerization
RSC Adv., **11** 13130 (2021).

266 M. Uchida, S. Sato, H. Ishizuka, R. Kurihara, T. Nakajima, Y. Nakazawa, M. Ohno, M. Kriener, A. Miyake, K. Ohishi, T. Morikawa, M. S. Bahramy, T. Arima, M. Tokunaga, N. Nagaosa, M. Kawasaki
Above-ordering-temperature large anomalous Hall effect in a triangular-lattice magnetic semiconductor
Sci. Adv., **7** abl5381 (2021).

267 Y. Ohtsuka, N. Kanazawa, M. Hirayama, A. Matsui, T. Nomoto, R. Arita, T. Nakajima, T. Hanashima, V. Ukleev, H. Aoki, M. Mogi, K. Fujiwara, A. Tsukazaki, M. Ichikawa, M. Kawasaki, Y. Tokura
Emergence of spin-orbit coupled ferromagnetic surface state derived from Zak phase in a nonmagnetic insulator FeSi
Sci. Adv., **7** eabj0498 (2021).

268 Y. Hao, H. Wo, Y. Gu, X. Zhang, Y. Gu, S. Zheng, Y. Zhao, G. Xu, J. W. Lynn, K. Nakajima, N. Murai, W. Wang, J. Zhao
Field-tuned magnetic structure and phase diagram of the honeycomb magnet $YbCl_3$
Sci. China Phys. Mech. Astron., **64** 237411 (2021).

269 Y. Su, K. Oikawa, T. Shinohara, T. Kai, T. Horino, O. Idohara, Y. Misaka, Y. Tomota
Neutron Bragg-edge transmission imaging for microstructure and residual strain in induction hardened gears
Sci. Rep., **11** 4155 (2021).

270 M. Akamatsu, K. Kobayashi, H. Iwase, Y. Sakaguchi, R. Tanaka, K. Sakai, H. Sakai
Rapid controlled release by photo-irradiation using morphological changes in micelles formed by amphiphilic lophine dimers
Sci. Rep., **11** 10754 (2021).

271 M. Kofu, R. Watanuki, T. Sakakibara, S. Ohira-Kawamura, K. Nakajima, M. Matsuura, T. Ueki, K. Akutsu, O. Yamamuro
Spin glass behavior and magnetic boson peak in a structural glass of a magnetic ionic liquid
Sci. Rep., **11** 12098 (2021).

272 R. Iizuka-Oku, H. Gotou, C. Shito, K. Fukuyama, Y. Mori, T. Hattori, A. Sano-Furukawa, K. Funakoshi, H. Kagi
Behavior of light elements in iron-silicate-water-sulfur system during early Earth's evolution
Sci. Rep., **11** 12632 (2021).

273 M. Busi, N. Kalentics, M. Morgano, S. Griffiths, A. S. Tremsin, T. Shinohara, R. Logé, C. Leinenbach, M. Strobl
A parametric neutron Bragg edge imaging study of additively manufactured samples treated by laser shock peening
Sci. Rep., **11** 14919 (2021).

274 H. Aoki, Y. Liu, T. Yamashita
Deep learning approach for an interface structure analysis with a large statistical noise in neutron reflectometry
Sci. Rep., **11** 22711 (2021).

275 M.-S. Lee, T. Kawasaki, T. Yamashita, S. Harjo, Y.-T. Hyun, Y. Jeong, T.-S. Jun
I*n-situ neutron diffraction study of lattice deformation behaviour of commercially pure titanium at cryogenic temperature*
Sci. Rep., **12** 3719 (2021).

276 H. Nakao, Y. Kimura, A. Sakai, K. Ikeda, M. Nakano
Development of membrane-insertable lipid scrambling peptides: A time-resolved smallangle neutron scattering study
Struct. Dyn., **8** 24301 (2021).

277 T. D. Vu, H. Shishido, K. Kojima, T. Koyama, K. Oikawa, M. Harada, S. Miyajima, T. Oku, K. Soyama, K. Aizawa, M. Hidaka, S. Suzuki, M. Tanaka, A. Malins, M. Machida, T. Ishida
Homogeneity of neutron transmission imaging over a large sensitive area with a four-channel superconducting detector
Supercond. Sci. Technol., **34** 15010 (2021).

278 S. Harjo, T. Kawasaki, N. Tsuchida, S. Morooka, W. Gong
Relation between Intergranular Stress in Austenite and Martensitic Transformation in TRIP Steels Revealed by Neutron Diffraction
Tetsu to Hagane, **107** 887-896 (2021).

279 H. Yoshida, A. Yamamoto, S. Hosokawa, S. Yamazoe, S. Kikkawa, K. Hara, M. Nakamura, K. Kamazawa, T. Tanaka
Observation of Adsorbed Hydrogen Species on Supported Metal Catalysts by Inelastic Neutron Scattering
Top. Catal., **64** 660-671 (2021).

280 N. Yamashita, T. Hirayama, N. L. Yamada, H. Watanabe, K. Onodera, T. Sato
Highly Swollen Adsorption Layer Formed by Polymeric Friction Modifier Providing Low Friction at Higher Temperature
Tribol. Lett., **69** 65 (2021).

281 K. Sakai, Y. Ayame, Y. Iwanami, N. Kimura, Y. Matsumoto
Observation of Grease Fluidity in a Ball Bearing Using Neutron Imaging Technology
Tribology Online, **16** 146-150 (2021).

282 A. Yoshiasa, T. Tobase, H. Arima-Osonoi, K. Funakoshi, O. Ohtaka, T. Nakatani, S. Kohara
High-temperature diffraction experiments and phase diagram of ZrO_2 and $ZrSiO_4$
Z. Naturforsch. B J. Chem. Sci., (2021).

283 J. Sugiyama, K. Ohishi, O. K. Forslund, M. Månsson, S. P. Cottrell, A. D. Hillier, K. Ishida
How Li diffusion in spinel $Li[Ni_{1/2}Mn_{3/2}]O_4$ is seen with $\mu^{\pm}SR$
Z. Phys. Chem., (2021).

Editorial Board - MLF Annual Report 2021

J-PARC

JAPAN PROTON ACCELERATOR RESEARCH COMPLEX

High Energy Accelerator Research Organization (KEK)
Japan Atomic Energy Agency (JAEA)

http://j-parc.jp/

Materials and Life Science Division
J-PARC Center

https://mlfinfo.jp/en

CROSS

Comprehensive Research Organization for Science and Society

https://neutron.cross.or.jp/en

J-PARC 22-02